Corrosion protection using conducting polymers

Jan Magnus Gustavsson
University of Wollongong

CORROSION PROTECTION USING CONDUCTING POLYMERS

A thesis submitted in fulfilment of the requirements
for the award of the degree

DOCTOR OF PHILOSOPHY

from the

UNIVERSITY OF WOLLONGONG

by

JAN MAGNUS GUSTAVSSON, B.Sc., M.Sc.

ACES
DEPARTMENT OF CHEMISTRY
March 2006

CERTIFICATION

I, Magnus Gustavsson, declare that this thesis, submitted in fulfilment of the requirements for the award of Doctor of Philosophy, in the Department of Chemistry, University of Wollongong, is wholly my own work unless otherwise referenced or acknowledged. The document has not been submitted for qualifications at any other university or institution.

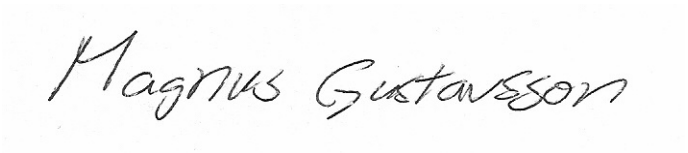

Magnus Gustavsson

31 March 2006.

TABLE OF CONTENTS

LIST OF FIGURES

Figure 6.5 Optical image of scribed PAn/co-polymer coating on AA2024-T3 in DHS after 15 min immersion using x10 magnification with area of Raman mapping are superimposed.

Figure 6.6 In-situ Raman spectroscopy of PAn/co-poly coated AA2024-T3 in DHS under ambient conditions with coating containing artificial defect. Spectra recorded after 10 min immersion. Black: 250 μm distance from defect, Red: At the very edge of the coating, Blue: Point within the defect. Immersion time: 10 min.

Figure 6.7 In-situ Raman map of the peak area ratio of 1610 cm^{-1}/1590 cm^{-1} of a scribed PAn/co-poly on AA2024-T3 immersed in DHS. Peak area was obtained with Gaussian peak fitting after intensity was normalised using the sum of the two peaks. TL: 15 min, TR: 1 hour, ML: 1 hour 40 min, MR: 5 hours 25 min, BL: 6 hours, BR: 7 hours 30 min

Figure 6.8 Optical image of scribed PAn/co-poly coating on AA2024-T3 in DHS after prior to immersion using x50 magnification with superimposed points were Raman spectra was recorded.

Figure 6.9 In-situ Raman spectroscopy of PAn/co-poly coated AA2024-T3 relative to an artificial defect recorded prior to immersion.

Figure 6.10 In-situ Raman spectroscopy of PAn/co-poly coated AA2024-T3 in DHS under N_2 atmosphere with coating containing artificial defect. Spectra recorded after 15 min immersion.

Figure 6.11 In-situ Raman spectroscopy of PAn/co-poly coated AA2024-T3 in DHS under N_2 atmosphere with coating containing artificial defect. Spectra recorded after 60 min immersion.

Figure 6.12 In-situ Raman spectroscopy of PAn coated AA2024-T3 in DHS under N_2 atmosphere with coating containing artificial defect. Spectra recorded after 3 hours 30 min immersion.

Figure 6.13 In-situ Raman spectroscopy of PAn/co-poly coated AA2024-T3 in DHS under N_2 atmosphere with coating containing artificial defect. Spectra recorded after 7 hours immersion.

LIST OF TABLES

ABSTRACT

Concern over the toxicity and environmental impact by use of chromate containing coating coatings has fuelled efforts to find suitable replacements. One class of materials considered as a potential replacement for chromate coatings are the intrinsically conducting polymers (ICP's). This thesis describes the synthesis and characterization of a range of ICP materials with emphasis on producing processable ICP and their use as corrosion protection coatings for aluminium alloy 2024-T3 and Zn-55%Al- hot dipped coated steel, two substrates that commonly employ chromate coatings for adequate protection. A general introduction to corrosion and ICP's are given in Chapter 1 with techniques employed to study corrosion inhibition detailed in Chapter 2.

Processability of Polyaniline was afforded by making of composite material to produce Polyaniline-HCSA/Poly(butyl acrylate-vinyl acetate) copolymer (PAn/co-poly) possessing moderate conductivity and electroactivity (Chapter 3). PAn/co-poly was highly soluble and could be applied as a coating to AA2024-T3 by airbrushing. Polypyrrole was afforded processability by monomer substitution to produce soluble Poly(3-octylpyrrole). Material synthesis was optimised to produce a maximum conductivity for the soluble ICP that could be applied to a metal surface by airbrushing or evaporative casting. Conductive, soluble P3OP was synthesised both through electrochemical and chemical synthesis P3OP route

Corrosion inhibition offered by ICP evaluated using Potentiodynamic polarisation and Electrochemical Impedance spectroscopy (EIS) (Chapter 4) suggests an interaction between the ICP coating and the underlying substrate. PAn/co-poly was observed to provide an anodic shift to the OCP of coated AA2024-T3. Increasing R_c and R_{ct} during exposure suggested that the coating converted towards a less conductive form. Exposure of conductive P3OP-ClO_4 coated AA2024-T3 also resulted in increasing R_{ct} overtime, ascribed to the formation of protective oxide.

Local corrosion behaviour within a coating defect was studied by SVET (Chapter 5). SVET demonstrated that PAn/co-poly accelerated corrosion within a defect without formation of protective oxide. Conductive fractions of P3OP exhibited decreasing oxidation within coating defect overtime suggesting the formation of an oxidation product that hinders further corrosion. Raman spectroscopy (Chapter 6) as well as visual observations (Chapter 4 and 5) suggest that oxidation of the substrate was promoted by the ICP that undergoes reduction. For P3OP this leads to lower corrosion current density within surface a defect suggesting that P3OP does protect against corrosion through anodic protection.

ACKNOWLEDGMENTS

This thesis, the conclusion of several years work, is a result that I could not have achieved without the support of many people to whom I would like to express my gratitude.

Foremost I would like to express gratitude towards my supervisors; Professor Gordon Wallace and Doctor Peter Innis to whom I am deeply indebted. Only with their insight, encouragement and unwavering support far beyond the call of duty has this work been possible.

I would also like to extend my appreciation to Professor Dennis E. Tallman (North Dakota State University, USA) who has allowed me to visit and work with the NDSU corrosion group as well as being an exceptionally good host during my visits. I furthermore wish to extend my appreciation to staff and student of the corrosion group at North Dakota State University, USA. In particular Doctor Jie He for providing training and assistance in operation of the SVET instrument. I would also like to acknowledge Dr. Evan Evans from BlueScope Steel Limited for his support during this entire project. Also special thanks to all staff and students at IPRI for creating a friendly and positive work environment.

This work was produced with the financial assistance of the Australian Research Council and BlueScope Steel Limited.

Chapter 1- General Introduction

1.1 Background

Corrosion is a process that takes place around us everyday. Its aspects are commonly recognised in everyday life ranging from; squeaking hinges, nuts and bolts that can't be loosened to the brittle red/brown material that's eating away our almost "brand new" car. These occurrences are the result of a thermodynamically driven process of a metal converting to a more stable state. Usually this state is a metal oxide, a similar state to the material commonly found in nature from which the metal was refined from in the first place. For this reason the processes of corrosion has been described as metallurgy in reverse. [1] The processes of "metals to ore conversion" or corrosion is the basis of significant cost to all developed nations. A 2001 report on corrosion costs in the United States determined a direct cost of $276 billion annually or 3.2 % of the U.S. gross domestic product with an estimated indirect cost at least equal to the direct cost. [2] In addition to the financial cost corrosion can, if unchecked result in failure of the metal structure leading to injuries and death. Hoeppner *et al.* [3] looked into the cause of aircraft incidents and accidents in the

USA from 1983 to 1994 and found; 91 incidents and accidents could be related to corrosion, with seven of those listings pitting corrosion as the main cause of failure.

The pursuit of means to delay the process of corrosion has led to today's world wide use of corrosion inhibition based on chromates. Chromates have for a long time provided unmatchable corrosion inhibition. A major drawback of using chromates is its toxicity and environmental effects which has resulted in legislative restriction on its use, with further usage restrictions being anticipated. [4] Among several new corrosion inhibition systems studied as a possible replacement for the use of chromates are the intrinsically conducting polymers (ICP's). ICP's were first observed to provide passivaton to stainless steel under highly acidic conditions by Deberry *et al.* in 1985. [5] The field of corrosion protection using ICP's has generated significant interest in the last 30 years.

1.2 Introduction to Corrosion

This section outlines the basic concept of corrosion and introduces terminology used in later chapters. Complete and more in depth introduction to corrosion can be found elsewhere. [1, 6]

Corrosion is the destruction of a metal by a chemical or electrochemical reaction. With a few exceptions all metals corrode in contact with water including moisture in air. Under these conditions metal atom (M) undergoes oxidation by donating electrons to an electron acceptor according to (1.1). The charge transfer process is

achieved by electrons moving within the conductive metal resulting in the reduction of a reduction species (N) according to (1.2), with the charge balance achieved by an ionic current path in the opposite direction. The two sites, connected electronically by the metal and ionically by the electrolyte, are together referred to as a corrosion cell, shown schematically in Figure 1.1. The site of oxidation is referred to as the anode and the reduction site as the cathode.

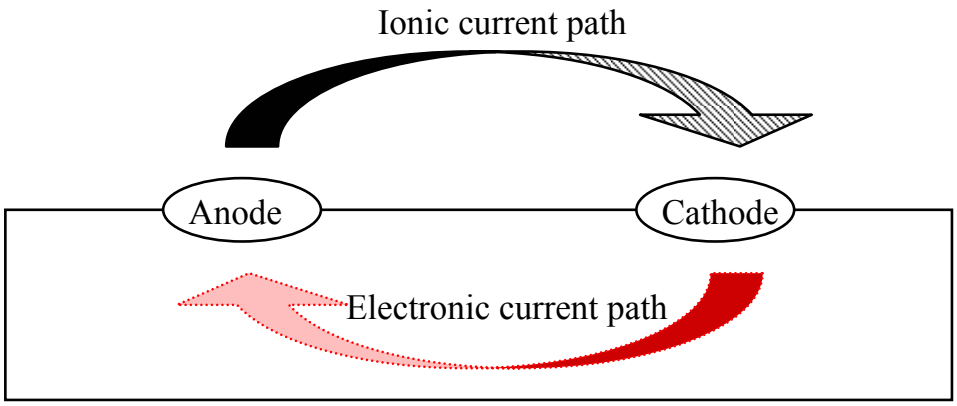

Figure 1.1 Schematic of electrochemical corrosion cell where a potential difference between the two sites drives the current.

$$M \rightarrow M^{m+} + m\, e^{-} \qquad (1.1)$$

$$N + n\, e^{-} \rightarrow N^{n-} \qquad (1.2)$$

A potential difference between the two sites drives the corrosion current. The rate at which a metal corrodes depends on the magnitude of the corrosion current. All methods of corrosion protection aim to limit the magnitude of the corrosion current. The current (i.e. the corrosion rate) can be reduced by limiting the production (oxidation at the anode) or consumption (reduction at the cathode) of electrons or by limiting the rate of ionic charge transfer. This can be achieved by removal of the

electrolytic pathways from the metal by application of a physical barrier such as an insulating coating. Though since no coating barrier removes the electrolytic path ways indefinitely, protection using a physical barrier is often employed together with other means of controlling corrosion.

1.2.1 Cathodic Protection

Cathodic protection is achieved by lowering the potential of the metal being protected by connecting the metal to a corrosion cell were the protected metal forms the cathode and another anodic reaction (the oxidation) instead takes place away from the metal. Two principal means are used to achieve such a corrosion cell; sacrificial anode and impressed-current. Sacrificial anode utilizes a less noble metal electrically connected to the metal being protected to form a corrosion cell where the sacrificial anode corrodes preferentially thus protecting the cathode from corrosion. Impressed-current method instead uses an external power source to produce a corrosion cell were the metal being protected is connected as the cathode.

1.2.2 Anodic Protection

Anodic protection is instead achieved by raising the potential of the metal being protected. The higher potential alters the corrosion product formed to create a protective surface keeping the metal in a “passive region” were the corrosion current is reduced.

1.2.3 Chemical Inhibition

Chemical corrosion inhibitors generally prevent corrosion by forming or promoting the formation of an adsorption layer on the metal surface thus separating the metal surface and the electrolyte containing water. The inhibitor can function either by limiting the anodic reaction (anodic inhibitor), the cathodic reaction (cathodic inhibitor) or both (mixed inhibitor). Some inhibitor also promotes the formation of a passive layer on the metal surface (passivating inhibitor).

1.3 Corrosion of Aluminium Alloy 2024-T3

Aluminium metal itself is thermodynamically a highly reactive metal but at the same time possesses considerable corrosion resistance due to the formation of a protective aluminium oxide layer or "passive film". The inert oxide layer, a few nm thick, prevents further corrosion and damage of the film by a scratch will result in immediately reforming the oxide layer. The passive film forms by aluminium oxidation with oxygen in air and in water according to (1.3).

$$2\ Al + 3/2\ O_2 \rightarrow Al_2O_3 \qquad (1.3)$$

Under conditions where the anhydrous oxide is not stable the oxide will hydrate and no longer provide protection leading to corrosion. Simplified, aluminium corrosion in most aqueous systems proceed with the anodic (oxidation) half reaction according to (1.4)

$$Al \rightarrow Al^{3+} + 3\ e^- \qquad (1.4)$$

The cathodic (reduction) reaction in neutral to alkaline electrolyte involves the reduction of dissolved oxygen (1.5). For acidic media the oxidant is either dissolved oxygen (1.6) or hydrogen ions (1.7) depending on the pH and physical conditions. In the absence of any other oxidant water undergoes reduction according to (1.8).

$$O_2 + 2H_2O + 4e^- \rightarrow 4OH^- \qquad (1.5)$$

$$O_2 + 4H^+ + 4\ e^- \rightarrow 2H_2O \qquad (1.6)$$

$$2H^+ + 2e^- \rightarrow H_2 \qquad (1.7)$$

$$H_2O + 2e^- \rightarrow H_2 + 2OH^- \qquad (1.8)$$

For many applications aluminium is alloyed to obtain desired mechanical properties. Aluminium has been alloyed with a wide range of elements such as: Cu, Mg, Mn, Si, and Cr so as to tailor the material for its intended use. Aluminium alloy 2024-T3 (AA2024-T3) is a high strength alloy containing about 4-5 % copper, 1-2 % Mg as well as minor quantities of other elements. Complete composition shown in Table 1.“T3” represents the treatment the material has undergone, where the alloy was solution-annealed, quenched and aged at ambient temperature until stable. [7] The alloy AA2024-T3 is used in high strength/low weight applications, particularly within the aerospace industry.

Table 1 Composition in % of AA2024-T3 in addition to aluminium

Cu	*Mg*	*Si*	*Fe*	*Mn*	*Zn*	*Ti*	*Cr*	*Other*
3.8-4.9	1.2-1.8	0.5	0.5	0.3-0.9	0.25	0.15	0.1	0.15

The alloying elements make AA2024T-3 significantly less corrosion resistant than pure aluminium metal due intermetallic compounds (IMC's) present in the alloy. These ICM's have different composition than the aluminium matrix resulting in the formation of galvanic cells. Copper rich Al-Cu-Mg particles acts as the anode with the matrix but also involves dealloying. These localised sites also make the alloy susceptible to localised corrosion such as pitting and intergranular corrosion.

1.3.1 Corrosion Protection of Aluminium Alloy 2024-T3

For some applications the alloy can be "alclad", meaning that the alloy is coated with a layer of pure aluminium thus providing corrosion resistant aluminium oxide. However, the aluminium layer can easily be damaged or removed, for instance during repainting. For applications in aggressive environments, such as an aerospace application, the alloy needs to be additionally protected. [7]

Chromating is the primary method used for corrosion protection of AA2024-T3. The use of chromate based coatings took off during World War II and is at present almost exclusively used. Coating systems used generally consist of a surface pre-treatment referred to as a chromate conversion coating (CCC) followed by chromate primer and a topcoat. The formation of CCC on aluminium alloys involves the oxidation of

the metal surface (1.9) by reduction of hexavalent chromium (chromate) to trivalent chromium (1.10). [8]

$$2Al \rightarrow Al^{3+} + 6e^{-} \quad (1.9)$$

$$Cr_2O_7^{2-} + 8H^{+} + 6e \rightarrow 2Cr(OH)_3 + H_2O \quad (1.10)$$

The trivalent chromium undergoes condensation reaction to produce hydrated Cr^{III} oxy-hydroxide [8] followed by inorganic polymerisation to form the conversion coating, Figure 1.2. [8, 9]

Please see print copy for Figure 1.2

Figure 1.2 The interactions of chromate on an Al surface. [10]

1.4 Corrosion of Zinc-55 % Aluminium Hot Dip Coated Steel

1.4.1 Corrosion of Zinc

Zinc is commonly used in a variety of applications though rarely as a pure metal due to rather poor mechanical properties. The main use of zinc is instead as coatings for ferrous metals or as an alloying element. [11] . Zinc coating on iron or steel, known as galvanized metal, provides an effective way to protect steel against corrosion.

Zinc is an active metal with standard redox potential of -0.763 V vs. standard hydrogen electrode (SHE), more electronegative than iron (-0.401 V vs. SHE). Zinc is nevertheless more corrosion resistant that steel in most atmospheric conditions, with one exception being certain highly corrosive atmospheres. The relatively slow corrosion of zinc compared to iron is due to the formation of protective corrosion product (zinc carbonate.)

Corrosion in atmospheric conditions is often complex because of the many factors involved. The predominant electrochemical reactions occurring under humid ambient conditions are the anodic dissolution of zinc (1.11) balanced by the cathodic oxygen reduction in (1.12) and (1.13) for acidic conditions and the reduction in (1.14) occurring in neutral to alkaline conditions.

$$Zn_{(s)} \rightarrow Zn^{2+} + 2e^- \quad (1.11)$$

$$O_2 + 4H_3O^+ \, 4e^- \rightarrow 6H_2O \quad (1.12)$$

$$2H_3O^+ + 2e^- \rightarrow 2H_2O + \rightarrow H_2 \quad (1.13)$$

$$O_2 + 2H_2O \, 4e^- \rightarrow 4OH^- \quad (1.14)$$

1.4.2 Corrosion Protection of Galvanic Coatings

The zinc coating in galvanised steel provides protection to the underlying steel initially through a highly protective barrier layer offered by the metal and as the zinc oxidises the corrosion product provides a secondary barrier layer. Since zinc is electronegative towards iron the zinc coating also provides cathodic protection to the steel once the zinc barrier has been breached.

1.5 Intrinsically Conducting Polymer

Intrinsically Conducting Polymers (ICP's) or conducting polymers also known as electroactive conducting polymers or synthetic metals are a class of organic polymers that posses the ability to conduct electricity without any addition of a separate conducting material. [12] Interest in ICP's increased dramatically after highly conducting ICP was first reported in 1977, with the discovery of (highly) conductive polyacetylene. The conductivity of polyacetylene was observed to increase from a semi conductor to metallic range with a conductivity of up to 10^5 S/cm after partial oxidation of the polymer by exposure to halogen vapours. [13] This discovery laid the foundation for a whole range of novel polymer material possessing electrical conductivity. In the year 2000, the Nobel Prize in Chemistry was awarded jointly to

Alan J. Heeger, Alan G. MacDiarmid and Hideki Shirakawa "for the discovery and development of electrically conductive polymers". Today numerous different ICP's have been synthesised (Table 2) but also prior to the discovery of (highly) conducting polyacetylene several ICP's have been reported though most of these materials had generated only minor interest. [12]

The common structure in all ICP's is an altering single and double bond along the polymer backbone. In neutral form the conductivity of these materials are in the insulator to semi conductor range. Partial oxidation (or in some cases reduction) of the polymer backbone produces delocalised mobile charge carrier (a radical cation or polaron) capable of moving along the conjugated carbon chain as well as hopping to adjacent chains which is attributed to its resultant electrical conductivity. The partial oxidation (or reduction) imparts a delocalised charge upon the polymer backbone. In order to maintain the charge neutrality of the polymer a counter ion, referred to as a "dopant" is incorporated into the polymer structure. The use of the term doping and dopant is taken from its analogue to semiconductor p- and n-doping. This doping process is in many cases reversible making it possible to "switch" the conductivity on and off by oxidising or reducing the polymer. In addition to the electric conductivity, mechanical, magnetic and optical properties can also be altered and controlled using the same process. [14]

Table 2 Typical conducting polymer structures (in undoped form). [14]

Please see print copy for Table 2

Polyacetylene is the ICP that displays the highest conductivity but due to poor stability in air the focus of developing applications using ICP's have been directed to other systems displaying a higher degree of stability. Among those ICP's that have been most thoroughly studied is polyaniline, polypyrrole and polythiophene. [14]

With the versatility of these materials, ICP's are envisioned in a wide range of applications including electrochromic devises [15-21], light emitting diodes [22-25], photovoltaics [26-31], electronic and physical sensors [32-41], battery devises [42-56] and as corrosion protection coatings. (Chapter 1.6.5) Despite showing promise in

many of these areas the use of ICP's has so far failed to lead to any commercialised product in most of these areas.

1.6 Synthesis

Typically, the polymerisation of an ICP is performed by either chemical or electrochemical means. In chemical polymerisation a chemical oxidant is used to oxidise the monomer as well as provide a counter ion to function as dopant, shown for the polymerisation of pyrrole in Figure 1.3.

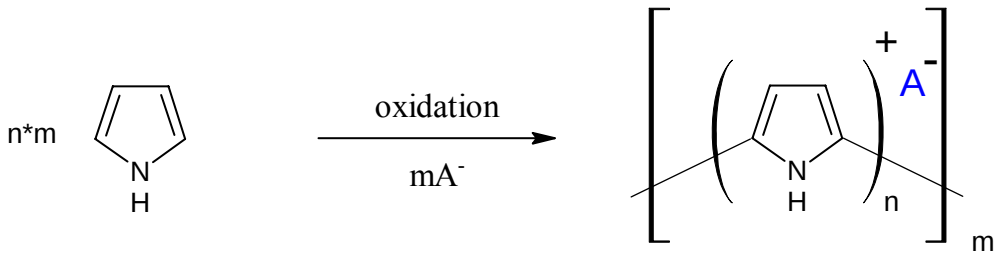

Figure 1.3 Schematic representation of the polymerization of pyrrole to give polypyrrole with the incorporation of a dopant anion A^-.

The same overall reaction applies to electrochemical polymerisation in which the oxidation of the monomer is performed by applying a potential between two electrodes immersed in an ionically conducting electrolyte containing the monomer as well as a suitable dopant. Initial growth occurs in the electrolyte near the electrode surface until the polymer/oligomer chain eventually deposits on the electrode as solubility of the longer chain decreases. If material formed show significant conductivity, the polymerisation can continue by deposition of new material on the

polymer by passing the current through the polymer layer. Alternatively, if the material deposited on the electrode is non-conductive the polymerisation could only continue until the whole electrode had been covered since the material eventually would insulate the electrode, preventing any current to pass. Electrochemical polymerisation is often slower and more difficult to scale but allows for greater control of the polymerisation. Also since no anion is formed as a consequence of the oxidation any anion added to the electrolyte can be incorporated as dopant, giving electrochemical synthesis greater flexibility than using a chemical oxidant. Chemical polymerisation has the advantage of easy large scale production and the possibility of directly forming a polymer solution or suspension.

1.6.1 Polypyrrole

Polymerisation of polypyrrole (PPy) is essentially a radical-radical terminating stepwise reaction occurring in several steps shown in Figure 1.4. Oxidation of the monomer unit forms a radical cation. The radical cation exists in three resonance forms with the α-position being the most stable. Using chemical polymerisation the α-radical cation couples with a neutral monomer unit to form a radical cation dimer adding monomer units until termination.

The mechanism for electrochemical polymerisation is slightly different. Higher concentration of radical cations at the electrode surface results in radical-radical coupling rather than radical-neutral coupling, producing a radical dication dimer. In the next step the radical dication dimer undergoes deprotonation to produce an aromatic neutral dimer. The polymerisation continues by oxidation of the dimer to form the radical cation dimer undergoing radical-radical coupling with monomeric

radical cation. As the chain length increase the solubility of the oligomer/polymer diminishes until it eventually precipitates out of solution and deposits on the electrode surface. [57]

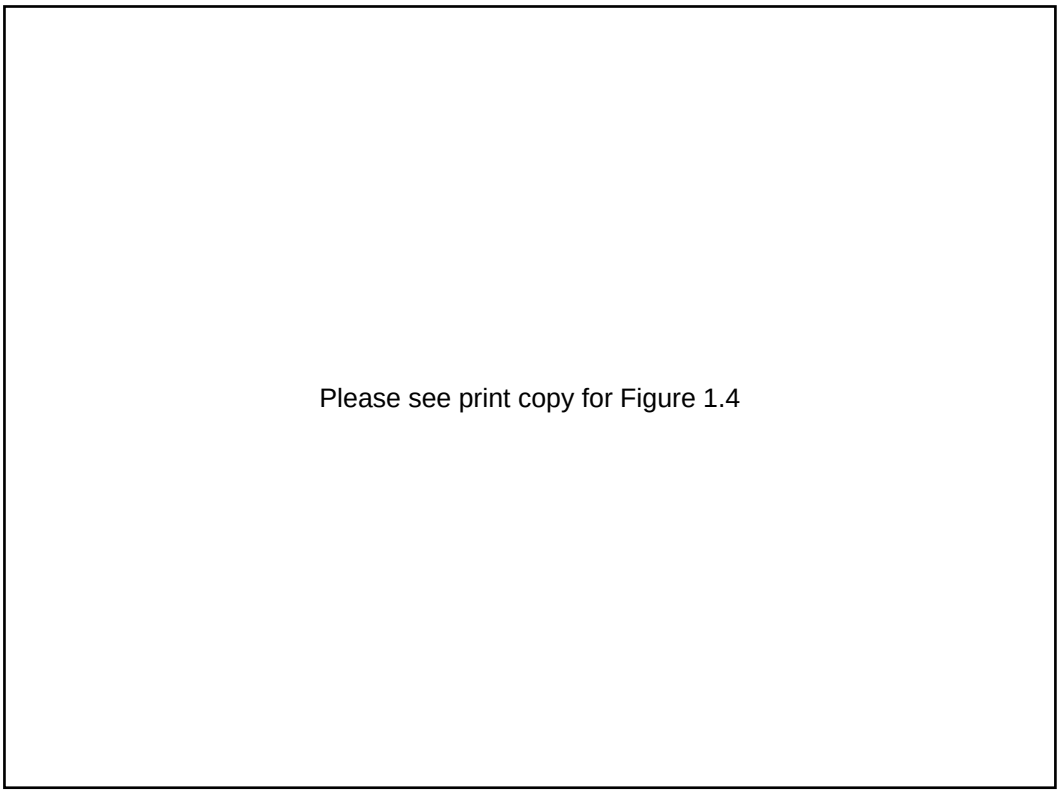

Figure 1.4 Mechanism of polypyrrole polymerisation. [57]

1.6.2 Polyaniline

Polymerisation of aniline is also a condensation polymerisation but differs from the synthesis of polypyrrole in the polymerisation mechanism. Oxidation of the monomer produces a radical cation, which exists in three different resonance forms. (Figure 1.5, step 1)

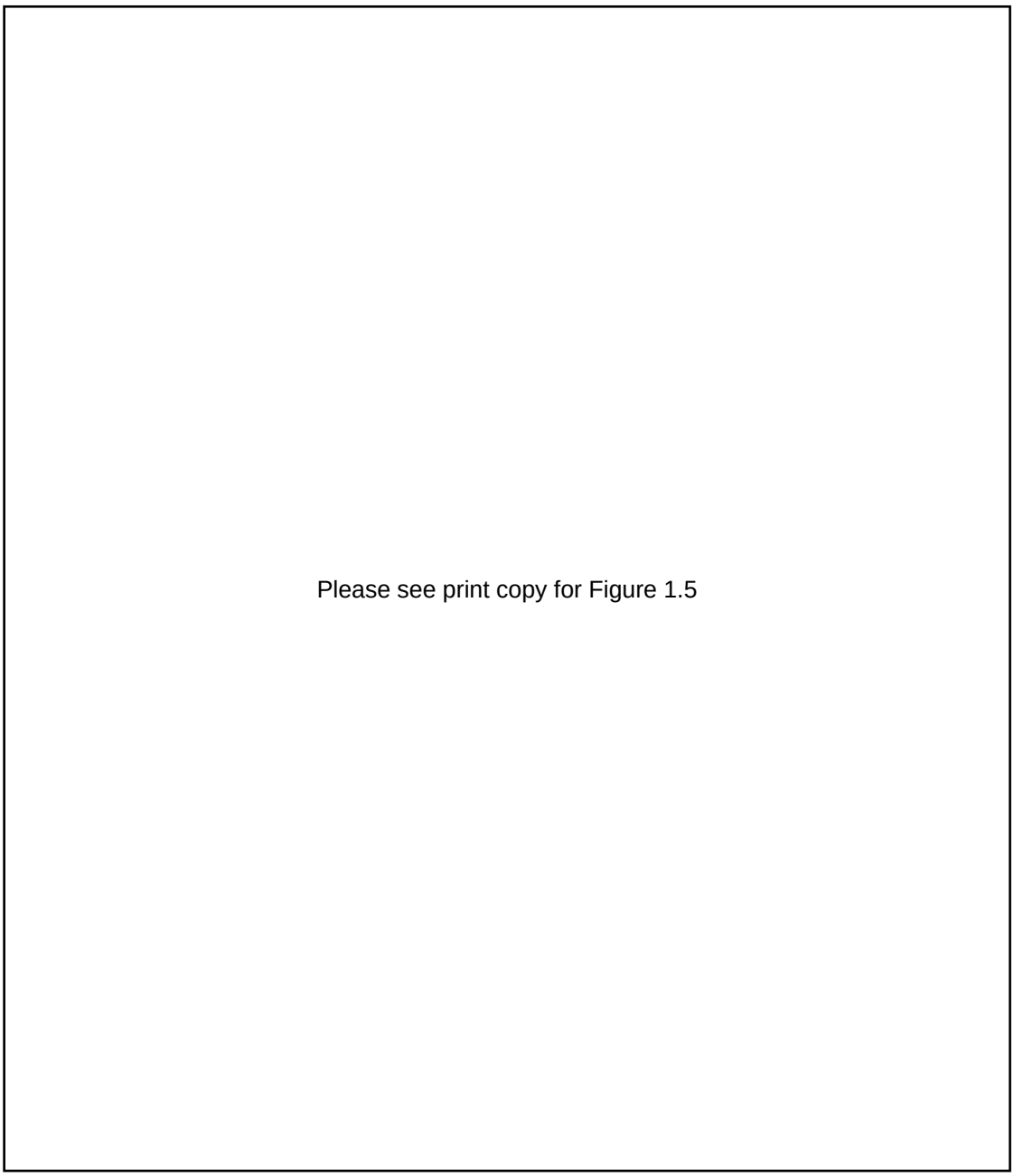

Figure 1.5 Reaction steps in electrochemical polymerisation of aniline forming polyaniline. [14]

In electrochemical synthesis shown in (Figure 1.5, step 2) radical-radical coupling, between a *para* radical and an amine radical, produce a dication dimer. The dication undergoes rearomatisation to form the neutral dimer. Oxidation of the dimer produces a radical cation dimer with the radical on the amine. Polymerisation continues through radical-radical coupling with oxidised aniline with radical in *para*

position. (Figure 1.5, step 3) After rearomatisation the polymer chain is oxidised with incorporation of HA to produce the doped and conducting form. (Figure 1.5, step 4) [14]

The chemical polymerisation of aniline (Figure 1.6) instead produces the fully oxidised chain structure with chain propagation though radical-radical coupling without the rearomatisation step. Instead the fully oxidised structure known as pernigraniline is reduced by neutral aniline to form the partially oxidised; emeraldine salt and an oxidised radical cation aniline monomer.

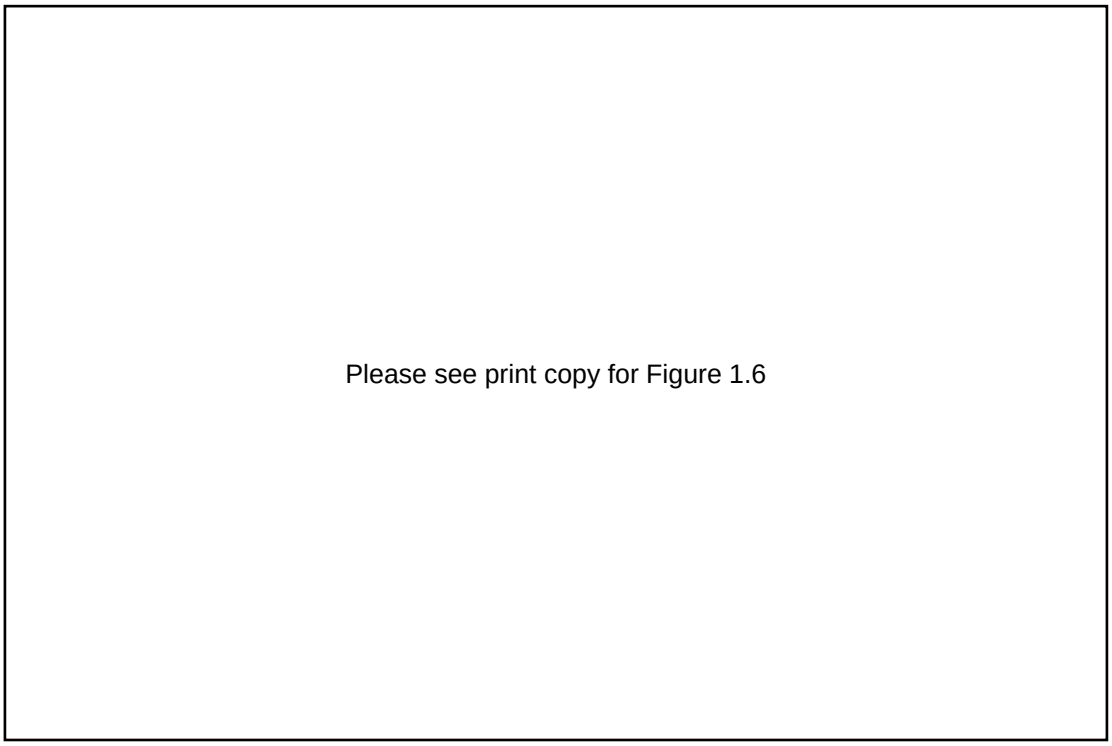

Figure 1.6 Reaction steps in chemical polymerisation of aniline forming polyaniline. [14]

1.6.3 General Properties of Polypyrrole

Polypyrrole was known well before Shirakawa *et al.* first published the work that would lead to the revolution in ICP research. Polypyrrole was known as "pyrrole

black", a black, conductive, polymeric material that formed spontaneously in air on the inside of pyrrole container. The material was synthesised and studied already in 1916. [12]

Polypyrrole is one of the ICP's that have received most attention, possessing good environmental stability, straight forward synthesis, using either chemical or electrochemical synthesis with conductivity of doped polymer usually ranging around 10^2 S/cm for electrochemically synthesised polypyrrole. [12], [58]

The redox activity of polypyrrole allows the polymer to be reversibly reduced and oxidised. In the oxidised state the material is conducting with charge neutrality maintained by incorporation of an anion. Reduction to the neutral polymer produces an insulator/semiconductor and expulsion of the anion as shown in Figure 1.7. In some cases where the expulsion of the anion is hindered, charge neutrality is maintained by incorporation of a cation as shown in Figure 1.8. The release of anion or incorporation of a cation upon reduction is utilised to use ICP as controlled release material.

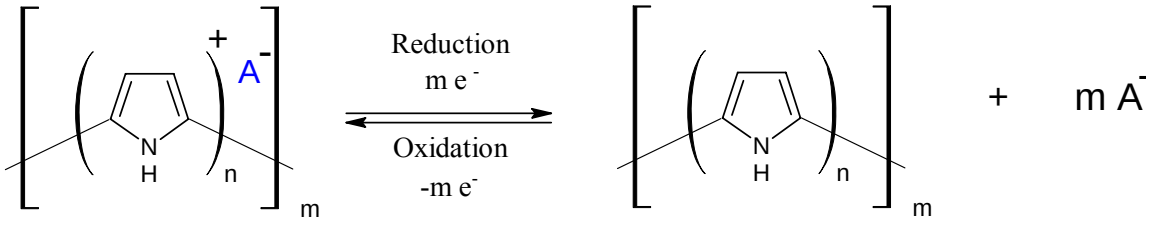

Figure 1.7 Redox reaction of PPy with expulsion of dopant anion upon reduction.

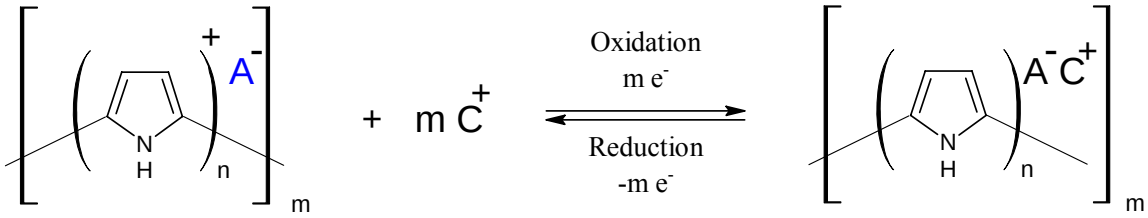

Figure 1.8 Redox reaction of PPy with inclusion of cation upon reduction.

Due to ionic and covalent crosslinking, Polypyrrole generally lacks solubility in all common solvents and can not be melted or fused. [14] Electrochemical polymerisation therefore presents an attractive option to form films and coatings, since it can be achieved via direct electrodeposition of the polymer onto desired substrate. Other means to obtain processable material has involved; making of polypyrrole dispersions, incorporation of anion with specific function and substitution groups on the pyrrole monomer.

1.6.4 General Properties of Polyaniline

Polyaniline (PAn) was first synthesised as a dye, known as "aniline black" in 1835 while electrically conducting polyaniline was first reported by MacDiarmid *et al.* in 1985. [59] Polyaniline is perhaps the one ICP that has generated the biggest research efforts. Exhibiting only moderate conductivity (1-10 S/cm) in most cases and limited heat resistance, the material exhibits complex redox reactions as shown in Figure 1.9. The only conductive form of polyaniline, known as emeraldine salt (ES), is the protonated form of the half oxidised polymer. The polymer has three oxidation states: emeraldine, pernigraniline (an insulating fully oxidised form), and the fully reduced leucoemeraldine. All oxidation states are insulating and stable in the base form. When acidified the protonated form Leucoemeraldine salt is not stable and

exists only as an intermediate converting to leucoemeraldine base. With the different redox and protonation stages the polymer has a number of distinct colour changes. The leucoemeraldine base light green/yellow, emeraldine base blue, emeraldine salt green, pernigraniline base violet, pernigraniline salt blue. [14]

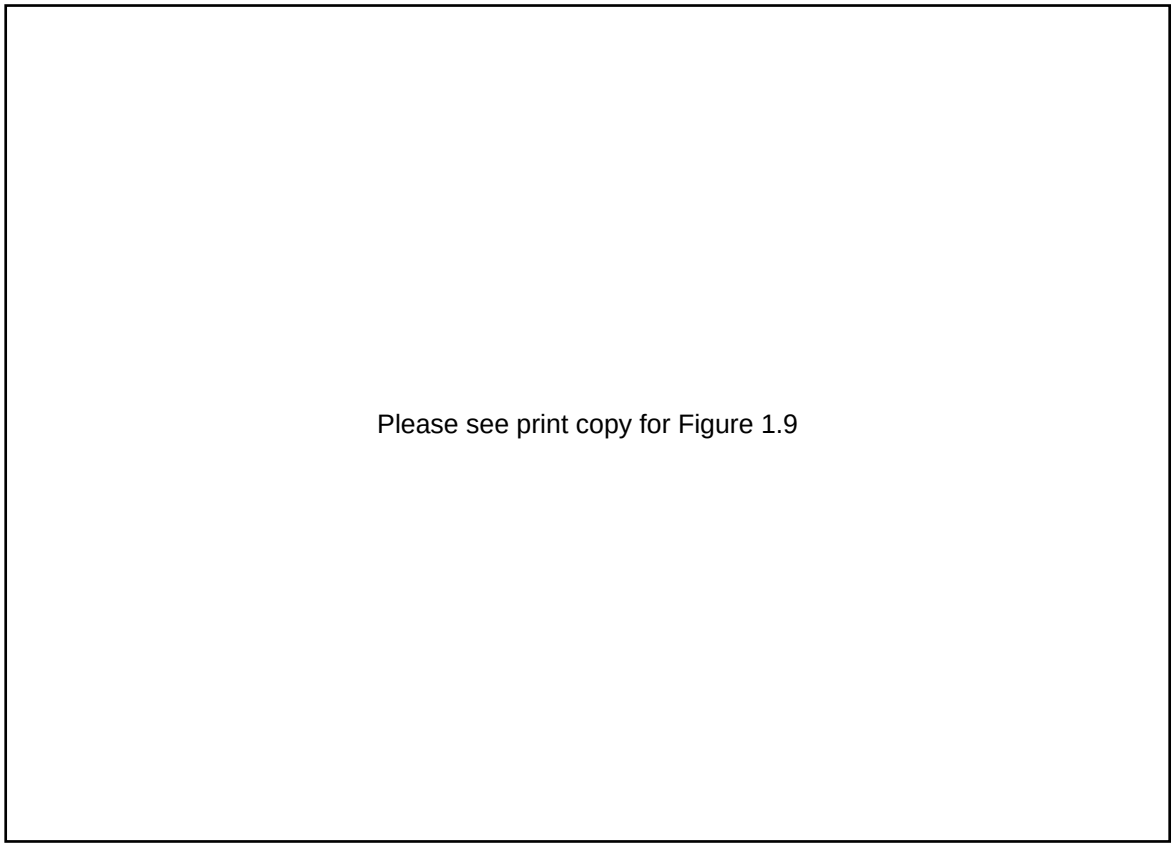

Figure 1.9 Protonation and redox reactions between various forms of PAn [14]

1.6.5 Processing of ICP

A major challenge in development of ICP coatings has been to overcome the issue of processability. ICP's generally lack solubility in common solvent and are not fusible. Several different methods have been employed in order to overcome processing difficulties of ICP's. Processability has been enhanced by addition of a dopant anion or monomer substitution to achieve solubility or the use of surfactants for making polymer dispersions and by making polymer composites and blends. By making ICP

composites and blends the processability and mechanical properties of the coating improve while maintaining the inherent electroactive properties of the polymer. ICP blends and composites are prepared mostly via chemical oxidation of aniline in the presence of a host polymer [60-65] although, electrochemical synthesis has also been employed in some cases. [14]

Chemical synthesis has been employed with a number of approaches. Emulsion polymerization in heterogeneous systems [66] was the approach used to produce processable conductive composites containing polyaniline-poly(alkyl methacrylate). Polyaniline composites were also prepared via dispersion polymerisation. [67]

Attempts to achieve processable polyaniline include incorporation of surfactant dopants such as 10-camphoresulphonic acid and dodecylbenzene sulphonic acid.

1.6.6 ICP for Corrosion Control of Aluminium Alloys

Initial work exploring corrosion inhibition of aluminium alloys using polyaniline was performed by Racicot *et al.* [68-72] utilising a polyaniline/polyanion complex which was non-covalently bonded in a side-by-side structure forming a "double-strand" polymer complex. The corrosion inhibition of aluminium alloy AA7075-T6 using polyaniline/poly(methyl acrylate-*co*-acrylic acid) was evaluated by electrochemical impedance spectroscopy (EIS) after immersion in 0.5 M NaCl and 0.5 M NaCl at pH 3.6 and compared with a chromate conversion coating. EIS showed a 10^5 Ohm low-frequency impedance for both PAn and chromated sample after 2 weeks immersion in neutral solution. In acidic solution the PAn displayed high (10^6 Ohm) low-frequency impedance for no less than 3 weeks, where the low-frequency impedance

for chromate samples decrease to $2*10^4$ Ohm in 3 days and continued to decrease to a non protective level (10^4 Ohm). The suggested protection mechanism involved formation of an oxide or oxide like layer on the metal surface facilitated by the polymer stabilising the metal against corrosion.

Yang *et al.* [73] utilised the same double stranded structure to form polyaniline/poly(acrylic acid) (PAn/PAA) which was blended at 1 % w/w with waterborne epoxy paint. Corrosion inhibition of AA2024-T3, AA7075-T6 and AA6061 coated with the paint formulation was examined by salt fog spray, acid-dip filiform corrosion testing and constant immersion in seawater. Samples coated with epoxy paint containing PAn out performed pure epoxy paint used as a reference coating. AA7075-T6 with artificial defect showed less blistering than control sample after 1000 hour in salt fog chamber. The PAn coating also performed better than control sample during constant immersion in seawater. Less filiform corrosion was observed for all three different alloys when coated with PAn/PAA/epoxy. The double strand structure also resisted dedoping in seawater at pH 8 and remained in its conductive state.

Tallman *et al.* investigated the corrosion protection afforded by a commercialised polyaniline supplied by Monsanto doped with 3,6-dinonylnaphthalene-1-sulfonic acid. [74] Corrosion protection of coated AA2024-T3, AA7075-T6 and AA7075-T6 "clad" was evaluated using Open Circuit Potential (OCP), Linear Polarization (LP), EIS and Electrochemical Noise Method (ENM). EIS of AA2024-T3 and AA7075-T6 "clad" materials revealed an increasing charge transfer Resistance (R_{CT}) during exposure accompanied by decrease in pH. The R_{CT} increased throughout 3 weeks

immersion. The increase was attributed to a combination of oxide formation at the polymer/metal interface and partial reduction of the Emeraldine Salt (ES) to the non-conductive Leuco Salt (LS), eventually leading to coating failure. LP of coated AA2024-T3 demonstrated a higher Corrosion Potential (E_{corr}) than bare metal and a Corrosion Current (I_{corr}) several times lower. Coated sample also exhibit a pseudo passive region >0.3 V. The PAn coated samples displayed a significant ennoblement with an OCP of around 0.2 V. The OCP was maintained for over 3 weeks for PAn coated AA7075-T6 "clad"

The reactions mechanism of protection proposed by Tallman *et al.* involve aluminium oxidation, (1.15) and reduction of the PAn ES to form LS (1.16), followed by partial dissociation of LS to form Leuco Base (LB) and acid. (1.17) Tallman *et al.* also emphasize that several other reactions such as oxidation of copper, complexation of copper and aluminium and the reaction of dissolved O_2 may be involved.

$$2Al + 3H_2O \leftrightarrow Al_2O_3 + 6H^+ + 6e^- \qquad (1.15)$$

$$3ES + 6H^+ + 6e^- \leftrightarrow 3LS \qquad (1.16)$$

$$3LS \leftrightarrow 3LB + 6H^+ \qquad (1.17)$$

Each ES, LS and LB represents 4 monomer units.

Cogan *et al.* [75] investigated galvanic interactions of PAn-HSCA and AA2024-T3 in 3.5 % NaCl using OCP, Galvanic coupled zero resistance ammeter and liner polarisation for an electrolyte both with and without the presence of O_2. The galvanic coupled ZRA experiment showed a small positive shift and increased anodic current

afforded by PAn on the uncoated metal substrate but the mixed potential was heavily dominated by the metal. At these conditions ES was rapidly reduced to LS, which in the presence of O_2 is re-oxidized to EB. The corrosion current, obtained from polarization measurements, were lower for coated samples. However it is argued that the small positive polarization afforded by PAn should lead to an increase in the corrosion rate, particularly at defects sites. The corrosion inhibition mechanism suggested involves suppression of O_2 reduction at the metal surface by reaction with LS to form EB.

In comparison Epstein *et al.* [76] investigated the oxidized but non-conductive polyaniline form as a possible corrosion inhibitor of AA2024-T3 and AA3003 in 0.1 M NaCl. LP scans of EB coated AA2024-T3 in 0.1 M NaCl revealed a more positive E_{corr} and lower I_{corr} compared to uncoated metal. X-ray photoelectron spectroscopy (XPS) studies performed showed less corrosion product on the surface after removal of the EB film compared to uncoated metal. Also, the EB coated substrate revealed the absence or reduced concentration of copper in the alloy for several hundred Å deep. A model proposed for the decreased corrosion rate involves EB dissolution of copper corrosion product, minimizing the galvanic coupling between Al and Cu resulting in a reduced corrosion rate. XPS studies of the backside of EB coated AA3003 immersed in 0.1 M HCl also shows reduction of aluminium oxide, demonstrating that EB has sufficient oxidation power to alter the corrosion performance of the alloy some distance away, despite being non conductive.

He *et al.* [77] also looked at EB, made by Epstein, as a corrosion inhibitor for AA2024-T3. The coating performance was investigated using Scanning Vibrating

Electrode Technique (SVET) in Dilute Harrison's solution (DHS) with an artificial defect introduced in the coating. An initial delay of the I_{corr} was observed. After 3.5 hours current begun to flow with both the anode and cathode confined to the defect area. At this point a colour change of the coating from blue (EB) to yellow-orange (LB) started to appear at localized sites. During exposure these sites change polarity and revert back to blue (EB) or green (ES). It is suggested that the apparent polymer re-oxidation is a result of reduction of dissolved O_2. Since the green (ES) was more predominant at the vicinity of the defect it is suggested that the polymer is doping with soluble aluminium ions.

1.7 Research Aim

A major challenge in the developments of ICP coatings is to overcome the issue of processability. ICP's generally lack solubility in common solvent and are not fusible. This work has been directed towards processable ICP's for use as corrosion protective coating for AA2024-T3 and Zinc-55 % Aluminium hot dip coated steel.

Polyaniline-HCSA/poly(Vinyl Acetate-*co*-Butyl Acrylate) composite (PAn/co-poly) was investigated as a corrosion protective coating for AA2024-T3 using DC polarisation, electrochemical impedance spectroscopy (EIS) and scanning vibrating electrochemical technique (SVET), together with *in situ* Raman Spectroscopy were used to evaluate coating performance and polymer/metal interaction with emphasis on the effect of heat treatment.

In order to render polypyrrole processable, an alkyl chain may be added to the pyrrole ring [1]. Previous studies using 3-octylpyrrole produced highly soluble but a non-conductive polymer. Even though the material was insulating, and the redox properties poor or non-existent, this material has been proven to provide significant corrosion inhibition to AA2024-T3. [2]

In this work the synthesis of poly(3-octylpyrrole) (P3OP) has been modified to produce a polymer with conductivity of the order of 5 S/cm. This material was investigated for use as a corrosion inhibitor on AA2024-T3 by electrochemical impedance spectroscopy.

Chapter 2- Review of Relevant Techniques

2.1 Introduction

Historically, durability of a coating was tested by exposure studies, where samples of the coated metal are exposed to a corrosive environment. These test conditions include real life environments such as those undertaken at atmospheric exposure sites or artificially accelerated testing conditions such as a salt spray chambers, were the panels are exposed to highly corrosive conditions far more aggressive than the environment for which the material is intended to be used. Coating suitability is then assessed by periodical inspection, looking for any sign of corrosion. Exposure studies such as these come with significant limitations. Tests in natural environments take significantly more time to produce results and the validity of the accelerated test maybe questionable. Another limitation is that these tests provide only qualitative data where no insight is given to the protection mechanism preceding visual coating failure.

The process of coating deterioration including under coating corrosion, ultimately leading to coating failure, can be studied using electrochemical techniques. These

techniques not only provide results on the corrosion protection capability in a completely different time frame, weeks instead of years as for exposure studies, but they also provide much more information in to the nature of the system than what can be obtained with visual observations alone. [78] This chapter will review the electrochemical techniques employed in thesis to evaluate corrosion.

2.2 DC Techniques

DC electrochemical techniques are an integral part in studies of metallic corrosion. It is less frequently used in the study of polymer coatings, thought when successfully applied it provides a simple tool to for use in the study of organic coatings.

2.2.1 Open Circuit Potential

One of the simplest electrochemical tests available, measuring of the Open Circuit Potential (OCP), also referred to as the equilibrium potential or corrosion potential. The OCP is by definition the electrical potential difference between two conductors in a specific electrolyte with zero current flow between them. [78] Monitoring OCP over time can provide vital information about the system being studied. Providing information about when system has reached a steady state and when transitions between different states, such as passive and transpassive behaviour will occur. Properties of the oxide formed on the test electrode can be evaluated by monitoring of the OCP which typically results in a positive shift in the OCP, indicative of the formation of a passive film (i.e. a surface oxide protecting the metal from further

oxidation). The formation of porous oxide films, which can hinder but not prevent further oxidation, typically results in a decrease in the OCP. [79]

2.2.2 Potentiodynamic Polarisation

By applying an external potential to the test electrode a resulting net current flows between the working and the counter electrode. In potentiodynamic polarisation a variable potential sweep is applied while the resulting current is measured. The relationship between the applied potential and the resulting current is used in several different corrosion experiments. [78]

In Linear polarisation (LP) the polarisation potential is restricted to ±20 mV of the measure corrosion potential, E_{corr}, [80] were the potential/current ratio is linear. The ratio of $\Delta E/\Delta I$ is referred to as the corrosion or the polarisation resistance (R_p). In conjunction with other data this can be used to calculate the corrosion current and ultimately a corrosion rate. In Tafel polarisation the scanning window is extended to typically ±250 mV vs. OCP. Where the anodic and cathodic branches displaying linearity (linear when plotting current in log) approximately 50 mV from the OCP, each branch corresponding to the respective half reactions of the electrochemical cell i.e. oxidation or reduction of the metal.

By extending the potential widow further in the anodic direction information about passivity can be obtained. In Potentiodynamic scanning (PDS) the anodic scan is extended to normally 1V vs. the OCP with a maximum current density cut-off added if needed. PDS is normally initiated -250 mV vs. the OCP.

Cyclic polarisation (CP) begins as PDS but as the maximum potential or the current limit is reached the scan direction is reversed back to the OCP. In the reverse scan the nature of any passive film can be evaluated. A schematic representation of PDS and CP is shown in Figure 2.1. In this figure the current, initially cathodic, decreases and eventually reach zero as the polarity changes. Continuing the polarisation in the anodic direction eventually leads to an abrupt current density decrease as the passivation potential (E_{PP}) is reached. At this potential a passive film protects the metal from further oxidation, limiting the current flow. At a more positive potential, the Breakdown Potential (E_b), this protective film fails and the current density begins to increase once more.

Once the scan has reached the potential or the current density limit the scan direction is reversed. A change in the current density during the reverse scan can be used to evaluate the system. A positive hysteresis is observed if the reverse scan shows a higher current density than the anodic scan, as shown in red in Figure 2.1, with a repassivation potential (E_{rp}) below the OCP. A negative hysteresis, shown in blue in Figure 2.1, display a reverse scan with lower current density than observed for the anodic scan and with a E_{rp} more positive than the OCP. It is generally assumed that initiation of pitting corrosion will occur at potentials above the E_b and that the healing of the passive film is associated with the E_{rp}. An E_{rp} below the OCP will lead to continuing pitting corrosion while pitting corrosion will not occur with an E_{rp} more positive than the OCP.

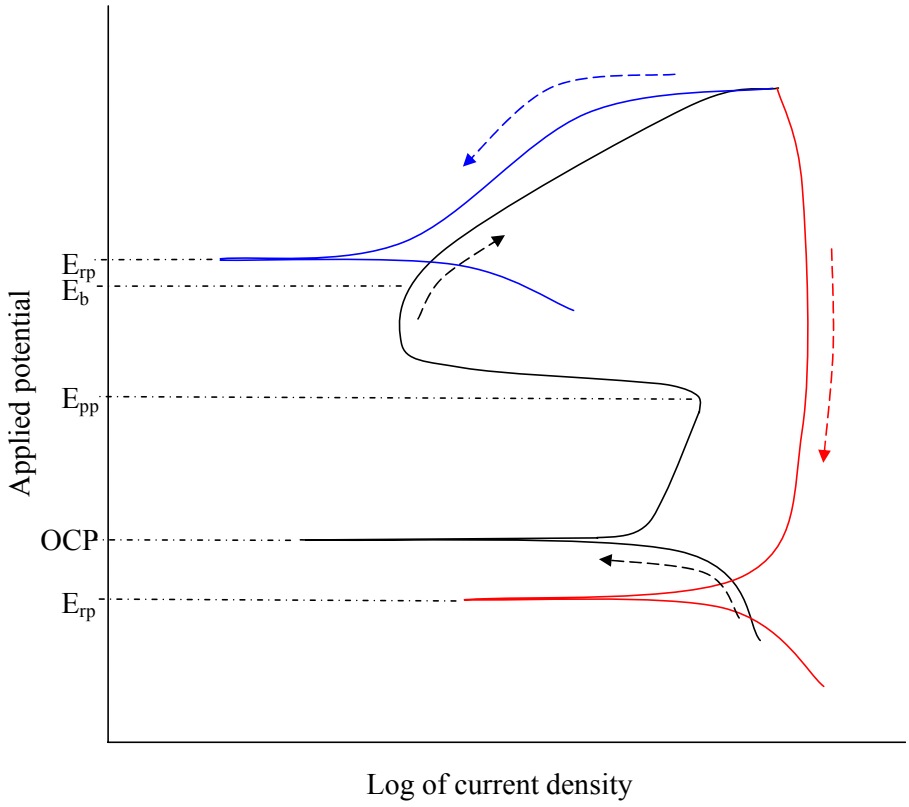

Figure 2.1 A schematic representation of Potentiodynamic scanning (PDS) (Black) with open circuit Potential (OCP), passivation potential (E_{pp}), breakdown potential (E_b). cyclic polarisation (CP) with positive hysteresis (Black+red) and negative hysteresis (Black +blue) both with repassivation potential (E_{pp}).

2.3 Electrochemical Impedance Spectroscopy (EIS)

Electrochemical impedance spectroscopy (EIS) is a well established technique for assessing metallic corrosion and protective coatings. The technique has proven particularly useful in the study of protective coatings, providing a non-destructive route to obtain specific information about coating and corrosion properties. [81]

EIS has been defined as "the method in which the impedance of an electrochemical system is studied as a function of the frequency of an applied AC wave". [82] Instead of applying a direct current or voltage, the technique utilise a continuous perturbation to a steady state system, using a low magnitude AC signal. Applying a sinusoidal AC potential centred on the OCP of the substrate causes the sample to cycle between anodic and cathodic polarisation, corresponding to a small AC current. Using a small perturbation signal, as with linear polarisation, allows for the assumption of current voltage linearity. The impedance of the system relates to the measured current and applied potential in the same way as resistance for a DC signal but it is also depended on the frequency of the signal. As shown in Figure 2.2 the measured current to an applied sinusoidal potential will be sinusoidal of the same frequency but shifted in phase. The impedance expression will therefore consist not only of a magnitude but also a phase shift. Mathematically the impedance can be expressed as complex number shown in (4.1) polar coordinates and in Cartesian coordinates (4.2).

$$Z(j\omega) = \frac{E}{I} e^{j(\varphi_E - \varphi_I)} = |Z| e^{j\varphi} \qquad (4.1)$$

$$Z(j\omega) = \frac{E(\omega)}{I(\omega)} = Z'(\omega) + jZ''(\omega) \qquad (4.2)$$

The impedance spectrum is obtained by varying the frequency of the AC signal resolving components in the system with different frequency dependent properties (time constants), data which can be used to evaluate corrosion and coating properties. High frequency spectra correspond to kinetically controlled reactions and to charge transfer processes usually associated with the coating interface, while low

frequencies correspond to slower processes generally occurring at the metal interface.

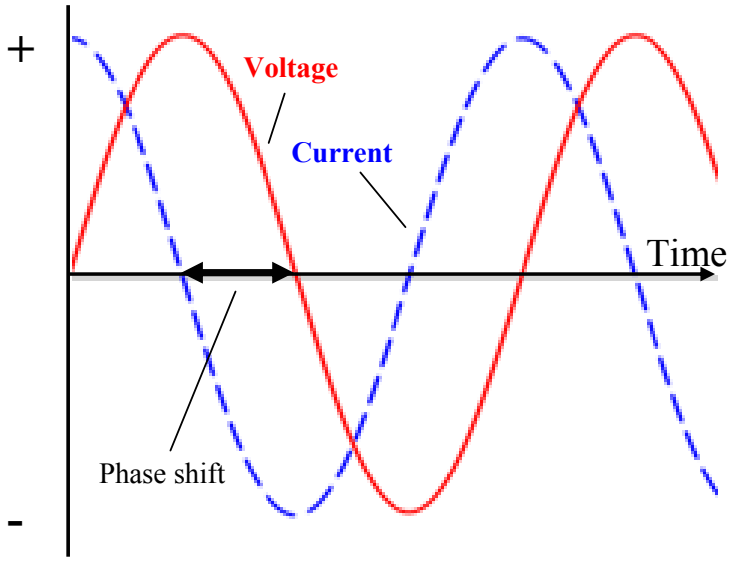

Figure 2.2 Sinusoidal current response to sinusoidal potential wave in a linear system.

2.3.1 EIS Experiment

The basic EIS experiment consists of an electrochemical cell connected to a potentiostat together with an AC generator/analyser. The cell is connected to a frequency response analyser (FRA) or phase sensitive (lock-in) amplifier directly or indirectly through the potentiostat. A potentiostat is used in most setup but not always necessary. It is used for potential control and to provide high input impedance if needed. It also eliminates would be bandwidth problems. The AC generator/analyser is either a frequency response analyser (FRA) or a lock-in amplifier, which is used to generate the perturbation waveform and analyse the response. Type of AC generator/analyser to use depends on the intended experiment.

Most instrumentation allow for measuring frequencies between 100 kHz down to 0.1 mHz, although for most corrosion studies the information of interest can be obtained using a more moderate frequency range. High frequency data can also contain artefacts caused by instrumentation, such as reference electrode, potentiostat and connecting cables. Low frequency measurements require significant time to perform and the system measured must display a high stability. Choice of lower frequency is often a compromise between acquisition time and resolution, with 7-10 points per decade and a lower frequency limit of 10-1 mHz being a common compromise between accuracy and time needed for data collection. [83]

2.3.2 EIS Analysis

A typical impedance spectrum for a corroding metal under charge transfer control is shown in Figure 2.3-4. Presentation of impedance data is often done by use of three different graphs. The Nyquist shown in Figure 2.3, plots the real (Z') and imaginary component (Z") of impedance on x and y axis respectively and since almost all corrosion data have a negative imaginary component the y axis is inverted to show – Z" above the x-axis. For a Nyquist plot, showing corrosion data it can be assumed that the frequency decrease from left to right but the graph doesn't display the frequency for data collected, hence the same data is often also displayed using Bode plot shown in Figure 2.4 were logarithm of the modulus of the impedance (log $|Z|$) and the phase angle (φ) is plotted on the y axis vs. logarithm of the frequency (log ω) in two separate graphs.

From the Nyquist and Bode plot several parameters regarding the system can be obtained with no or only minor calculations, as shown in Figure 2.3-4. The solution

resistance (R_s) can be determined from the high frequency limit (4.3), shown in Figure 2.3, and represents the uncompensated solution resistance between the working and reference electrode. The polarisation resistance (R_p) relates to the electrochemical (corrosion) processes occurring in the system can be obtained from the low frequency end of the spectra according to (4.4).[84]

$$R_s = \lim_{f \to \infty} |Z| \qquad (4.3)$$

$$R_s + R_p = \lim_{f \to 0} |Z| \qquad (4.4)$$

$$C_{dl} = \frac{1}{2\pi f_{\max} R_p} \qquad (4.5)$$

The electrical double layer capacitance (C_{dl}) is due to the electrical double layer existing on the interface between an electrode and its surrounding electrolyte. The double layer forms as charged ions from the electrolyte attracted to the metal surface remains separated by insulating layer. C_{dl} can be obtained from the frequency corresponding to the maximum imaginary impedance f_{max} and the R_p according to (4.5).

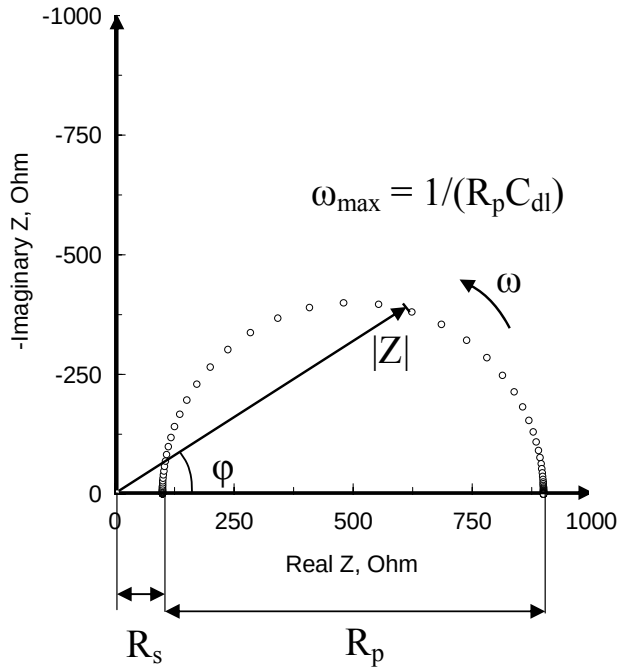

Figure 2.3 Typical Nyquist plot for a corroding metal under charge transfer control. With impedance vector (arrow) of length |Z| and the angle between the vector and the x-axis is φ. Frequency decreases from left to right.

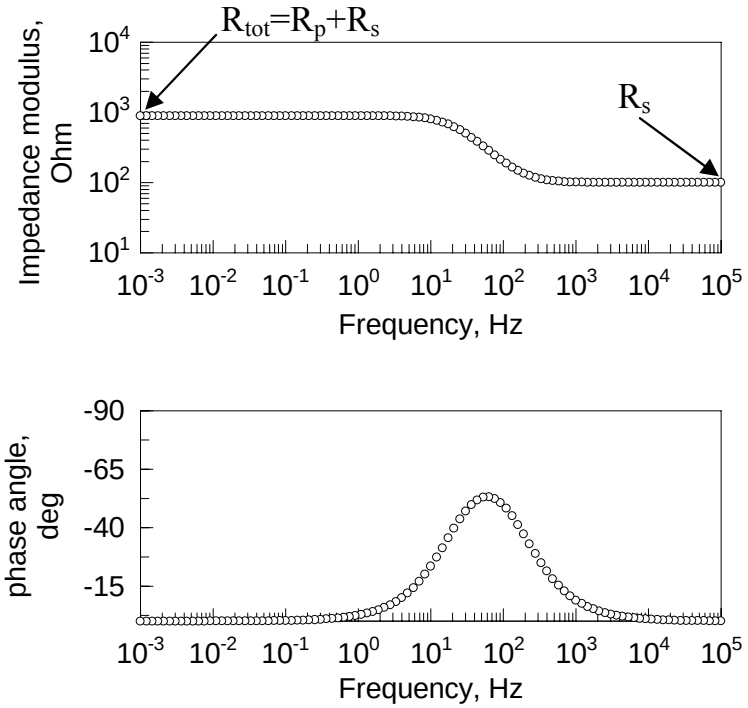

Figure 2.4 Typical Bode plot for a corroding metal under charge transfer control.

2.3.3 Equivalent Circuit

Instead of manual extraction of parameters one by one the whole spectra can be analysed simultaneously using computer calculations. The analysis is often performed by use of an equivalent circuit (EC). An EC is an electrical circuit model constructed by combining passive electrical components in to a circuit, a circuit displaying the same impedance as the system over all frequencies. Once an EC has been selected "fitting" can be performed using any of several existing modelling software. The values of the components are optimised by the program to produce a model with the minimum deviation possible from the measured data. The accuracy of the "fit" can be viewed graphically and an by "weight sum of squares" (calc modulus weighting) (or chi-squared parameter (X^2)). [85]

Many electrochemical processes occurring in the system can be described using circuit elements such as those available in any electronics store. However the translation from "electrochemical" to "electrical" does not always have a corresponding physical element and use of additional "components" is needed to describe the system. The most commonly used circuits and their impedance expression are shown in Table 3. A standard **Resistor** (R) is used for modelling resistance in the system. Charge and discharge behaviour corresponds to an electronic **capacitor** (C). An **inductor (L)** models behaviour that resists changes in the current.

Other elements used to describe the impedance are; **Warburg impedance (W),** used to model impedance due to diffusion processes. The impedance increases with length

of diffusion. At high frequencies the diffusion path is short resulting in low Warburg impedance and vice versa. The **Constant Phase Element (CPE)** is an "all-purpose" element with the exponent n ($-1 \leq n \leq 1$). By varying n CPE can depict; resistance (n=0), capacitance (n=1), inductance (n=-1) or diffusion (n=0.5). Commonly the CPE it is used to model non ideal capacitance ($0.5 \leq n \leq 1$). Y_0 is the admittance constant (amplitude) in s^n/Ω of the CPE; ω is the angular frequency (rad/s). [86]

Table 3 Impedance element and their expression

Element	***Impedance expression***
Resistance (R)	$Z = R$
Capacitance (C)	$Z = (j\omega C)^{-1}$
Inductance (L)	$Z = j\omega L$
Warburg (W or Z_{diff})	$Z = Y_0(j\omega)^{-0.5}$
Constant Phase Element (CPE)	$Z = Y_0(j\omega)^{-n}$

2.3.4 EC Fitting

Selecting an appropriate EC, to model the system, from an infinite number of different circuits can not only be based on "fit", since a better fit always will be available by adding additional elements. Guidelines to EC "fitting" proposed by Boukamp [87] defines the "best fit" as the simplest EC with the smallest "weight sum of squares" (calc modulus weighting) (or chi-squared parameter (X^2)) unless an additional element decreases the "weight sum of squares" by a factor of ten.

In some instances there will be more than one EC with the same number of elements providing an equally accurate fit of the data. The selection of an EC for a particular system has to represent the system in a physical meaningful way. Different EC's providing an identical frequency response sometimes depict very different electrochemistry. [84]

2.3.5 EC of a Corroding Metal

The impedance spectra for a corroding metal under charge transfer control as shown in Figure 2.3-4 can be modelled using by using either of the two EC shown in Figure 2.5. Both circuits model the data with the same accuracy. The choice of circuit B over circuit A as EC can instead be made from understanding of the system. The polarisation resistance related to the electrochemical (corrosion) process occur together with the double layer capacitance associated with any solution-metal interface; hence R_p is arranged parallel with C_{dl}. The solution resistance being the only connection to the electrodes occurring separate from the surface-processes must appear in series with both the R_p and the C_{dl} as shown in Figure 2.6. [84]

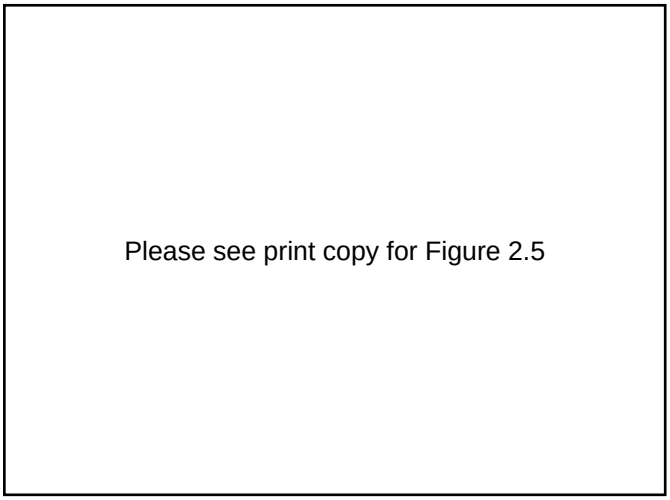

Figure 2.5 Two different equivalent circuits with the same frequency response [84]

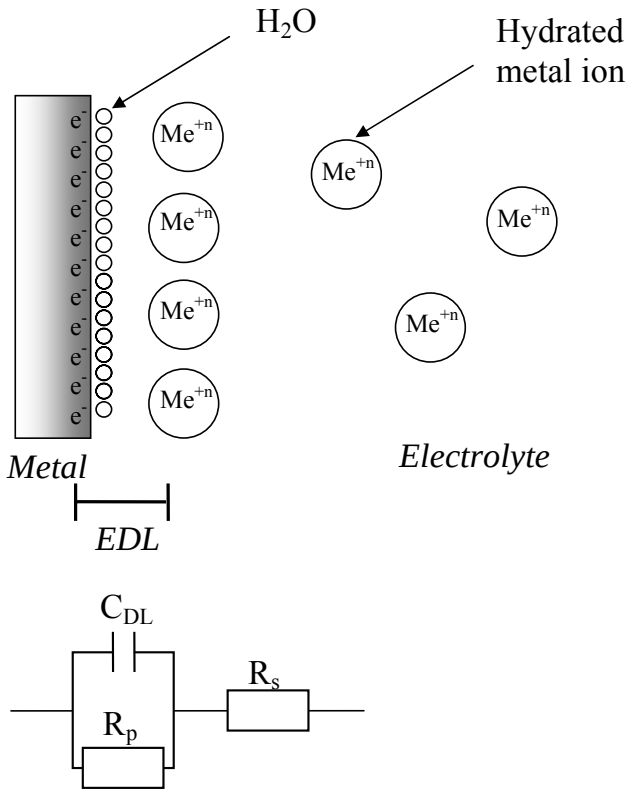

Figure 2.6 Schematic of the electric double layer of a corroding metal in electrolyte with corresponding EC.

For real systems the C_{dl} is often seen to deviate from the ideal capacitive behaviour seen in the Nyquist plot as a suppressed semi-circle. The reason given for this behaviour is that the charge in the electrolyte, making up one side of the capacitor, is distributed through the diffuse layer. Another factor given is the surface properties of the electrode, such as porous or rough surface. The double layer capacitance can then be modelled using a CPE. [86]

2.3.6 EIS of a Polymer Coated Metal

To evaluate coating performance and the mechanism of coating deterioration EIS is performed periodically on exposed samples to monitor changes correlating to the state of the system. By applying the data to corresponding EC, trends of specific parameters regarding the coating and the underlying metal can be monitored.

2.4 Scanning Reference Electrode Technique (SRET) and Scanning Vibrating Electrode Technique (SVET)

2.4.1 Introduction

The study of corrosion processes has been made possible through a range of new scanning microprobes techniques that can provide spatial resolution over a scanned electrode surface permitting study of local corrosion behaviour. These techniques are employed in the field of corrosion science to provide in-situ information on local corrosion features such as pitting, delamination, blister formation etc.

The scanning reference electrode technique (SRET) is a non invasive, in-situ technique used to study galvanic activity with spatial resolution by measuring potential gradients over a current source within an electrolyte and has been used in a wide variety of applications and was first reported to monitor current flow .

SRET uses two micro electrodes in a dual probe arrangement with the two probes separated laterally with about 2 mm to measure a potential difference by use of a differential amplifier. By scanning the probe at a constant height above the surface, shown schematically in Figure 2.7, the potential difference may be presented as a function of probe position. The potential difference can then, by use of a conversion factor, be related to the current flow. Calibration is obtained in a separate experiment by measuring the potential difference above a working electrode in a separate circuit, using the same electrolyte and applying a known current density.

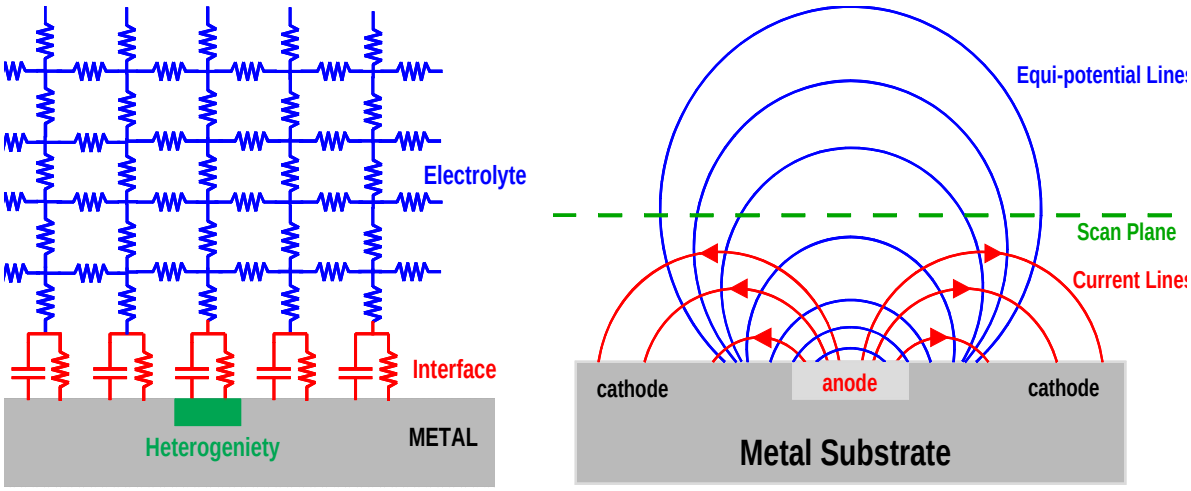

Figure 2.7 Illustration a resistance model for a surface in an electrolyte and equi-potential lines forming above a corroding metal with local anodic and cathodic sites.

The technique becomes limited in its application when the observed corrosion current is small, as in early stage formation of galvanic processes on an electrode surface, such that it falls below the lower limit of current detection for the instrumentation. Studying low activity surfaces, typically producing low currents, or using a highly conductive electrolyte creates a minimal potential difference to that can be difficult to detect. The lowest potential difference limit measurable is around 200 μV using a dual probe setup with small electrodes. A calculation of a typical experimental current that would yield significant signal-to-noise issues can be calculated, assuming a probe spacing of 1 mm and electrolyte with conductivity of 200 μS/cm. Under these conditions the minimum measurable current would be 400 nA. Employing the same calculations and data parameters, but replacing the electrolyte with a highly conductive electrolyte such as sea water with a conductivity of 80 mS/cm, the minimum measurable current would be 160 μA, well above the current observed in most freely corroding materials.

An improvement on this technique is the Scanning vibrating electrode technique (SVET). SVET also known as scanning vibrating probe (SVP) or current density probe (CDP) provides a lower detection limit and higher resolution than SRET. Instead of the dual probe arrangement used in SRET, in SVET solitary electrode is vibrated perpendicular to the surface using a piezoelectric vibrator. The potential is recorded at the highest and lowest probe position, resulting in a sinusoidal AC signal. Signal processing is performed using a lock-in amplifier and a differential electrometer. The lock-in amplifier, set to the frequency of vibration, clears the signal by filtering out noise from all other frequencies. In a version of the SVET instrumentation, designed by Applicable Electronics, the probe vibration is performed both horizontally and vertically. By using different vibration frequencies for the two orthogonal vibration directions the resulting signal can be separated into the vector components enabling measurement of the current movement or direction as well as current magnitude and sign (anodic or cathodic).

The detection limit and resolution is improved considerably by using a vibrating probe over a stationary dual probe. Probe vibration amplitudes, typically 1μm to100μm, decreases the magnitude signal observed with respect to the SRET, but due to an increased signal to noise ratio achievable by use of a lock-in amplifier and signal averaging, low current measurements in a minimal time can be achieved with a detection limit reported by Uniscan Instrument, for their SVP100, to be below 5 $\mu A/cm^2$.

2.5 Raman Spectroscopy

The Raman scattering is a vibrational molecular spectroscopy technique. When light hits a samples surface it is typically scattered in all directions at the same frequency as the incident light in a process referred to a Raleighy Scattering. Raman scattering occurs in about 1 in 10^7 photons when the wavelength of the scattered photon does not equal the absorbtion wavelength due to either an emission or absorption process. This occurs as the exited electron returns to a different vibrational state as illustrated schematically in Figure 2.8. The amount of energy lost is seen as a change in energy (wavelength) of the scattered photon. This energy loss is therefore characteristic for a particular bond in the molecule and is equivalent to the frequency absorption bands found in FT-IR spectroscopy

The scattering of light at lower and higher energy (lower wavelength or higher frequency) than the Rayleigh scattered wavelength is referred to as Stokes ($E = h\nu - \Delta E$) and anti-Stokes ($E = h\nu + \Delta E$) respectively. Since the Raman effect is a very weak phenomenon sample irradiation is achieved using laser light sources. By using a diffraction grating coupled with a photo detector (CCD) the wavelength or energy of the scattered photon can be determined. This energy difference will be characteristic for a particular bond or molecular structure in the irradiated sample.

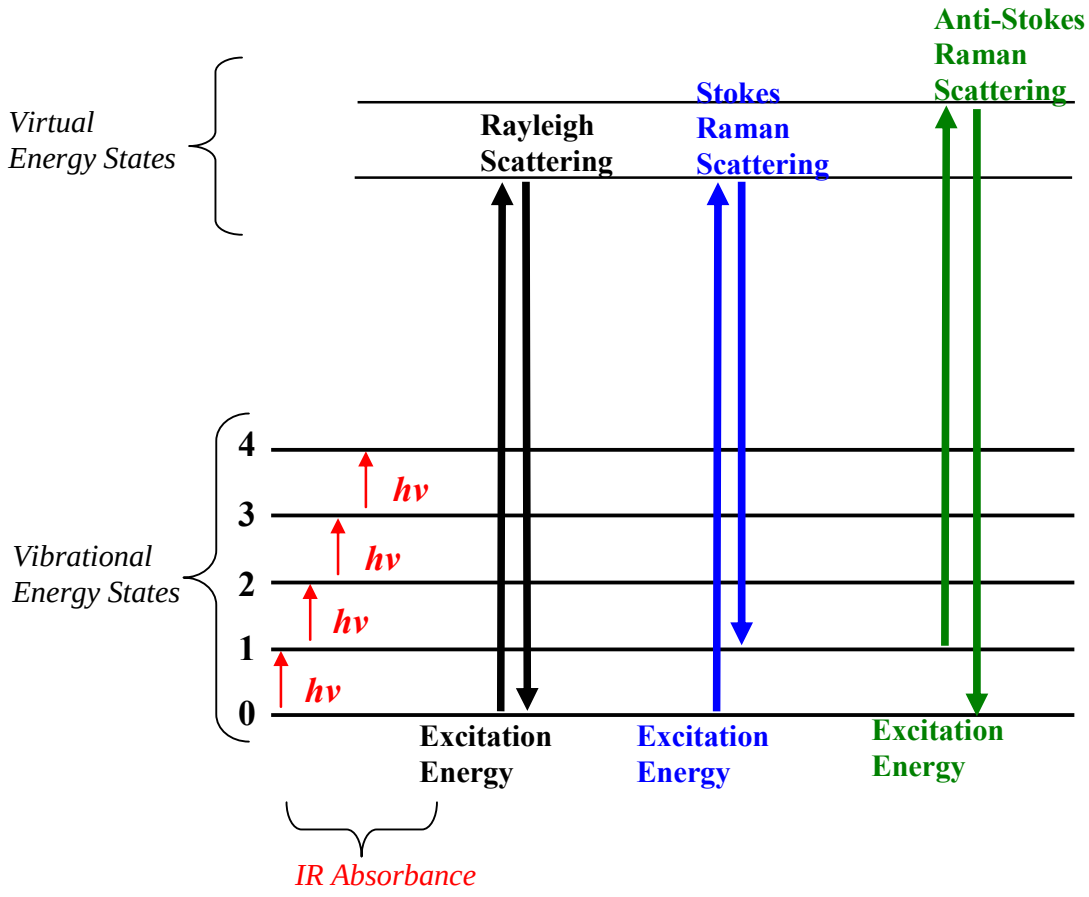

Figure 2.8 Schematic energy diagram for Raman scattering

There are a number of clear advantages of Raman spectroscopy over FT-IR. Firstly, the bond structures in Raman are independent of the dipole moment. The Raman technique typically uses an optical microscope to focus the laser to a localised point which means that there is little or no sample preparation required. Combination of the microscope with a confocal pin hole means that depth profiling and analysis of a isolated sample volume is possible in transparent samples. Raman can analyse samples under aqueous solutions as it does not suffer the large water absorption effects found with the FT-IR technique. Raman is also largely unaffected by sample cell materials such as glass. The use of the microscope also means that there is generally little or no sample preparation required. Finally, the intensity of spectral

features are directly proportional to the concentration of the particular species. The combination of the laser and confocal microscope provides a unique opportunity to Raman map the surface of a sample. This can be achieved by automating an x-y-z (microscope z-focus) movement on the microscope stage.

There are some draw backs associated with the Raman technique. A major limitation is that the Raman signal is weak and can be swamped by sample fluorescence. Fluorescence is strongly dependent upon wavelength and can be avoided by using longer wavelengths. Unfortunately, the energy available at longer wavelength is lower such that stronger and more intense lasers are required to observe the Raman effect. This increase in power can result in sample damage and therefore changes the surface chemistry being investigated. Raman does not need bonds with dipole moments for sample interaction but rather bond polarisability. Typically asymmetric stretching vibrational modes are non polarisable and therefore non detectable, for example as one bond increases or lengthens the other associated bond decreases or shortens resulting no net change in the molecular polarisation.

2.6 Summary of Electrochemical Techniques

Any single electrochemical technique used to study a process as complex as corrosion will not yield information on all the aspects of the corrosion process.

The use of standard DC techniques possesses limitations in the practical application of the method as well as in the information one can obtain. Experimental limitations

include the destructive nature of the test. The large polarisation potential used results in irreversible changes of the sample, invalidating any further test using the same sample. The study of any time dependent process therefore requires large number of samples. The use of high potential, presents another issue when dealing with metals protected by an insulating coating. The physical barrier introduces an additional factor making some experiments difficult to evaluate. The data obtained from these experiments can be used to determine when certain changes occur and the magnitude of the electrochemical activity but data from DC experiments alone often yields little insight in to the underlying corrosion mechanism.

EIS is considered a non destructive test since the small polarisation potential used is assumed to have a negligible effect on the sample. Therefore any time dependent processes can be studied using the same sample, hence requiring a smaller number of samples. The more complex data obtained using EIS can also be more revealing of the corrosion mechanism since several processes occurring simultaneously can be separated.

A limitation of EIS as well as of DC techniques is that the information obtained is a result of activity from all over the sample surface, naturally dominated by the most active regions. Local scanning techniques such as SVET present a way to study the distribution of activity, revealing processes such as small coating defects or blister formation. The different information obtainable from the different techniques can combined produce greater reliability and a yield more complete picture into the corrosion mechanism that what can be obtained using any individual technique.

Chapter 3- Material Synthesis and Characterisation

3.1 Introduction

This chapter outlines material synthesis and procedure used in applying said materials as coatings as well as characterisation of materials and coatings. All procedures outlined were standard for all conditions, unless otherwise noted in later chapters. Materials were made with the aim of producing processable ICP. Poly(butyl acrylate-vinyl acetate) copolymer was used as the insulating material to produce a polyaniline composite with the aim of producing a conductive, soluble and heat treatable composite material with improved coating properties. Polymerisation of 3-octyl pyrrole was performed with the aim to produce a soluble, conductive ICP without the use of insulating composite material.

3.2 Materials

3.2.1 Monomer Purification

Pyrrole (Merck), aniline (Aldrich Chemical Company) were purified by distillation and stored in a freezer under N_2 prior to use. Purification and removal of MEHQ stabiliser in Vinyl acetate (Aldrich Chemical Company) was also performed by distillation prior to use. Butyl acrylate (Aldrich Chemical Company) containing MEHQ was distilled under reduced pressure at 65 °C, approx corresponding to 40 mmHg. 3-Octyl pyrrole (3OP) was synthesised in house using method outlined in [88]. Product was purified by distillation under reduced pressure at 90 °C corresponding to a pressure of about 2 mmHg and stored under N_2 in a freezer until used.

3.2.2 Reagents

Chemicals, unless noted, were obtained from Aldrich Chemical Company and used without any further purification. Sodium lauryl sulphate and sodium bicarbonate were obtained from Ajax chemicals and tetrabutylammonium perchlorate was purchased from Fluka. Iron(III)-*p*-toluenesulfonate was made in house using method outlined in [89].

3.2.3 Solvents and Aqueous Acids

AR grade solvent and aqueous acids were obtained from Ajax Chemicals unless otherwise noted and used as received. All water used was of MilliQ grade (18MΩ).

Solvents used in this work include; acetonitrile (AN), dichloromethane (DCM), carbontetrachloride (CCl_4), N-metylpyrrolidone (NMP) (Sigma), ethanol (EtOH), dimethylsulfoxide (DMSO) (Sigma), acetone (Acet), toluene (Tol), Isopropanol (IP).

3.3 Preparation of Polyaniline-HCSA/Poly(butyl acrylate-vinyl acetate) Copolymer Composite

The synthesis of polyaniline/poly(butyl acrylate-vinyl acetate) copolymer composite (PAn/co-polymer) doped using (1s)-(+)-10-Camphorsulfonic acid (HCSA) has been described previously [62]. Briefly, the copolymer latex was synthesised using a reagent list, given in Table 3.1, in a 500 mL glass reactor. Firstly; 120 mL water, 40 mL of monomer mixture, sodium lauryl sulphate and sodium bicarbonate were charged into the reactor under constant stirring using an overhead stirrer. The reactor was heated to 70 °C and the remaining monomer and potassium persulphate solution (0.3 g in 80 mL water) were individually fed into the reactor at a rate of 1 and 0.4 mL/min, respectively. The reaction was completed after 6hours.

Table 3.1 Composition used for synthesis of poly(butyl acrylate-vinyl acetate) copolymer

	Mass (g)	***Mol***
Vinyl acetate	152	1.77
Butyl acrylate	48	2.67
H_2O	200	11
Sodium lauryl sulphate	3	0.01
K_2SO_4	0.3	1.74e-3
$NaHCO_3$	0.3	3.57e-3

The PAn/co-polymer was then synthesised in a 500 mL glass reactor using 130 mL of the co-poly emulsion diluted with H_2O to 20 % w/w. 6 g (0.064 mol) aniline, dissolved in 70 mL 0.5 M HCSA was then fed into the emulsion at 5 ^{0}C under vigorous stirring. 50 mL (0.064 mol) ammonium persulphate solution was then slowly added using one to one molar ratio aniline/oxidant. Once polymerisation was initiated (about 30 minutes) the reaction temperature was reduced to between 0 and -3 ^{0}C. The reaction mixture was stirred for 5 hours resulting in a thick dark green suspension. Unreacted chemicals were removed by repeated washing with deionised water, collecting the product by centrifugation at 4000 rpm for 10 min.

3.4 Preparation of Poly(3-octyl pyrrole)

3.4.1 Electrochemical Polymerisation

Electrochemical polymerisation of poly(3-octyl pyrrole)-*p*-toluenesulfonate (P3OP-*p*TS) was made using was made using a method reported by Ashraf *et. al.* [88] in using a one compartment, two electrode, electrochemical cell with a 35 cm^2 Pt plate working electrode and a platinum mesh counter electrode. The polymerisation solution consisted of 500 mL 20/80 v/v Dichloromethane/Carbon tetrachloride (DCM/CCl_4) with 0.12 M 3OP and 0.12 M TBA*p*TS. Polymerisation was performed under galvanostatic control applying a charge density of 260 C/cm^2 at 1 mA/cm^2 for 72 hours using a generic power supply. The total charge was calculated to correspond to approximately 70 % of charge needed for 100 % conversion of monomer to doped polymer based on 100 % current efficiency and doping level of 0.3 dopant/monomer unit. At regular intervals small amounts of electrolyte were removed and examined by UV-vis. Material was recovered as two fractions; deposited material peeled off from the working electrode and material recovered from solution after removing electrolyte. The two fractions were filtered and repeatedly washed in AN to remove monomer, short chained oligomer and excess dopant.

Smaller scale polymerisations were performed in a one compartment three electrode electrochemical cell under galvanostatic control using a EG&G Princeton Applied Research Galvanostat/Potentiostat Model 263A operated from a PC computer running M270 (v4.30) software by EG&G Princeton Applied Research. A 6cm^2 Pt

electrode was used as working electrode, Pt-mesh as counter electrode with potential monitored vs. Ag/Ag^+ reference electrode. Polymerisation was performed in 15mL electrolyte containing 0.12 M 3OP and 0.12 M tetrabutylammonium perchlorate ($TBAClO_4$) or tetrabutylammonium *p*-toluenesulfonate (TBA*p*TS) as dopant. The experiments were performed at two current densities of 0.6 C/cm^2 in a short experiment and a longer deposition using 10 C/cm^2, corresponding to approximately 15 % of charge needed for 100 % conversion of monomer to doped polymer. DCM and acetonitrile (AN) were used as electrolyte. Polymer material recovered was filtered and repeatedly washed using AN.

3.4.2 Chemical Polymerisation

P3OP synthesised by oxidative polymerisation using a chemical oxidant was performed by slowly feeding a 40 mL oxidant solution into a 40 mL monomer solution containing 0.12 M OP and 0.12 M dopant. Alternately a 40 mL monomer solution not containing dopant was feed into an oxidant solution. Polymerisation was performed at -5 °C under N_2 atmosphere after pre purging both solutions with N_2. Reagent addition was performed by vigorously stirring at a rate of 1 mL/min. The reaction was stirred for 2 hours after which the temperature was slowly allowed to reach room temperature. After 1 hour at room temperature the precipitate was collected on a glass frit and washed with AN. Polymerisation was performed in AN using $Cu(ClO_4)_2$ or in methanol (MeOH) using Fe(*p*TS)$_3$ as oxidant. Conditions were optimised in terms of conductivity for soluble material by varying monomer to oxidant ratio.

3.5 Material Characterisation

3.5.1 Solubility

Solubility of the material was tested using a wide range of solvents listed in Table 3.2.

Table 3.2 Solvents used to solute polymer material

Dichloromethane(DCM)	Acetonitrile (AN)
Tetra hydro furan (THF)	N-Methyl-2-Pyrrolidone (NMP)
Ethanol	Dimethyl Sulfoxide (DMSO)
Acetone	Toluene
Isopropanol	Carbon tetrachloride

3.5.2 Cyclic Voltammetry

Cyclic Voltammetry (CV) was carried out in a conventional three electrode electrochemical cell using a Pt working electrode (A = 0.25 cm^2), Pt-mesh counter electrode and Ag/AgCl reference electrode. The potential was applied using potentiostat by EG&G Princeton Applied Research Galvanostat/potentiostat Model 263A operated from a PC running M270 (v4.30) software by EG&G Princeton Applied Research.

3.5.3 Ultraviolet-Visible Spectroscopy

Ultraviolet-visible spectroscopy (UV-vis) absorption spectra were measured using a Shimadzu (UV-1601) spectrophotometer operating from 300-1100 nm. UV-visible studies of polymer solutions were carried out in 1 cm path length quarts cell. Spectroscopy measurements of films were performed on microscopy slides coated by airbrushing.

3.5.4 Raman Spectroscopy

Raman spectroscopy was recorded using a JOBIN Yvon Horiba Raman Spectrometer model HR800 employing 10 mW Helium/Neon laser with a frequency of 632.8 nm and a charge-coupled detector (CCD) with a spatial resolution of 1.5 cm^{-1}. The laser was focused using a microscopy lens with ten times magnification producing a 5 μm diameter spot size. All data was recorded using a neutral density filter to minimise localised laser spot heat degradation.

3.5.5 Electrical Conductivity Measurement

DC conductivity was measured on pellets of the material pressed with a force of 5 Nm using 4-point contact probe (Jandel Engineering Limited) configured with the probes arranged in-line with 0.635 mm probe separation. Current was applied over the two outer probes and the potential drop measured between the two inner probes.

Volume conductivity was calculated using basic equation (3.1) were the volume conductivity σ (S/cm) is the inverse of the volume resistivity R_v (Ω*cm) expressed

as a geometrical factor; π/ln2, the potential drop (V), the applied current (I) and thickness of the sample (t) in cm.

$$\sigma = \frac{1}{R_v} = \left(\frac{\pi}{\ln 2} * \frac{V}{I} * t \right)^{-1} \qquad (1)$$

3.6 Coating Preparation

3.6.1 Surface Treatment

Aluminium alloy 2024-T3 panels, 5 by 3 inches (Q-panel), initially cleaned by sanding using 600 grit Si-Carbide sandpaper, followed by thorough polishing using Kimwipe® tissue and hexane. Hexane polishing was repeated until no black Si-carbide particles could be seen on the Kimwipe. Samples were then rinsed in hexane and left to dry in ambient conditions. This process was performed immediately prior to coating.

Zinc-55 % Aluminium hot dip coated steel (ZA) (Zincalume®) was supplied by BlueScope Steel Limited, Wollongong, Australia. Samples were cut into sections from a larger sheet removed from the production line and were not oil or otherwise treated. The panels were then stored in heat sealed vacuum bags until use. Prior to coating, the substrate was polished with Kimwipe® tissue and hexane, followed by a hexane rinse and drying in ambient conditions.

3.6.2 Coating of Substrate

3.6.2.1 Air Brushing

Coatings were applied from a dilute polymer solution in DCM using a hand held air brush (Paasche VL) propelled by pressured nitrogen onto a vertically oriented panel. Panels were then dried at ambient temperature followed by further drying in desiccator for a minimum of 24 hours. Samples were subject to heat treatment of 110 °C for 15 min with the aim of improving coating properties.

3.6.2.2 Evaporative Casting

Polymer solution was dropped onto the metal substrate placed on a flat surface allowing for the solvent to evaporate. Once a solid polymer film had formed the coating was further dried in an oven at 40 °C for approximately 20 min and stored in desiccator.

3.7 Coating Characterisation

3.7.1 Coating Thickness

Thicknesses of coatings were measured, unless noted, using a coating thickness gauge, Elcometer model 345 for non-ferrous substrate with integral probe. Same thickness gauge also was used to measure coating thickness on the galvanized steel after recalibrating and verifying that the underlying steel didn't in any significant

way influence the measurement. The substrates were also weighed pre- and post-coating as an alternate assessment of the coating "thickness" and reproducibility of the coating method.

3.7.2 Coating Adhesion

Adhesion of the dry coating prior to testing was measured according to ASTM D3359A tape test with tape from 3M. For PAn/co-polymer on AA2024-T3 adhesion was also measured using pull off adhesion tester by Elcometer (model 106). In this instance a test dolly of 3.2cm² was bonded to the coating using a two part epoxy (Miller-Stephenson 907). After allowing the adhesive 24 hours to cure the dolly was pulled off the surface using an adjustable spring arrangement which applies an incremental lift force to the dolly until the dolly dislodge from the substrate. Adhesion tests according to ASTM D3359A were performed on a minimum of 3 samples while for pull off adhesion, using Electrometer, testing included 6 measurements on 2 separately prepared coatings.

3.8 Results and Discussion

3.8.1 Preparation and Characterisation of Polyaniline/poly(butyl acrylate-vinyl acetate) Copolymer Composite

PAn/co-polymer exhibited lower solubility than the pure co-polymer but was highly soluble in dichloromethane and DMSO and partial solubility in acetone, THF and toluene. The composite was not soluble in ethanol or isopropyl alcohol, Table 3.3.

Table 3.3 Solubility of PAn/co-polymer/co-poly in various solvents

Solvent	***Solubility (w/v)***
DCM	>6 %*
THF	0.5 %
Ethanol	Not soluble
Acetone	<1.0 %
Isopropanol	Not soluble
DMSO	>13 %*
Toluene	<0.1 %

*High viscosity made solubility above this value difficult to determine

UV-Vis spectra of a spray coated PAn/co-polymer on glass substrate obtained after heat treatment at 40-200 °C (Figure 3.1) was consistent with spectra for PAn-ES. [14] Peaks observed at 350 and 425 nm corresponds to π-π^* transition and polaron to

π^* transition respectively. [90] Peak observed at approximately 800 nm corresponds to compact coil conformation. [91] For samples treated at 150 °C a minor decrease in the peak at 800 nm can be observed. After exposure at 280 °C the polymer undergoes significant change and rapid degradation of the free carrier tail occurs.

CV of PAn/co-polymer film coated Pt electrode obtained after heat treatment (Figure 3.2) showed an unaltered electroactivity after coating exposure to up to 110 °C. Exposure to 280 °C show to significantly altered redox properties thought to be a result of an unidentified degradation process.

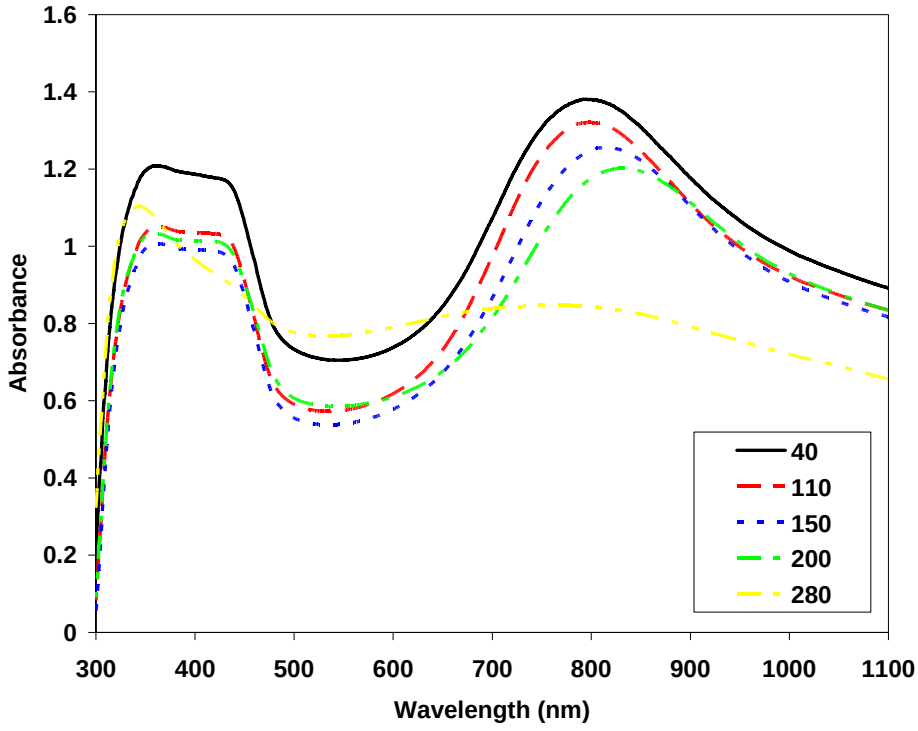

Figure 3.1 UV-vis spectra of PAn/co-polymer film after 20 min heat treatment. Films were formed by airbrushing polymer solution onto glass slide.

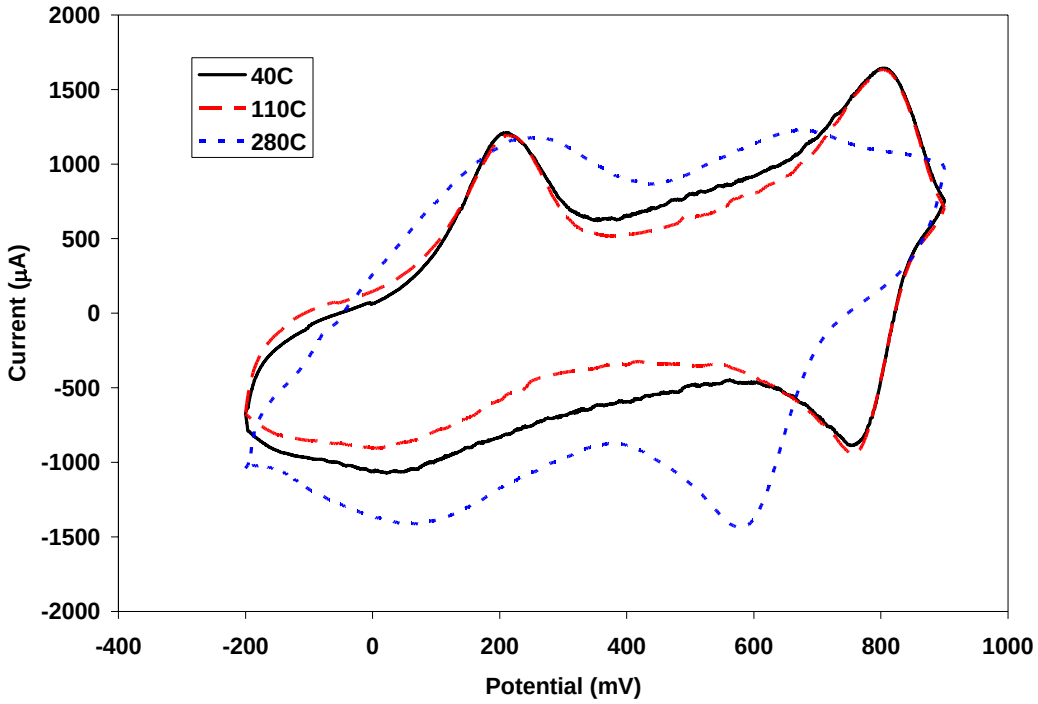

Figure 3.2 CV of PAn/co-polymer film after 20 min heat treatment Films were formed by airbrushing polymer solution onto a Pt electrode. CV was performed in 0.5 M HCl at 50 mV/s vs. Ag/AgCl.

The electrical conductivity measured on pellets pressed from powdered material after 20 min heat treatment showed no major change in conductivity for material treated up to 120 °C. For samples treated at 200 °C the conductivity decreased significantly.

The Raman spectra showed no significant changes after heat exposure to temperatures up to 110 °C, Figure 3.4 displaying typical spectra for primary doped PAn-ES. Notable features are peaks 1166 cm^{-1} due to a resonance form of –C–N–C– stretch while at 1321 and 1341 cm^{-1} bands due to the –C–NH–C– and —C=NH^{+}–C– resulting from the π-bond delocalisation forming a polaron (charge carrier) on the polymer back bone are observed. Bands at 1580 and 1610 cm^{-1} were related to the stretching vibration forms of –C=C– and –C-C– respectively. When exposed to

higher temperatures the polyaniline undergoes some distinct changes with a notable reduction of the peaks at 1321 and 1341 cm^{-1} indicating a loss of polymer charge carriers reduction of the –C-C-band at 1610 cm^{-1} in favour of the -C=C- band at 1590 cm^{-1}. Also a new band at 1420 cm^{-1} appears which is ascribed to irreversible crosslinking of the -C-N-C-.

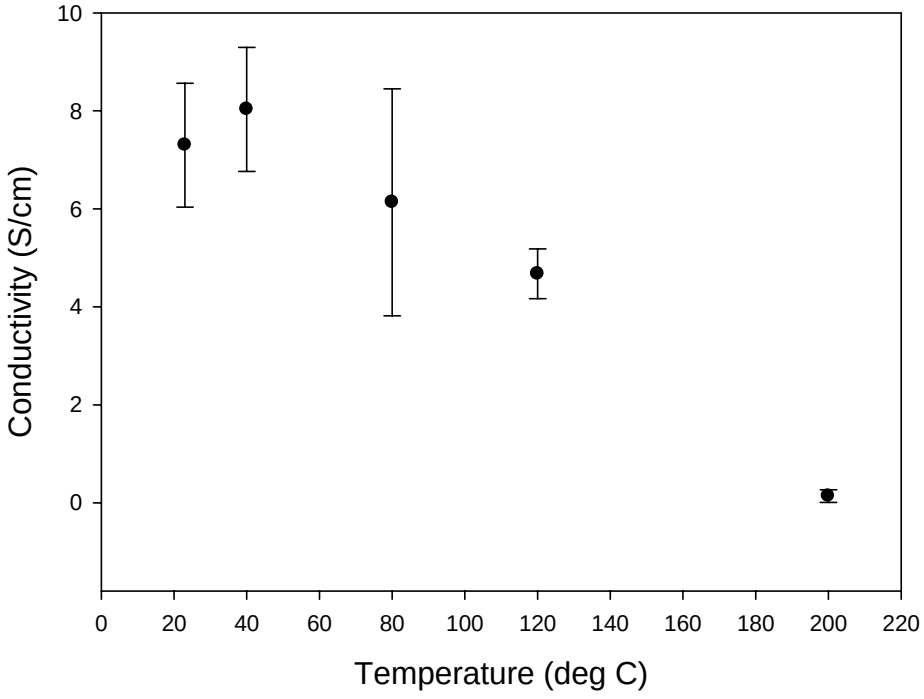

Figure 3.3 Conductivity of PAn/co-polymer pellet after 20 min heat treatment.

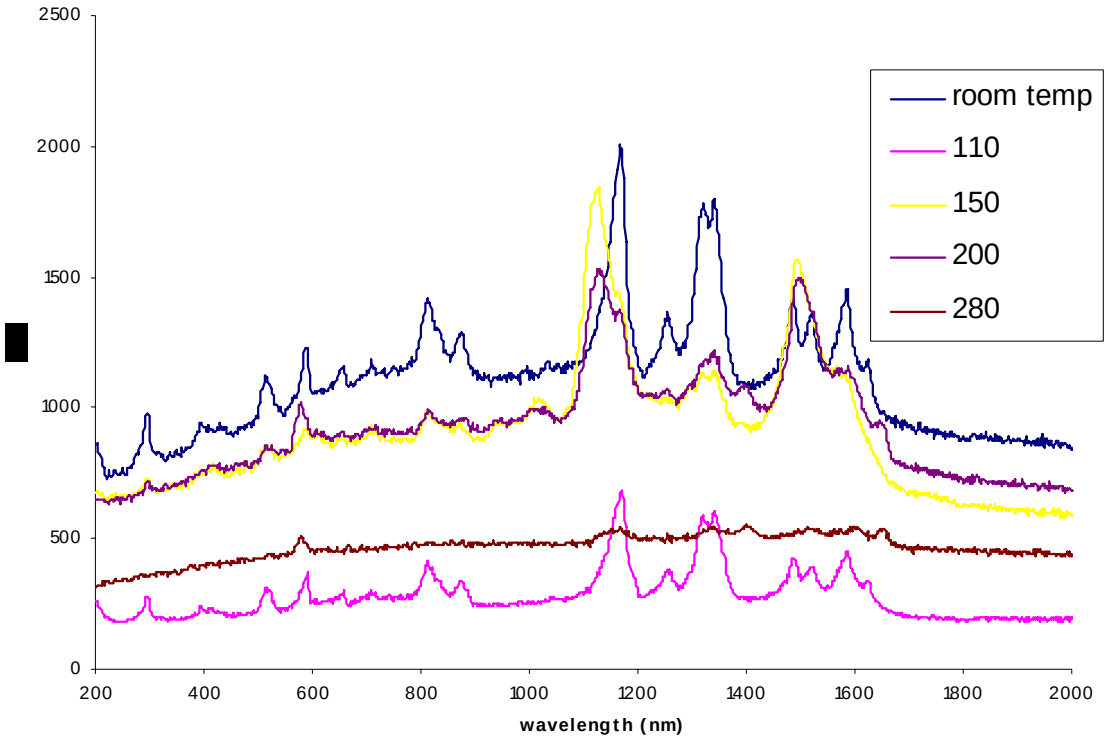

Figure 3.4 Raman spectra of PAn/co-polymer film after 20 min heat treatment. Films were formed by airbrushing polymer solution onto glass slide.

3.8.2 Preparation and Characterisation of Poly(3-octyl pyrrole)

3.8.2.1 Electrochemical Synthesis of P3OP-pTS from 80/20 CCl_4/DCM

P3OP-*p*TS was made by electrochemical polymerisation with galvanostatic control at 1 mA/cm^2 from 0.12 M OP 0.12 M TBA*p*TS in CCl_4/DCM (80/20) and produced two separate fractions; soluble material recovered from solution and polymer deposited on the working electrode. UV-vis of the soluble electrolyte fraction at different times during the polymerisation shown in Figure 3.5 showed spectra mostly resembling that previously observed for neutral P3OP [92-94] with peak observed at approximately 340 nm ascribed to the π-π^* transition in the polymer backbone. Peaks

observed at 490 nm and 980 nm correspond to the presence of bipolarons seen in P3OP-tetraflouroborate at 477 mn and 1127 nm [93, 94] suggesting that the polymer was not fully, though mostly, undoped. Also a minor shoulder at 580 nm could be seen, a feature ascribed to the presence of a polaron band [93]. Increase of the 350 nm, π-π^* transition peak and decrease of bipolaron peaks at 480 and 990 nm suggest that longer polymerisation produce material with even lower doping level.

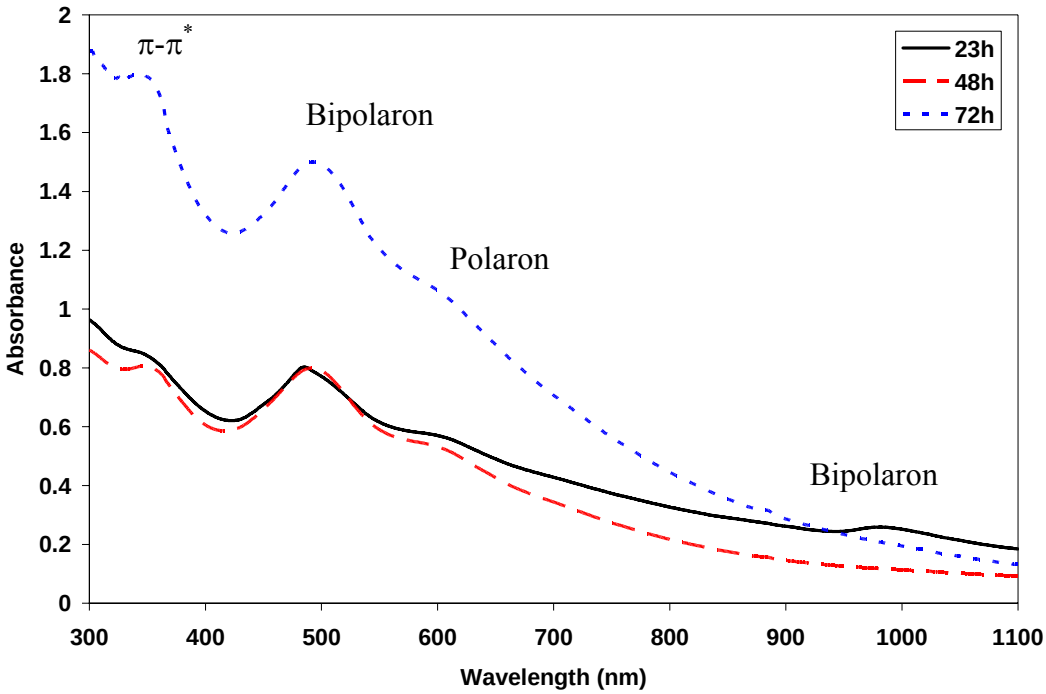

Figure 3.5 UV-vis of P3OP-*p*TS solution fraction made by electrochemical polymerisation in DCM/CCl_4 (80/20 v/v) for different polymerisation times.

Conductivity measurement of DCM-soluble fraction recovered after 72 hours showed the material to be insulating, in part contradicting the observed UV-vis spectra. The material was not conductive enough to allow measurement using 4-point probe technique. Instead an estimated conductivity of 10^{-8} S/cm was calculated from using a 2-point probe were the potential drop is measured between the electrodes

supplying the current. Deposited material, measured using 4-point probe, was slightly more conductive at $4*10^{-4}$ S/cm although this fraction was not soluble in DCM and only had minimal solubility in THF.

3.8.2.2 Electrochemical Synthesis of P3OP in AN

Chronopotentiograms recorded during galvanostatic polymerisation of P3OP-ClO_4 in AN (Figure 3.6) showed an initial potential spike after only a few seconds after which the potential decreased and levels out. This is consistent with initial deposition of a conducting polymer on the Pt electrode followed by continued deposition of polymer onto the polymer film at a lower potential, as the polymer grows more readily of polymer film than on Pt. UV-vis spectra of material formed using 0.6 C/cm^2 dissolved in DCM (Figure 3.7) displayed peaks at approximately 400 and 1000 nm that can be ascribed to bipolaron bands, while the peak observed at 670 nm corresponds to the polaron band. Polymerisation of the material using 0.6 C/cm^2 produced soluble conductive product. Material made using 10 C/cm^2 charge revealed lower conductivity and a significantly lower solubility (Table 3.4). P3OP-*p*TS displayed lower conductivity and was insoluble in both DCM and THF for a total synthesis charge passed of 0.6 C/cm^2.

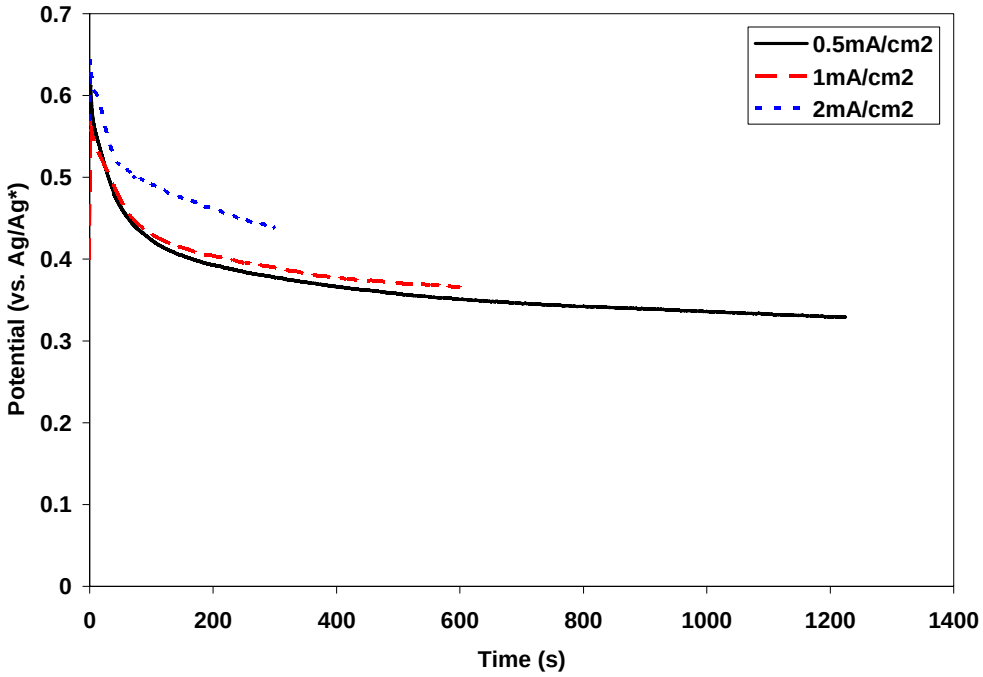

Figure 3.6 Chronopotentiogram of electrochemical polymerisation of P3OP-Cl0$_4$ in AN using different current densities.

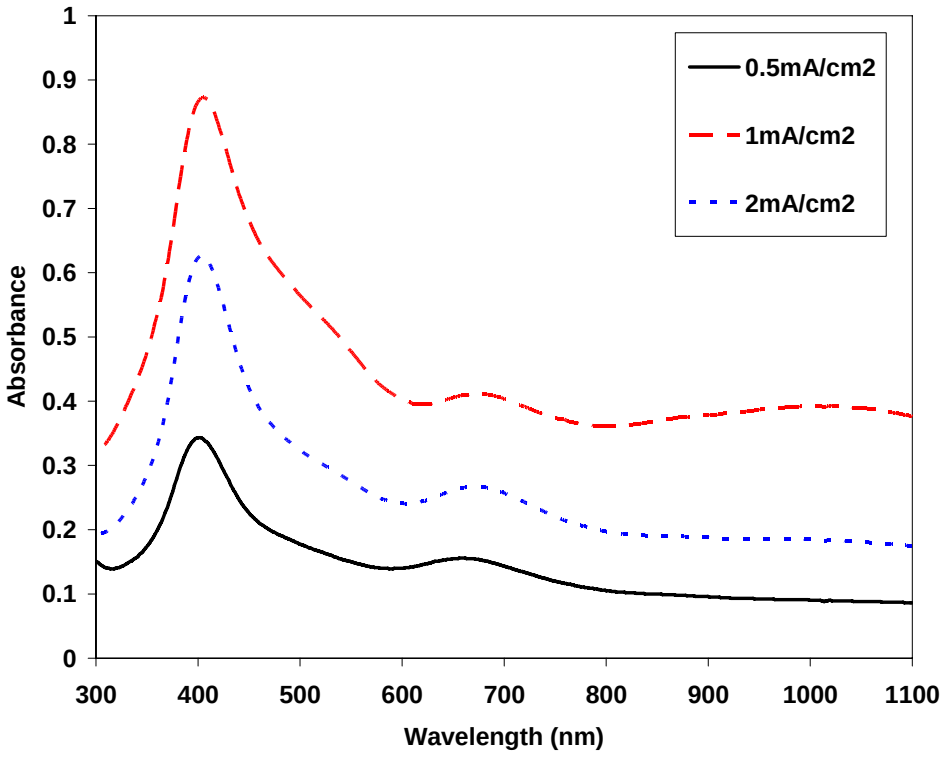

Figure 3.7 UV-vis of P3OP-Cl0$_4$ in THF made by electrochemical polymerisation in AN using different current densities.

Table 3.4 Effect of current density and charge passed on conductivity, yield and solubility of P3OP made by electrochemical polymerisation in AN.

Current density (mA/cm^2)	***Dopant***	***Charge passed***	***Conductivity (S/cm)***	***Solubility***	
				DCM	***THF***
0.5	TBAP	0.6C/cm^2	3	Yes	Yes
1	TBAP	0.6C/cm^2	3	Yes	Yes
2	TBAP	0.6C/cm^2	1	Limited	Yes
1	TBAP	10C/cm^2	0.6	Limited	Limited
1	TBA*p*TS	0.6C/cm^2	0.1	No	No

3.8.2.3 Electrochemical Synthesis of Poly(3-octyl pyrrole) in DCM

Chronopotentiograms recorded during galvanostatic polymerisation of P3OP-ClO_4 in DCM was similar to that observed for AN synthesis followed by a potential decrease that levels out (Figure 3.8). Both a soluble and an insoluble product were formed during polymerisation in DCM.

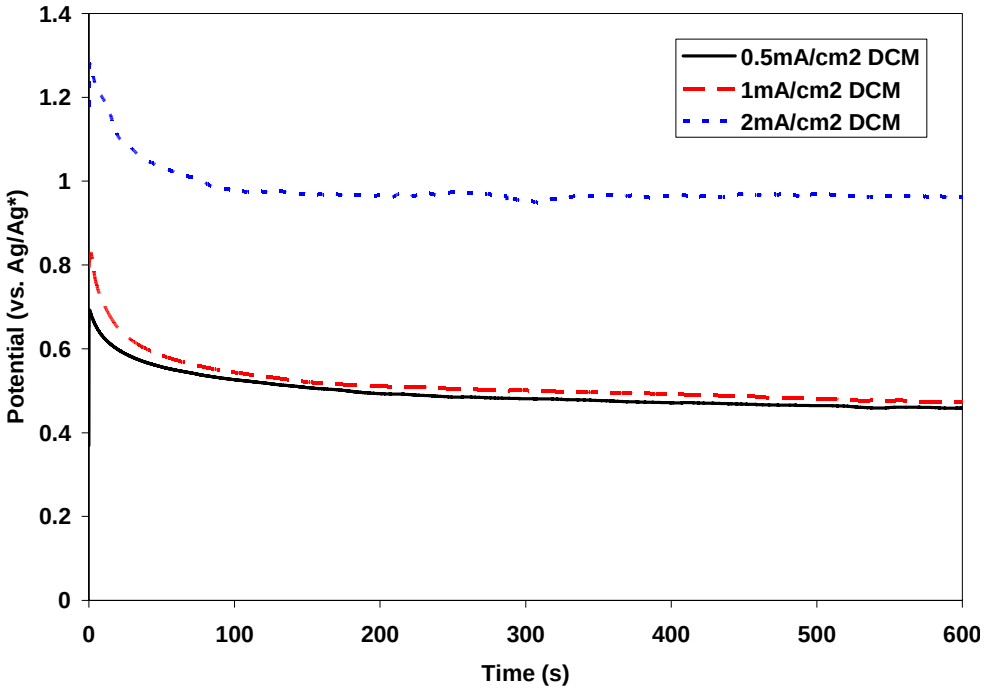

Figure 3.8 Chronopotentiogram of electrochemical polymerisation P3OP-$Cl0_4$ in DCM using different current densities.

For material synthesised using 0.6 C/cm^2, a greater part of the product deposited on to the electrode. The fraction of polymer formed in solution increased at longer synthesis times forming approximately 1/10 of total polymer formed at 0.6 C/cm^2 compared to 1/3 for 10 C/cm^2. Using 0.6 C/cm^2 the deposit material was insoluble in DCM but soluble in THF.

UV-vis for material recovered from working electrode made using 0.6 C/cm^2 solute in THF shown in Figure 3.9, displayed two distinct peaks at 390 and 680 nm ascribed to π-π^* transition and polaron transition respectively. Using a total charge of 0.6 C/cm^2 produced an insufficient amount of soluble fraction material to measure conductivity. Polymer recovered from the working electrode was found to be electrically conductivity as listed in Table 3.5. Material deposit on the Pt electrode at

10 C/cm^2 was as equally conducting as when using 0.6 C/cm^2. This material was not soluble in DCM and displayed low solubility in THF. P3OP-*p*TS obtained under the same conditions was deposited in conductive form but also showed a low solubility in THF when grown at 0.6 C/cm^2 and was mostly insoluble when using 10 C/cm^2.

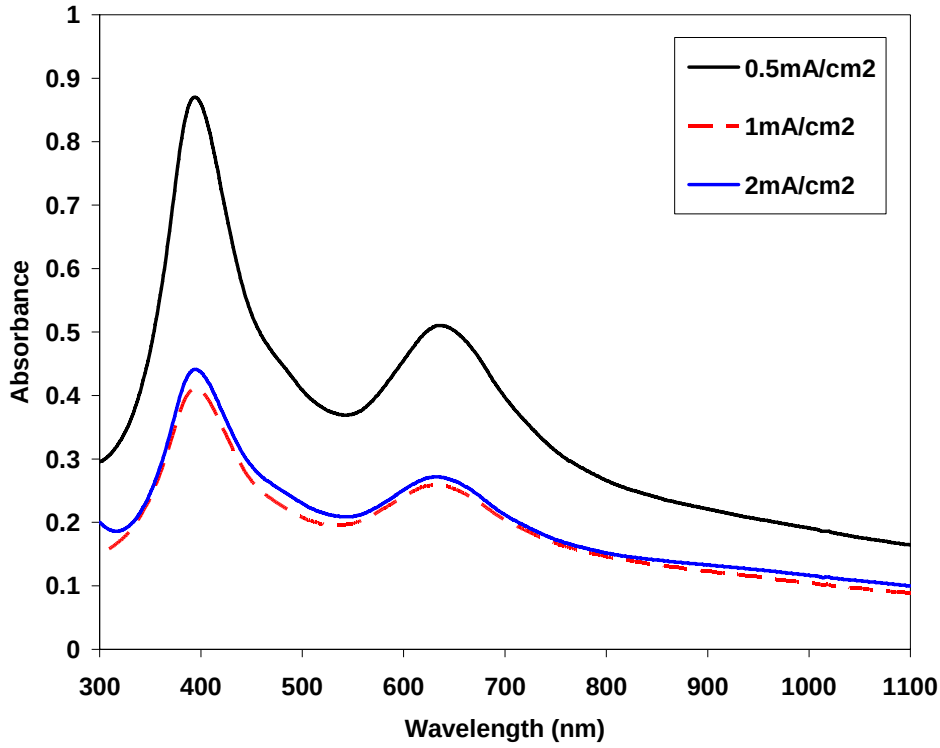

Figure 3.9 UV-vis of P3OP-Cl0$_4$ in THF made by P3OP-Cl0$_4$ made by electrochemical polymerisation in DCM using different current densities.

Table 3.5 Effect of current density and charge passed on conductivity, yield and solubility of P3OP made by electrochemical polymerisation in DCM.

Current density (mA/cm^2)	***Dopant***	***Charge passed (C/cm^2)***	***Conductivity (S/cm)***	***Solubility in THF***
0.5	ClO_4	0.6	1.2	Yes
1	ClO_4	0.6	4.2	Yes
2	ClO_4	0.6	2.2	Yes
1	ClO_4	10	**Deposit:** 4.0 **Solution:** 0.1	Low
1	TBA*p*TS	0.6	0.8	Low
1	TBA*p*TS	10	**Deposit:** 0.1 **Solution:** 10^{-6}	No

3.8.2.4 Chemical Synthesis of P3OP-ClO_4 made in AN

Addition of Oxidant to Monomer

Polymerisation was seen to initiate immediately when adding oxidant to the monomer solution with the solution turning black once the first drop was added. As polymerisation continued a fine polymer suspension was formed. Recovery of the material was made by filtering and washing repeatedly with AN, resulting in a powdery material with high solubility in DCM. UV-visible spectra (Figure 3.10) was consistent with formation of P3OP in doped form [93, 94]. The peak at around 420 nm can be assigned to a π-π^* transition in the polymer backbone, while shoulder at

480 nm and broad peak above 800 nm may be ascribed to bipolaron charge transfer bands.

Higher oxidant/monomer ratios produce a higher yield while maximum conductivity was observed when using an oxidant monomer ratio of 1.8 mol/mol. The conductivity observed for these systems was in the order of one magnitude lower than that observed for electrochemically synthesised material.

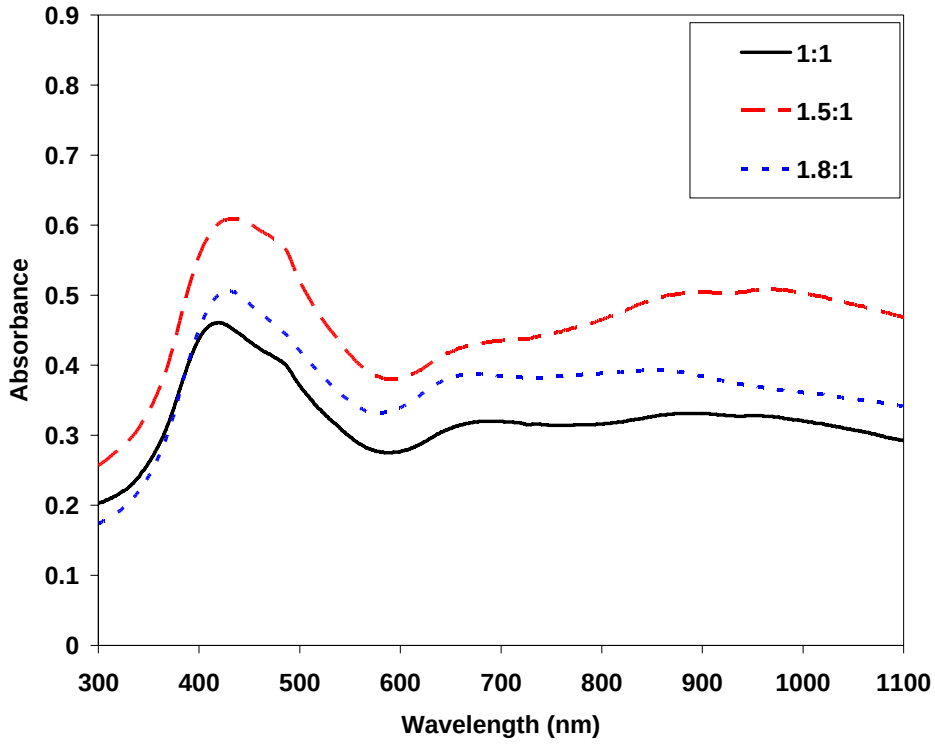

Figure 3.10 UV-vis of P3OP-$Cl0_4$ made by addition of oxidant solution ($Cu(ClO_4)_2$ in AN) to monomer solution (0.12 M OP in AN) using different oxidant/monomer ratio.

Table 3.6 Effect oxidant/monomer ratio on conductivity, yield and solubility of P3OP-$Cl0_4$ made by addition of oxidant solution ($Cu(ClO_4)_2$ in AN) to monomer solution (0.12 M OP in AN).

Oxidant/Monomer (mol/mol)	***Yield*** * ***(g polymer/g monomer)***	***Conductivity (S/cm)***	***Solubility in DCM (g/mL)***
1:1	50	15e-3	>2 %
1.5:1	80	12e-3	>2 %
1.8:1	105	170e-3	>2 %
2.25:1	120	82e-3	>2 %

*Yield was calculated using mass of polymer/mass of monomer i.e. assumes product formed is neutral.

Addition of Monomer to Oxidant

Addition of monomer solution to the oxidant solution produced material of similar appearance and solubility with respect to when feeding oxidant to monomer. UV-vis spectra Figure 3.11, was also comparable to that above with peak at 420 nm and a large broad peak above 800 nm. The peak at around 420 nm correlates to π-π^* transition, while the shoulder at 480 nm and broad peak above 800 nm corresponds to bipolaron charge transfer bands. Maximum conductivity was obtained using an oxidant/monomer ratio of 1.8, measuring 2.1 S/cm. The significant conductivity increase observed by adding monomer solution to the oxidant solution instead of vice versa may be a result of the higher oxidation "potential" in the case of the prior.

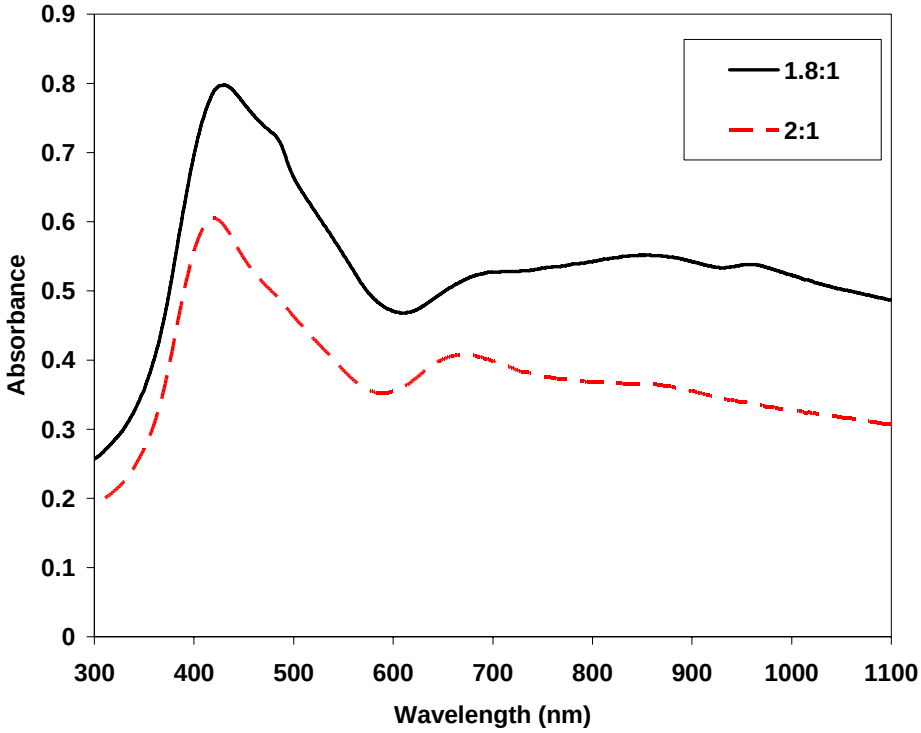

Figure 3.11 UV-vis of P3OP-$Cl0_4$ made by addition of monomer solution (0.12 M OP in AN) to oxidant solution ($Cu(ClO_4)_2$ in AN) solution using different oxidant/monomer ratio.

Table 3.7 Effect oxidant/monomer ratio on conductivity, yield and solubility of P3OP-$Cl0_4$ made by addition of monomer solution (0.12 M OP in AN) to oxidant solution ($Cu(ClO_4)_2$ in AN) solution.

Oxidant/ Monomer (mol/mol)	***Yield* (g polymer/g monomer)***	***Conductivity (S/cm)***	***Solubility in DCM (g/mL)***
1:1	40	0.5	>2 %
1.5:1	70	1.9	>2 %
1.8:1	80	2.1	>2 %
2.25:1	105	1.3	>2 %

*Yield was calculated using mass of polymer/mass of monomer i.e. assumes product formed is neutral.

3.8.2.5 Chemical Synthesis of P3OP-pTs made in using $Fe(pTS)_3$ in MeOH

Polymerisation of P3OP-pTS in MeOH produced a powdery material highly soluble in DCM with UV-visible spectra shown in Figure 3.12. The spectra indicated the formation of doped polymer with the peak observed at 390 nm assigned to π-π^* transition, the shoulder observed at 480 nm, together with the broad peak above 800 nm, corresponding to bipolaron charge transfer bands. A maximum conductivity of 1.3 S/cm was obtained using an oxidant/monomer ratio of 1.8.

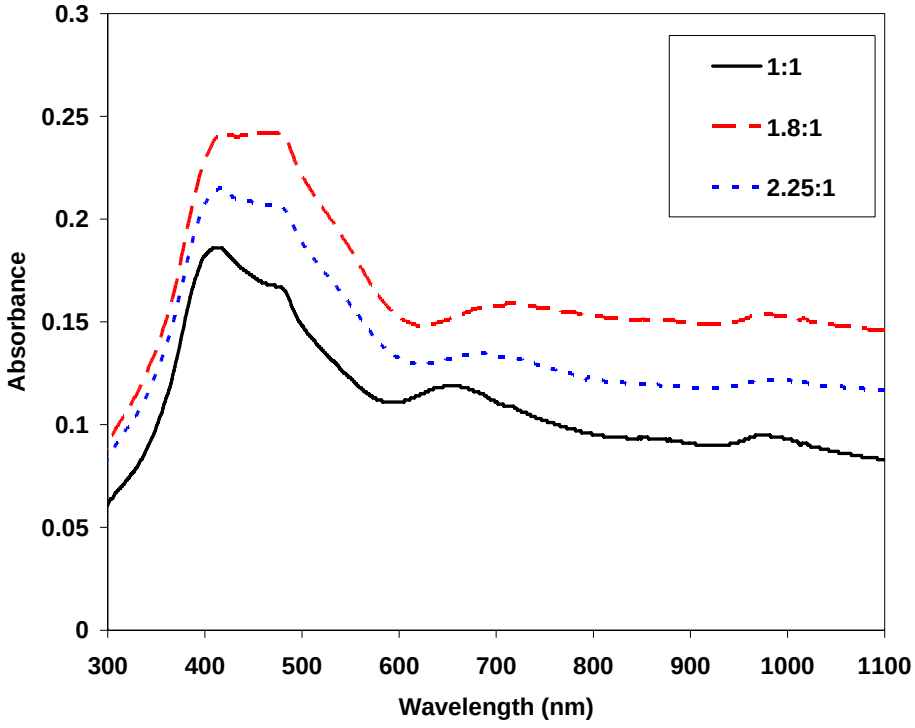

Figure 3.12 UV-vis of P3OP-*p*TS made by addition of monomer solution (0.12 M OP in MeOH) to oxidant solution ($Fe(pTS)_3$ in MeOH) solution using different oxidant/monomer ratio.

Table 3.8 Effect oxidant/monomer ratio on conductivity and yield of P3OP-*p*TS made by addition of monomer solution (0.12 M OP in MeOH) to oxidant solution ($Fe(pTS)_3$ in MeOH) solution.

Oxidant/ Monomer (mol/mol)	***Yield* % (g polymer/g monomer)***	***Conductivity (S/cm)***	***Solubility in DCM (g/mL)***
1:1.5	37	0.56	>2 %
1:1.8	50	1.3	>2 %
1:2.25	67	0.9	>2 %
1:2.75	69	0.13	>2 %

*Yield was calculated using mass of polymer/mass of monomer i.e. assumes product formed is neutral.

3.8.3 Coating Characterisation

3.8.3.1 PAn/co-polymer Coating

Substrate coating with PAn/co-polymer was preformed by air brushing a dilute DCM solution of 0.5-1 % w/v. This method produced a thin continuous coating without visible defects or variations. The coating thickness was measured using a thickness gauge, taking 24 measurement points distributed over a 97 cm^2 area on 3 individually spray coated panels and gave a mean thickness of 3.6 μm (σ 0.65), with a loading of 0.42 mg/cm^2 for "air dried" coating and 3.4 μm (σ 0.57) with a loading of 0.41 mg/cm^2 for "heat dried" coating. Adhesion testing of the coating using ASTM D3359A tape test removed no part of the material for either of the coatings thus corresponding to 0A rating. The pull off adhesion for "air dried" and "heated" PAn/co-polymer was 68 N/cm^2 (σ 28), 99 N/cm^2 (σ 47) respectively with the coating showing consistent adhesive failure i.e. at the coating/metal interface with total removal of PAn/co-polymer from the substrate. The adhesion for the "heat treated"

sample exhibited no statistical difference from the non-heated treated coated samples.

3.8.3.2 P3OP-pTS Coating of Electrochemical Synthesis in 80/20 DCM/CCl_4

Coating with P3OP-*p*TS soluble fraction made electrochemically in 80/20 v/v DCM/CCl_4 using a total charge density of 260 C/cm^2 at 1 mA/cm^2 was made by evaporative casting onto a 2.5x2.5 cm sample from a 1 % w/w DCM solution. After the solvent evaporated the coating was completely dried in a desiccator overnight to produce a smooth uniform coating. Mean coating thicknesses measured using thickness gauge on 8 individually cast samples was 6 μm (σ 1.15), with a loading of 0.73 mg/cm^2 (σ 0.07). Adhesion testing of the coating using ASTM D3359A tape test removed no part of the material thus corresponding to 0A rating.

3.8.3.3 P3OP-TBAP Coating of Electrochemical Synthesis in DCM

Coating with P3OP-ClO_4 deposited fraction prepared electrochemically with a total charge of 10 C/cm^2 at 1 mA/cm^2 in DCM was applied by airbrushing a 0.5 % w/v polymer solution in THF containing 1 % NMP. NMP was added to solution as a plasticiser to prevent cracking of the coating as solvent evaporated. Samples were then dried in a vacuum oven at 60 ºC for 4 hours to remove any NMP. The resulting films were smooth uniform coatings with a coating thickness of 3-4 μm measured using a digital micrometer with a 0.5 mg/cm^2 loading. Adhesion testing of the coating using ASTM D3359A tape test removed no part of the material thus corresponding to 0A rating.

Coating with P3OP-ClO_4 soluble fraction made electrochemically in DCM with a total charge of 10 C/cm^2 at 1 mA/cm^2 was applied by airbrushing a 0.5 % w/v polymer solution of made from DCM. Method produced smooth uniform coating with a coating thickness of 3-4 μm measured using a digital micrometer with 0.5 mg/cm^2 loadings. Adhesion testing of the coating using ASTM D3359A tape test removed no part of the material thus corresponding to 0A rating.

3.8.3.4 P3OP-pTS Coating of Electrochemical Synthesis in DCM

Coating with P3OP-pTS soluble fraction made electrochemically in DCM was applied by airbrushing a 0.5 % w/v polymer solution in DCM. The method produced smooth uniform coating with a coating thickness of 4-5 μm measured using a digital micrometer with a 0.6 mg/cm^2 loading. Adhesion testing of the coating using ASTM D3359A tape test removed no part of the material thus corresponding to 0A rating.

3.8.3.5 P3OP-ClO_4 Coating of Chemical Synthesis in AN

Coating with chemically synthesised P3OP-ClO_4 was applied by evaporative casting onto a 2.5x2.5 cm sample from a 1 % w/w DCM solution. After solvent evaporation the coating was completely dried in a desiccator overnight. The method produced a uniform but brittle coating with a mean thickness of 5.2 μm (σ 1.5), measured using a thickness gauge on 8 individually cast samples with a loading of 0.63 mg/cm^2 (σ 0.11). Adhesion testing of the coating using ASTM D3359A tape test removed minor parts of the coating thus corresponding to 1A rating.

3.8.3.6 P3OP-pTS Coating of Chemical Synthesis in MeOH

A coating with chemically synthesised P3OP- *p*TS was applied by evaporative casting onto a 2.5x2.5 cm sample from a 1 % w/w DCM solution. After solvent was evaporated the coating was completely dried in a desiccator overnight. The method produced a uniform coating with a mean thickness of 4.7 μm (σ 0.7), measured using thickness gauge on 8 individually cast samples with a loading of 0.62 mg/cm^2 (σ 0.05). Adhesion testing of the coating using ASTM D3359A tape test removed no part of the material thus corresponding to 0A rating.

3.9 Conclusions

polyaniline/Co(polyButyl Acrylate –Vinyl acetate)/composite doped with HCSA was successfully prepared. The material was soluble in several organic solvents to a high degree, possessing relatively high conductivity and was electroactive. The material could successfully be applied to AA2024-T3 by air brushing, forming continuous, uniform and reproducible coating with adhesion of about 70 N/cm^2. The material could also be heat treated to 110 °C without any significant change to the electrochemical properties and only a minor decrease in electrical conductivity observed, though the heat treatment did not produce any observable effect on the coating adhesion.

P3OP-*p*TS could not, using the conditions investigated, be prepared electrochemically in solution to form a soluble conductive polymer. By

electrochemical deposition from either AN or DCM conductive P3OP-ClO_4 was obtained. The resultant polymer could then be solubilised in DCM or THF for material synthesised in AN or in THF for material synthesised in DCM. Solubility and conductivity of the synthesised polymer decreased for longer synthesis times using deposition from AN, while conductive P3OP-ClO_4 with partial solubility could be obtained from DCM after 15 % monomer conversion. Lower conductivity P3OP-*p*TS was obtained at monomer conversion of 15 %, from DCM, although most material formed was insoluble.

P3OP-*p*TS made from 80/20 v/v CCl_4/DCM was used to form continuos uniform coatings by evaporative casting from DCM on AA2024-T3 and ZA with 0A adhesion. Continuos coatings with P3OP-ClO_4 obtained from deposition in DCM was only obtained by airbrushing, using a 1 % NMP addition to the THF solution, showing a 1A type adhesion. The solution fraction obtained using ClO_4 or TBA*p*TS in DCM formed uniform coatings by air brushing from a dilute DCM solution coating displaying 0A adhesion on AA2024-T3.

Conductive and highly soluble P3OP-ClO_4 and P3OP-*p*TS was obtained at high yield using chemical polymerisation by $Cu(ClO_4)_2$ in AN or Fe(*p*TS)$_3$ in MeOH. Material could be used to form continuos uniform coatings with 0A adhesion on AA2024-T3 by evaporative casting from DCM.

Chapter 4- Electrochemical Characterisation of ICP Coated AA2024-T3

4.1 Introduction

The EIS response of an ICP coating will differ from the response that is typically observed for a traditional insulating polymer coating. These differences are due to the inherent electrical conductivity, the redox cyclability of the ICP and the possibility of the ICP to act as an inhibitor release coating. EC modelling of ICP's in the context of corrosion protective coatings has resulted in several different and sometimes conflicting EC models. This review attempts to summarise the suggested EC for ICP coating systems and the reasoning behind them.

4.1.1 EC of Polyaniline Coated Steel

Polyaniline coated steel has been extensively investigated by use of EIS. Schauer *et al.* [95] investigated the corrosion of mild steel coated using a commercial ICP coating system by Ormecon Chemie, Ahrensburg Germany, consisting of a primer loaded with polyaniline powder and an insulating polymer binder followed by an

epoxy topcoat. Schauer *et al.* [95] suggested an equivalent circuit model for their EIS data, Figure 4.1. The polyaniline employed in this work was in the form of ES, although the conductivity of the polyaniline blend was in the insulating range ($7x10^{-7}$ S/cm). Experiments were performed in 0.5 M NaCl using a frequency range of 100 kHz to 0.01 Hz. No raw data or data fitting of the model was provided nor any reasoning behind the choice of model.

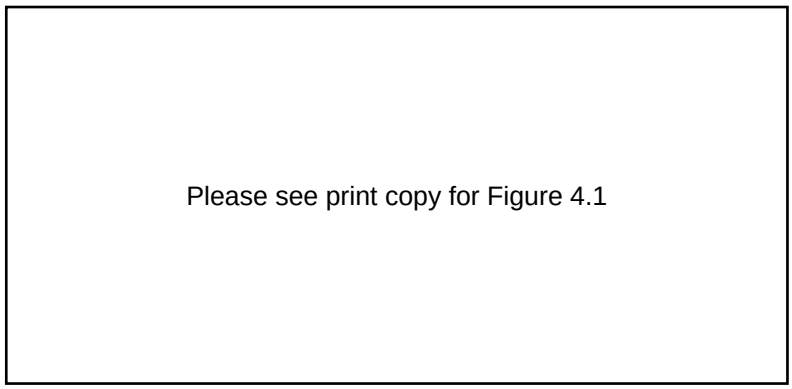

Figure 4.1 Equivalent circuit suggested by Schauer *et al.* for steel coated with a PAn blended primer covered by an epoxy topcoat tested in 0.5M NaCl. [95]

Primer coatings consisting of PAn blended with an insulating polymer was also investigated by Li *et al.* [96] who examined the composite blend both with and without a topcoat under saline and acidic conditions over a frequency analysis range of 100 kHz-0.05 Hz. Electroactive coatings under acidic conditions (1 M HCl), that were not sealed by an insulating topcoat, exhibited a two time constant system. Li *et al.* suggested the EC model shown in Figure 4.2 with the high frequency semicircle assigned to charge transfer reaction at the metal/polymer interface, and the low frequency time constant assigned to the polymer/solution interface. It was suggested that "the high frequency semicircle may correspond to the repassivation of a scratched metal surface by PAn". PAn was subsequently reduced in the process and

the process of reoxidation, "by a suitable cathodic depolariser in the environment" (notably dissolved oxygen), was represented by the low frequency semicircle.

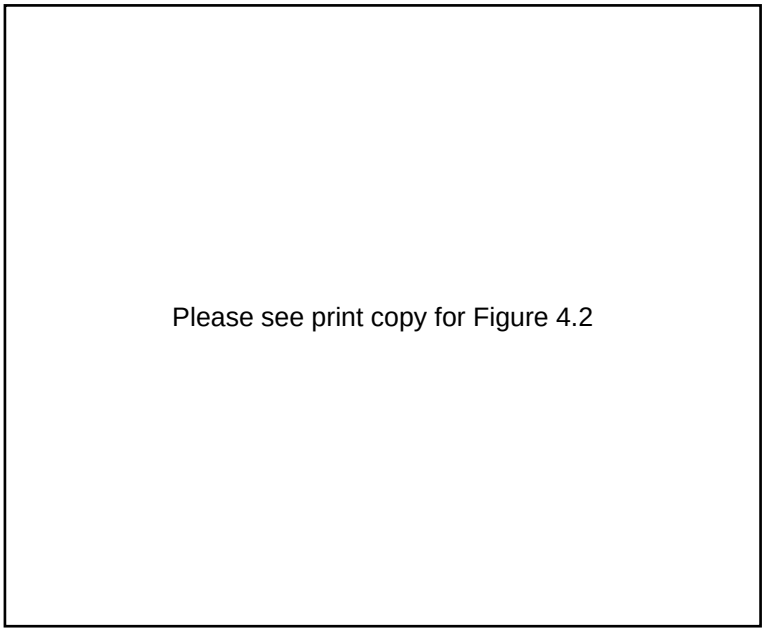

Figure 4.2 Equivalent circuit suggested by Li *et al.* for steel coated with a PAn blended primer without use of an insulating topcoat tested in 1 M HCl. [97]

When an insulating topcoat was employed so as to protect the ICP, Li *et al.* proposed the model shown in Figure 4.3 Equivalent circuit suggested by Li et *al. for* steel coated with a PAn blended primer with use of an insulating topcoat tested in 1 M incorporated an additional element modelling the diffusional barrier properties of the insulating topcoat.

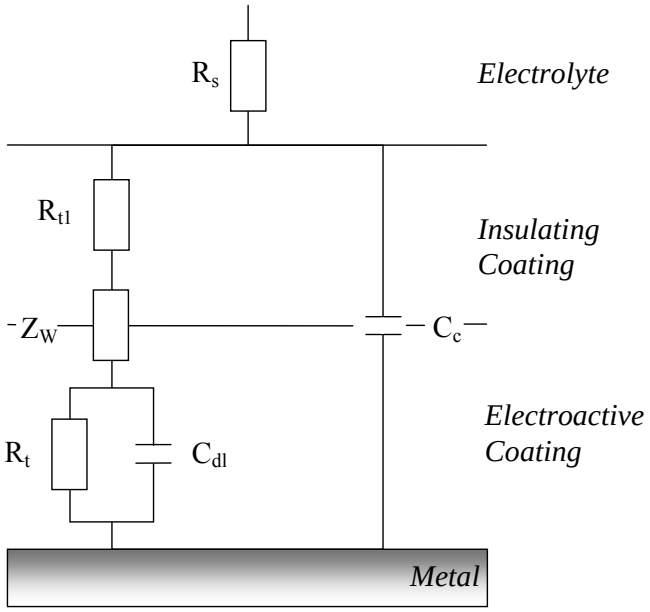

Figure 4.3 Equivalent circuit suggested by Li *et al.* for steel coated with a PAn blended primer with use of an insulating topcoat tested in 1 M

4.2 Experimental Procedure

4.2.1 Sample Preparation

The experimental cell used for coating testing was fabricated by fixing a PVC tubing onto a substrate using a silicon adhesive, as shown in Figure 4.4. The tubing employed had an inner diameter of 18mm and a nominal height of 35 mm creating a cell with a sample area of 2.5 cm^2 and holding about 9 mL of electrolyte.

Experiments were performed under ambient conditions in an open cell, allowing any gas formed to escape. Measurements were performed using a three electrode cell with a Pt-mesh counter electrode and a Ag/AgCl in 3M NaCl as reference electrode.

The corrosive electrolyte used in this study consisted of 0.35 % $(NH_4)_2SO_4$ and 0.05 % NaCl in deionised water, a solution known as Dilute Harrison's solution (DHS). DHS is used to simulate industrial coastal conditions, used for testing of high strength aluminium alloys by research groups working on behalf on the U.S. Air force. [97]

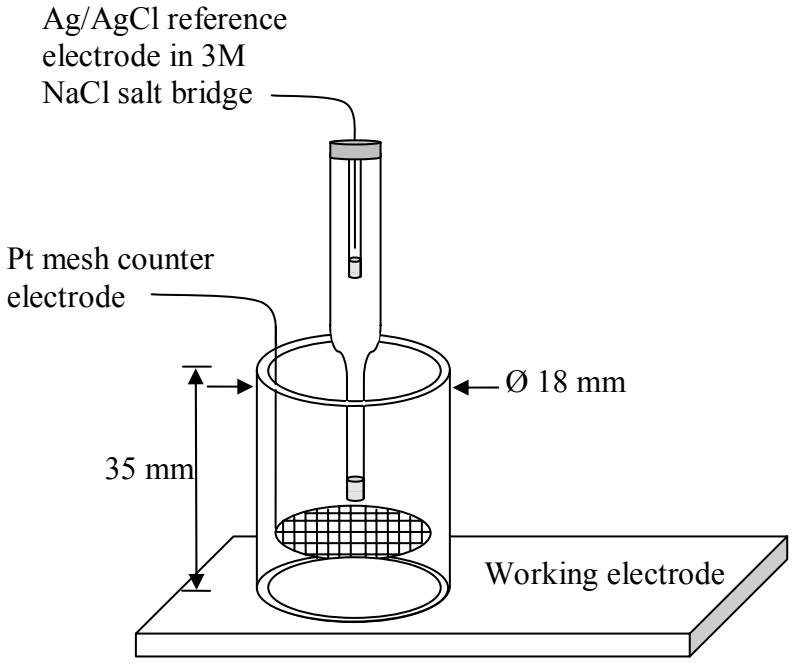

Figure 4.4 Schematic of electrochemical cell used to perform polarisation, OCP and EIS experiments.

4.2.2 Polarisation Measurements

Cyclic polarisations (CP) were performed using CorrWare software by Scribner and a Solartron 1287A potentiostat. The scan was performed after allowing 30 min for the open circuit potential (OCP) to stabilise and was scanned in the positive direction initiated at -30 mV from the observed OCP. The scan direction was reversed at 0.5 V

vs. Ag/AgCl or at a current density limit of 1 mA/cm^2 and scanned in the cathodic direction to -100 mV of the initially observed OCP using a scan rate of 10 mV/min.

Linear polarisations were performed using a potentiostat, Model 273A (Princeton Applied Research, EG&G Instruments Inc), using 352 SoftCorr III v3.06 software (EG&G Instruments Inc.). Polarisation experiments were executed by allowing 30 min for the OCP to stabilise followed by scanning from 0 V vs. OCP to -1.80 V vs. OCP at a scan rate of 10 mV/min. All polarisations were performed in duplicates.

4.2.3 EIS and Open Circuit Potential (OCP) Measurements

OCP and EIS were performed using a Solartron 1287A potentiostat together with a Solartron 1260A impedance/gain-phase analyser. EIS was performed by applying an AC perturbation at a maximum of 10 mV versus the OCP over a frequency range scanned from 100 kHz to 1 mHz. The frequency range and the perturbation were adjusted for selected samples. Experiments were performed and analysed post execution using Scribner software CorrWare/Zplot and CorrView/ZView respectively. Unless otherwise specified, a minimum of 6 replicates were tested to ensure reproducible data, presented by a representative sample.

Data was analysed by fitting the data to an equivalent circuit model (ECM) using fitting guidelines developed by Boukamp [87]. The guidelines define the "best fit" as the simplest EC with the smallest "weight sum of squares" (calc modulus weighting) or chi-squared parameter ($\boldsymbol{X^2}$), unless an additional element decreases the "weight sum of squares" by a factor of ten. In those instances where there are more than one ECM with the same number of elements providing an equally accurate fit of the data,

the selection of ECM used was based on the circuit used to model barrier coatings penetrated by electrolyte (Figure 4.5) and slight variations base upon this EC model.

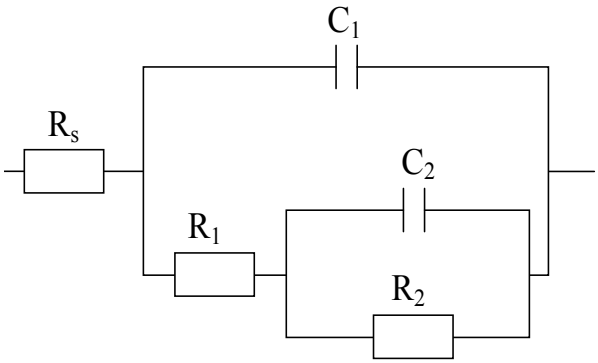

Figure 4.5 ECM commonly used for failed barrier coatings

Values of the individual elements obtained from the ECM vs. exposure time are shown in Appendix A, where R is a resistance element in Ohm, Y_0 is the admittance constant of the constant phase element in seconds^n/Ω with the power n relating to impedance with the equation shown in (4.1). [86]

$$Z = \frac{(j\omega)^{-n}}{Y_0} \qquad (4.1)$$

4.3 Results and Discussion

4.3.1 PAn/co-poly Coated AA2024-T3

4.3.1.1 Open Circuit Potential (OCP)

The initial OCP of "air dried" and "heat treated" PAn/co-poly coated AA2024-T3, as outlined in Chapter 3.8.3.1, and for uncoated AA2024-T3 immersed in DHS is given in Figure 4.6. The OCP for bare AA2024-T3 revealed little change in the early stages of immersion while the PAn/co-poly coated substrate initially displayed a potential at *ca.* 0.3 V vs. Ag/AgCl, a potential significantly more positive than observed for bare substrate. The observed shift was however only temporary and, within 30 min immersion the OCP of the PAn/co-poly coated substrate, was only marginally more positive than the bare substrate. After a period of 24 hours the OCP for the coated substrates was stable at *ca.* -440 ± 20 mV vs. Ag/AgCl, an OCP equal to that observed for the bare alloy. The minor OCP difference observed between "air dried" and "heat treated" PAn/co-poly coating can possibly be attributed to slower water penetration of the "heat treated" coating.

The control of the mixed potential by the metal substrate has also been observed by Cogan *et al.* investigating PAn-ES on AA2024-T3. [75] Observations made by Tallman *et al.* noted a significant anodic shift over a longer period for PAn coated AA7075-clad. [98] The more pronounced anodic shift observed by Tallman *et al.* could be attributed to the aluminium layer on top of the substrate used.

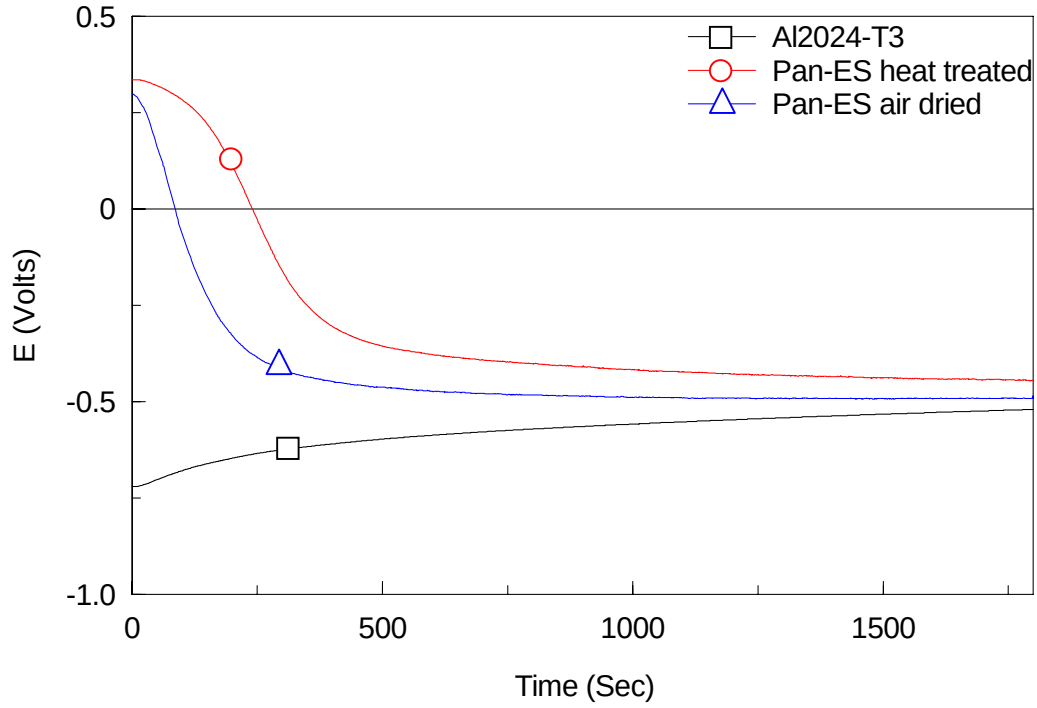

Figure 4.6 OCP of AA2024-T3, AA2024-T3 coated with heat treated PAn/co-poly composite and 2024-T3 coated with air dried PAn/co-poly composite immersed in DHS vs. Ag/AgCl reference electrode

4.3.1.2 Potentiodynamic Polarisation

Cyclic polarisation (CP) studies performed after 30 min immersion (Figure 4.7) display for bare AA2024-T3 a pseudo passive behaviour without any clear passivation potential (E_{pp}). The sharp current increase at -380 mV is suggestive of a breakdown potential (E_b) followed by a transpassive region. Positive hysteresis was observed during the reverse scan without any evidence of repassivation within the scanning range, suggesting a continuos oxidation of the substrate in the form of pitting corrosion.

The CP curve obtained for PAn/co-poly coated substrate showed no reproducible difference between "air dried" and "heat treated" sample. The "heat treated" PAn/co-poly coated (Figure 4.7) substrate produced an anodic shift in the OCP of around 90 mV and a higher corrosion current with respect to uncoated substrate. No pseudo passive region, as observed for the bare metal was observed. At a potential of about -200 mV the sample exhibited limited current behaviour at high current density. On the reversed scan, negative hysteresis was observed with the current density dropping three orders of magnitude, compared to the anodic branch.

Interaction between the metal and the coating was observed as a higher OCP and increased I_{corr} compared to the bare metal, with the negative hysteresis during the reverse sweep. The higher I_{corr} observed could possible be explained by polymer oxidation contributing to the total observed current, hence the higher I_{corr} does not necessarily reflect a higher rate of metal oxidation. The negative hysteresis may suggest formation of a protective oxide but given the high current observed during the scan and the absence of any repassivation it could also be the result of a more resistive coating acting as a barrier.

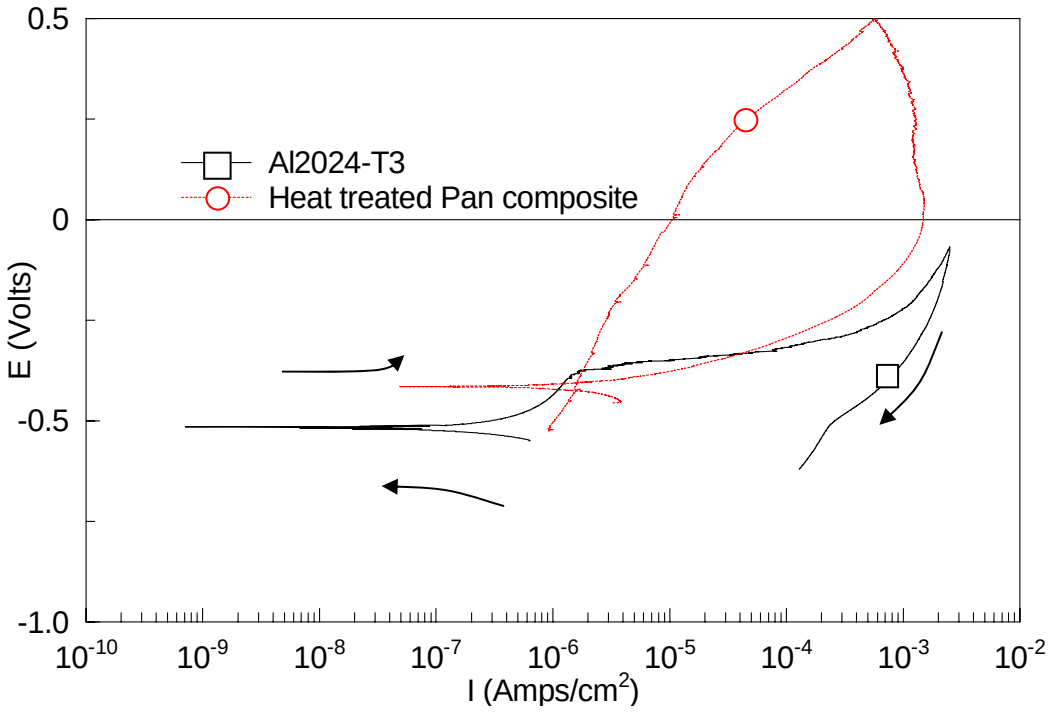

Figure 4.7 Cyclic polarisation curves for AA2024-T3 exposed to DHS with and without and heat treated PAn/co-poly composite coating. Scan initiated 30 min after immersion using a scan rate of 10 mV/min vs. Ag/AgCl reference electrode.

Cathodic polarisation of the "heat treated" PAn/co-poly coated AA2024-T3 displayed a more active behaviour when compared to the bare substrate. In this case the PAn/co-poly coated substrate appeared to limit the cathodic water reduction, Figure 4.8. The higher initial currents observed for CP and cathodic polarisation of PAn/co-poly coated substrate may be due to competitive reduction of the polymer. These issues have received additional consideration later in Chapters 5 and 6.

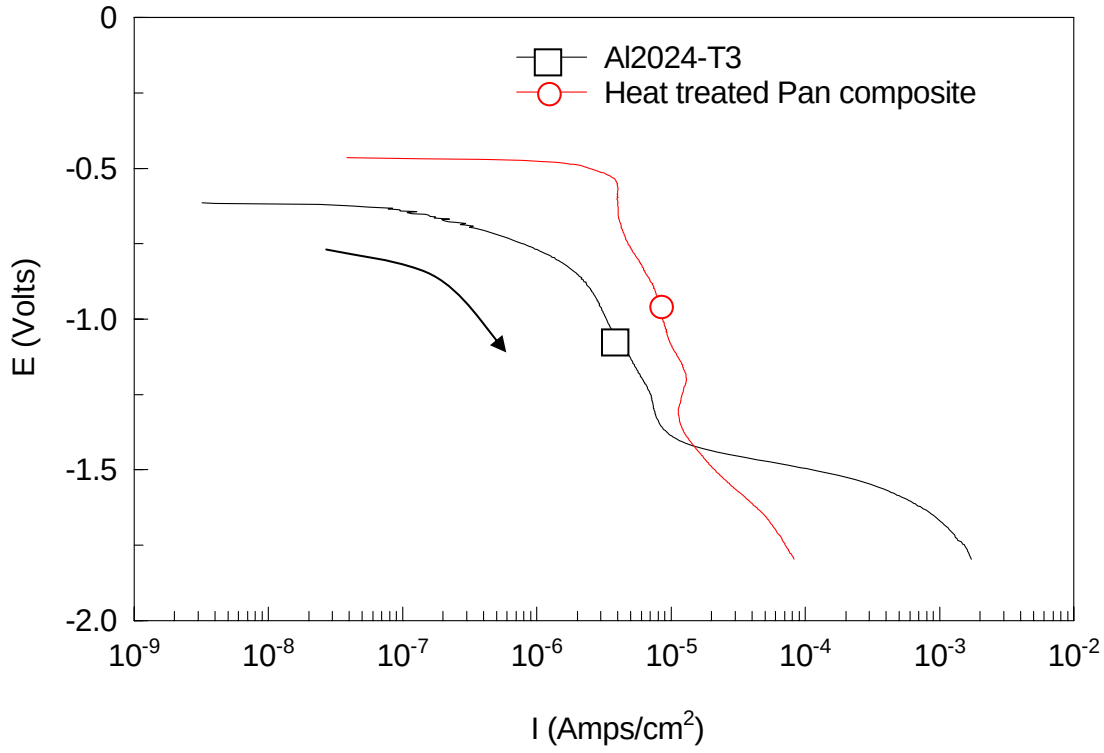

Figure 4.8 Cathodic polarisation curves for AA2024-T3 exposed to DHS with and without and heat treated PAn/co-poly composite coating. Scan initiated 30 min after immersion using a scan rate of 10 mV/min

4.3.1.3 EIS of Uncoated AA2024-T3

EIS btained for bare AA2024-T3 immersed in DHS initially displayed a single maximum in phase angle, as shown in the Bode plot (Figure 4.10). This correlated to a single time constant element for the uncoated metal which shifted to higher frequencies with exposure time. This feature was also observed in the Nyquist plot (Figure 4.9) which displayed a corresponding semi circle that decreased in size with sample exposure.

Ideally, this impedance spectra could be modelled using the ECM shown in Figure 4.11 consisting of a charge transfer resistance (R_{ct}), i.e. the Faradic impedance, due

to the electrochemical corrosion process, arranged parallel to a capacitance element representing the capacitance observed as a result of the double layer forming at a metal-electrolyte interface. The non-ideal capacitance behaviour observed for an electrochemical system such as a corroding metal was modelled using a constant phase element (CPE_{dl}). An additional resistance element was added in series with the above RC circuit representing solution resistance (R_s).

Y_{dl} was noted to increase with prolonged immersion while R_{ct} decreased with time. (Appendix A.1) These changes were observable from the very initial measurement suggesting that an initial oxide layer, formed by handling the substrate in air, broke down under the immersion conditions. During prolonged sample exposure the metal substrate was observed to turn slightly dull after 1-2 days immersion, a process which can be attributed to oxide formation. The overall system impedance was observed to decrease with time signifying that the oxide formation was non-protective.

After 9 days immersion the bare AA2024-T3 began to display a second time constant element observed as the second maximum in phase angle in the Bode Plot. (Figure 4.10) Corrosion products continued to develop during prolonged exposure and red/brown pits surrounded by loose white precipitate were visually detected a few days after the appearance of the second time constant. This link strongly suggests that the second time constant observed arrises as a result of the extensive pitting process.

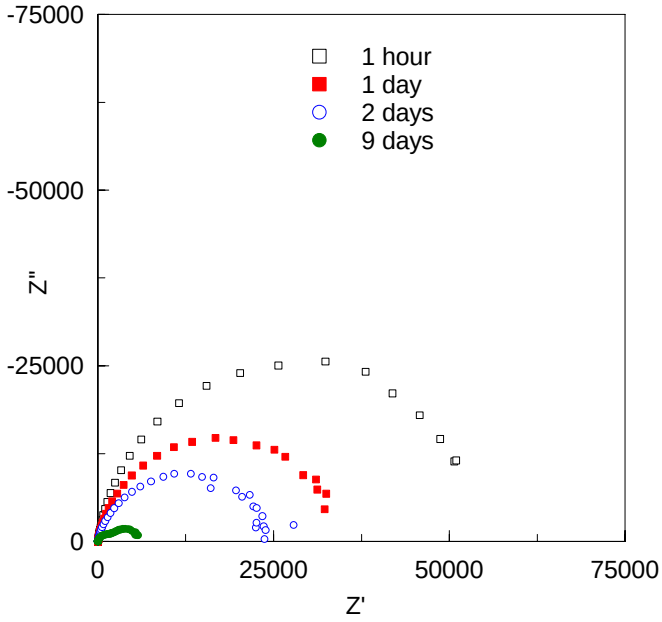

Figure 4.9 Nyquist plot of uncoated AA2024-T3 immersed in DHS (exposed area: 2.5 cm^2)

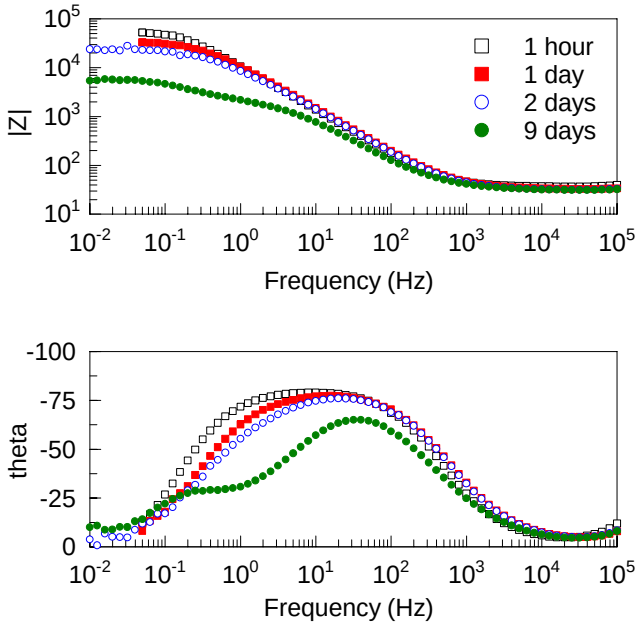

Figure 4.10 Bode plots of uncoated AA2024-T3 immersed in DHS (exposed area: 2.5 cm^2)

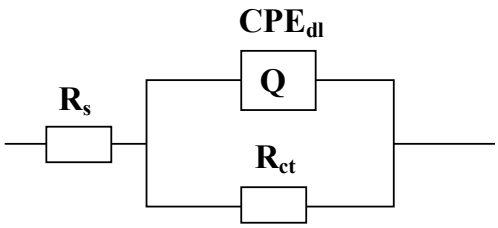

Figure 4.11 ECM used model bare AA2024-T3 in DHS before 9 days immersion.

4.3.1.4 EIS of "Air Dried" PAn/co-poly Coated AA2024-T3

EIS spectra of "air dried" PAn/co-poly coated AA2024-T3 after 1h displayed a single time constant, observable as a semi circle in the Nyquist plot of Figure 4.12, gradually increasing in diameter over the first 24 hours. A second high frequency RC time constant was noted to develop over the proceeding days, as observed in Nyquist plot (Figure 4.13), with a third less distinct time constant bserved after 5 days immersion.

The single time constant EIS response obtained after 1h could be explained by the still dry polymer, a highly conductive polymer surface, acting as an electrode using the ECM shown in Figure 4.11. EIS obtained after 2 days was modelled using the ECM shown in Figure 4.15 containing two embedded RC circuits representing the coating/electrolyte and metal/coating interface. The high frequency loop was ascribed to the capacitance (CPE_c) and resistance (R_c) of the polymer coating, while the low frequency response corresponds to the double layer capacitance (CPE_{dl}) and charge transfer resistance (R_{ct}) of the underlying metal. By using circuit fitting guidelines by Boukamp [87] subsequent spectra were also modelled using the circuit shown in Figure 4.15. Keeping within the guidelines, no additional circuit elements were added to model for the minor third time constant observed in spectra of 5 and 9

days (Figure 4.14) as this did not provide a one order of magnitude better fit than the simpler circuit. The third time constant that was not fully resolved maybe a result of lateral diffusion of electrolyte, another potential electrochemical process occurring under and/or within the intact part of the coating film. [99]

In early exposure both Y_c and R_c increase in magnitude. (Appendix A.2) The increasing Y_c can be contributed to water uptake. For an inactive polymer coating R_c is expected to decrease with immersion time as water penetrates and pores develop. The increase in R_c observed for the first 2 days of immersion can be ascribed to the conversion of the conductive partially oxidised emerald salt (ES) to a less conductive form. This conversion could be either a reduction/deprotonation reaction to form leucoemeraldine base (LB) or a deprotonation to form emeraldine base (EB). Visual observations of the coating noted that the green coloured coating, corresponding to ES turned to a lighter shade within the first hours of immersion, suggestive of LB formation followed by a change to a dark blue colour, corresponding to EB.

Y_{dl} and R_{ct} of the second time constant corresponding to the metal/coating interphase also increase with time. After 5 days R_{ct} reached a maximum value after which it started to decrease. This process suggests that oxide formation initially restricts further oxidation until after approximately 5 days were failure was observed.

These observations support a mechanism involving reduction of the ES to form LB followed by reoxidation of LB to form the non conducive but partially oxidised EB. The increase of R_{ct} also suggests that a metal oxide forms under the coating, possibly as a result of PAn/co-poly reduction. After 2 days the high frequency loop decreased

as a result of water penetration, a typical behaviour of pore-formation within a barrier coating. The Nyquist plot after 5 days (Figure 4.14) shows that both the high and low frequency loops decreased in diameter suggesting that the coating and underlying oxide were deteriorating. After 9 days immersion visual blister formation could be observed and was accompanied by the formation of a white corrosion product after 2 weeks exposure.

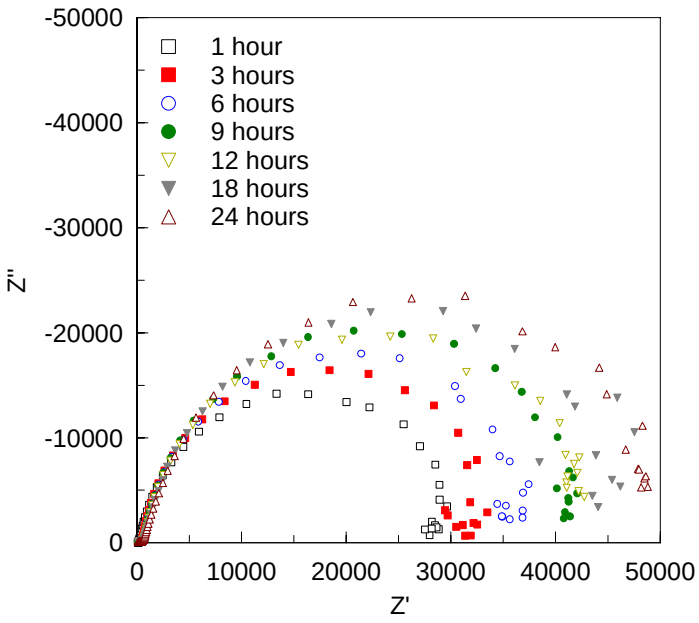

Figure 4.12 Nyquist plot of air dried PAn/co-poly coated AA2024-T3 immersed in DHS (exposed area: 2.5 cm^2)

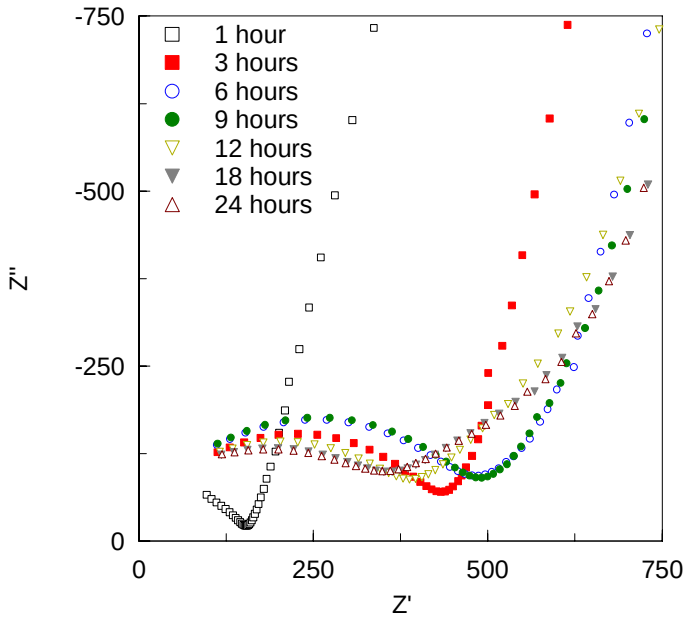

Figure 4.13 Nyquist plot of high frequency spectra of air dried PAn/co-poly AA2024-T3 immersed in DHS. The "developing" of the high frequency capacitive loop

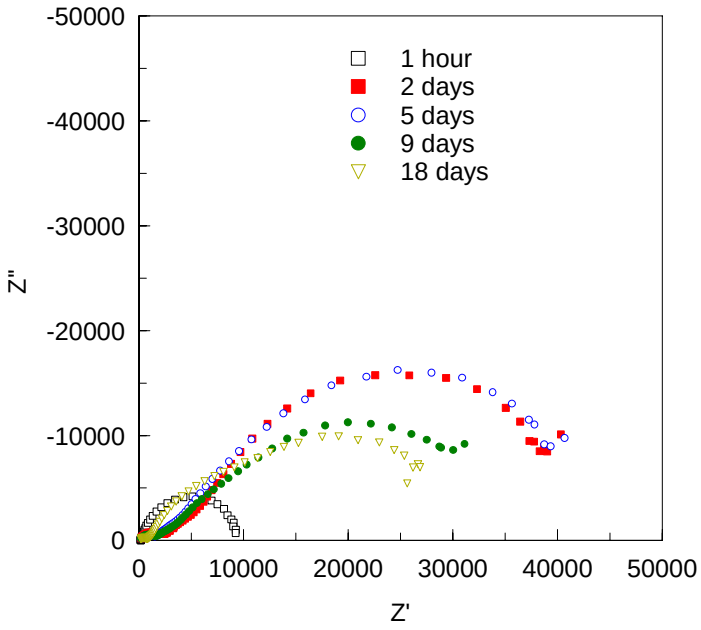

Figure 4.14 Nyquist plot of air dried PAn/co-poly coated AA2024-T3 immersed in DHS (exposed area: 2.5 cm^2)

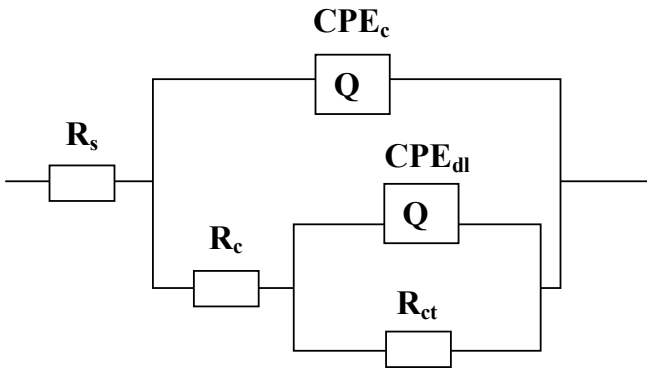

Figure 4.15 ECM for "air dried" PAn/co-poly coated AA2024-T3 after 2 days exposure.

4.3.1.5 EIS of "Heat Dried" PAn/co-poly Coated AA2024-T3

The EIS for "heat dried" PAn/co-poly coated AA2024-T3, shown in Figure 4.17-Figure 4.19, revealed a two time constant behaviour after 3 hours, with the high frequency loop displaying increasing capacitance and resistance over the first 7 days. R_{tot} also increased by almost one order of magnitude within the 7-day period. A third time constant partially observed for "air dried" PAn/co-poly was more clearly noted for "heat dried" coatings after 2 days immersion.

EIS up to 3 hours were modelled using ECM's as shown in Figure 4.15. Subsequent data was modelled using ECM shown in Figure 4.16. Changes in Y_c and R_c (Appendix A.3) are smaller in magnitude and progress at a slower rate than observed for "air dried" coating. Changes in Y_{dl} and R_{ct} over time also show a significant R_{ct} increase possibly due to the formation of an underlying oxide. Within two weeks green spots and blisters started to develop within the coating. The appearance of theses blisters correlates to a decrease observed in the R_{ct}. These observations could suggest breakdown of a current limiting oxide.

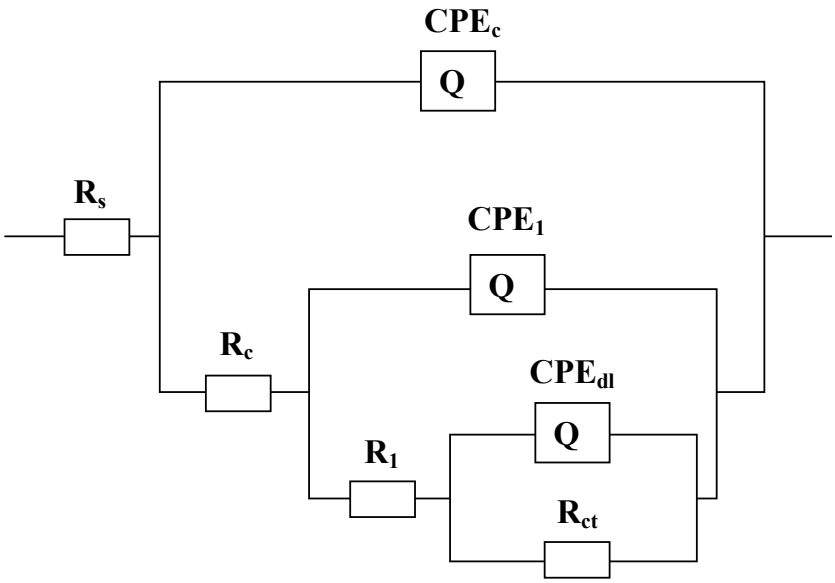

Figure 4.16 EC for "heat dried" PAn/co-poly coated AA2024-T3 after 2 days exposure.

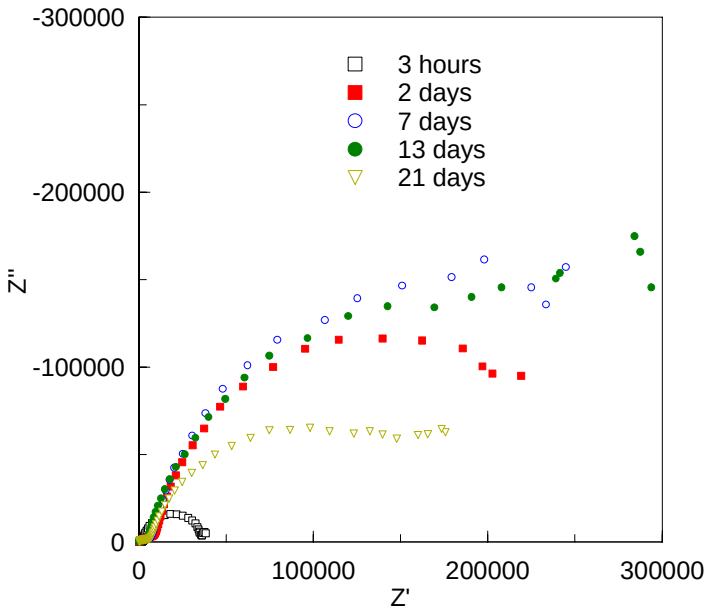

Figure 4.17 Nyquist plot of heat exposed PAn/co-poly coated AA2024-T3 immersed in DHS (exposed area: 2.5 cm^2)

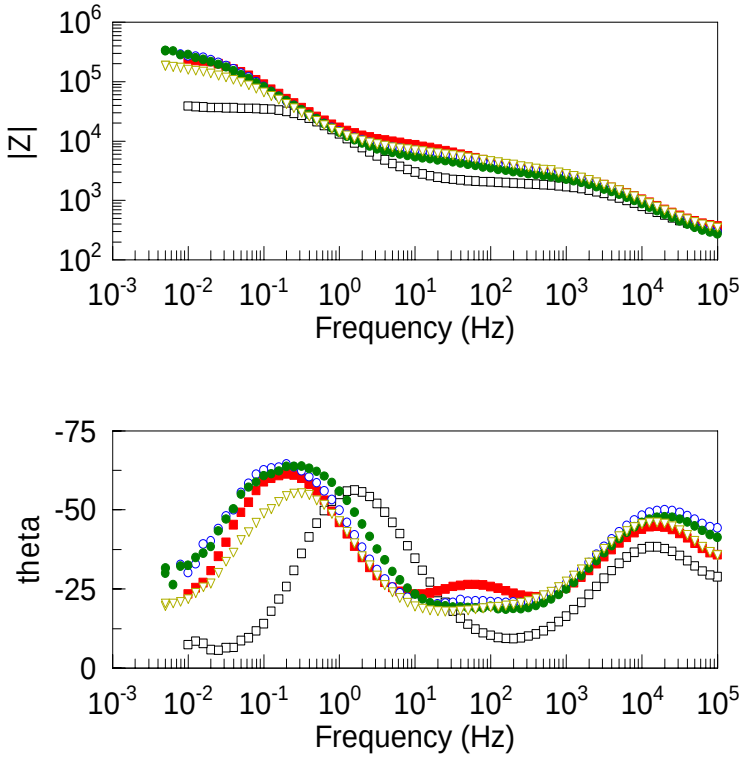

Figure 4.18 Bode plots of heat exposed PAn/co-poly coated AA2024-T3 immersed in DHS (exposed area: 2.5 cm^2)

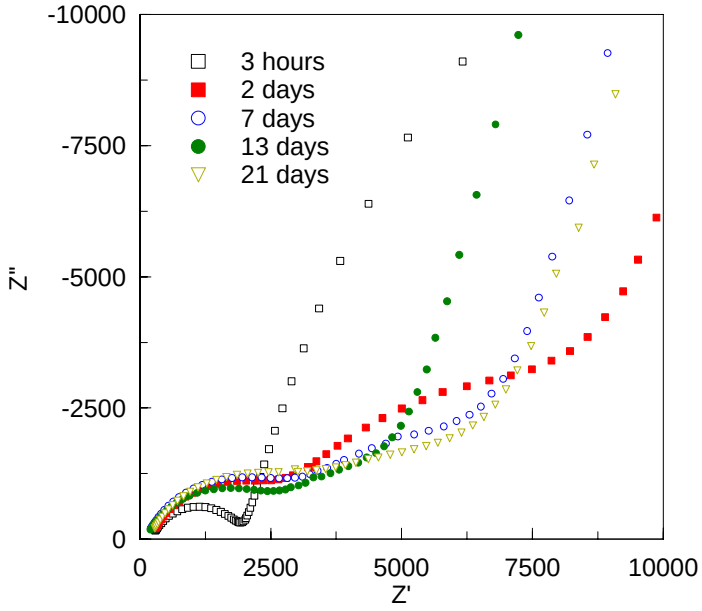

Figure 4.19 Nyquist plot of high frequency spectra of heat exposed PAn/co-poly coated AA2024-T3 immersed in DHS (exposed area: 2.5 cm^2)

4.3.2 Electrochemically Synthesised Poly(3-octyl pyrrole) Coated AA2024-T3

P3OP prepared electrochemically in a small scale synthesis, as outlined in Chapter 3.8.2.3, was isolated in two different fractions for P3OP-ClO_4 and soluble fraction from P3OP-*p*TS synthesis. These fractions as well as P3OP-*p*TS, synthesised by a method described by Ashraf *et al.* [88] outlined in Chapter 3.8.2.1, were investigated as potential corrosion inhibitors for AA2024-T3 in a preliminary study by monitoring of the OCP followed by EIS. The small amounts of material produced using this method, combined with the limited solubility of some fractions restricted the scope of this study to only duplicate samples. The coatings tested are listed in Table 9.

Table 9 Description and labelling of materials examined as corrosion inhibitors for AA2024-T3

Material	***Description***	***Conductivity (S/cm)***	***Label***
P3OP-*p*TS	Electrochemical synthesised using method described by Ashraf *et al.* [88] outlined in chapter 3.8.2.1	$<10^{-8}$	Ashraf
P3OP-ClO_4	Soluble fraction of material deposit on Pt electrode using synthesis method outlined in chapter 3.8.2.3	4	P3OP-ClO4 deposit
P3OP-ClO_4	Material recovered from synthesis solution using synthesis method outlined in chapter 3.8.2.3	10^{-1}	P3OP-ClO4 solution
P3OP-*p*TS	Material recovered from synthesis solution. Using synthesis method outlined in chapter 3.8.2.3	$<10^{-6}$	P3OP-*p*TS solution

4.3.2.1 Open Circuit Potential (OCP)

The OCP under ambient conditions (Figure 4.20) revealed no initial substrate ennobling for any coating system, as was observed for PAn/co-poly coating. Rather all coatings displayed an initial OCP similar to that observed for the bare metal. The change in OCP over time was the same as was observed for bare substrate in all but one system. For samples coated with the conductive material "P3OP-ClO_4 deposit" the OCP decreased to -0.6V after which the OCP shifted in the positive direction by

more than 100 mV after 9 days immersion. This ennobling effect is discussed in more detail in the context of EIS measurements in this chapter.

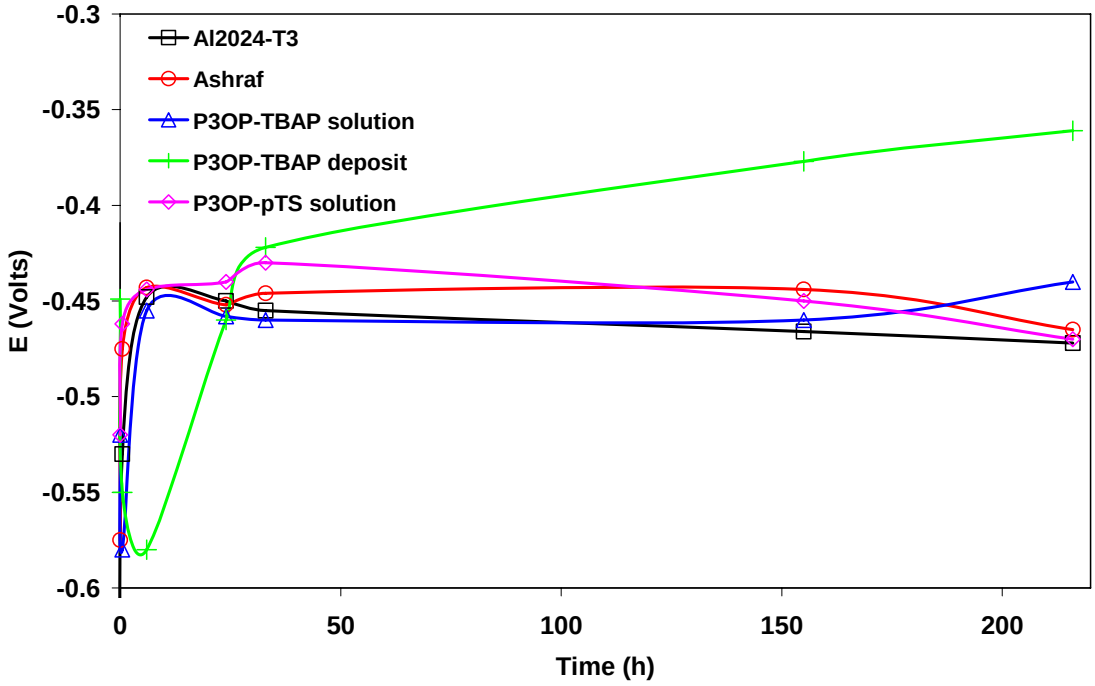

Figure 4.20 OCP measurement of electrochemically synthesised P3OP coated AA2024-T3 immersed in DHS.

4.3.2.2 EIS of "Ashraf" Coated AA2024-T3

EIS of AA2024-T3 coated with P3OP-*p*TS prepared via the Ashraf method (Figure 4.21 and Figure 4.22) suggests diffusion dominated processes with the "loop back" observed at low frequencies due to non steady state behaviour or possible a result of some inductive process. The ECM used for data fitting shown in Figure 4.23. The high frequency time constant could be ascribed to the coating/electrolyte interface represented in the ECM by an RC element using a CPE coupled with a short circuit (limited) Warburg diffusion element. Y_c and R_c decreased with immersion time while

W_R and W_T (Warburg elements) increased in the first 24 hours followed by a slower decrease. Over this period coating failure became obvious from visual observations.

The decrease in Y_c and R_c (Appendix A.4) was consistent with a barrier coating that developed pores over time within the coating. This result could also be interpreted for ICP coatings as a result of an increase in the coating conductivity which would produce a similar response.

The increase for the total Warburg impedance observed during the first day suggests the formation of surface oxide beneath or through the coating, resulting in the initial impedance increases observed. Although with the further decrease of R_c and $Y_{c,}$ the total impedance drop over time suggests that the additional oxidation does not provide any further protection towards corrosion.

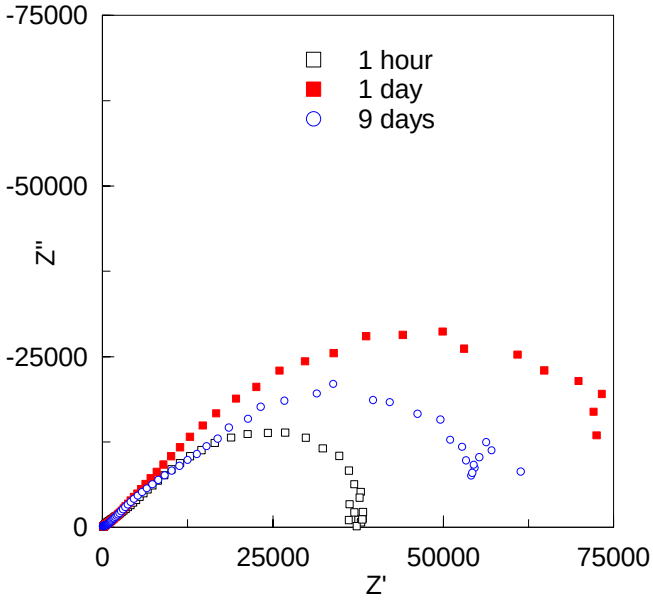

Figure 4.21 Nyquist plot of thin air brushed "Ashraf" coated AA2024-T3 immersed in DHS (exposed area: 2.5 cm^2)

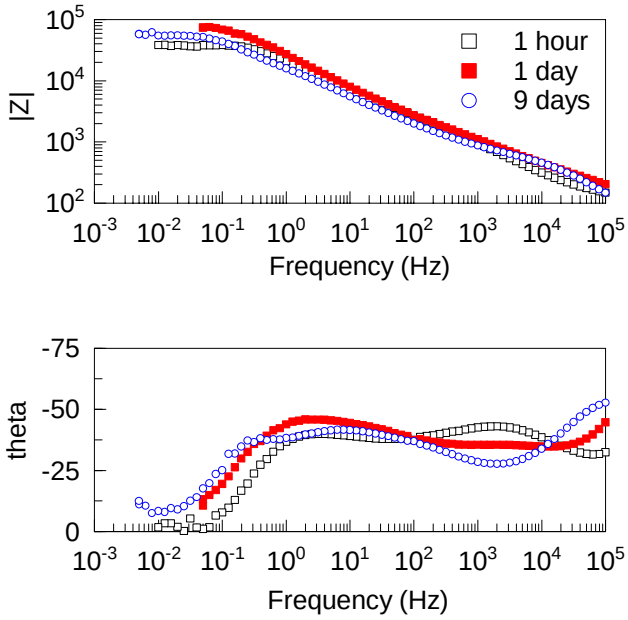

Figure 4.22 Bode plots of thin air brushed "Ashraf" coated AA2024-T3 immersed in DHS (exposed area: 2.5 cm^2)

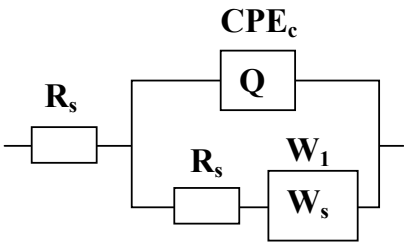

Figure 4.23 EC for thin air brushed "Ashraf" coated AA2024-T3 immersed in DHS

*4.3.2.3 EIS of "*P3OP-Cl*O4 Deposit" Coated AA2024-T3*

EIS for the conductive fraction (4 S/cm^2) of "P3OP-ClO4 deposit" coated on AA2024-T3 revealed, in addition to the two-time constant response, commonly observed for poor barrier coatings, a positive capacitance at low frequency (Figure 4.24). The origin of positive capacitance (i.e. inductance) has been observed for various corrosion systems as well as for bare metals and has been attributed to absorption processes. [84] [100]This system was accurately modelled using the ECM shown in Figure 4.25. Data parameters at longer times (Appendix A.5) are based on the ECM shown in Figure 4.15 following the circuit fitting guidelines by Boukamp [87].

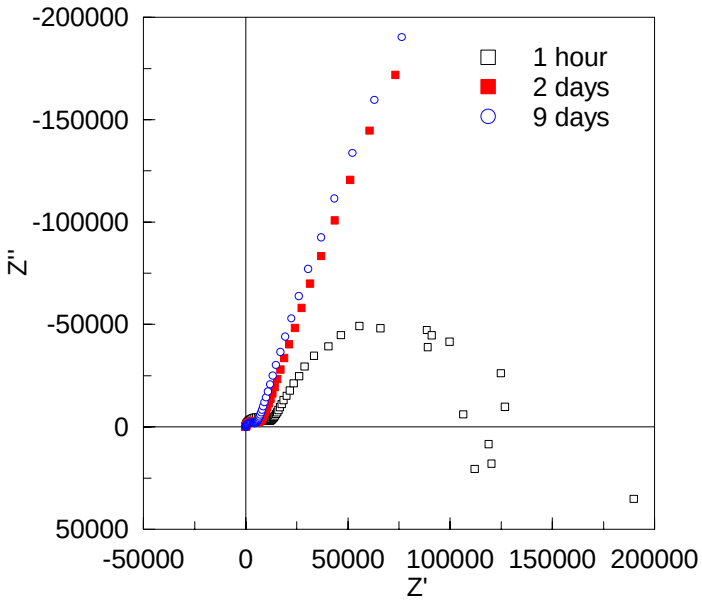

Figure 4.24 Nyquist plot 1 hour immersion of thin air brushed "P3OP-ClO4 deposit" coated AA2024-T3 immersed in DHS (exposed area: 2.5 cm^2)

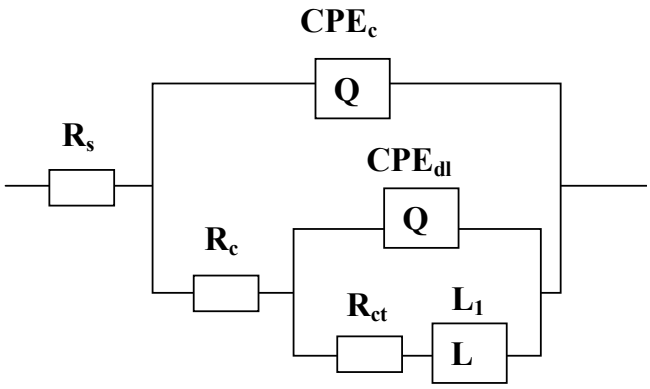

Figure 4.25 EC for thin air brushed "P3OP-ClO4 deposit" coated AA2024-T3 after 1 hour immersed in DHS.

After 2 days immersion the induction process was no longer observed, rather a two time constant response (Figure 4.26 to Figure 4.28) was noted and modelled using the ECM shown in Figure 4.15.

The high frequency time constant, ascribed to the coating-electrolyte interphase, diminish with time, as seen graphically by the reduction of the semi circle diameter (Figure 4.28) and also shown through the increase of Y_c and decrease of R_c obtained from ECM (Appendix A.5). This observation would be, in referring to an inert insulating coating, consistent with water penetration and generally degradation [99]. Use of ICP coatings could introduce an additional variable where changes in polymer conductivity could influence the EIS response.

The low frequency semi circle ascribed to the metal interface increased in diameter with immersion time. Y_{dl} undergoes little change while R_{ct} increased by more than one order of magnitude (Appendix A.5). The experiment was terminated after 9 days immersion with no corrosion product detected or any visual change to the coating.

Coating-metal interaction, supported by the observed shift in the OCP, suggests a galvanic coupling between the metal and the polymer coating. Such coupling would arguably promote metal oxidation while the polymer coating undergoes reduction. The polymer reduction would be accompanied with release and expulsion of dopant anion. The initial inductive process observed using EIS could hence be explained by absorption of dopant, released during polymer reduction, to the metal surface. After 2 days immersion the underlying surface displayed an order of magnitude higher R_{ct} suggesting formation of a protective surface formed as a result metal oxidation and dopant absorption.

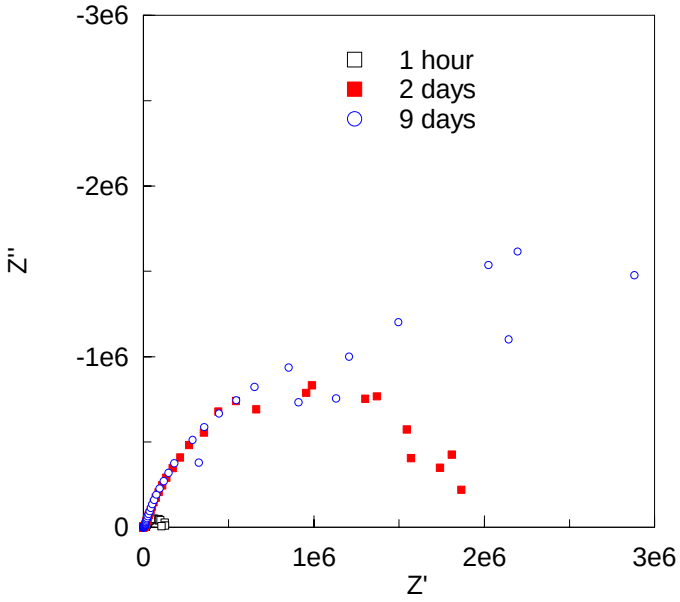

Figure 4.26 Nyquist plot of thin air brushed "P3OP-ClO4 deposit" coated AA2024-T3 immersed in DHS (exposed area: 2.5 cm^2)

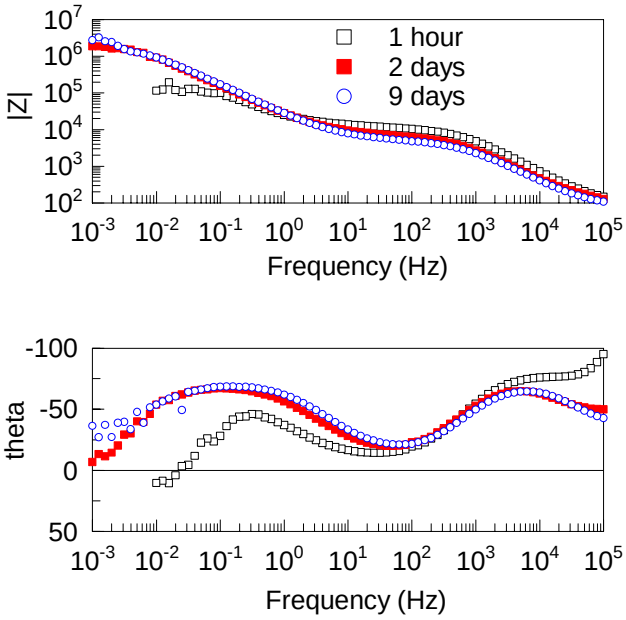

Figure 4.27 Bode plot of thin air brushed "P3OP-ClO4 deposit" coated AA2024-T3 immersed in DHS (exposed area: 2.5 cm^2)

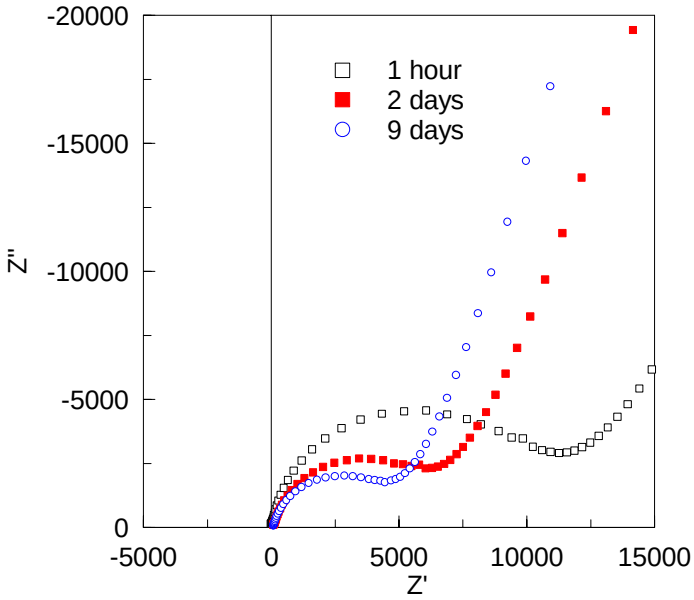

Figure 4.28 Nyquist plot of high frequency end of thin air brushed "P3OP-ClO4 deposit" coated AA2024-T3 immersed in DHS (exposed area: 2.5 cm^2)

4.3.2.4 EIS of "P3OP-ClO4 Solution" Coated AA2024-T3

EIS spectra for "P3OP-ClO4 solution" (0.1 S/cm) coated AA2024-T3 obtained displayed a two time constant response, plus a low frequency inductive behaviour (Figure 4.29) that was similar to that observed after 1 hour for "P3OP-ClO4 deposit" coated on AA2024-T3. After 2 days only two time constants, consisting of a minor high frequency arc and a low frequency semicircle remained. Data was modelled using the ECM shown in Figure 4.15 with the high frequency arc attributed to the polymer coating and the lower frequency semicircle due to the metal interface. The formation of a high frequency arc after 2 days immersion could be an indication of a decrease in polymer conductivity possibly as a result of polymer reduction. As the high frequency time constant developed, the total impedance increased by about one order of magnitude with respect to initial observations, possibly as result of an oxide

formation under the polymer coating. After 9 days exposure Y_c and R_c decreased, as had Y_{dl} and R_{ct}, suggesting coating and oxide deterioration (Appendix A.6). Failure of the coating was also confirmed by visual observations revealing the formation of pits in the coating containing loose white corrosion product.

For the first two days of this experiment the changes observed were an analogue to that observed with "P3OP-ClO4 deposit" coated on AA2024-T3. Differences were evident after prolonged exposure when the arc of the second time constant diminished for "P3OP-ClO4 solution" within the experiment time frame. Following the same reasoning as for in "P3OP-ClO4 deposit", the increase seen in R_{tot} (after 2 days) is probably a result of oxide formation under the coating hindering further oxidation. However, contrary to "P3OP-ClO4 deposit" the protective oxide layer formed breaks down. The accelerated degradation of the surface compared to "P3OP-ClO4 solution" could stem from less of a barrier protection observed for "P3OP-ClO4 solution" as seen by the much lower R_c.

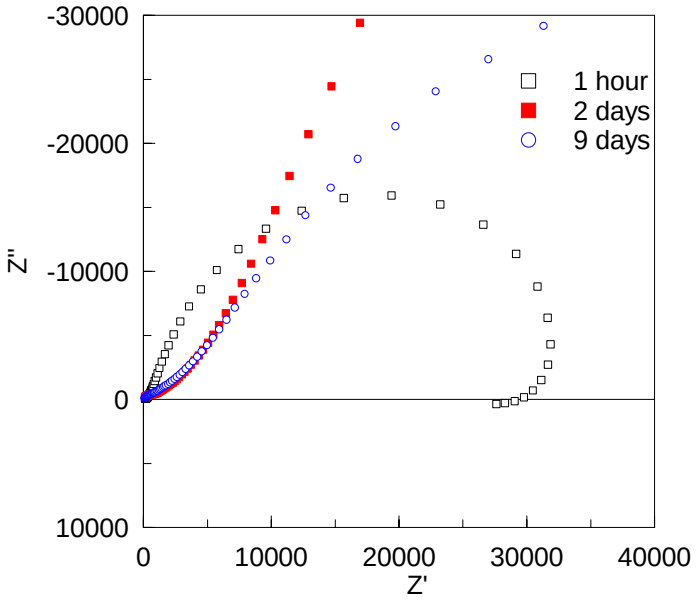

Figure 4.29 Nyquist plot at 1 hour immersion of thin air brushed "P3OP-ClO4 solution" coated AA2024-T3 immersed in DHS (exposed area: 2.5 cm^2)

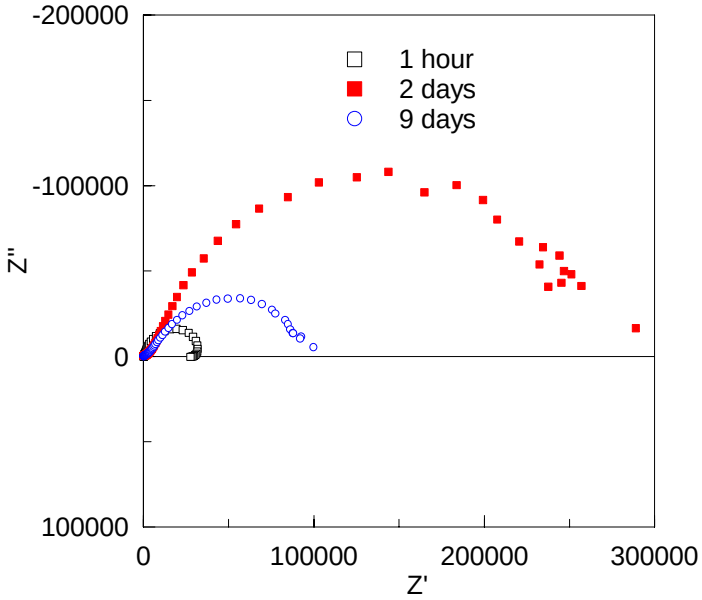

Figure 4.30 Nyquist plot of thin air brushed "P3OP-ClO4 solution" coated AA2024-T3 immersed in DHS (exposed area: 2.5 cm^2)

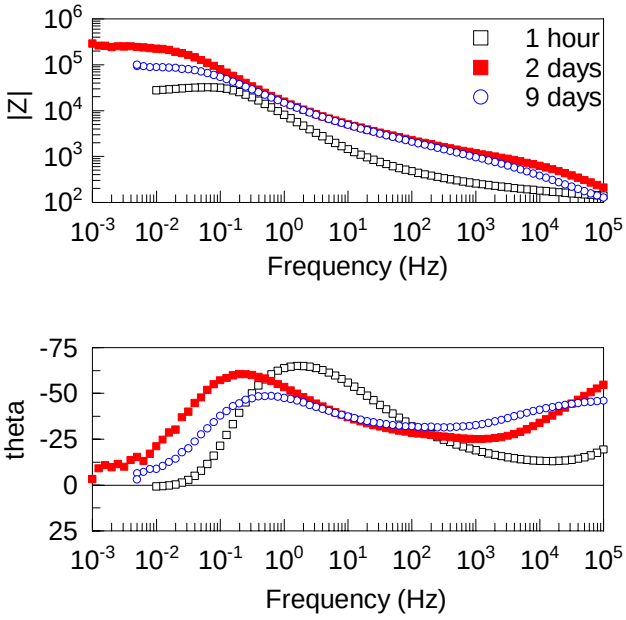

Figure 4.31 Bode plot of thin air brushed "P3OP-ClO4 solution" coated AA2024-T3 immersed in DHS (exposed area: 2.5 cm^2)

*4.3.2.5 EIS of "*P3OP-p*TS Solution" Coated AA2024-T3*

EIS data obtained for "P3OP-*p*TS solution" (10^{-6} S/cm) coated on AA2024-T3 after 1h exposure displayed a single time constant response (Figure 4.32 to Figure 4.33) (Appendix A.7). A second time constant was detected after 9 days immersion possibly due to corrosion products formed through defects in the coating or doping of the polymer by O_2 rendering the polymer partially conductive as suggested by Tallman *et al*. in a related system. The behaviour of this system was modelled over 5 kHz-0.05 Hz using ECM shown in Figure 4.11. The smaller frequency range was used due to sample signal-to-noise problems. These results suggest no electrochemical effect and only limited barrier protection possible due to the low conductivity in combination with poor mechanical properties.

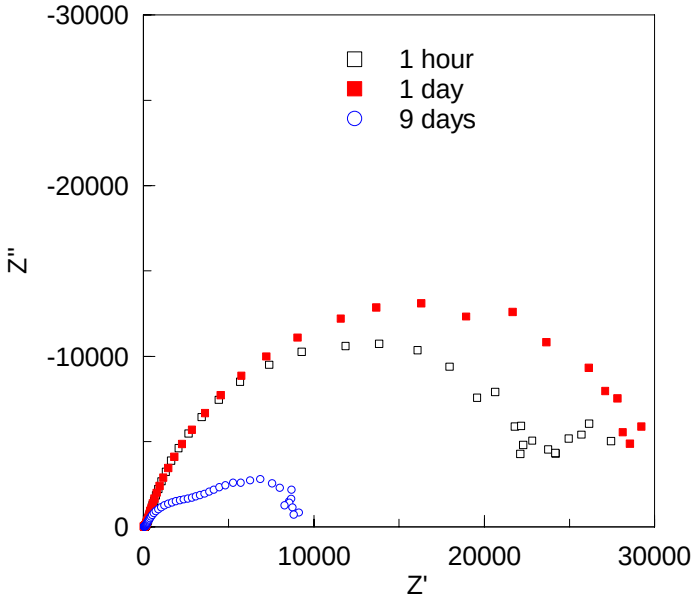

Figure 4.32 Nyquist plot of thin air brushed "P3OP-*p*TS solution" coated AA2024-T3 immersed in DHS (exposed area: 2.5 cm^2)

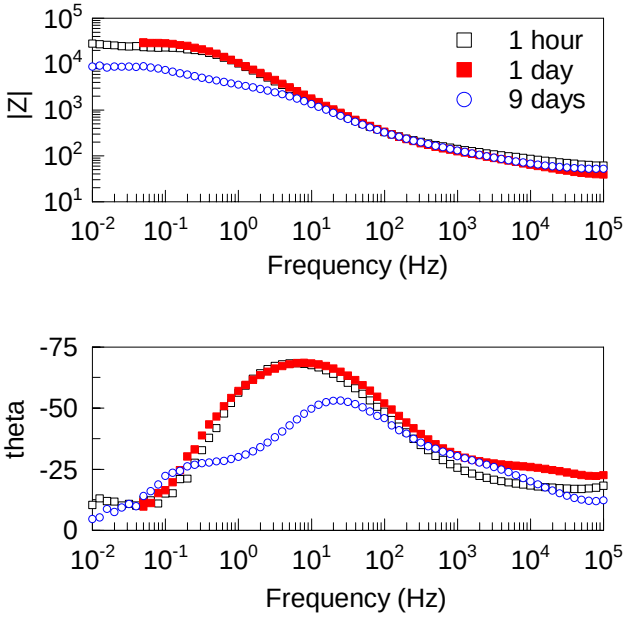

Figure 4.33 Bode plot of thin air brushed "P3OP-*p*TS solution" coated AA2024-T3 immersed in DHS (exposed area: 2.5 cm^2)

4.3.3 Chemically Synthesised Poly(3-octyl pyrrole) Coated AA2024-T3

P3OP synthesised chemically was used in a more comprehensive corrosion inhibition study as the synthesis method permitted the production of the material at a larger scale, with a higher yield and solubility. Films of P3OP-ClO_4, P3OP-*p*TS as well as P3OP-*p*TS synthesised electrochemically (by the Ashraf *et al.* method [88]) and cast from DCM were studied using DC polarisation, EIS and monitored OCP. Coatings tested are listed in Table 10.

In order to study any influence of the dopant used in the conducting polymer, bare AA2024-T3 substrate was also investigated in DHS containing 0.1 M $NaClO_4$ or Na*p*TS.

Table 10 Description and labelling of materials examined as corrosion inhibitors for AA2024-T3

Material	***Description***	***Conductivity (S/cm)***	***Label***
P3OP-*p*TS	Polymer synthesised using method outlined in Chapter 3.8.2.1 cast from DCM.	$<10^{-8}$	Ashraf
P3OP-ClO_4	Material chemically synthesised using synthesis method outline in Chapter 3.8.2.4 (1:1.8 monomer:oxidant ratio)	2	Chem. P3OP-ClO4
P3OP-*p*TS	Material chemically synthesised using synthesis method outline in Chapter 3.8.2.4 (1:1.8 monomer:oxidant ratio)	0.5	Chem. P3OP-*p*TS

4.3.3.1 Open Circuit Potential (OCP)

Initial OCP data obtained for P3OP coatings cast on AA2024-T3 (Figure 4.34) revealed an anodic shift for all coated substrates compared to that of the bare alloy. On the other hand OCP for the bare substrate exposed to DHS with $NaClO_4$ or Na*p*TS dopant (Figure 4.35) displayed an initial minor cathodic shift. Within 24h exposure the observed OCP reached that of the bare substrate in DHS for all samples with the exception of two: Chem. P3OP-ClO_4" and "Chem. P3OP-*p*TS", where an anodic shift of 60 mV was observed for up to 7 days immersion.

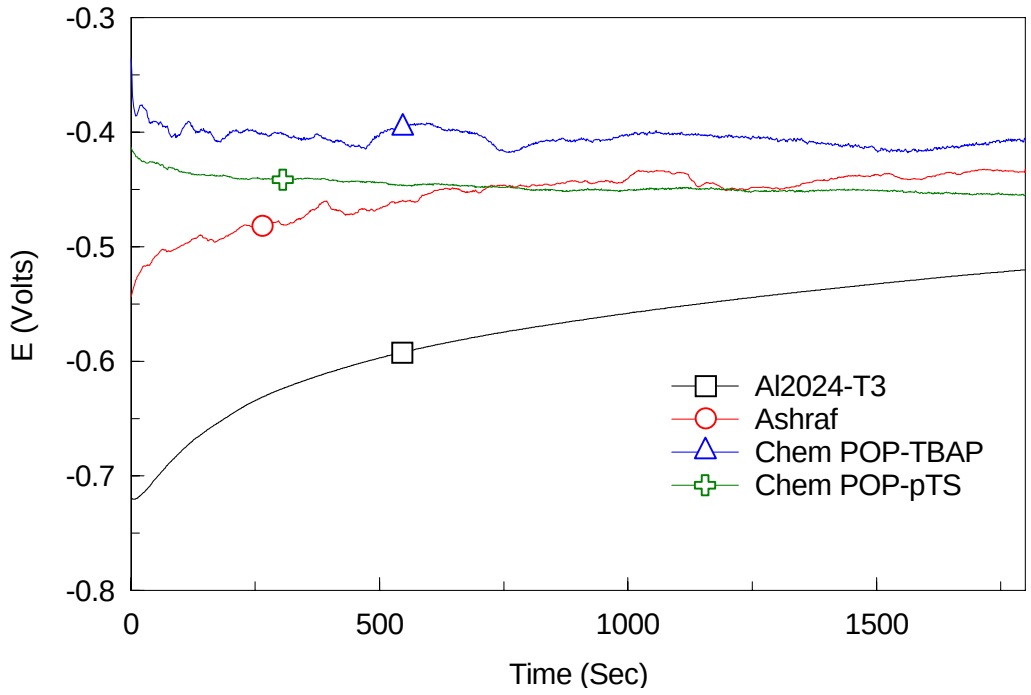

Figure 4.34 OCP for bare and P3OP coated AA2024-T3 exposed to DHS.

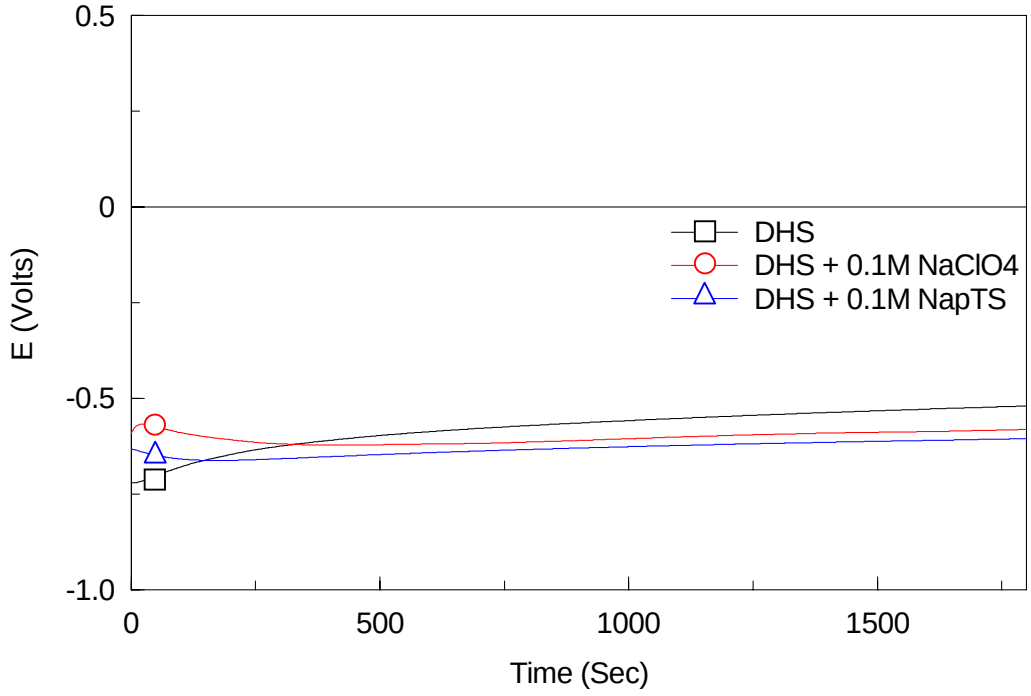

Figure 4.35 OCP for bare AA2024-T3 exposed to DHS with and without addition and 0.1 M $NaClO_4$ or 0.1 M Na*p*T*S*.

4.3.3.2 Potentiodynamic Polarisation

CP data obtained for AA2024-T3 coated with P3OP (Figure 4.36) displayed a modest anodic shift in the OCP with respect to the uncoated surface. "Chem P3OP-ClO_4" and "Ashraf" coated samples displayed a slightly reduced I_{corr}. The slow current increase observed during polarisation of these two samples suggests some pseudo passivity. Breakdown potential (E_b) was observed at around -300 mV for "Chem P3OP-ClO_4" where no E_b was observed for "Ashraf" which instead displayed a slow steady current increase. Contrary to this a slightly higher I_{corr} was observed in sample "Chem P3OP-*p*TS" and showing no passivation. Positive hysteresis with similar shape and current density was observed for all coated samples as well as for the bare alloy. The positive hysteresis observed for "Chem P3OP-ClO_4" and "Ashraf" coated AA2024-T3 implies that once the potential has been returned to the initial OCP, regeneration of any protected surface is slow or doesn't occur.

CP of bare substrate in DHS containing $NaClO_4$ or Na*p*TS (Figure 4.37) showed no significant influence in the corrosion behaviour. The only difference compared to DHS without dopant was a minor cathodic shift of the OCP.

Cathodic polarisation for coated substrates, shown in Figure 4.38, revealed a reduction in the kinetics for "Ashraf" coated AA2024-T3 while both chemically synthesised coatings displayed increased activity. This could be explained via polymer reduction and/or catalytic O_2 reduction on the polymer. For "Chem P3OP-*p*TS" coated AA2024-T3 the potential required for water reduction shifts cathodically. Cathodic polarisation for bare substrate exposed to DHS with 0.1 M $NaClO_4$ or Na*p*TS (Figure 4.39) displayed no major change in cathodic behaviour.

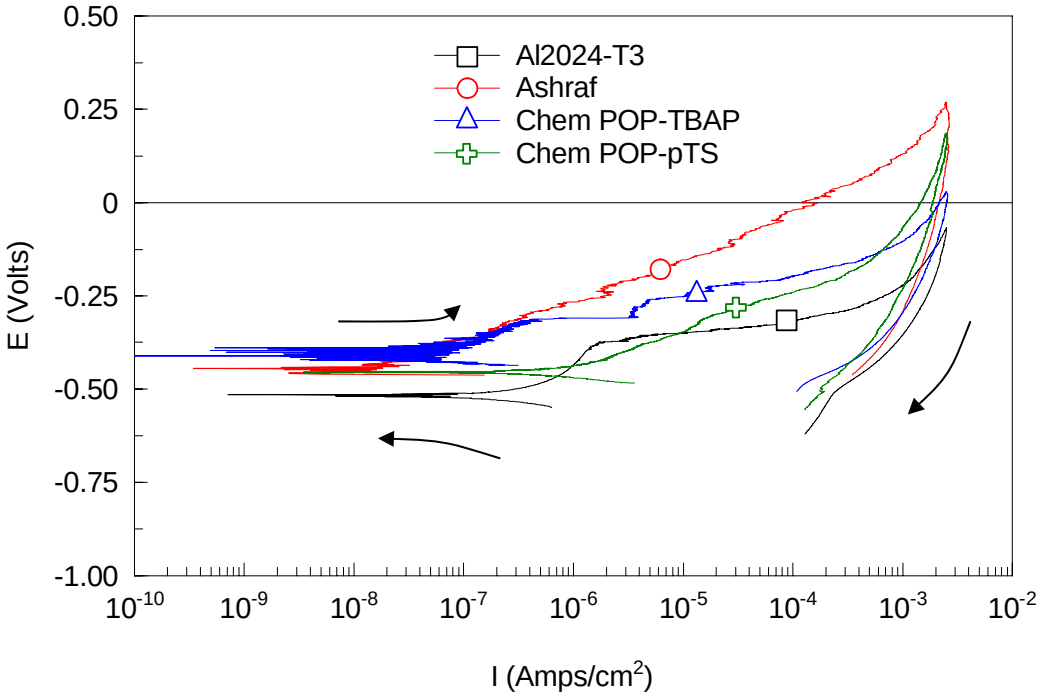

Figure 4.36 Cyclic polarisation curves for bare and P3OP coated AA2024-T3 exposed to DHS. Scan initiated 30 min after immersion using a scan rate of 10 mV/min.

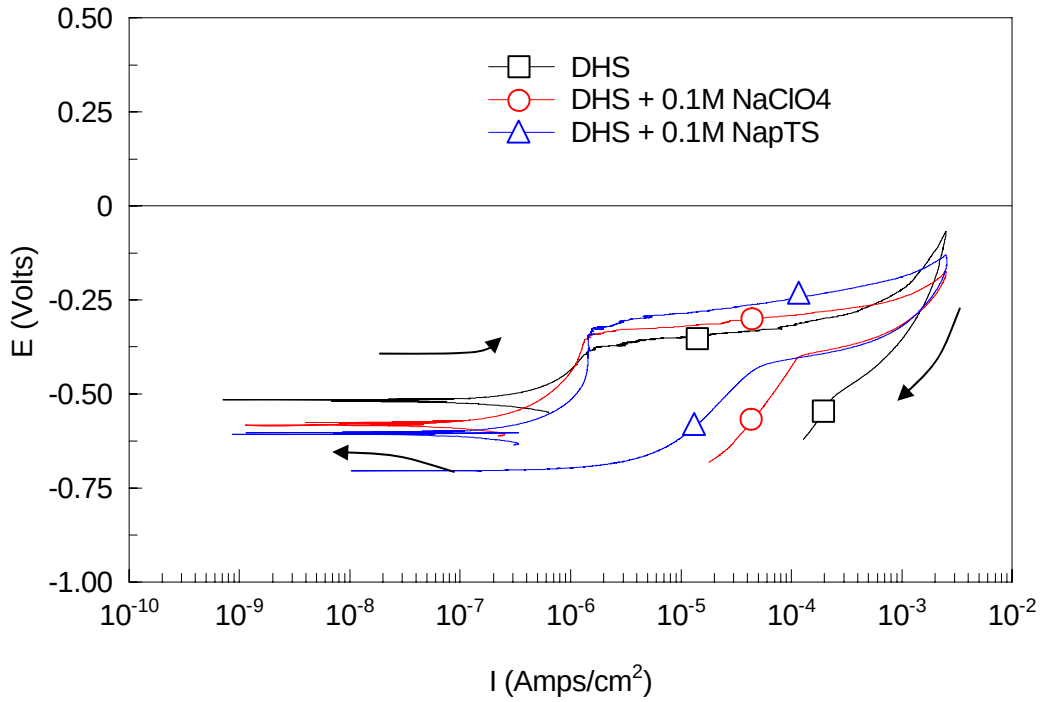

Figure 4.37 Cyclic polarisation curves for bare AA2024-T3 exposed to DHS. Scan initiated 30 min after immersion using a scan rate of 10 mV/min.

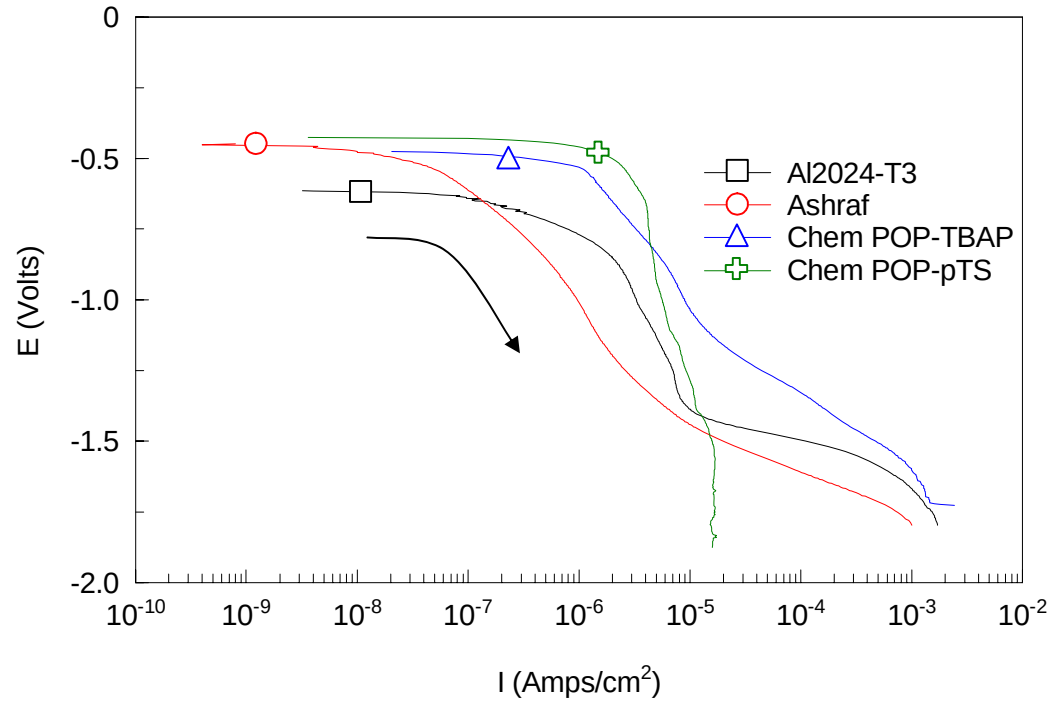

Figure 4.38 Cathodic polarisation curves for bare and P3OP coated AA2024-T3 exposed to DHS. Scan initiated 30 min after immersion using a scan rate of 10 mV/min.

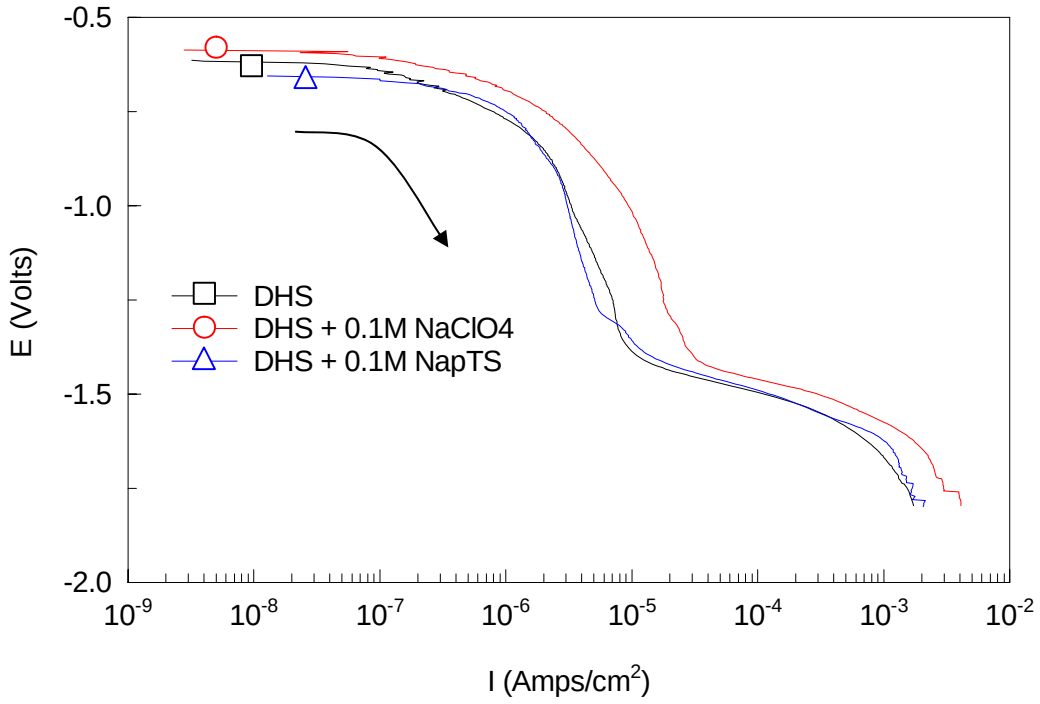

Figure 4.39 Cathodic polarisation curves for bare AA2024-T3 exposed to DHS. Scan initiated 30 min after immersion using a scan rate of 10 mV/min.

4.3.3.3 EIS of Chemically Synthesised P3OP-*ClO_4 Coated on AA2024-T3*

The chemically synthesised P3OP-ClO_4 coated on AA2024-T3 that was used in this EIS study contained surface cracks and small defects prior to immersion. EIS after 1h immersion (Figure 4.40 and Figure 4.41) displayed a high degree of noise, possibly due to the unstable OCP. After a few hours immersion large parts of the coating had delaminated and cracked so as to expose the underlying metal. After 2 days immersion the OCP had settled and a single time constant EIS response was observed. Data fitting was performed using a simple RC circuit used to model bare the metal (Figure 4.11) where the CPE_{dl} and R_{ct} were ascribed to the exposed metal.

Y_0 remained mostly unchanged reflecting that the majority of metal area was exposed from the first measurement at 2h (Appendix A.8). Despite the poor properties of the coating with exposed metal, the substrate exhibited a high and increasing R_{ct}. After 2 days R_{ct} was 7 times higher than observed for bare substrate as shown in Appendix A.1. After 16 days immersion the arc (Figure 4.40) reaches a maximum with an R_{ct} well over one order of magnitude higher than a for bare substrate with no corrosion product observed. This could possibly be a result of a protective oxide forming on the substrate during initial exposure. The oxide layer continued to grow and remain protective for 16 days despite the fact that a large part of the substrate wasn't physically covered by the coating.

After 28 days the impedance decreased dramatically indicating a breakdown of any protective oxide. White non-adherent corrosion product could be detected about 4 days thereafter.

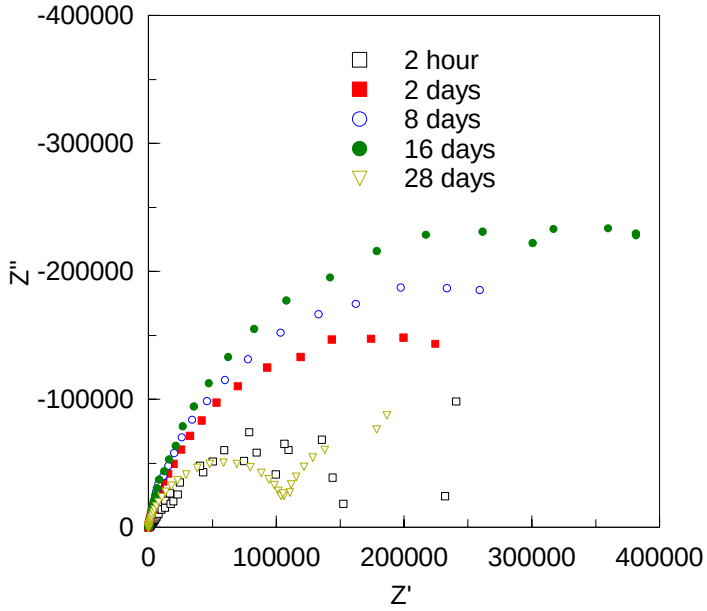

Figure 4.40 Nyquist plot of cast "Chem. P3OP-ClO4" coated AA2024-T3 immersed in DHS (exposed area: 2.5cm^2)

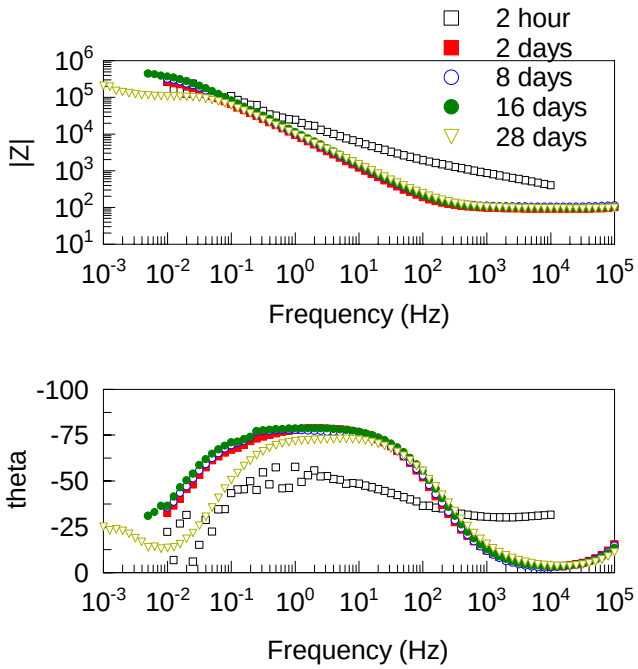

Figure 4.41 Bode plot of cast "Chem. P3OP-ClO4" coated AA2024-T3 immersed in DHS (exposed area: 2.5cm^2)

4.3.3.4 EIS of Chemically Synthesised P3OP-p*TS Coated AA2024-T3*

EIS spectra for chemically synthesised P3OP-*p*TS coated AA2024-T3 are shown in Figure 4.42 and Figure 4.43. Initially the lower frequency data was noisy but appeared to consist of two time constants. After 2 days the 2 separate time constants were clearly observed and were accurately modelled by using the ECM shown in Figure 4.15.

The R_{coat} derived from the high frequency time constant (Appendix A.9) increased with immersion time for the first 6 days while Y_c decreased, indicating the conversion of the polymer toward a less conductive form. Increase of Y_{dl} and R_{ct} derived from the lower frequency time constant also observed suggests a simultaneous formation of a protective oxide.

After 13 days $Y_{coat,}$ R_{coat} and R_{ct} decreased while C_{dl} increased indicating coating failure. This was confirmed visually with small pinhole defects observed on the polymer film filled with white corrosion product.

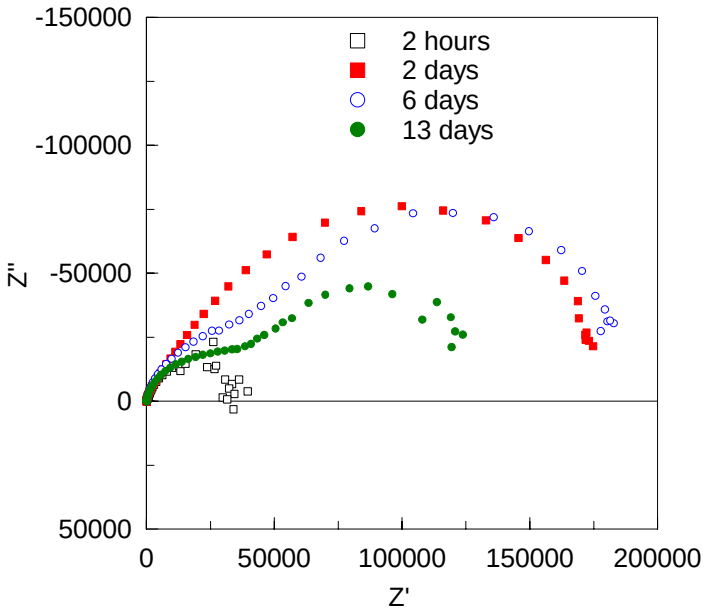

Figure 4.42 Nyquist plot of cast "Chem. P3OP-*p*TS" coated AA2024-T3 immersed in DHS (exposed area: 2.5cm^2)

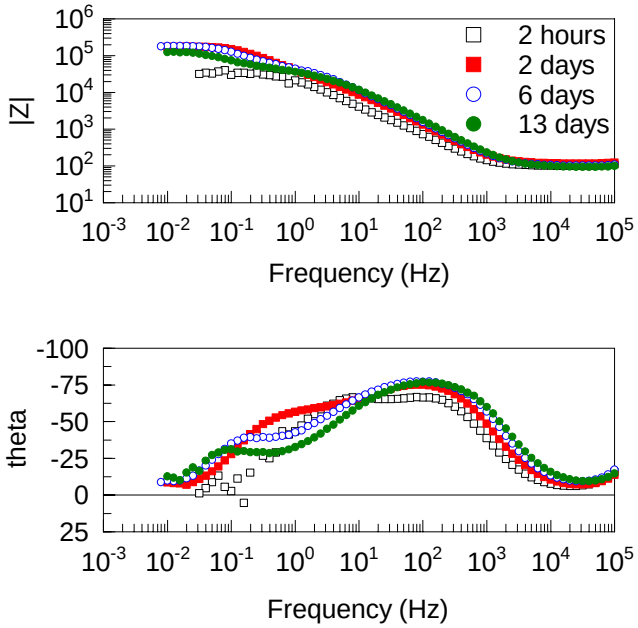

Figure 4.43 Bode plot of cast "Chem. P3OP-*p*TS" coated AA2024-T3 immersed in DHS (exposed area: 2.5cm^2)

4.4 Conclusions

Electrochemical techniques were used to investigate corrosion inhibition afforded AA2024-T3 by ICP coatings. Coatings studied were:

- Polyaniline/poly(butyl acrylate-vinyl acetate) copolymer composite (PAn/co-polymer) doped with (1s)-(+)-10-Camphorsulfonic acid (HCSA) "air dried" or "heat treated".
- Soluble fraction of electrochemically synthesised P3OP doped with $p\text{TS}^-$, synthesised in 80/20 CCl_4/DCM and DCM.
- Soluble and deposited fraction of electrochemically synthesised P3OP doped with $-ClO_4$ synthesised in DCM.
- Soluble fraction of electrochemically synthesised P3OP doped with –pTS synthesised in DCM.
- Chemically synthesised P3OP doped with ClO_4.
- Chemically synthesised P3OP doped with $p\text{TS}^-$.

Potentiodynamic polarisation, OCP and EIS were performed with results presented. Samples coated with "air dried" PAn/co-poly displayed an initial ennoblement with rapid formation of a more resistive coating restricting the corrosion reaction. This was followed by a penetrative wetting of the coating at longer immersion times eventually leading to an increasing corrosion rate. Similar behaviour was observed for "heat dried" PAn/co-poly with the only major difference being a higher R_{ct} and Y_{dl} observed for heat treated sample, attributed to slower rate of water penetration into the polymer film.

Electrochemically synthesised P3OP-*p*TS "Ashraf" initially showed minor ennobling and reduced I_{corr} while EIS suggested any longer exposure to be mostly analogous to a poor barrier coating. The electrical conductivity of this material was observed to be in the insulating range, further supporting a mechanism dominated by an inactive physical barrier. A simple poor barrier protection was also observed for electrochemically synthesised "P3OP-*p*TS solution". Material used exhibited both low conductivity as well as poor mechanical properties.

Electrochemically synthesised P3OP-ClO_4 of two fractions; "deposited" and the "solution" fraction as well as chemically synthesised P3OP-ClO_4^- and P3OP-*p*TS^- displayed anodic shift of the OCP and increased R_{ct} of the metal interface suggesting the formation of a protective oxide layer. Though different degrese of protection were observed for the different coatings, a general mechanism of corrosion inhibition to include and describe all observations made based on corrosion protection through anodic inhibition was suggested.

From the observed shift in the OCP a mechanism of ICP coating-metal interaction suggests a galvanic coupling between the metal and the polymer coating. Such coupling would arguably promote metal oxidation while the polymer coating undergoes reduction. The polymer reduction would be accompanied with release and expulsion of dopant anion.

Any initial inductive process observed using EIS could hence be explained by dopant absorption to the metal surface. Increasing R_{ct} indicated the build up of a protective surface formed as a result metal oxidation and dopant absorption.

Chapter 5- Characterisation of Local Corrosion Behaviour for ICP Coatings

5.1 Introduction

The ability of ICP's to provide corrosion protection within a coating defect has been investigated by the use of bulk measuring techniques such as DC polarisation and EIS. [101, 102] Lu *et al.* studied mild steel coated with and without a polyaniline primer and an epoxy topcoat. The samples with polyaniline primer exhibited a significant decrease in corrosion rate compared to epoxy topcoat alone. XPS (X-ray photoelectron spectroscopy) and Auger spectroscopy revealed the presence of passivating iron oxide within the defect. [103]

In other studies by Kinlen *et al.* corrosion within surface defects in polyaniline/polyvinyl butyral blends on carbon steel were studied using SRET (scanning reference electrode technique). [104] Several defects of varying sizes were introduced by drilling through the surface coating. These experiments, carried out in tap water, revealed anodic behaviour restricted to the defect sites and cathodic reactions taking place on the polyaniline coating. This initial behaviour was followed

by a rapid decrease in the observed corrosion activity which was attributed to passivation of the underlying metal.

The mechanism proposed by Kinlen *et al.* (Figure 5.1**)** suggests that an anodic potential shift of the metal, provided by the polyaniline through the galvanic coupling between PAn-ES and the steel, leads to oxidation within the defect as well as reduction of the polymer coating. With the reduction of PAn-ES to PAn-LS dopant counter ion is expelled into the defect area. A passivating oxide subsequently formed due to dopant and soluble iron oxide reacted to form an insoluble iron dopant complex in the defect area limiting the cathodic reaction.

Please see print copy for Figure 5.1

Figure 5.1 Mechanistic view of pinhole passivation. PAn "anodises" exposed Fe surface. Dopant complexes with iron to form passive layer. ES= Emeraldine salt of PAn. LS= Leuco salt of PAn. DOP= Dopant anion. [104]

He *et al.* has used SVET to study the interaction of poly(3-alkylpyrrole) coatings on cold rolled steel and aluminium alloy AA20204-T3. Scribed samples used to simulate a coating defect were exposed to 3.5 % NaCl and DHS [105]. For P3OP coated steel, a corrosion onset delay time was observed before any activity was detected. This was followed by strong anodic behaviour at the defect with the associated cathodic current uniformly distributed over the polymer surface. With prolonged exposure the corrosion activity decreased as corrosion product covered the defect site. He *et al.* postulated that O_2 reduction occurs at the polymer/electrolyte interface with the electron transfer from the metal to O_2 being mediated by the coating. The corrosion behaviour observed was consistent with observations made by He *et al.* for chromated epoxy primer [97]. Observations were also similar to those made for polyaniline/PVB blend on carbon steel, although no corrosion onset delay time was reported [104].

P3OP coated AA2024-T3 exhibited a dramatically different behaviour with no sizable current flow detected over 22 hours exposure time. After this extended period, a reduction current was observed within the defect with a corresponding oxidation current observed to be localised over the polymer surface. He *et al.* attributed the oxidation current observed to pitting of Cu-rich sites in the aluminium alloy rather than oxidation of the polymer. He *et al.* also suggested that an anodic current, of noise level magnitude, observed in the initial phase could result in passivation within the defect. Current flow was subsequently restricted for 22 hours with local oxidation current at coated Cu-rich sites inhibited by P3OP forming stable polymer-metal oxide complexes.

In this study SVET experiments were carried out to monitor the local interaction of ICP applied to the active substrate. Corrosion behaviour was monitored for typically 24h to study the initial corrosion mechanism. For some sample the experiment was extended to observe a clear trend. The application of a range of P3OP synthesis strategies aims to provide insight into the mechanism of corrosion protection. Also, P3OP materials previously studied by He *et al.* for corrosion inhibition of AA2024-T3 were studied as a potential corrosion inhibitor of Zinc-55 % Aluminium hot dip coated steel (ZA).

5.2 Experimental Procedures

Polymer synthesis, coating method and coating characterisation procedures are given in detail in Chapter 3.

Local oxidation/reduction reactions within ICP coating defects were monitored in-situ using a Scanning Vibrating Electrode Technique (SVET) instrument by Applicable Electronics. The instrument employs a single vibrating probe with a Pt-ball tip 20 μm diameter. Probe vibration was performed in both z and y axis positioned approximately 100 μm above the surface.

Samples were prepared by mounting a 1x1cm coated substrate in the centre of a Perspex disk. All edges and the backside of the sample were sealed using a two component epoxy (5 min Araldite, 3M). The exposed area was then reduced to 4mm^2 by covering the surface with adhesive tape (3M) where a 2x2mm square window had

been cut out. Adhesive tape was wrapped around the Perspex disc creating a round cell with a 5 ml capacity. Data collection was initiated within 10 min of immersion and collected as a grid of 20x20 points over the exposed area. Additional scans were initiated every 30 min with an acquisition time of about 8 minutes. Experiments were performed in DHS at OCP with electrolyte exposed to ambient conditions.

An artificial defect was also introduced onto each sample by scribing the coating with a stainless steel scalpel to expose the underlying metal. In the case of ZA two different types of defects were employed. A plastic needle was used to introduce a coating defect exposing the Zn/Al layer and a stainless steel scalpel was used to penetrate both the polymer coating and the Zn/Al layer exposing underlying steel. The latter defect is denoted “deep” and the former “shallow”.

The current density of the mapped area is presented both as 3D plots, where the current density is plotted as the z-axis with anodic current plotted as positive values over the x-y area, and as anodic/cathodic current vectors superimposed onto an optical image. Minimum of 3 replicates were performed on each sample and representative data presented.

5.3 Results and Discussion

5.3.1 SVET of AA2024-T3

Typical SVET of bare AA2024-T3 immersed in DHS (Figure 5.2) exhibited an initial period of low activity possibly due to a thin protective oxide formed by oxidation in air prior to immersion. Within 1 hour local anodic current sites develop. After 2 hours immersion the anodic current density reached a magnitude of 200μA/cm^2, as shown in Figure 5.2. The strong local current observed manifest the susceptibility of pitting corrosion for AA2024-T3. This data was collected by Dr. Jie He, NDSU, ND, USA.

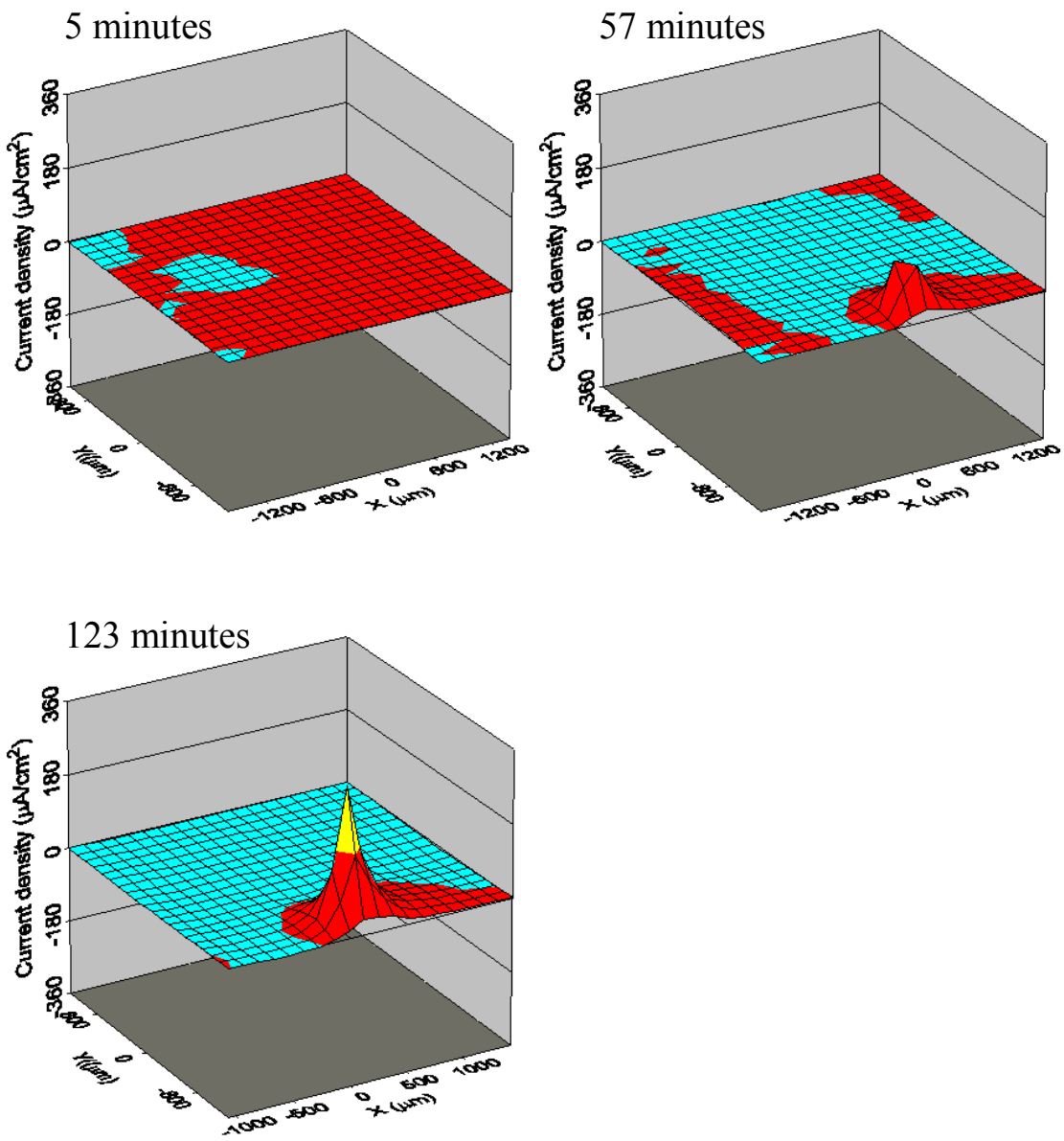

Figure 5.2 SVET current density distribution of AA2024-T3 in ambient DHS (data was collected by Dr. Jie He, NDSU, ND, USA.) Top left: 5 min immersion, Top right: 57 min immersion, Bottom left: 123 min immersion.

5.3.2 SVET of "Air Dried" PAn/co-polymer Coated AA2024-T3 Containing Artificial Defect

AA2024-T3 coated with PAn/co-poly "air dried" and scribed displayed a strong oxidation current centred over the defected area after 10 min immersion. The

corresponding reduction current was observed to be uniformly distributed over the polymer coating as shown in Figure 5.4. Occasionally bubble formation could be detected within the defect, presumably H_2 evolution, produced by according to Figure 5.3.

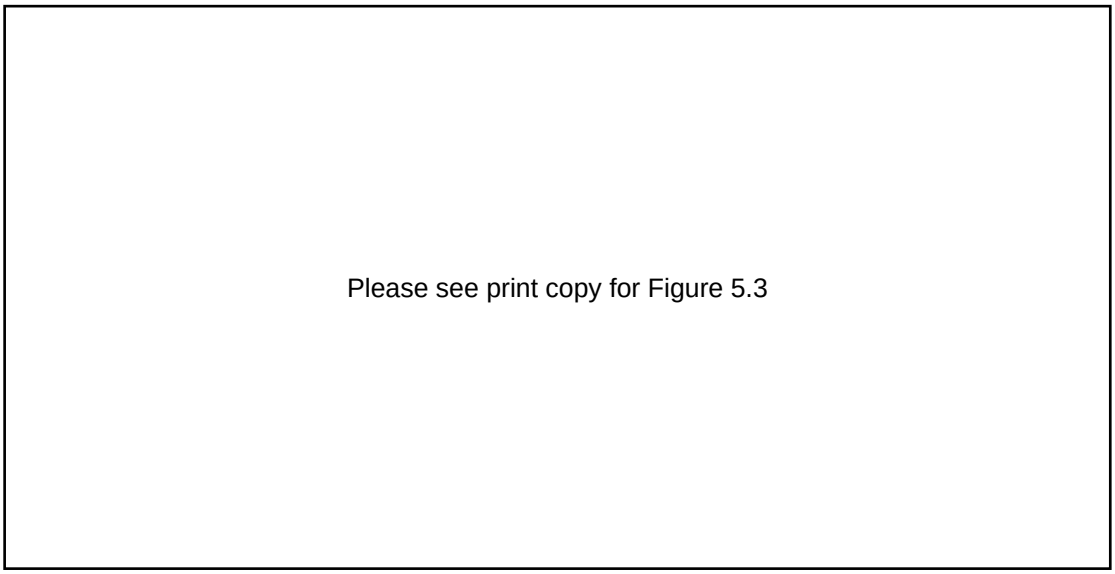

Figure 5.3 Mechanism of pitting corrosion of aluminium [106]

The strong oxidation current observed in the early stage of immersion decreased over time. The decrease in current density was accompanied with a colour change in the polymer film, Figure 5.5. The initial green colour, associated with the partially oxidised, doped and conductive state of ES, rapidly took on a darker shade with a more bluish appearance, corresponding to the deprotonated form of EB. The conversion (colour change) appeared to proceed more rapidly in areas further away from the defect area. Colour change towards a lighter green was observed for polymer covered by the tape surrounding the exposed area showing the extent of electrolyte creeping underneath the tape or reduction of polymer covered by tape. (Figure 5.5)

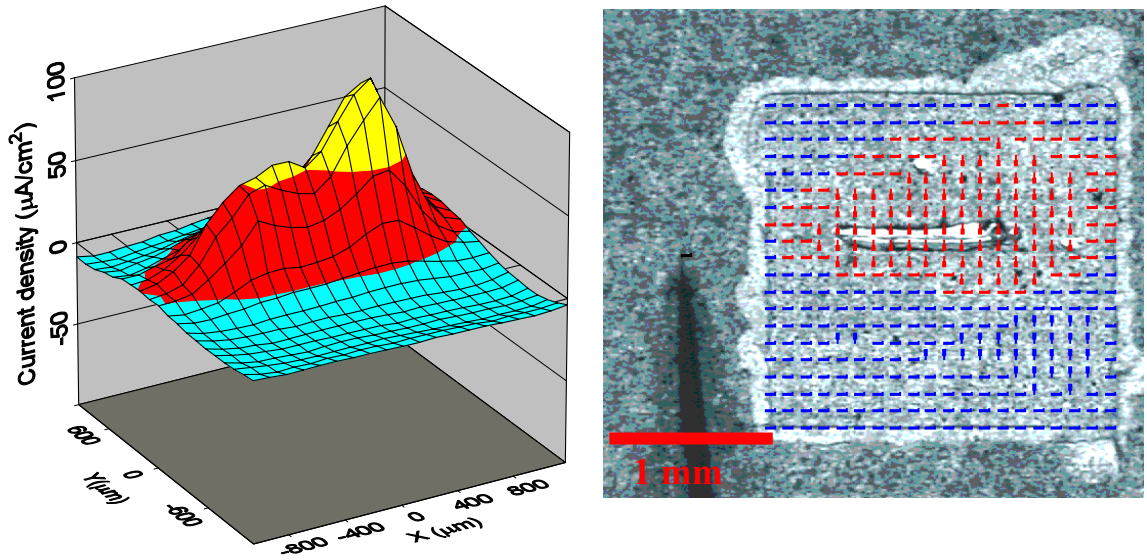

Figure 5.4 SVET of "air dried" PAn/co-poly coated AA2024-T3 containing artificial defect in ambient DHS. Left: Current density distribution Right: current vectors superimposed on optical image. Data collected after 10 minutes immersion.

The corrosion activity within the defect, which until this point had continuously decreased from an anodic initial maximum of 100 µA/cm^2, levelled off at an anodic current density of 5 µA/cm^2 after 6 hours. At this point the entire exposed polymer area had taken on a darker shade with the exception of a small area surrounding the defect. (Figure 5.6)

Decrease in current density could be suggestive of the formation of a passivating oxide within the defect as postulated by Kinlen *et al.* [104]. The observations could also be associated with the lesser galvanic coupling between the metal and the coating as the PAn-ES converts to a less conductive form.

Continued exposure revealed a localised second colour change in the vicinity of the scribe in the coating towards a lighter yellow/green colour, which is indicative of reduced PAn-LS. (Figure 5.7) After less then 12 hours immersion a grey/white fluffy precipitate appears within and around the defect. This corrosion product was assumed to be $Al(OH)_3$.

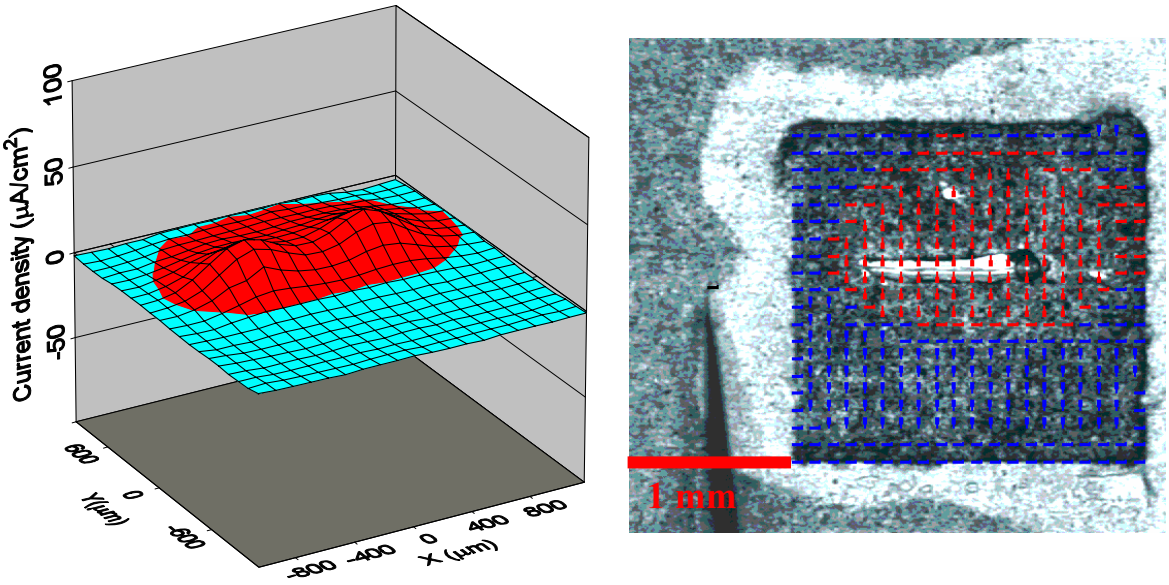

Figure 5.5 SVET current density distribution and current vectors superimposed on optical image of "air dried" PAn/co-poly coated AA2024-T3 with artificial defect. Scan performed 40 minutes immersion in DHS.

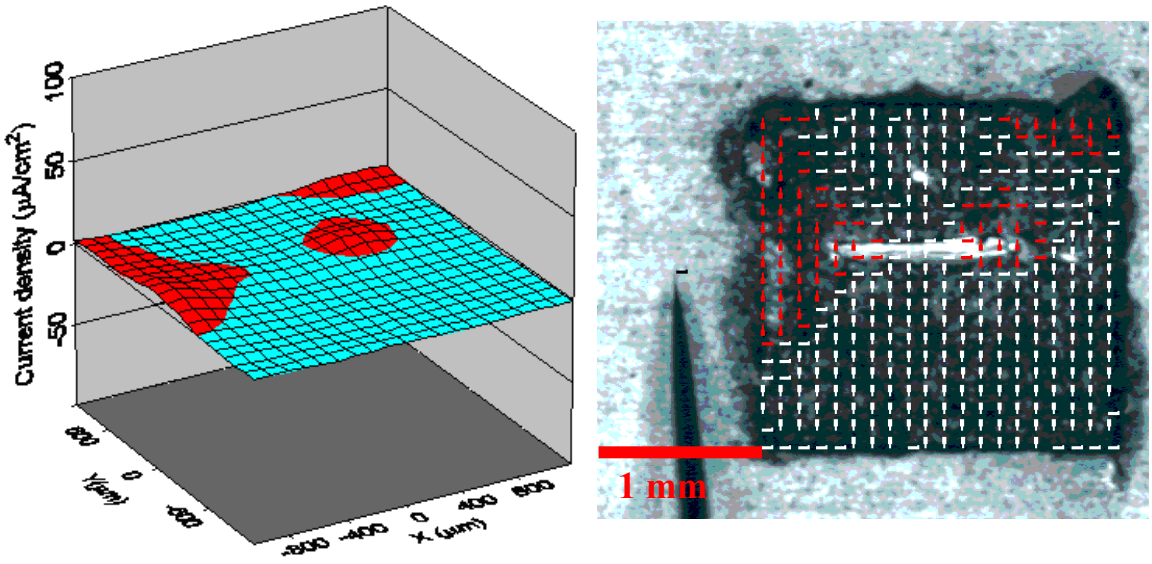

Figure 5.6 SVET current density distribution and current vectors superimposed on optical image of "air dried" PAn/co-poly coated AA2024-T3 with artificial defect. Scan performed after 6 hours and 10 minutes immersion in DHS.

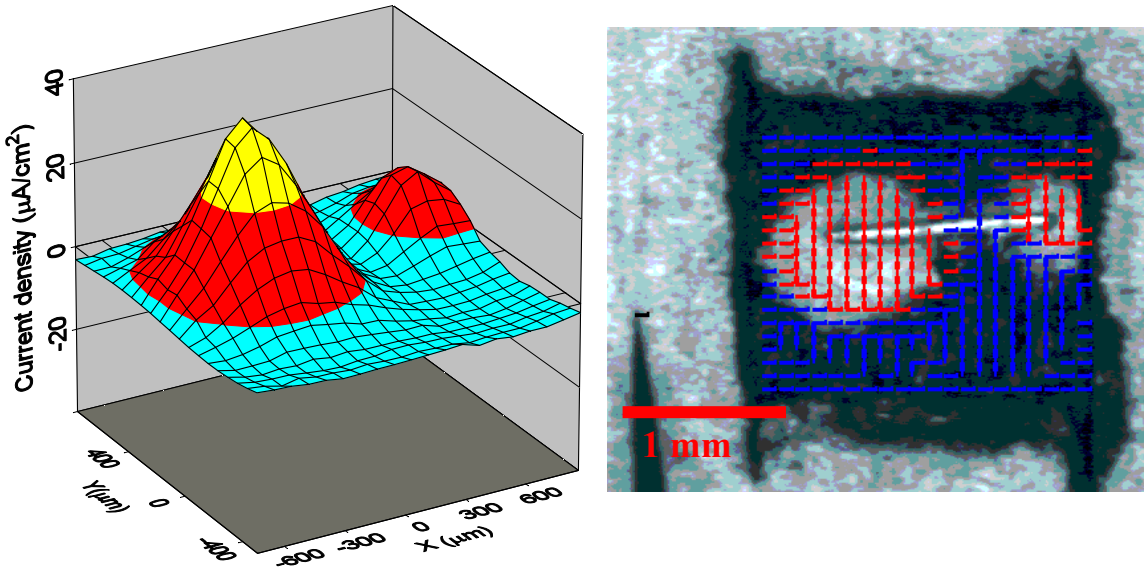

Figure 5.7 SVET current density distribution and current vectors superimposed on optical image of "air dried" PAn/co-poly AA2024-T3 with artificial defect. Scan performed after 9 hours and 10 minutes immersion in DHS.

5.3.3 SVET of "Heat Dried" PAn/co-poly Coated AA2024-T3 Containing Artificial Defect

AA2024-T3 coated with the "heat treated" PAn/co-poly and scribed displayed strong anodic current within the scribe immediately upon immersion as seen in Figure 5.8. In addition to strong anodic current, rapid gas evolution was observed from within the defect. After two hours immersion, the coating had changed from green to a darker blue colour, indicative of conversion from PAn-ES to PAn-EB, with the exception of the polymer in the absolute vicinity of the scribe corresponding to the oxidation site. The area surrounding the anodic peak instead converted to a paler green/yellow colour corresponding to formation of PAn-LS as seen in Figure 5.9.

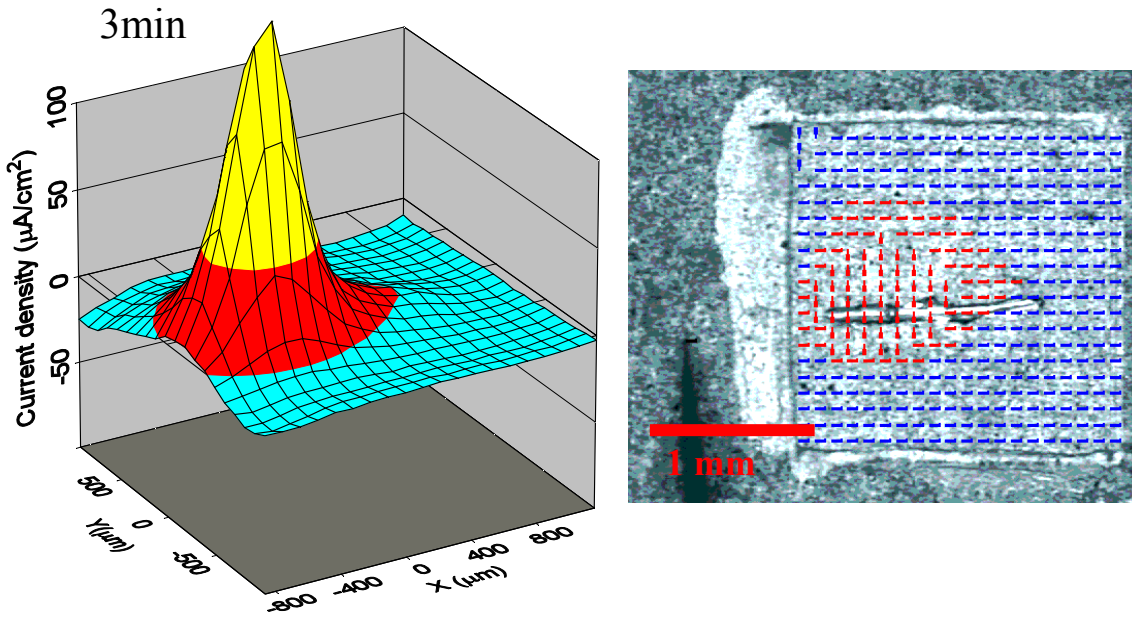

Figure 5.8 SVET current density distribution and current vectors superimposed on optical image of "heat treated" PAn/co-poly coated AA2024-T3 with artificial defect. Scan performed after 3 minutes immersion in DHS.

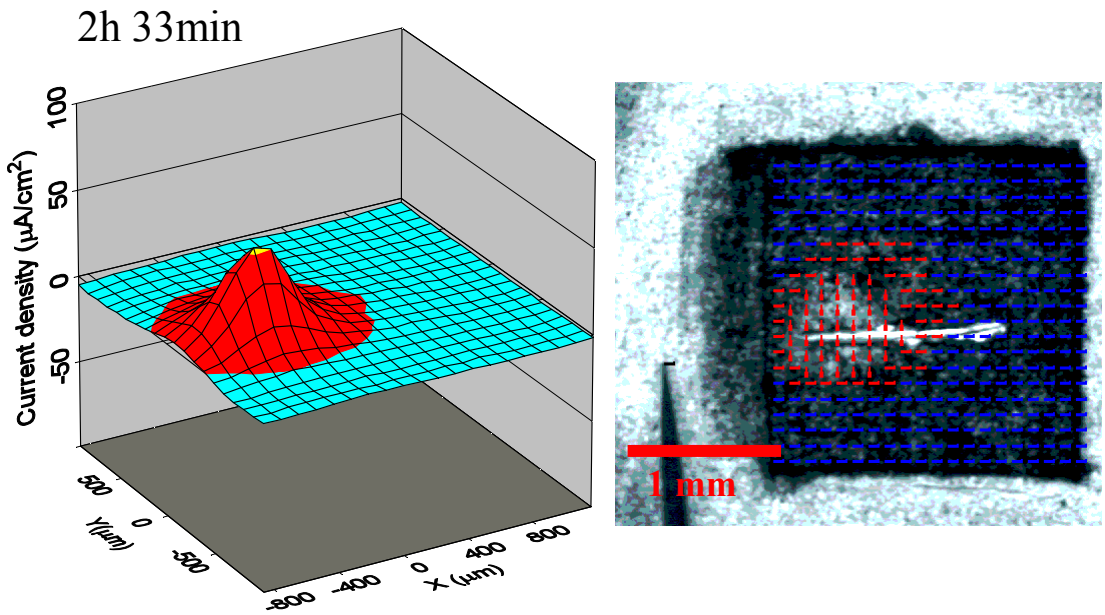

Figure 5.9 SVET current density distribution and current vectors superimposed on optical image of "heat treated" PAn/co-poly coated AA2024-T3 with artificial defect. Scan performed after 2 hours and 33 minutes immersion in DHS.

A maximum current density was observed immediately upon immersion and this decreased steadily, reaching a minimum after about 6 hours with a peak anodic current of 15 μA/cm^2. The oxidation current within the scribe continued to decrease while the peak oxidation slowly shifted onto the polymer coating towards the edge of the exposed area as shown in Figure 5.10. With prolonged exposure white corrosion product was observed in and around the scribe. The current density peak remained constant at 15-30 μA/cm^2 even after 40 hours exposure and the white product was postulated to be to be $Al(OH)_3$

The conversion of ES to EB could be a result of O_2 reduction on the Pan coating leading to higher pH at the coating surface which, in turn, leads to deprotonation.

Near the defect, Al^{3+} hydrolysis leads to low pH which maintains the Pan in the protonated or salt form.

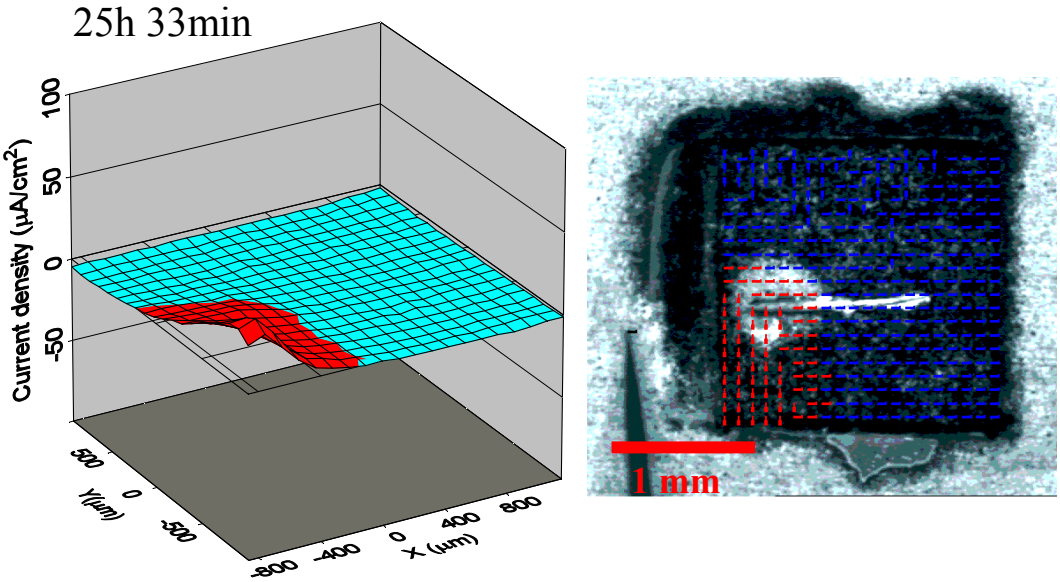

Figure 5.10 Current density distribution and current vector superimposed on optical image of "heat treated" PAn/co-poly coated AA2024-T3 with artificial defect. Scan performed after 25 hours and 33 minutes immersion in DHS.

5.3.4 SVET of Electrochemically Synthesised P3OP-*pTS Coated AA2024-T3 Containing Artificial Defect*

P3OP-*p*TS synthesised electrochemically according to the method of Ashraf *et al.* [88] was used to coat AA2024-T3. Without a defect this material exhibited a small initial anodic shift of the OCP and reduced I_{corr}. Longer immersion indicated some increase in the total impedance after 24 hours followed by slow degradation of the coating and reduction of the total impedance. Current density mapping of the coated substrate containing an artificial defect exhibited initially a current density

magnitude within the noise level of the experimental technique. [107] Scans initiated after 1 hour 7 min immersion revealed a low activity cathodic area centred over the defect with anodic current located along the tape on either side of the defect, Figure 5.11. The anodic current slowly increased to reach a maximum current density of less than 10 $\mu A/cm^2$ after approximately 4 hours, Figure 5.12. The oxidation current remained low for the whole experiment duration of 20 hours (Figure 5.13) with the oxidation peak located at the edge of the exposed area. At no point during the exposure was oxidation observed within the defect area. The area inside the scribe remained shiny for the whole 20 hours with no visible corrosion product observed.

The minimal activity observed correlates with the initial changes observed for undamaged coating (chapter 4) using EIS. The absence of any significant current flow also correlates with the low conductivity of the material.

These observations were in good agreement to previous studies for corrosion inhibition using P3OP-*p*TS made by Gelling *et al.* using a polymer made with an identical synthesis method[108]. Results observed by He *et al.* with material containing both *p*TS and perchlorate as dopant were also similar[105]. The study by He *et al.* also noted a minor anodic current within the defect in the very early stages of immersion and suggested that the initial oxidation current observed within the defect may result in the formation of a protective oxide coating which would account for a 22 hours delay time where no significant current was observed.

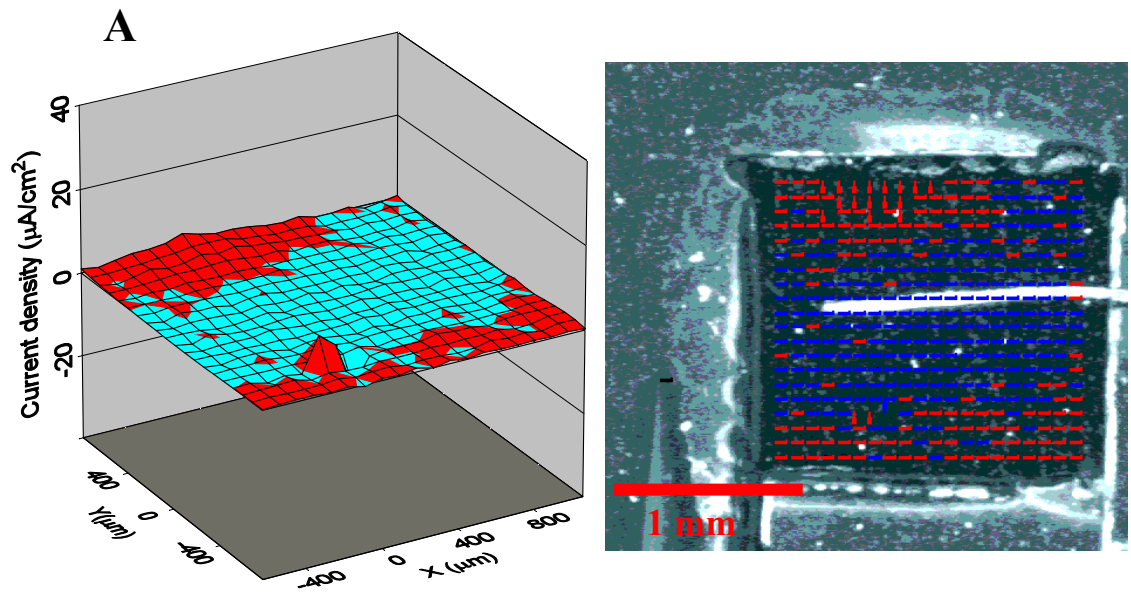

Figure 5.11 SVET current density distribution and current vectors superimposed on optical image of AA2024-T3 coated electrochemically synthesised P3OP-*p*TS containing an artificial defect. Scan performed in DHS after 1 hour 7 min.

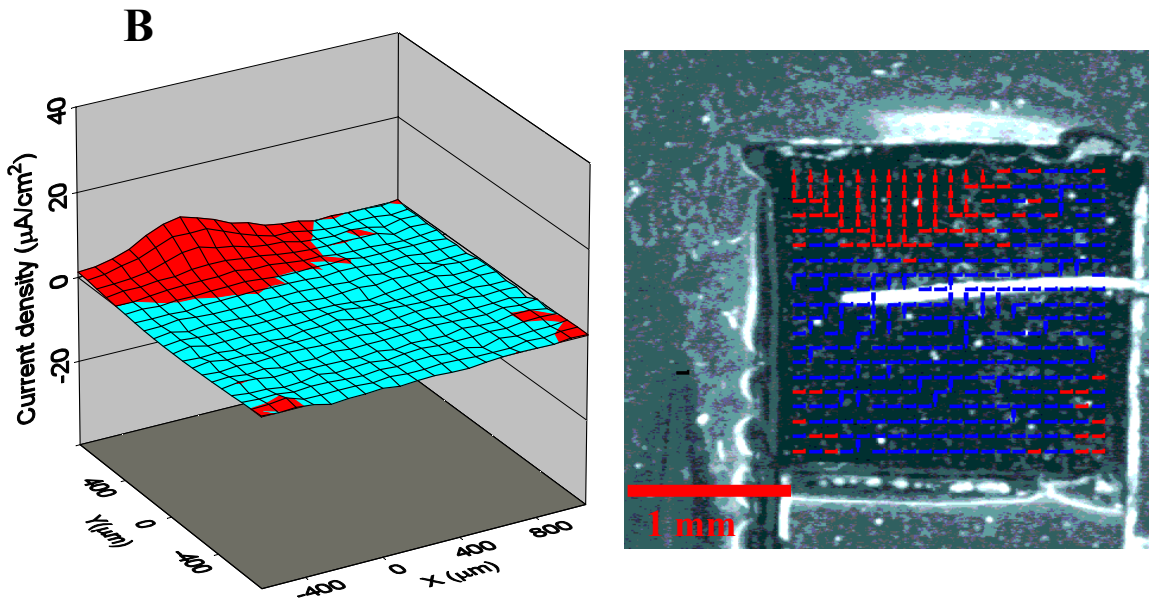

Figure 5.12 SVET current density distribution and current vectors superimposed on optical image of AA2024-T3 coated electrochemically synthesised P3OP-*p*TS containing an artificial defect. Scan performed in DHS after 4 hours 37 min.

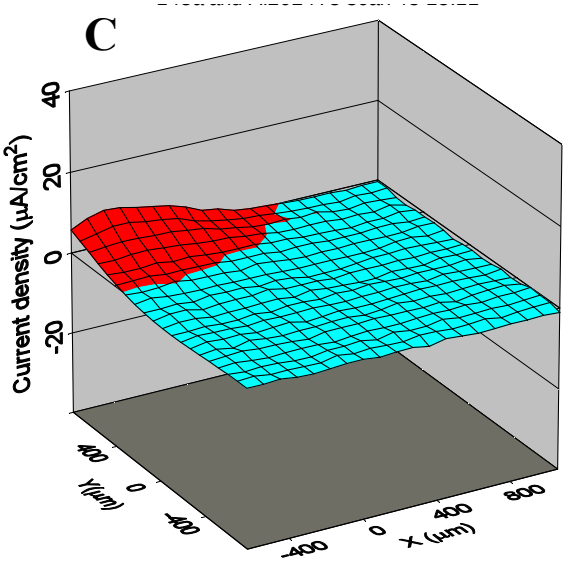

Figure 5.13 SVET current density distribution and current vectors superimposed on optical image of AA2024-T3 coated electrochemically synthesised P3OP-*p*TS containing an artificial defect. Scan performed in DHS after 20 hours 37 min.

5.3.5 SVET of Chemically Synthesised P3OP-*ClO_4 Coated AA2024-T3 Containing Artificial Defect*

Chemically synthesised P3OP-ClO_4 used as coating without a defect displayed some initial anodic shift of the OCP and reduced I_{corr}. Longer term immersion resulted in a slowly increasing R_{ct} reaching a maximum value after 16 days. The underlying surface remained protected despite that the poor coating properties of the material had resulted in cracks forming in the coating.

Chemically synthesised P3OP-ClO_4 exhibited very poor film formation. Casting of films resulted in a large number of small cracks in the coating. Due to the poor film formation mapping of chemically synthesised P3OP-ClO_4 on AA2024-T3 was performed using a coating twice the standard coating thickness, and in some

experiments a significantly wider artificial defect was used. The thicker coating produced a more homogenous coating, though cracks were observed also in the thicker coatings. The wider scribe was therefore used to produce a distinct difference between naturally formed cracks in the coating and the artificial defect.

Standard scribed coatings initially displayed anodic behaviour within the defect with a current density of 10-20 μA/cm^2 with corresponding cathodic current distributed over the polymer coating. However when using a thinner scribe anodic sites were occasionally also observed over the polymer coating as shown in Figure 5.14.

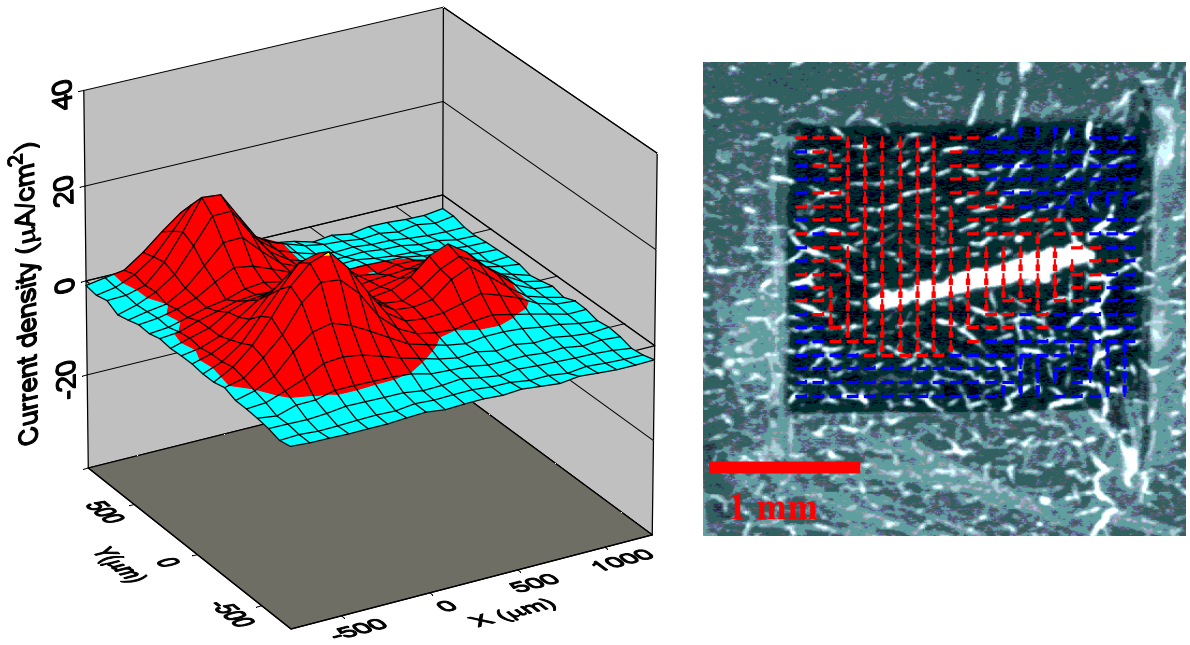

Figure 5.14 AA2024-T3 coated chemically synthesised P3OP-ClO_4 containing an artificial defect. Scan performed in DHS. Upper left: 10 min. Upper right: current vector superimposed on optical image 10 min.

The anodic current observed over the exposed metal decreased slowly to reach a minimum after about 5 hours but the overall activity remained constant for the 73 hours duration of the experiment, Figure 5.15. The surface remained shiny and no corrosion product could be detected within 73 hours.

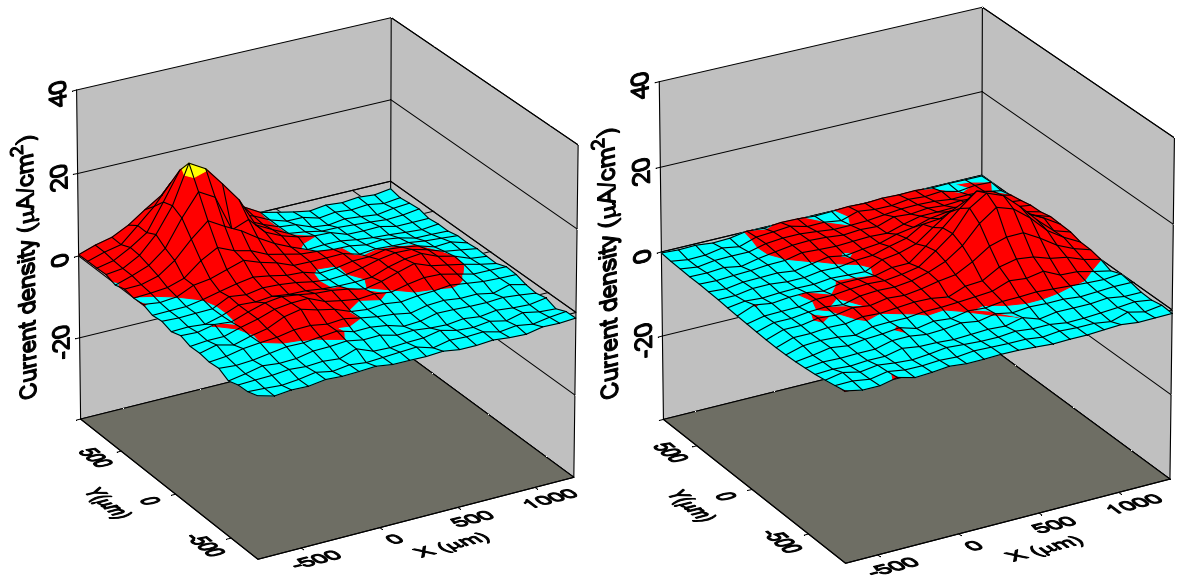

Figure 5.15 AA2024-T3 coated chemically synthesised P3OP-ClO_4 containing an artificial defect. Scan performed in DHS. Left: 5hours immersion. Right: 73hours immersion

Current density mapping of samples containing a wider defect reveal an initial anodic current of around 20 µA/cm^2 and some H_2 evolution in the defect site. The corresponding reduction was observed uniformly distributed over the coating as shown in Figure 5.16. The rate of H_2 evolution was low with less that 1 bubble a minute but the formation of H_2 was observed for a period stretching over several hours as shown in Figure 5.17. The initially observed oxidation current of around 20 µA/cm^2 remained fairly constant over a period of 40 hours. Minor colour changes were observed on the polymer adjacent to anodic sites after prolonged exposure. The

polymer shifted from a deep black towards a grey/black with shades of blue/green, indicating reduction of the polymer surrounding the anodic defect.

Despite a constant oxidation current of above 20 μA/cm^2 for 40 hours, the defect area remained visibly corrosion-free as seen in Figure 5.18.

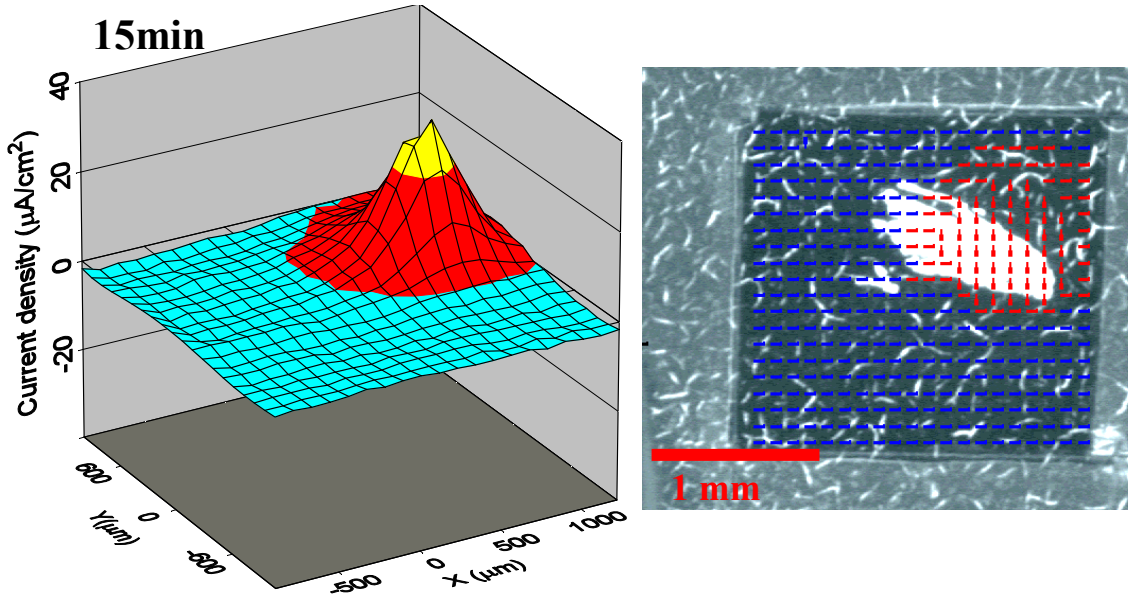

Figure 5.16 Left: Current density distribution Right: optical image of AA2024-T3 coated with chemically synthesised P3OP-ClO_4 containing a wide artificial defect. Scan performed in DHS after 15 min

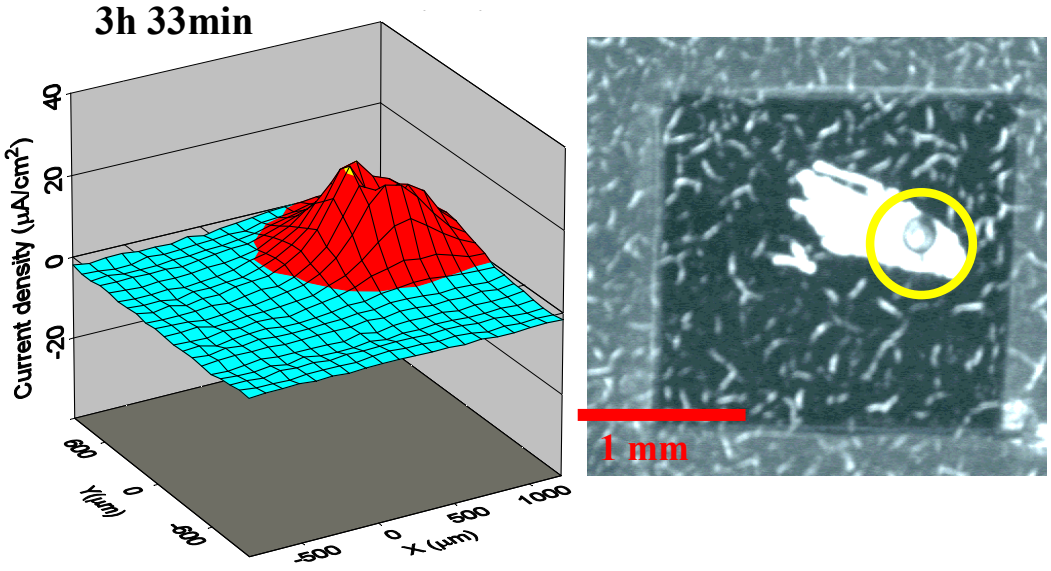

Figure 5.17 Left: Current density distribution Right: optical image of AA2024-T3 coated with chemically synthesised P3OP-ClO_4 containing a wide artificial defect. Scan performed in DHS after 3 hours 33 min. Bubble formation highlighted with drawn yellow ring in optical micrograph.

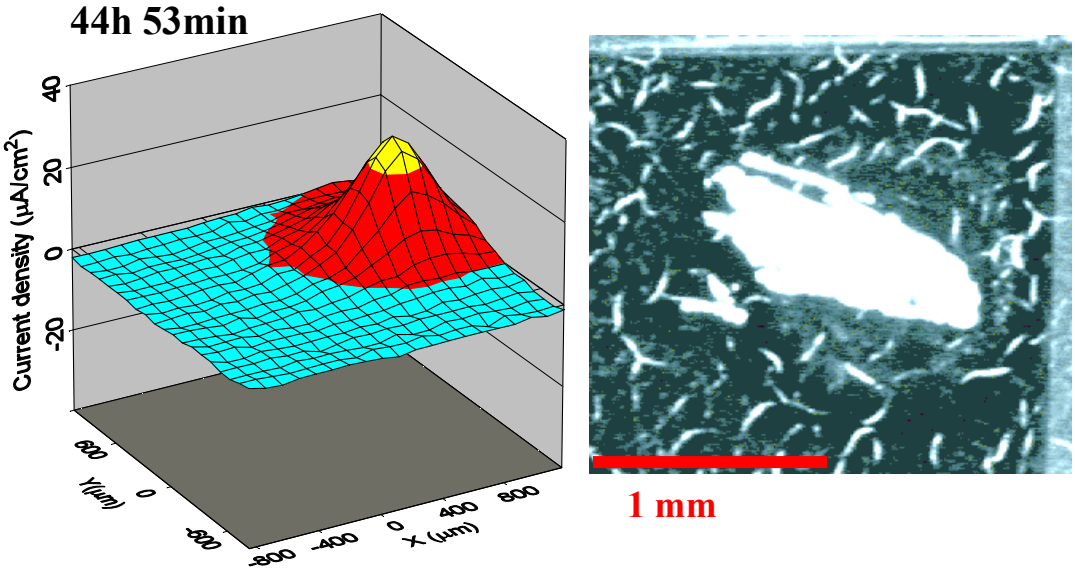

Figure 5.18 Left: Current density distribution Right: optical image of AA2024-T3 coated with chemically synthesised P3OP-ClO_4 containing a wide artificial defect. Scan performed in DHS after 44 hours 53 min

5.3.6 SVET of Chemically Synthesised P3OP-*p*TS *Coated AA2024-T3 Containing an Artificial Defect*

Chemically synthesised P3OP-*p*TS cast onto AA2024-T3 without an introduced defect displayed some initial anodic shift of the OCP and a minor I_{corr} increase. Longer term immersion resulted in an increasing R_{ct} of one order of magnitude above value observed for uncoated. Maximum impedance was observed after 6 days followed by a slow decrease.

Current density mapping of chemically synthesised P3OP-*p*TS cast onto AA2024-T3 with an artificial defect introduced into the coating demonstrated a low magnitude single oxidation peak within the narrow defect just after immersion (initiated after 3 min), as shown in Figure 5.19. After 30 min the anodic current within the scribe decreased in magnitude to about 5 $\mu A/cm^2$ and remained constant for several hours, Figure 5.20.

After 68 hours immersion, only current flow close to the background noise level was detected over the whole sample surface with the scribe appearing to be free from corrosion products. The polymer coating at the site corresponding to the initial anodic behaviour turned less opaque and took on a grey/green tone as shown in Figure 5.21.

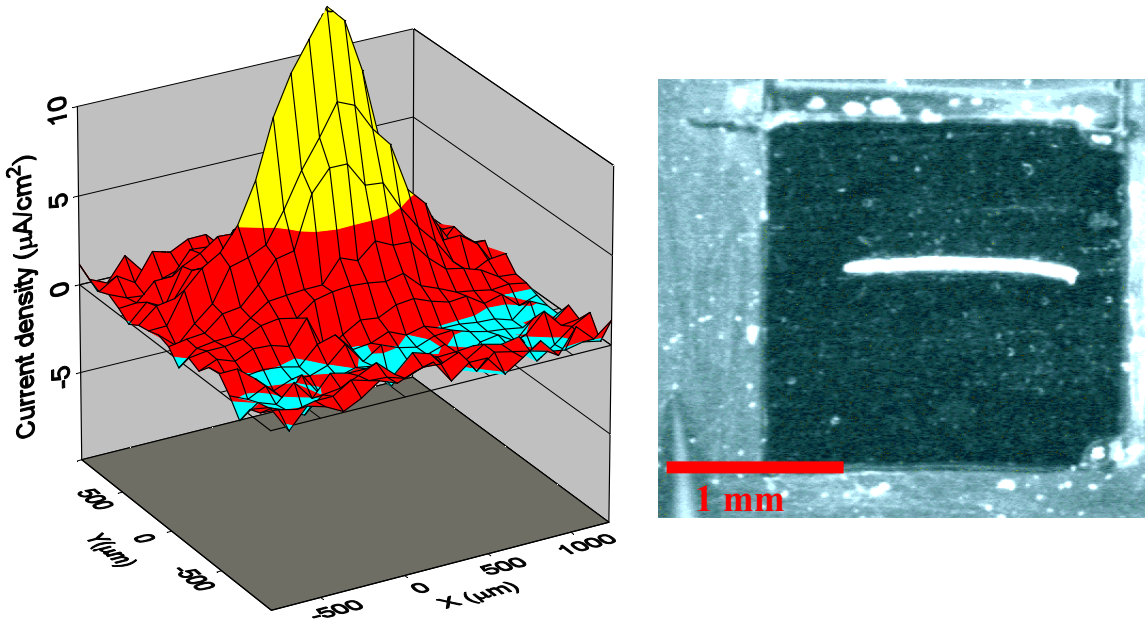

Figure 5.19 AA2024-T3 coated conducting, chemically synthesised P3OP-*p*TS containing an artificial defect after 3 min exposure in DHS

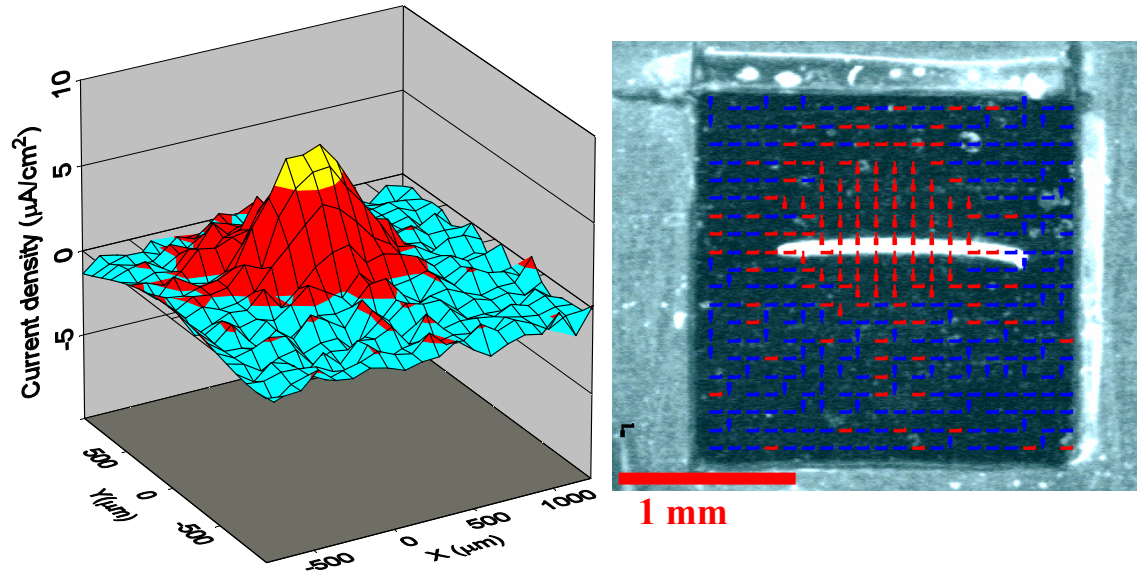

Figure 5.20 AA2024-T3 coated conducting, chemically synthesised P3OP-*p*TS containing an artificial defect after 1 hour 40 min exposure in DHS

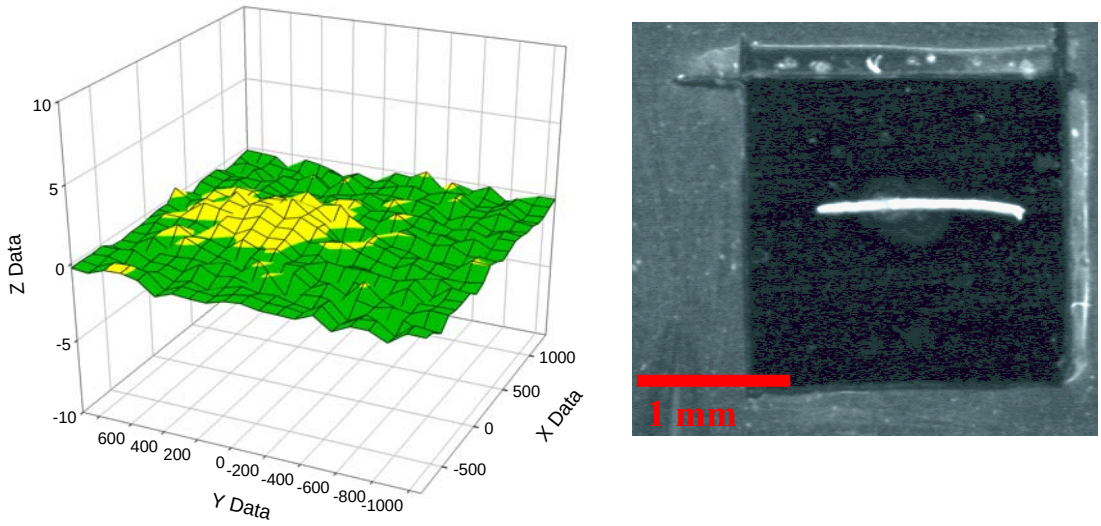

Figure 5.21 AA2024-T3 coated conducting, chemically synthesised P3OP-*p*TS containing an artificial defect after 68 hours exposure in DHS.

5.3.7 SVET of Zinc-55 % Aluminium Hot Dip Coated Steel

SVET study using P3OP by He *et al.* showing corrosion inhibition on AA2024-T3 suggests its use as a possible replacement of Cr(VI) coatings currently used commercially. [106] This prompted the SVET study of the same material as coatings on Zinc-55 % Aluminium hot dip coated steel (ZA). Currently corrosion protection of ZA commercially is also afforded by Cr(VI) containing coatings.

ZA with bare but intact Zn/Al layer exposed to DHS displayed immediate corrosion activity. Early SVET scans show activity with local and temporary anodic and cathodic sites. Temporary local sites appear at specific locations, shutting down only to appear at sites previously displaying opposite activity, Figure 5.22. Within hours the surface turned from a shiny metal to a dull grey as an oxide developed on the surface. This oxide did not appear to impart any passivating effect as reflected by the

mostly static current. After prolonged exposure the oxidation and reduction sites became more permanent without any indication of passive film formation. After 20 hours exposure, oxidation sites were mostly located along the edge of the exposed area, possibly assisted by delamination of the insulating tape and this was accompanied by a non adherent clearly visible white corrosion product. (Figure 5.23)

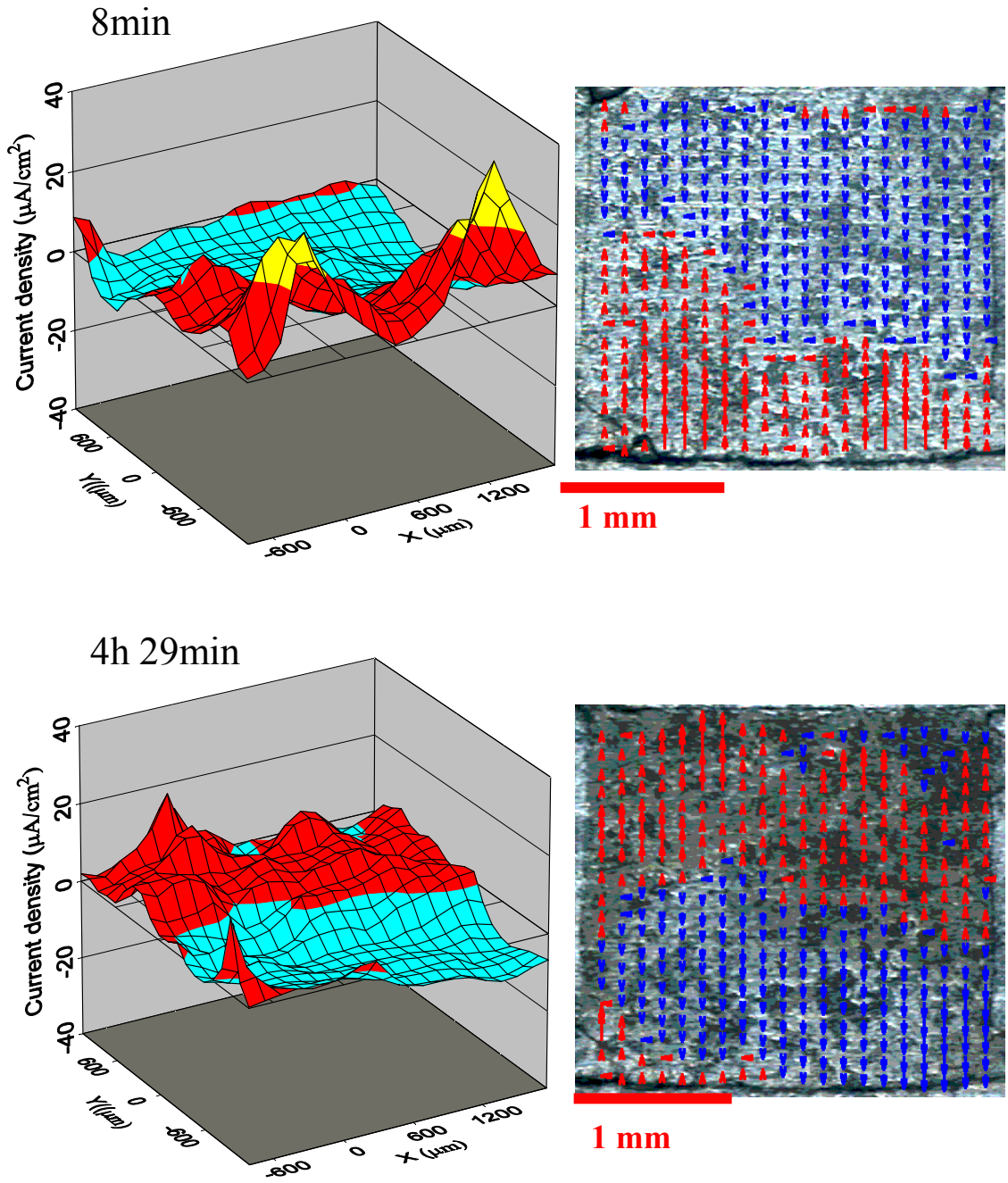

Figure 5.22 SVET of bare Zinc-55 % Aluminium hot dip coated steel. Scan performed in DHS. Upper left: Current density map after 8 min exposure. Upper right: current vector superimposed on optical image after 8 min exposure. Lower left: Current density map after 4 hours 29 min exposure. Lower right: current vector superimposed on optical image after 4 hours 29 min exposure.

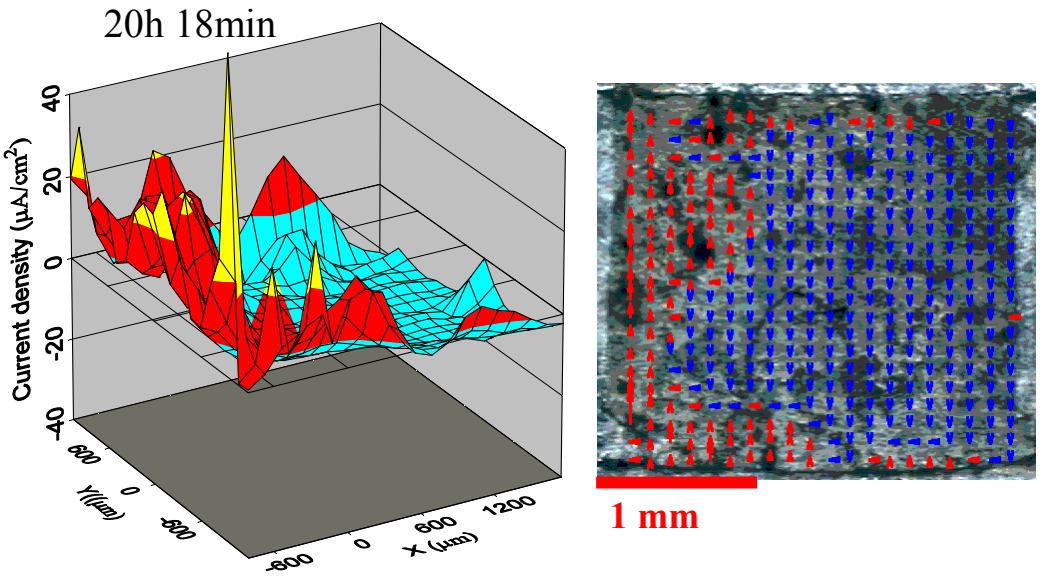

Figure 5.23 SVET of bare Zinc-55 % Aluminium hot dip coated steel. Scan performed in DHS. Left: Current density map after 20 hours 18 min exposure. Right: current vector superimposed on optical image after 20 hours 18 min exposure.

5.3.8 SVET of Zinc-55 % Aluminium Hot Dip Coated Steel with "Deep" Artificial Defect

SVET of bare Zinc-55 % Aluminium hot dip coated steel was scored with a penetrating deep defect so as to expose the underlying steel. These samples were then exposed to DHS and exhibited sacrificial oxidation of the Zn/Al layer protecting the underlying steel via an imposed reduction process, Figure 5.24. The current density observed reached a maximum after approximately 1 hour exposure with anodic peaks in the order of 20 μA/cm^2. The observed current density decreased with immersion time as the Zn/Al surface turned from shiny metallic to dull grey due to oxide formation. Over the 20 hours duration of the experiment only a cathodic current was observed within the defect, Figure 5.25. The presence of this cathodic

current together with the observation that no iron rust was visible within the defect suggests that the Zinc-55 % Aluminium hot dip coating provides sufficient sacrificial cathodic protection of steel under the set conditions.

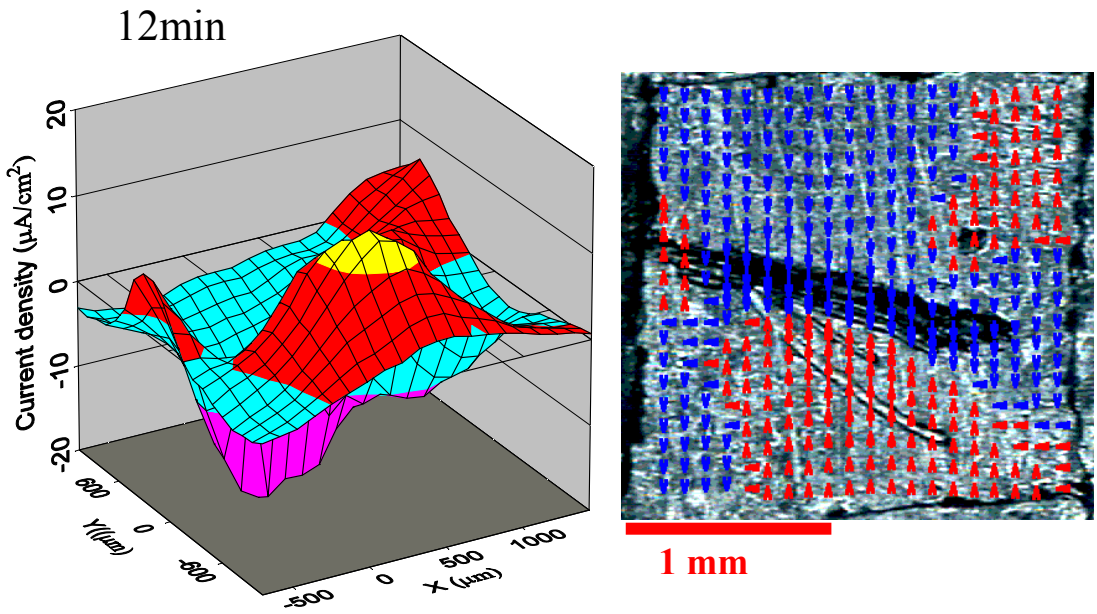

Figure 5.24 SVET of bare Zinc-55 % Aluminium hot dip coated steel with deep penetrating defect exposing underlying steel. Scan performed in DHS. Left: Current density map after 12 min exposure. Right: current vector superimposed on optical image after 12 min exposure.

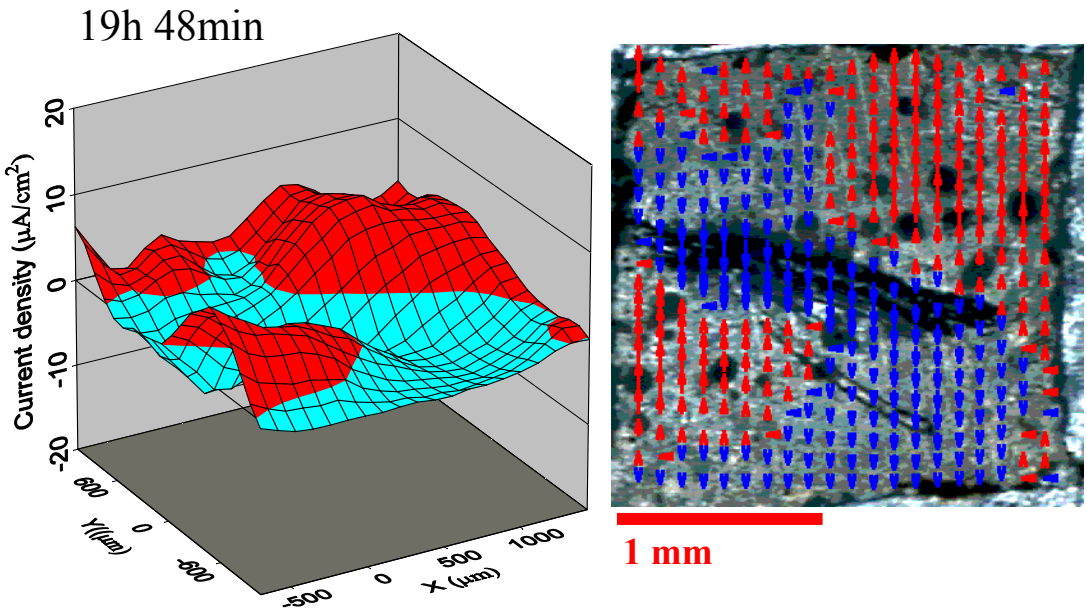

Figure 5.25 SVET of bare Zinc-55 % Aluminium hot dip coated steel with deep penetrating defect exposing underlying steel. Scan performed in DHS. Left: Current density map after 19 hours 48 min exposure. Right: current vector superimposed on optical image after 19 hours 48 min exposure.

5.3.9 SVET of Electrochemically Synthesised P3OP-p*TS on Zinc-55 % Aluminium Hot Dip Coated Steel with "Shallow" Artificial Defect*

Electrochemically synthesised P3OP-*p*TS coated ZA containing a "shallow" artificial defect was mapped using SVET. A "Shallow" defect denotes that the sample was scribed only to remove the polymer coating exposing the Zn/Al alloy and not penetrating the Zn/Al coating exposing the underlying steel.

In the very first scan, initiated after 2 min immersion, an oxidation current of 2 µA/cm^2 was observed within the defect, Figure 5.26. In the next scan, initiated 11

min after immersion, the observed currents were small but inverted with respect to the initial scan with the scribed area displaying cathodic behaviour and a general oxidation current distributed over the polymer area, Figure 5.27. The scribe area remained purely cathodic for the duration of the 21 hours exposure as shown in Figure 5.28.

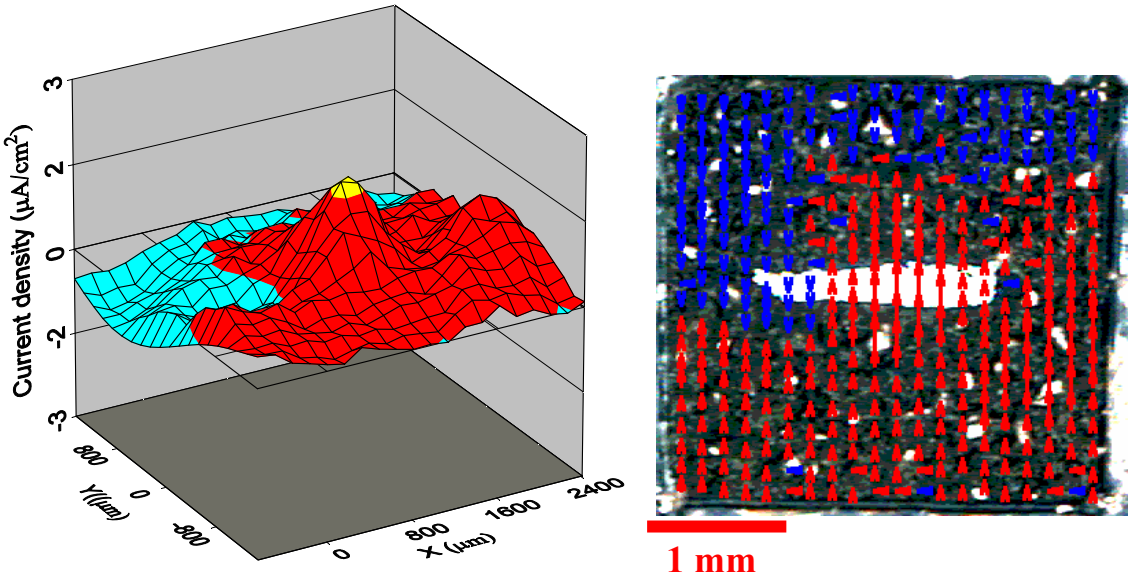

Figure 5.26 SVET current density distribution and current vectors superimposed on optical image of coated Zinc-55 % Aluminium hot dip coated steel electrochemically synthesised P3OP-*p*TS containing a "shallow" artificial defect. Scan performed in DHS after 2 min.

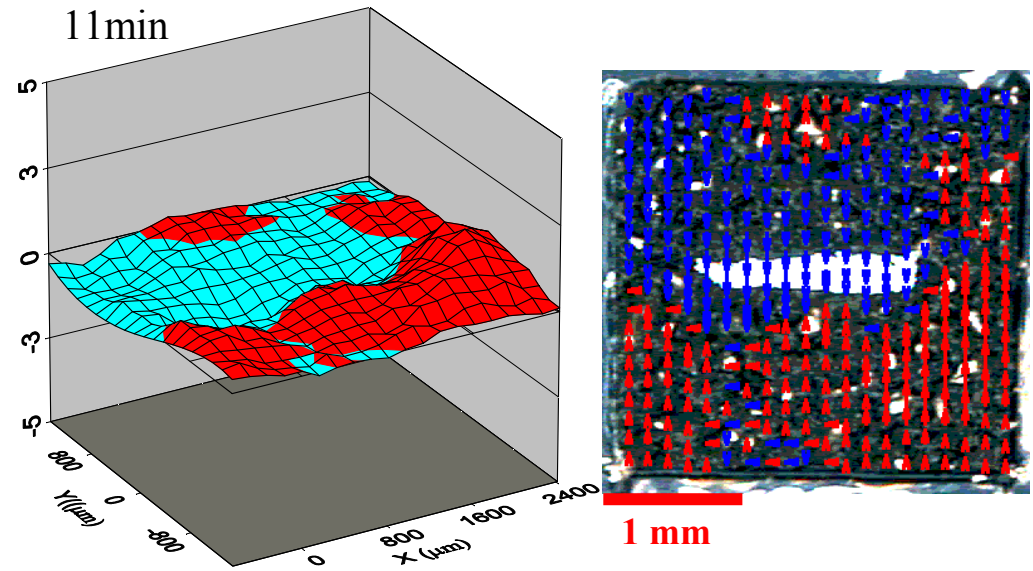

Figure 5.27 SVET current density distribution and current vectors superimposed on optical image of coated Zinc-55 % Aluminium hot dip coated steel electrochemically synthesised P3OP-*p*Ts containing a "shallow" artificial defect. Scan performed in DHS after 11 min.

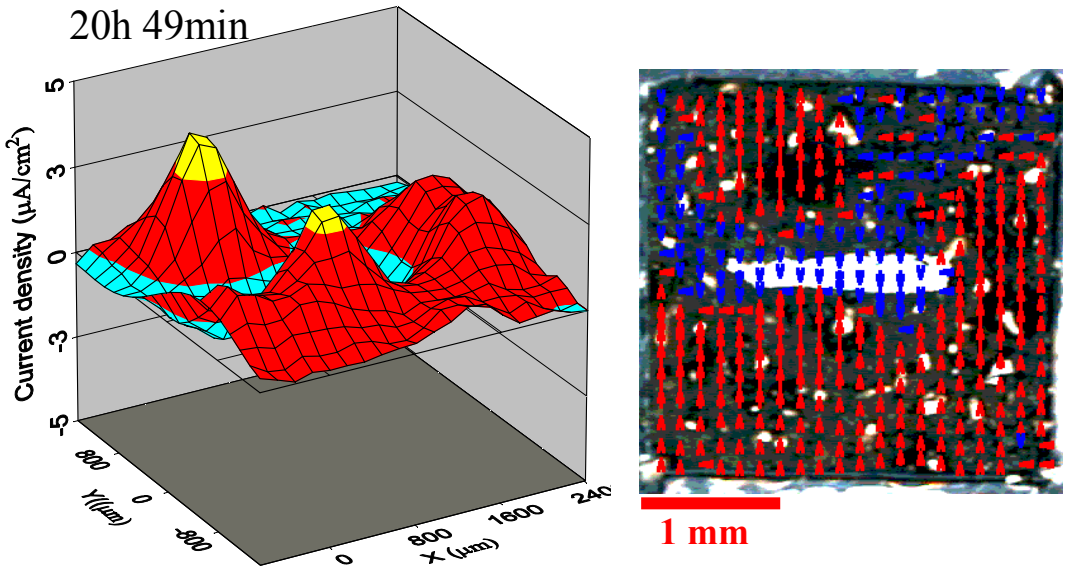

Figure 5.28 SVET current density distribution and current vectors superimposed on optical image of coated Zinc-55 % Aluminium hot dip coated steel electrochemically synthesised P3OP-*p*Ts containing a "shallow" artificial defect. Scan performed in DHS after 20 hours 49 min.

The current density observed for these samples was very low with the signal measured often within the observed noise level of the SVET instrument. Despite this, consecutive scans produced consistent data and acceptable signal to noise ratios were observed, such that the data could be evaluated showing a progression of current flow, permitting local areas to be characterised as anodic or cathodic, as for all previous samples.

The cathodic behaviour of exposed metal surface and corresponding anodic current observed over the polymer coated area resembled potential mapping observations made using the same material on AA2024-T3, Chapter 3.4.1 and in the study by *Gelling et al.* [108] and as well as by He *et al.* using similar material though containing both *p*TS and perchlorate as dopant [105]. The initial anodic current observed in the above experiment also correlates with observations on AA2024-T3 by He *et al.,* though in contrast to He's observations on AA2024-T3, once oxidation was observed over the polymer area the current distribution did not appear to be localised as in the case of Zn/Al. The current distribution observed for Zn/Al coated areas resembled the current distribution observed by He *et al.* for pure Aluminium [105] suggesting that any Zn/Al corrosion occurred uniformly under the polymer coating.

5.3.10 SVET of Electrochemically Synthesised P3OP-*p*TS *on Zinc-55 % Aluminium Hot Dip Coated Steel Without Artificial Defect*

Without any defect, as shown in Figure 5.29, no measurable current was initially observed. After 48 hours immersion, an area near the tape edge displayed an anodic

current of 2 μA/cm^2. This behaviour remained for the 68 hour duration of the experiment as shown in Figure 5.30.

The 48 hour delay time and the continued low current magnitude observed, despite the poor barrier properties afforded by the coating, suggest that protective properties other than simple barrier protection is afforded by the polymer coating.

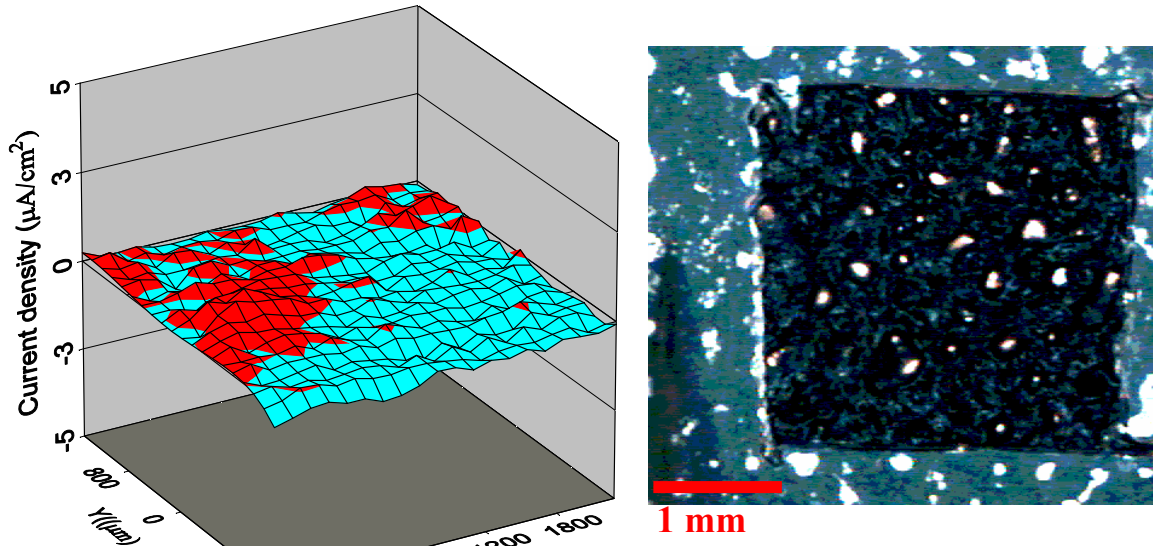

Figure 5.29 SVET current density distribution and current vectors superimposed on optical image of coated Zinc-55 % Aluminium hot dip coated steel electrochemically synthesised P3OP-*p*TS. Scan performed in DHS after 3 min

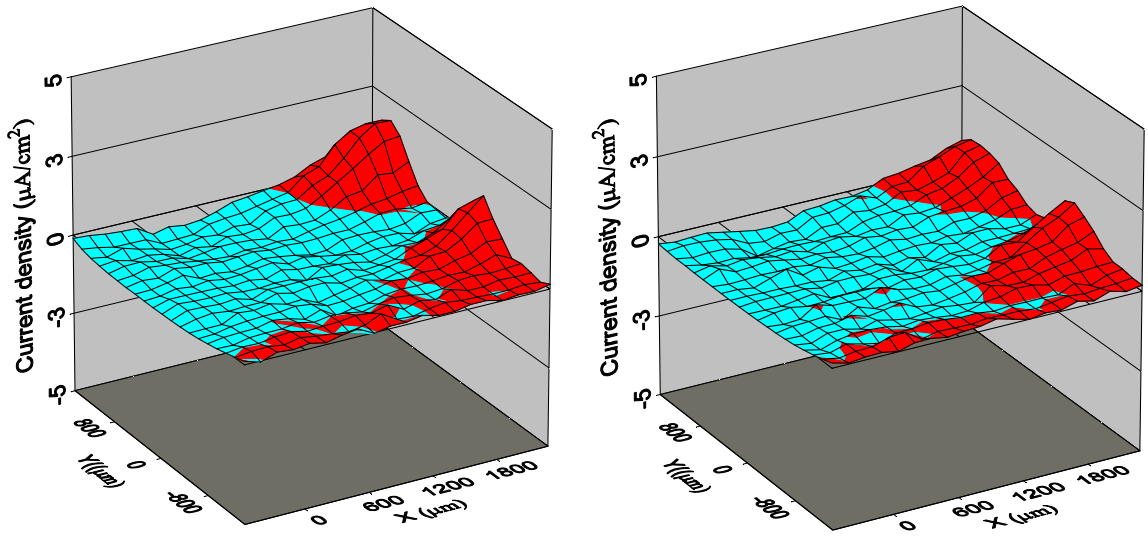

Figure 5.30 Current density distribution of coated Zinc-55 % Aluminium hot dip coated steel electrochemically synthesised P3OP-*p*TS. Scan performed in DHS after Left: 47 hours 38 min, Right: 68 hours 35 min.

5.3.11 SVET of electrochemically synthesised P3OP-p*TS on Zinc-55 % Aluminium Hot Dip Coated Steel with "Deep" Artificial Defect*

Electrochemically synthesised P3OP-pTS coated ZA scribed to expose underlying steel measured low current densities with all data within commonly observed noise levels. Though contrary to observations made for bare ZA with "deep" scribe, P3OP-pTS coated ZA with a "deep" defect on the initial scan (Figure 5.31), exhibited partial oxidation over the defected area with the reduction processes also partially located over both defect and non-defect sites. After 2 hours 35 min as shown in Figure 5.32 virtually no current flow was observed. The minor anodic behaviour observed at the exposed metal increased gradually to around 4 µA/cm^2 after 10 hours. This current magnitude and distribution was then maintained over the duration of the exposure, 19 hours 49 min, Figure 5.33.

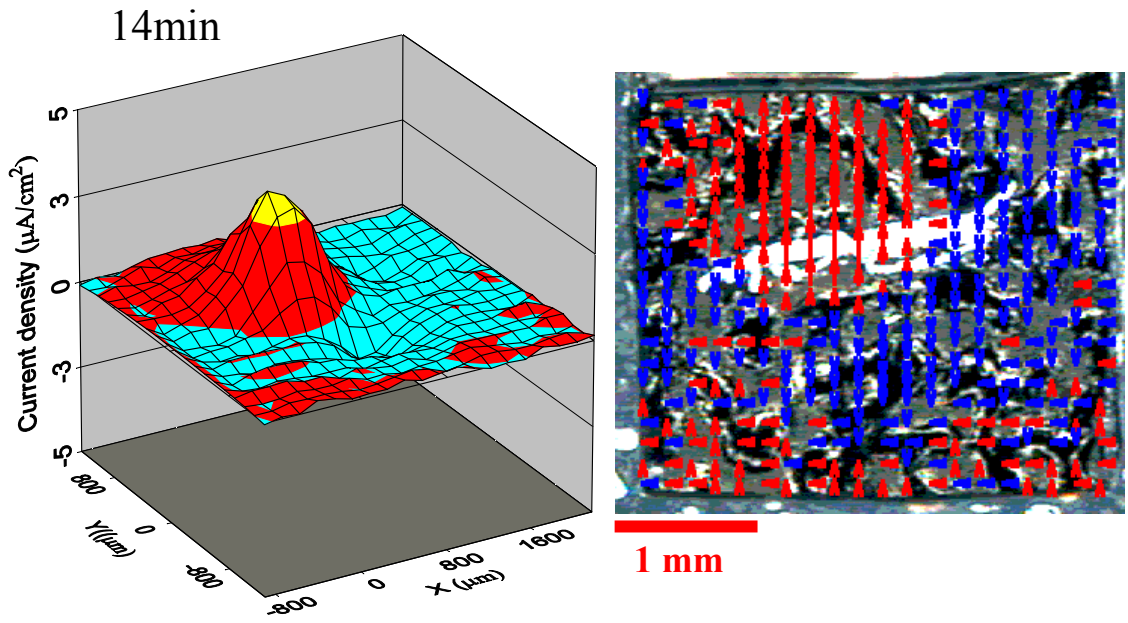

Figure 5.31 SVET current density distribution and current vectors superimposed on optical image of coated Zinc-55 % Aluminium hot dip coated steel electrochemically synthesised P3OP-*p*TS containing a "deep" artificial defect. Scan performed in DHS after 14 min.

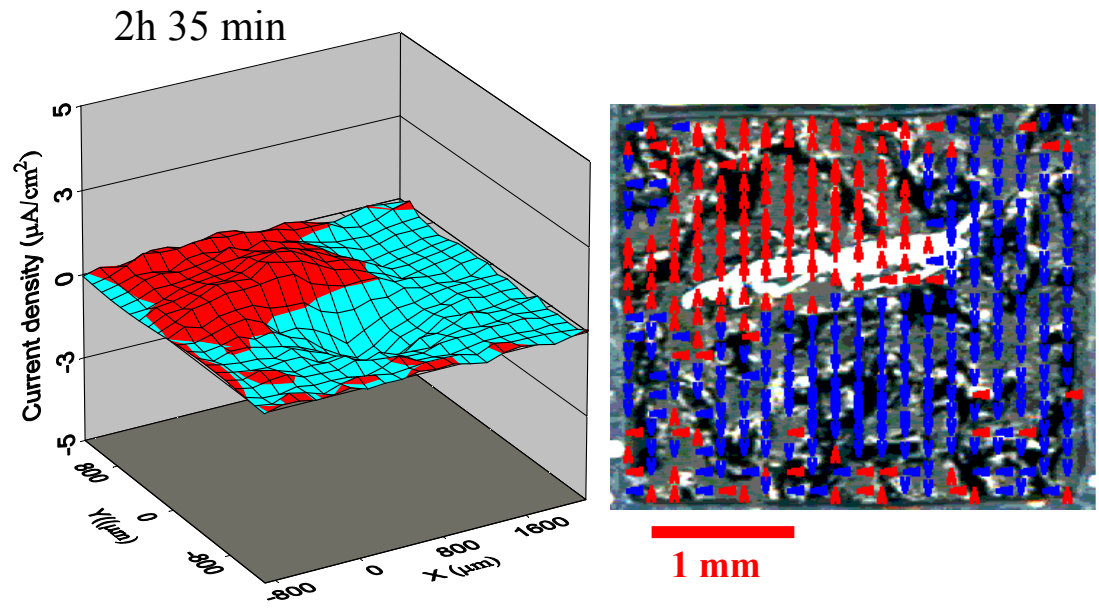

Figure 5.32 SVET current density distribution and current vectors superimposed on optical image of coated Zinc-55 % Aluminium hot dip coated steel electrochemically synthesised P3OP-*p*TS containing a "deep" artificial defect. Scan performed in DHS after 2 hours 35 min.

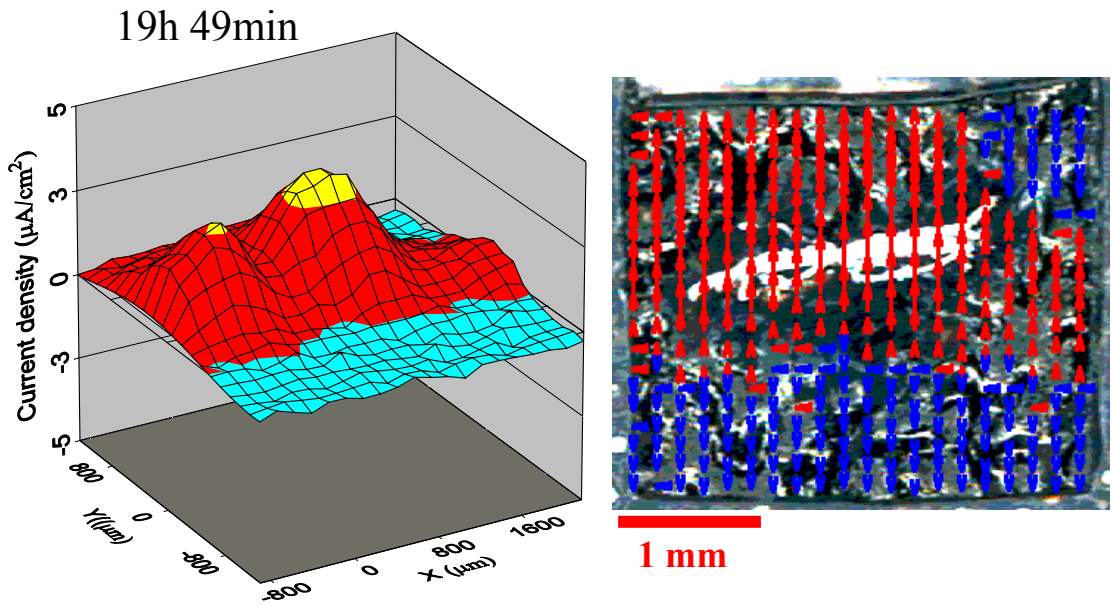

Figure 5.33 SVET current density distribution and current vectors superimposed on optical image of coated Zinc-55 % Aluminium hot dip coated steel electrochemically synthesised P3OP-*p*TS containing a "deep" artificial defect. Scan performed in DHS after 19 hours 49 min.

Despite poor barrier properties, as well as low electroactivity and conductivity of electrochemically synthesised P3OP-*p*TS, significant changes in the current flow were observed when used as a coating of Zinc-55 % aluminium galvanised steel. The cathodic protection observed on steel from the Zn/Al layer could not be seen with the current flow fully reversed when compared to uncoated sample containing a "deep" defect.

The observed current distribution correlates to observations on steel made by He *et al.* using P3OP-pTS/ClO_4 and the observations of PAn coatings on both steel and aluminium [105]. Despite oxidation currents observed over the defect for almost 20 hours, no corrosion product could be detected within the defect. This could possibly

be due to the overall low current flow not resulting in sufficient corrosion product to be observed visually.

5.4 Conclusions

SVET analysis of PAn coated AA2024-T3 showed strong interaction between PAn and AA2024-T3 for both "air" and "heat" dried PAn coatings. These strong interactions between PAn and AA2024-T3 causes rapid oxidation within the defect while the polymer coating undergoes both reduction and dedoping evidenced by the observed green to blue colour changes. Continued current flow throughout exposure and visual detection of corrosion product suggested that no protective oxide was formed under the set conditions.

In contrast to what was observed for these PAn coatings, only minimal activity was seen for AA2024-T3 coated with electrochemically synthesised P3OP-*p*Ts. However SVET suggested that the coating could afford the defect corrosion protection since no oxidation current was observed within the defect site. This coupled with the observation that no corrosion product was detected, even after prolonged exposure, correlates with previous studies. [105]

Reverse behaviour with oxidation of the defect area was observed for AA2024-T3 coated with chemically synthesised P3OP-ClO_4. The decreasing oxidation current within the defect was observed upon longer immersion accompanied by colour changes in the polymer coating near the defect area, suggesting that the polymer

induces oxidation of the metal within the defect area as the polymer itself undergoes reduction. The presence of a decreasing anodic current and the absence of any visible corrosion product could indicate that a protective oxide is formed within the defect.

Similar behaviour was observed for AA2024-T3 coated with chemically synthesised P3OP-*p*TS. A minor anodic current initially observed within the defect, accompanied by the overall coated polymer reduction, was evident from the polymer colour change, resulting in minimal current flow for prolonged exposure. The absence of any visually detectable corrosion product even after 68h immersion suggests that the coating affords AA2024-T3 significant corrosion protection within a coating defect.

Zinc-55 % Aluminium hot dip coated steel corrodes rapidly under observed conditions, and failed to form any passive or pseudo passive layer to limit metal dissolution. When a defect is introduced into the substrate, exposing the underlying steel, the Zn/Al layer cathodically protects the steel via sacrificial oxidation of the Zn/Al while the reduction reaction occurs within the defect.

Coating of electrochemically synthesised P3OP-*p*TS on Zinc-55 % Aluminium hot dip coated steel clearly affects the corrosion processes occurring. When a coating defect only exposed the Zn/Al surface, minimal current flow was observed. Reduction current within the defect and the absence of any visible corrosion product implies that electrochemically synthesised P3OP-*p*TS provided protection against corrosion for the zinc/aluminium surface underneath the coating as well as within a coating defect. When the underlying steel was exposed the electrochemically

synthesised P3OP-*p*TS alters the corrosion process otherwise observed, with oxidation observed within the defect only after prolonged exposure.

Chapter 6- Characterisation of PAn/co-poly Coating During the Corrosion Process

6.1 Introduction

The interaction between an ICP and the substrate is fundamental to the way ICP can act as a protective corrosion protection coating. Kinlen *et al* concluded polymer reduction from SRET measurement of PAn coating on an iron substrate exposed to a corrosive electrolyte [109] with the reaction between ICP and metal M at the interface expressed by (6.1-6.2). [110]

$$M + \frac{n}{m} ICP^{m+} + yH_2O \rightarrow M(OH)_y{}^{(n-y)+} + \frac{n}{m} ICP^0 + yH^+ \qquad (6.1)$$

$$\frac{m}{4} O_2 + \frac{m}{2} H_2O + ICP^0 \rightarrow ICP^{m+} + m(OH)^- \qquad (6.2)$$

Beard *et al.* while studying PAn-EB on mild steel using XPS noted during exposure under atmospheric conditions that the PAn-EB underwent reduction to form PAn-LB while causing oxidation of the mild steel. [111] Bernard *et al.* used Raman spectroscopy to study electrochemically formed PAn coating on iron in sulphate

electrolyte. Raman spectroscopy used to monitor changes in the coated substrate revealed deprotonation and reduction of the PAn coating with more reduced material observed closer to a coating defect. [112]

The galvanic coupling between ICP's and AA2024-T3 was studied by Cogan *et al* who used potentiodynamic polarisation and zero resistance amperiometry to study the interaction of PAn/co-poly doped with CSA and AA2024-T3 in 3.5 % NaCl. The mixed potential observed was dominated by the metal substrate leading to rapid reduction on the PAn. [75]

Tallman *et al.* used a PAn composite and proposed a mechanism of ICP corrosion protection in ferrous metals which involved anodic ennobling of the substrate, where an anodic OCP shift was observed for ICP coated metals. [74] Torresi *et al.* used a PAn-CSA/PMMA blend on Fe, Cu, Ni and Zn substrates and noted that polymer reduction was greater for coating on a less noble metal. [113] Using Raman spectroscopy Seegmiller *et al.* observed greater polymer reduction at close proximity to an artificial defect made in PAn acrylic blend coated on AA2024-T3. The presence of a defect was concluded to induce reduction of the polyaniline in the vicinity extending up to 30μm from the scribe. [114]

Nyguyen *et al.* reported a contradicting effect with respect to the finding noted above. Raman spectroscopy of polymer close to an artificial defect was reported to be in a more oxidised state than a point "far" from the defect. Clearly the nature of PAn system inclusive of the dopant type, oxidation state and nature of the corrosive

test environment will influence the processes occurring both in the ICP coating and the substrate.[115]

In this work the interaction between the ICP coating and the underlying substrate during exposure to DHS was studied using Raman spectroscopy. In-situ Raman spectroscopy mapping was used to detect changes in doping level, redox state and to detect polymer degradation for PAn coated AA2024-T3 exposed to DHS. The spatial resolution of the mapping resolves changes relative to areas of exposed metal. A major limitation of Raman spectroscopy is that the technique fails when the sample of interest fluoresces. In the case of P3OP, strong fluorescence was encountered at a 632 nm laser excitation line. For this reason this study has been limited to the PAn systems listed above.

6.2 Experimental

6.2.1 Raman Spectroscopy

Raman spectra was recorded using a JOBIN Yvon Horiba Raman Spectrometer model HR800 with an 800 mm optical path length employing a 10 mW Helium/Neon laser at 632.8 nm filtered by a neutral density filter to reduce the laser intensity and coupled with a charge-coupled detector (CCD). Raman spectra were resolved by a 300 line/mm grating giving a resolution of 1.5 cm^{-1}. The laser was focused using a microscopy lens at a 10x magnification or a special long-range lens providing 50x magnifications with sufficient clearance to allow recoding of spectra at the substrate

surface under electrolyte solution. The size of the laser focus point was approximately 2μm in diameter. To ensure data reproducibility all experiments were performed in triplicate with typical results presented.

6.2.2 Sample Preparation

Raman spectroscopy of PAn/co-poly was recorded in-situ during exposure to DHS using an electrochemical cell fabricated by attaching a 4 mm tall polyethylene cylinder, with an inner diameter of 8mm, onto a 2 x 2 cm substrate. The cell formed held a volume of approximately 1 mL and had an exposed area of approximately 0.5 cm^2. The cylinder-substrate attachment was made using commercial silicon sealant that was room temperature cured in a desiccator for minimum of 24hours prior to immersion.

Raman spectra of PAn/co-poly as a function of time and distance to a coating defect were recorded in-situ during exposure to DHS. Prior to immersion an artificial defect was introduced in the PAn/co-poly coating using a surgical scalpel. The defect measured 2-4 mm in length with a width of approximately 50 μm. Raman spectra were recorded at multiple points over the exposed area by use of an x-y moving stage. Unless noted, experiments were performed at ambient conditions.

The intensity of the observed Raman bands were analysed by dividing spectra into subcomponents by peak deconvolution using Gaussian peaks. Changes in the Raman spectra were analysed by comparing the relative Raman intensity between suitable bands by first normalising each individual band with respect to the sum of the bands

being compared. This method provided relative information about changes in spectra but can not be used quantitatively. [116]

6.3 Results and Discussion

6.3.1 In-situ Raman Spectroscopy of PAn/co-poly Coated Pt

Raman spectra of a dry PAn/co-poly coating approximately 5μm thick airbrushed on a Pt electrode displayed characteristic spectra for primarily doped polyaniline emeraldine salt (Figure 6.1) [117], [118, 119] with large double peak observed at 1320 cm^{-1} and 1338 cm^{-1} commonly associated with the stretching mode of the radical cation (–C-$N^{+\bullet}$-). [117] The band observed at 1169 cm^{-1} corresponds to two peaks not clearly separated; the C-H stretch of the quinoid ring 1163 cm^{-1} and the C-H stretch of the benzoid ring band observed at 1178 cm^{-1}. [119] A band observed at 1590cm^{-1} can be ascribed to the stretching mode of the C=C bond in the quinoid ring with a small shoulder at 1603 cm^{-1} assigned to the stretching mode of the benzoid ring (C-C bond) observed at 1610 cm^{-1}. [120, 121]

Raman spectra of PAn/co-poly coated on Pt observed as a function of immersion time in-situ in DHS (Figure 6.1) show a reduction of the 1320 cm^{-1}/1338 cm^{-1} doublet without any shift of the 1169 cm^{-1} band or shift in the ratio of the 1590 cm^{-1} /1610 cm^{-1} (C=C/C-C) indicating that the polymer remained in the same redox state while the material underwent dedoping. After 24 hours immersion Raman spectra for PAn/co-poly under N_2 and under ambient conditions exhibited almost no radical

cation doublet peak and an increase in the C=N band intensity observed at 1480 cm^{-1}, Figure 6.2. Significantly, no reduction was observed as a result of the galvanic coupling even though an OCP of 0.2 V was observed during immersion.

In this instance any reduction processes occurring were concluded to be minor when compared with the more rapid dedoping process that underlies these conditions. The progress of the dedoping was noted to occur at the same rate and to the same degree under N_2 atmosphere as under ambient conditions with no significant difference observed between the two conditions at the conclusion of the experiment after 72 hours.

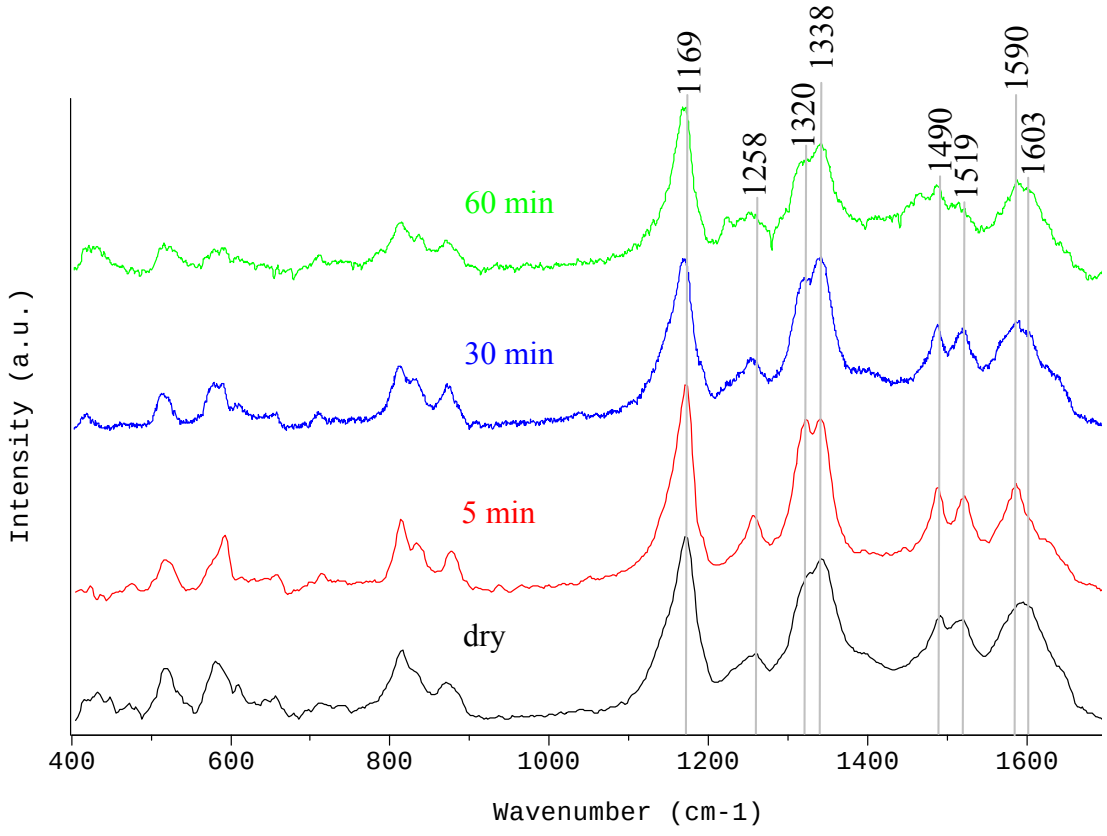

Figure 6.1 Raman spectroscopy of PAn/co-poly coated Pt. Dry and in-situ after immersion in DHS with an OCP of 220 mV.

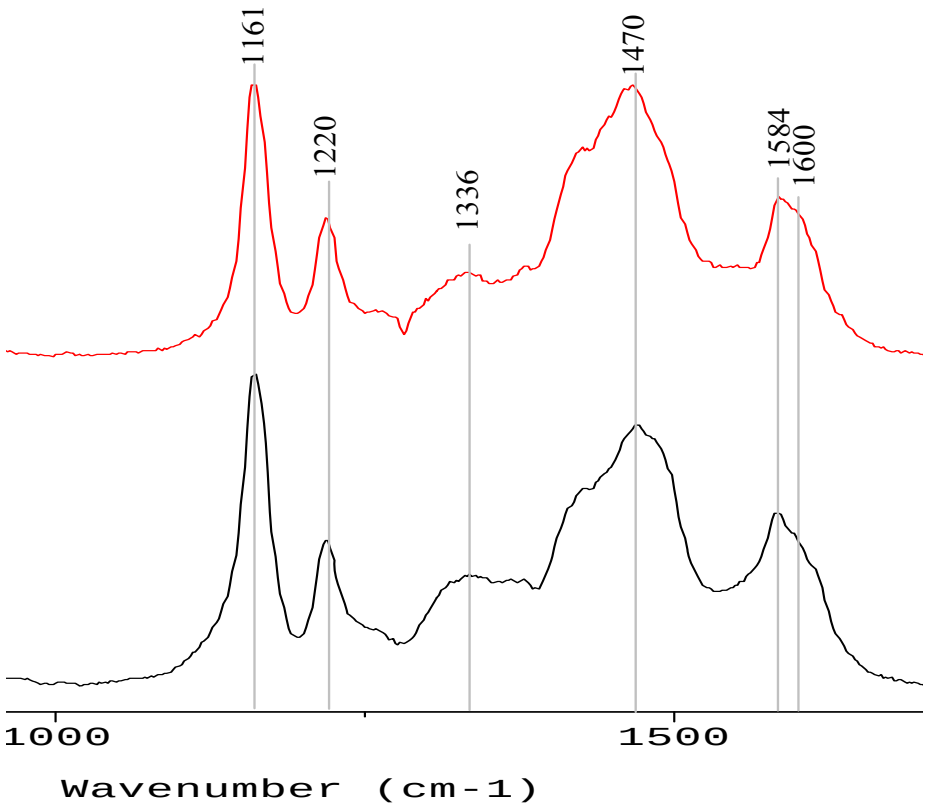

Figure 6.2 Raman spectroscopy of PAn/co-poly coated Pt immersed in DHS at OCP for 24 hours under N_2 (top) and ambient conditions (bottom).

6.3.2 In-situ Raman Spectroscopy of PAn/co-poly Coated Pt Containing Defect

Raman spectra of PAn/co-poly coated on Pt exposed to DHS were studied in-situ as a function as distance relative to a coating defect. PAn/co-poly coated onto Pt, approximately 5 μm thick, was scribed using a surgical scalpel. Raman spectra were recorded using 25 points over a 50 μm line situated over the edge of the defected PAn/co-poly coating giving a resolution of 2 μm/step. The line scan was repeated every two hours for a total of 12 hours.

Changes in PAn/co-poly doping level were evaluated by comparing the relative intensity of the C-C band observed at 1610 cm^{-1} and the C=N band observed at 1460 cm^{-1}. Changes to the PAn/co-poly oxidation state were evaluated using the relative intensity of the C-C band and C=C band observed at 1610 cm^{-1} and 1590 cm^{-1} respectively. Changes in doping level were noted to be relative to immersion time and were similar for samples without a coating defect. No change in the relative intensity ratio of bands at 1610 cm^{-1}/1590 cm^{-1} could be observed as a function of distance to the coating defect. (Figure 6.3)

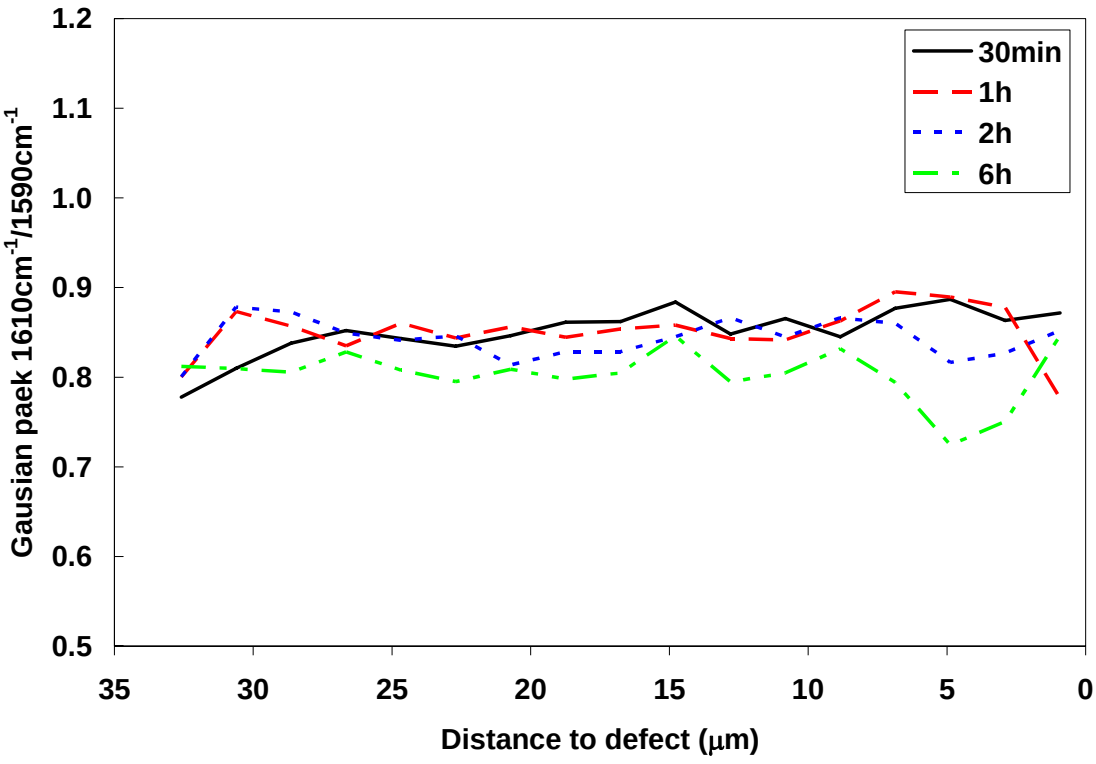

Figure 6.3 Relative intensity ratio of bands at 1610 cm^{-1}/1590 cm^{-1} as a function of distance to a coating defect.

6.3.3 In-situ Raman Spectroscopy of PAn/co-poly Coated AA2024-T3

Raman spectra of PAn/co-poly coated AA2024-T3 in DHS observed after 40 min immersion revealed a rapid decrease in the intensity of radical cation double band observed at 1314 cm^{-1}/1333 cm^{-1} accompanied by an increase of C=N band at 1460 cm^{-1}. Also, the band at 1168 cm^{-1} shifted to lower wave numbers, corresponding to reduced benzoic units. (Figure 6.4) These changes indicate that the polymer undergoes some reduction as well as dedoping while the observed colour change, from green to dark green/blue, would suggest formation of EB as the major process.

After 13h immersion small areas or spots of a notably lighter green coloured polymer was observed while the majority of the surface remained dark blue/green. Raman spectroscopy at these regions confirmed the presence of a slightly more reduced state, Figure 6.4.

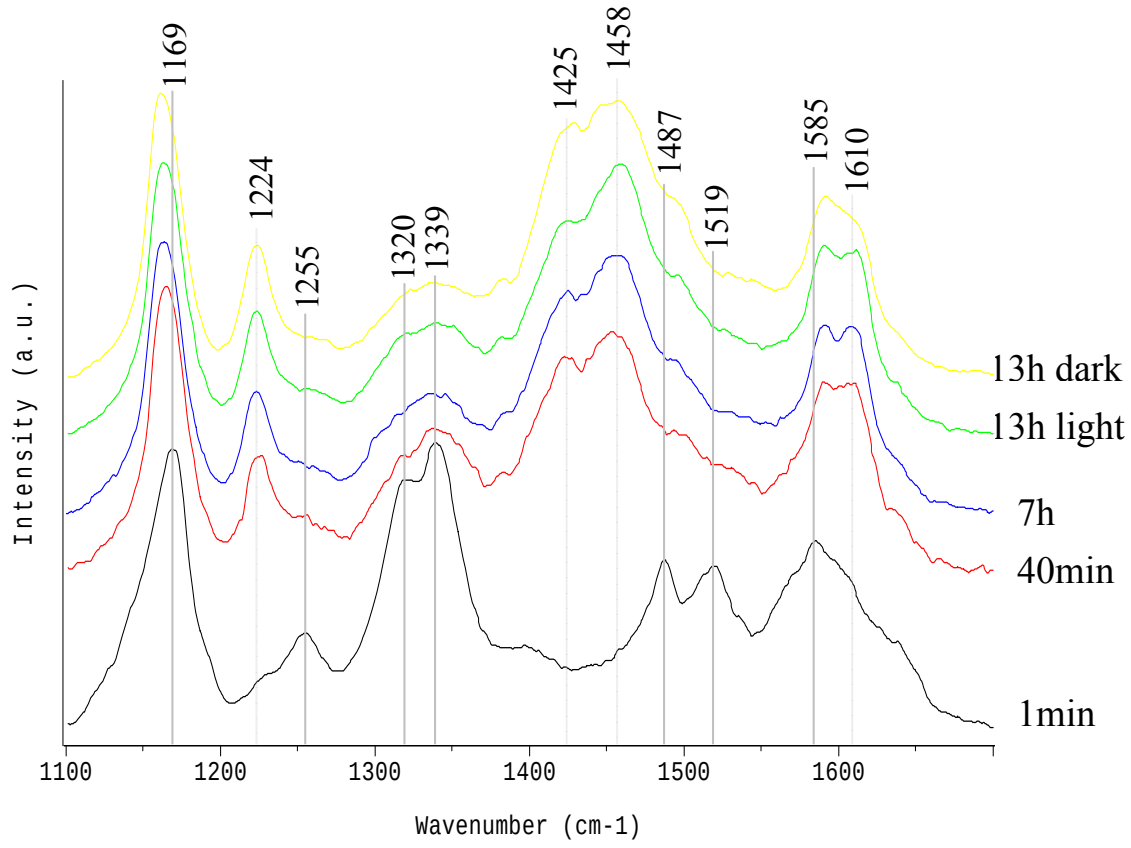

Figure 6.4 Raman spectra of PAn/co-poly on AA2024-T3 as a function of immersion time in DHS performed under ambient conditions

6.3.4 In-situ Raman Spectroscopy of PAn/co-poly Coated AA2024-T3 Containing Defect

6.3.4.1 Ambient Conditions

Changes in the PAn/co-poly coating on AA2024-T3 as a function of proximity to a defect was investigated in-situ under ambient atmosphere by collecting a grid of Raman spectra at points over a selected area containing the defect. Raman scans were performed using x10 magnification optical microscope over an area of 45 µm x

450 µm using 3 x 30 points at a resolution of 15 µm. The optical micrograph with the scan area and points superimposed is shown in Figure 6.5.

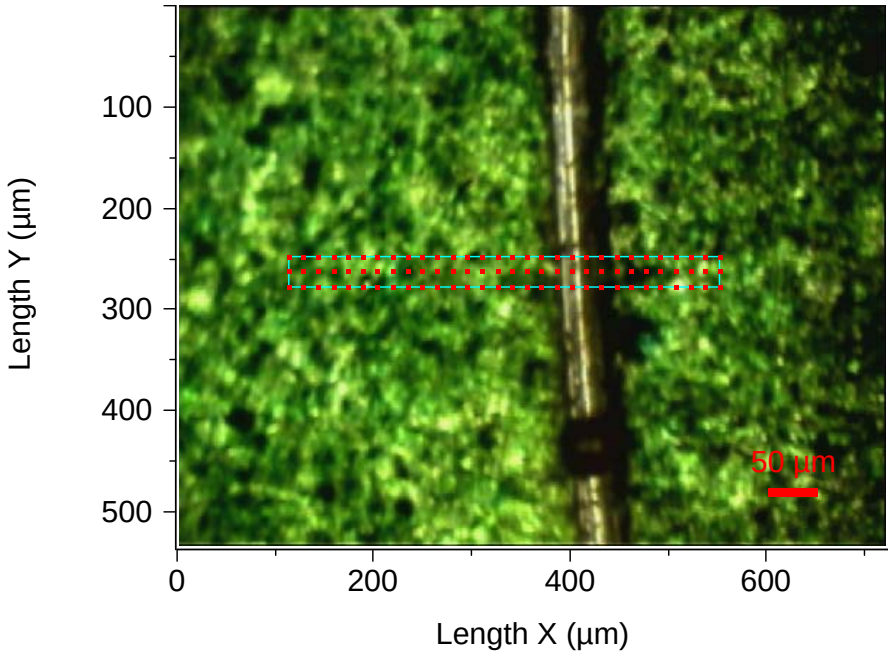

Figure 6.5 Optical image of scribed PAn/co-polymer coating on AA2024-T3 in DHS after 15 min immersion using x10 magnification with area of Raman mapping are superimposed.

Three points were extracted from the Raman grid recorded after 10 min immersion, corresponding to points; 250 µm from the defect, right at the edge of the defect (±2 µm) and from within the scribe. (Figure 6.6) From Raman spectra of the scribed area, it was evident that some residual polymer remained within the defect, an observation that was typical of all defected coatings in this study.

Spectra recorded after 15 min immersion showed a decrease in the radical cation double band at 1314 cm^{-1}/1333 cm^{-1}, an increase in the C=N band intensity at 1460 cm^{-1} as well as an increase in the C-C band at 1610 cm^{-1}, indicating polymer reduction as well as dedoping. (Figure 6.6) Polymer reduction can also be observed

to be more complete for polymer within the scribe showed by higher C-C/ C=C ratio (1610 cm^{-1}/1590 cm^{-1}) and a lesser band observed at 1314cm^{-1}/1337cm^{-1}.

Subsequent maps plotted as the ratio of C-C/ C=C band intensities (Figure 6.7) show that a maximum C-C/C=C ratio is noted within the first observed map, suggesting that after initial reduction the PAn/co-poly undergoes re oxidation. After 6h immersion a similar C-C/C=C ratio was observed in and close to the defect as for bulk coating with spectra corresponding to dedoped partially oxidised EB/LB.

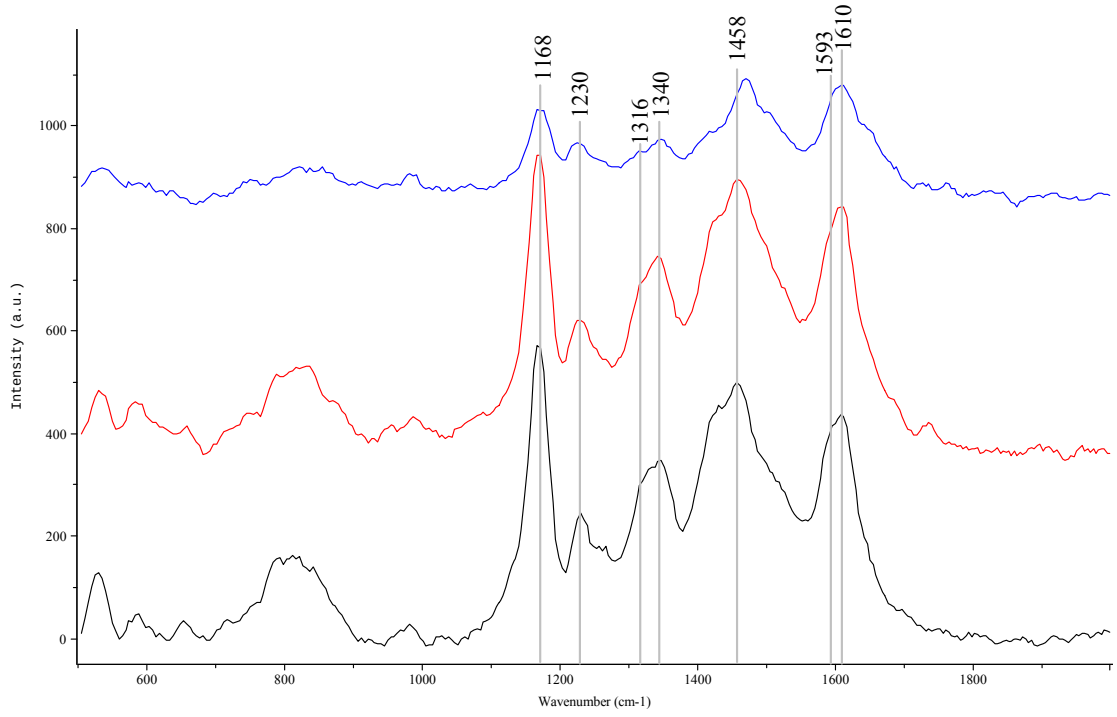

Figure 6.6 In-situ Raman spectroscopy of PAn/co-poly coated AA2024-T3 in DHS under ambient conditions with coating containing artificial defect. Spectra recorded after 10 min immersion. Black: 250 µm distance from defect, Red: At the very edge of the coating, Blue: Point within the defect. Immersion time: 10 min.

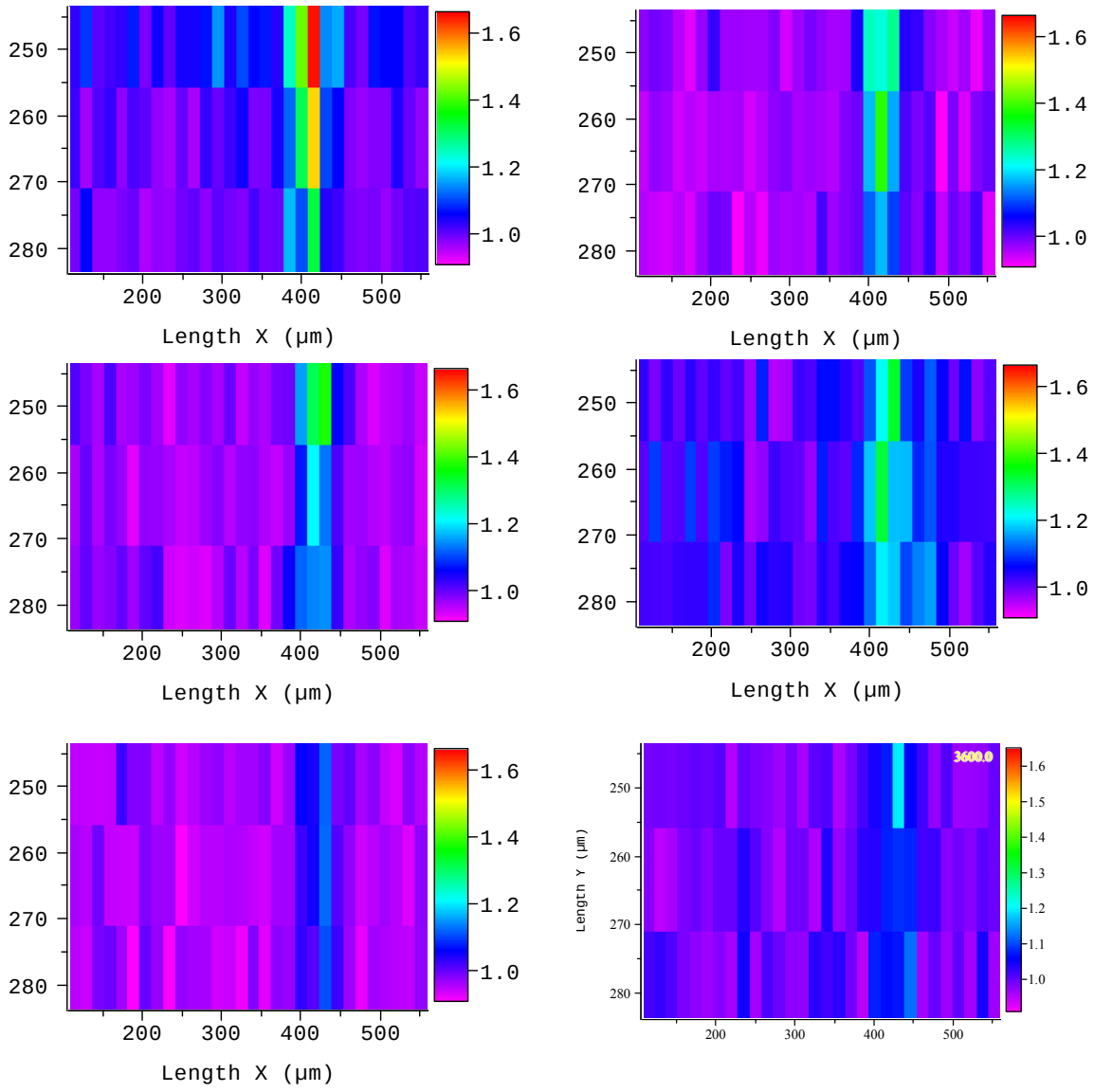

Figure 6.7 In-situ Raman map of the peak area ratio of 1610 cm^{-1}/1590 cm^{-1} of a scribed PAn/co-poly on AA2024-T3 immersed in DHS. Peak area was obtained with Gaussian peak fitting after intensity was normalised using the sum of the two peaks. TL: 15 min, TR: 1 hour, ML: 1 hour 40 min, MR: 5 hours 25 min, BL: 6 hours, BR: 7 hours 30 min

6.3.4.2 N_2 Atmosphere

Raman mapping of PAn/co-poly coated AA2024-T3 was performed without the presence of oxygen by first purging the electrolyte with N_2 prior to immersion. Once the electrolyte had been added the cell was sealed using a microscopy cover glass

slide and silicon adhesive. Changes in doping level and oxidation state were monitored overtime with respect to the defect by recording Raman spectra at selected points shown overlayed on optical micrograph shown in Figure 6.8.

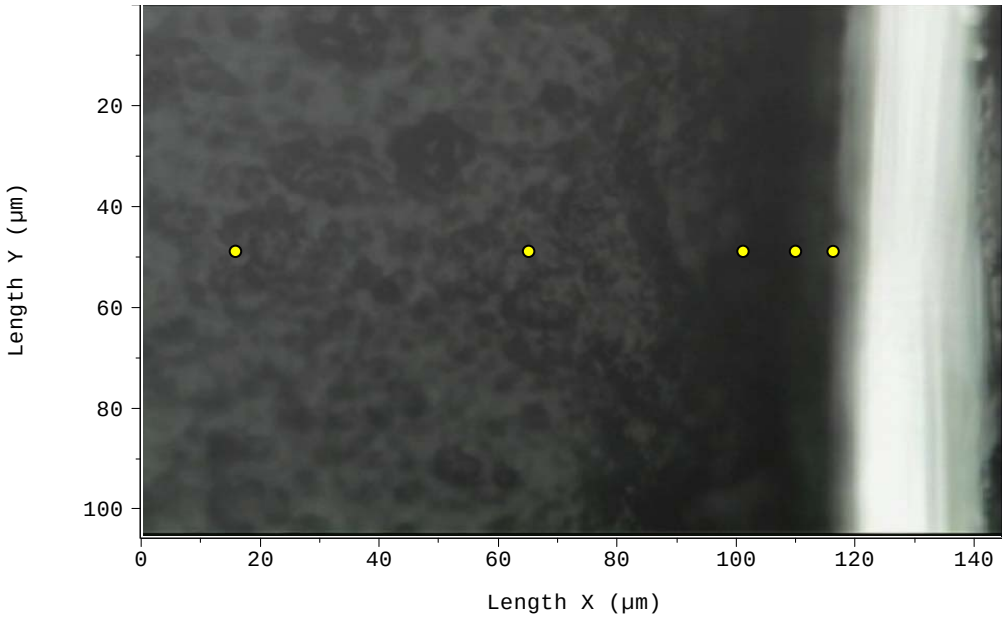

Figure 6.8 Optical image of scribed PAn/co-poly coating on AA2024-T3 in DHS prior to immersion using x50 magnification with superimposed points where Raman spectra were recorded.

Raman spectroscopy of PAn/co-poly coated AA2024-T3 prior to immersion displayed no effect on spectra as a function of the distance relative to the defect. (Figure 6.9)

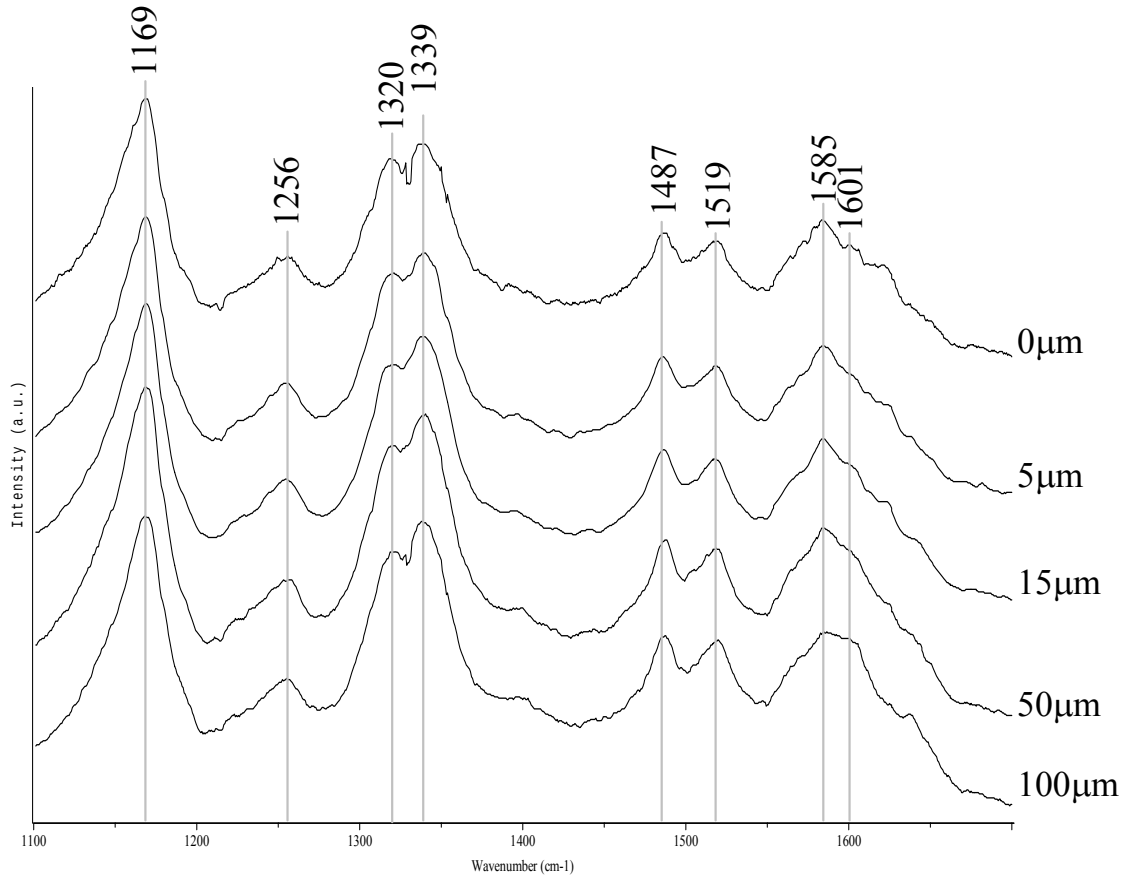

Figure 6.9 In-situ Raman spectroscopy of PAn/co-poly coated AA2024-T3 relative to an artificial defect recorded prior to immersion.

Immediately upon immersion of the substrate rapid $H_2(g)$ formation was observed at the exposed metal. Raman spectra performed after 15 min immersion at multiple points, Figure 6.10, showed that the polymer had undergone reduction as evidenced by an increase in the 1610 cm^{-1}/1590 cm^{-1} peak ratio. Reduction was noted to progress from the defect area, with a higher C-C/C=C (1610 cm^{-1}/ 1590 cm^{-1}) peak ratio and no C=N band (1460 cm^{-1}) observed within 50 μm from the scribe. A point located 100 μm from the defect also displayed reduction although a significant C=N band could also be observed, indicating dedoping as the major process with only

minor reduction. After 1 hour immersion the point 100 μm from the defect also showed significantly reduced C=N band. (Figure 6.11)

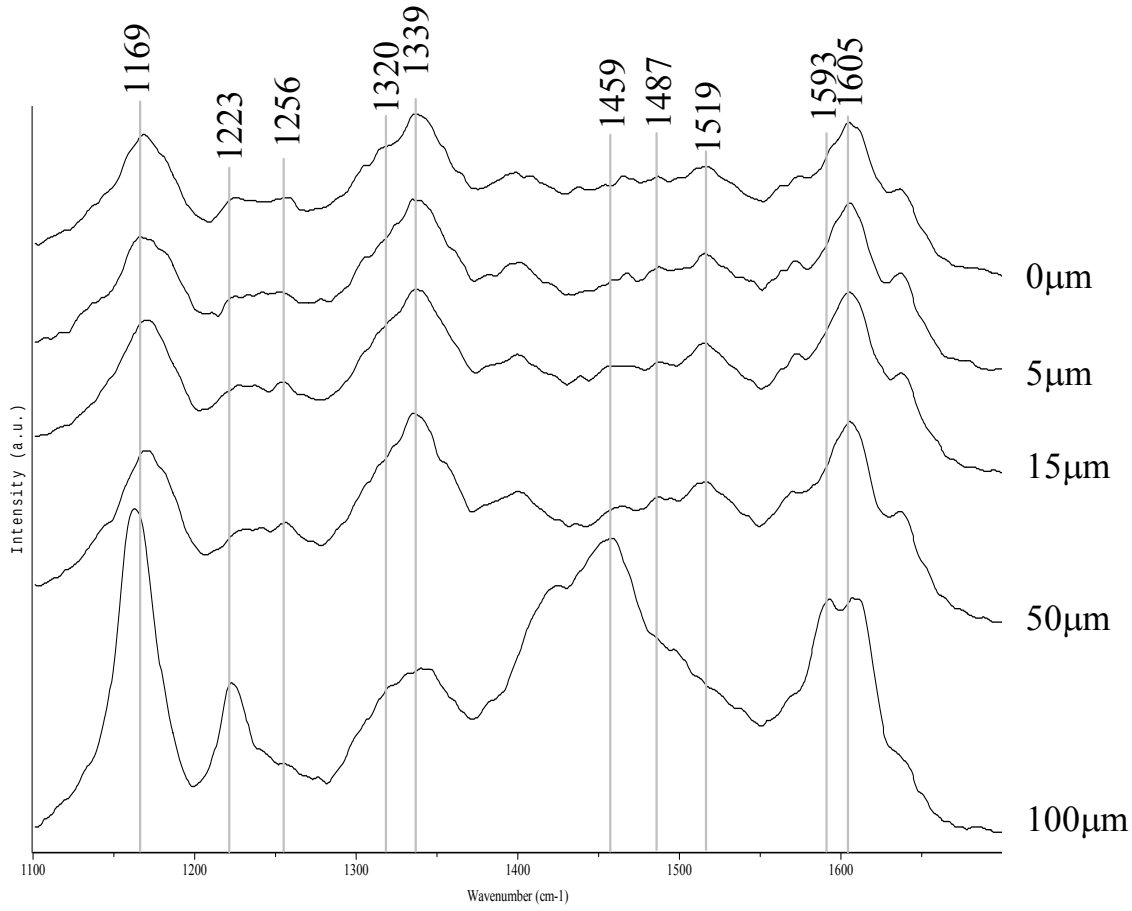

Figure 6.10 In-situ Raman spectroscopy of PAn/co-poly coated AA2024-T3 in DHS under N_2 atmosphere with coating containing artificial defect. Spectra recorded after 15 min immersion.

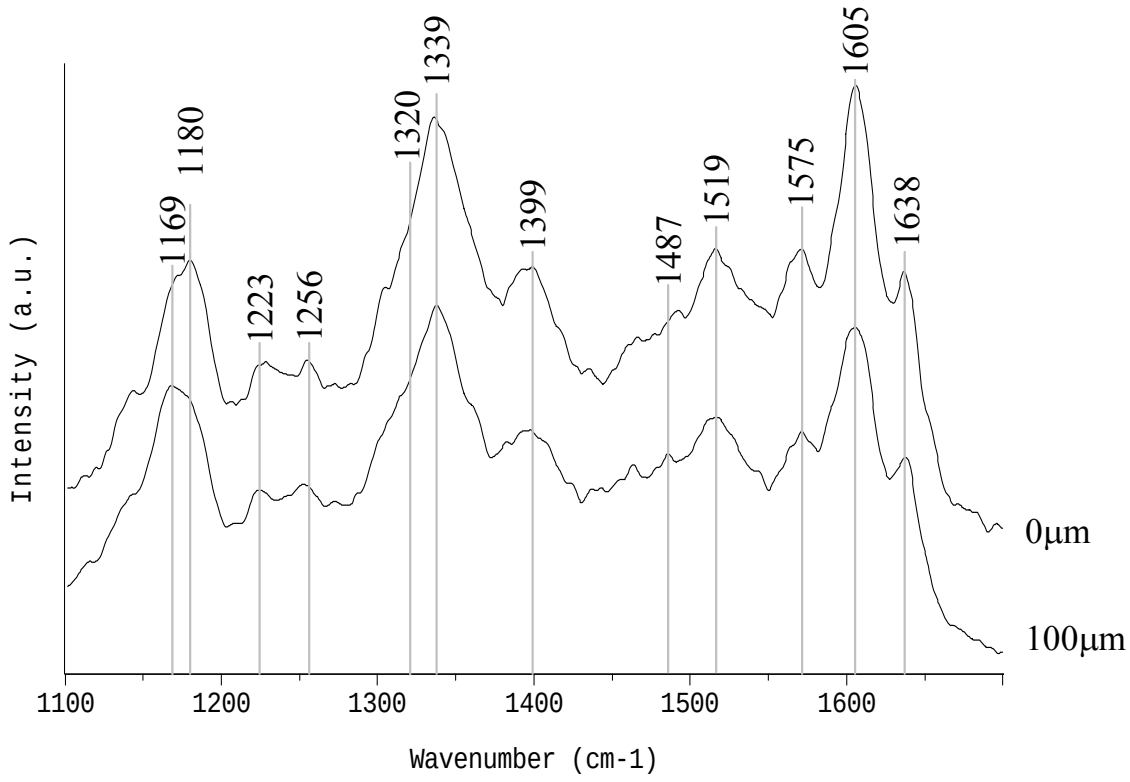

Figure 6.11 In-situ Raman spectroscopy of PAn/co-poly coated AA2024-T3 in DHS under N_2 atmosphere with coating containing artificial defect. Spectra recorded after 60 min immersion.

After 1 hour 40 min the electrolyte was exposed to ambient conditions by removing the glass slide. After 2 hours 10 min total immersion and exposure to air for 30 min, the point furthest from the scribe has undergone reoxidation evident by the increase in band corresponding to C=N at 1460 cm^{-1} and a decrease in the C-C/C=C ratio. After 3 hours 30 min of total exposure with the last 1 hour 50 min exposed to air, the point 50 μm from the defect also displayed sign of reoxidation. (Figure 6.12) Eventually all points of the polymer film undergo oxidation as seen in Figure 6.13, recorded after 7 hours total immersion where 5 hours 20 were min under ambient conditions. These observations strongly suggest that oxygen is involved in the reoxidation of the PAn/co-polymer. The ability to regenerate partially oxidised PAn has been observed by others. [104] Also, as oxygen dissolved in to the electrolyte,

polymer further away from the defect is preferentially oxidised. Raman spectra of regenerated PAn/co-poly display no increase in the 1314 cm^{-1}/1333 cm^{-1} double peak indicating that under these conditions O_2 can not regenerate the conductive PAn/co-poly film, instead producing the insulating form of EB. From this it can also be suggested that EB formation observed under ambient conditions forms via reduced polymer rather than direct dedoping.

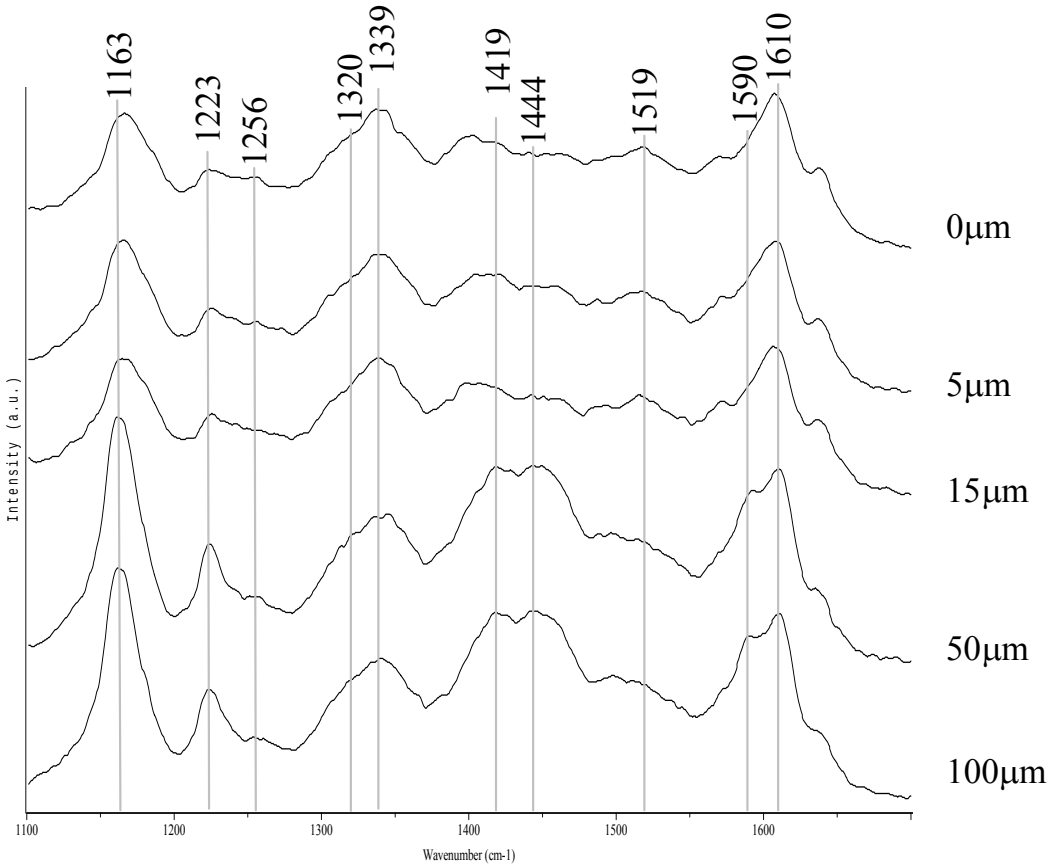

Figure 6.12 In-situ Raman spectroscopy of PAn coated AA2024-T3 in DHS after 1 hour 50 minute exposure to ambient atmosphere with coating containing artificial defect. Spectra recorded after total of 3 hours 30 min immersion.

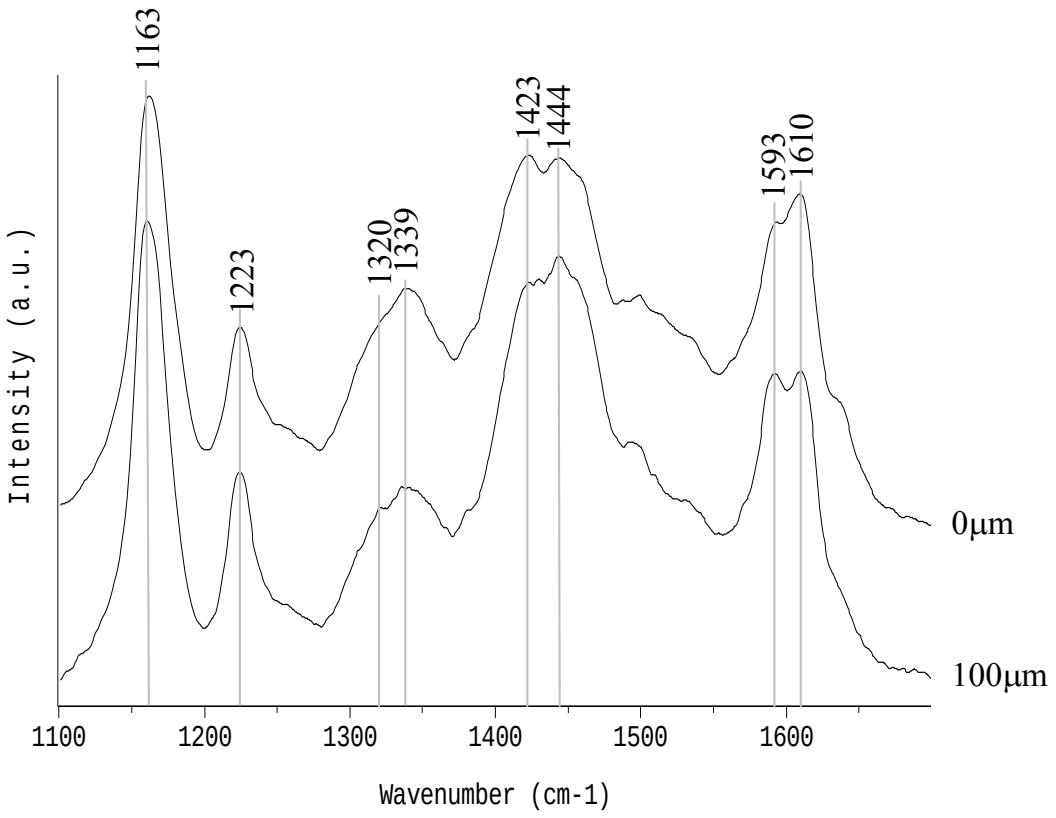

Figure 6.13 In-situ Raman spectroscopy of PAn/co-poly coated AA2024-T3 in DHS after 5 hours 20 minute exposure to ambient atmosphere with coating containing artificial defect. Spectra recorded after total of 7 hours immersion.

6.4 Conclusions

Raman spectroscopy was used to characterise PAn/co-poly as well as monitor changes in the PAn/co-poly coating on Pt and AA2024-T3 during exposure to DHS in the order to study the interaction of PAn/cop-poly and the underlying metal.

Dry pristine PAn/co-poly displayed Raman spectra typical of primary doped PAn-ES. PAn/co-poly coated on Pt was not stable as ES under the conditions investigated

and converted to form a less conductive form upon immersion in DHS. PAn/co-poly coated on Pt converted towards EB without any noticeable change in the redox state. PAn conversion appears to be independent of proximity to an artificial coating defect exposing underlying Pt.

PAn/co-poly coated on AA2024-T3 was not stable as ES under the conditions investigated and converted to form a less conductive form upon immersion in DHS. PAn/co-poly coated on AA2024-T3 converted to a slightly more reduced form of EB/LB showing interaction between the PAn/co-poly and the underlying substrate. Reaction was observed to be proportional to the distance from an artificial defect, initially yielding a slightly more reduced material in close proximity of a coating defect, suggesting an interaction between the PAn/co-poly other than a barrier effect.

Exclusion of O_2 from the reaction resulted in more pronounced reduction reaction towards LB. Experiments performed under an initial N_2 atmosphere and later exposed to air showed that the reduction proceeded more readily in close proximity to a defect. EB was reoxidised by introduction of O_2 to the electrolyte. The reoxidation step occurred more readily at greater distance from the artificial defect. Under the conditions investigated, reoxidation of reduced polymer by O_2 formed the partially oxidised non- conductive form of EB.

Chapter 7- Conclusions

A range of conducting polymer materials were synthesised to yield solution processable conducting polymers that could be applied as a coating to an active metal. Corrosion inhibition of ICP coated AA2024-T3 and Zinc-55 % Aluminium hot dip coated steel (ZA) was then investigated using electrochemical techniques. Major findings are summarised below.

7.1 Material Synthesis, Polymer and Coating Characterisation

Polyaniline/Co(polyButyl Acrylate –Vinyl acetate)/composite doped with HCSA was successfully prepared. The material was soluble in DCM in excess of 5 % and was successfully applied as coating to AA2024-T3 by air brushing. The material possessed a relatively high conductivity of 6 S/cm and was electroactive. The material could also be heat treated to 110 °C without any significant change to the electrochemical properties.

Soluble conductive P3OP-*p*TS was not successfully prepared electrochemically via conditions investigated. The soluble fraction was non conductive with maximum conductivity of 10^{-6} S/cm and possessed UV-vis spectra indicative of an undoped polymer. This fraction was soluble in DCM in excess of 5 % and was successfully applied as coating to AA2024-T3 or ZA by air brushing. Low conductivity (0.1 S/cm) P3OP-*p*TS obtained by electrochemical deposition was not soluble in any of the solvents investigated.

A soluble conductive (5 S/cm) P3OP-ClO_4 was prepared using electrochemical deposition to form a product that was soluble in DCM or THF and applied as a polymer coating. Material that was formed as a soluble fraction by this method possessed a lower conductivity (0.5 S/cm). Both soluble fractions could be applied as coatings on AA2024-T3 and ZA by airbrushing.

Conductive and highly soluble P3OP-ClO_4 was also obtained at high yields using oxidative chemical polymerisation by $Cu(ClO_4)$ in AN. The material showed poor film formation, producing a brittle coating containing microscopic cracks on AA2024-T3 by evaporative casting from DCM.

Conductive and highly soluble P3OP-*p*TS was obtained at high yields using chemical polymerisation by $Fe(pTS)_3$ in MeOH. This material was used to form continuos uniform coatings on AA2024-T3 by evaporative casting from DCM.

7.2 Electrochemical Characterisation of ICP Coated AA2024-T3

Electrochemical techniques were used to investigate corrosion inhibition afforded AA2024-T3 by ICP coatings. Coatings studied were:

- Polyaniline/poly(butyl acrylate-vinyl acetate) copolymer composite (PAn/co-polymer) doped with (1s)-(+)-10-Camphorsulfonic acid (HCSA) "air dried" or "heat treated".
- Soluble fraction of electrochemically synthesised P3OP doped with $p\text{TS}^-$, synthesised in 80/20 CCl_4/DCM and DCM.
- Soluble and deposited fraction of electrochemically synthesised P3OP doped with $-ClO_4$ synthesised in DCM.
- Soluble fraction of electrochemically synthesised P3OP doped with –pTS synthesised in DCM.
- Chemically synthesised P3OP doped with ClO_4.
- Chemically synthesised P3OP doped with $p\text{TS}^-$.

Potentiodynamic polarisation, OCP and EIS were performed with results presented. Samples coated with "air dried" PAn/co-poly displayed an initial ennoblement with rapid formation of a more resistive coating restricting the corrosion reaction. This was followed by a penetrative wetting of the coating at longer immersion times eventually leading to an increasing corrosion rate. Similar behaviour was observed for "heat dried" PAn/co-poly with the only major difference being a higher R_{ct} and

Y_{dl} observed for heat treated sample, attributed to slower rate of water penetration into the polymer film.

Electrochemically synthesised P3OP-*p*TS "Ashraf" initially showed minor ennobling and reduced I_{corr} while EIS suggested any longer exposure to be mostly analogous to a poor barrier coating. The electrical conductivity of this material was observed to be in the insulating range, further supporting a mechanism dominated by an inactive physical barrier. A simple poor barrier protection was also observed for electrochemically synthesised "P3OP-*p*TS solution". Material used exhibited both low conductivity as well as poor mechanical properties.

Electrochemically synthesised P3OP-ClO_4 of two fractions, "deposited" and the "solution" fraction, as well as chemically synthesised P3OP-ClO_4^- and P3OP-*p*TS^- displayed anodic shift of the OCP and increased R_{ct} of the metal interface suggesting the formation of a protective oxide layer. Though different degrees of protection were observed for the different coatings, a general mechanism of corrosion inhibition to include and describe all observations made based on corrosion protection through anodic inhibition was suggested.

From the observed shift in the OCP, a mechanism of ICP coating-metal interaction suggests a galvanic coupling between the metal and the polymer coating. Such coupling would arguably promote metal oxidation while the polymer coating undergoes reduction. The polymer reduction would be accompanied with release and expulsion of dopant anion.

Any initial inductive process observed using EIS could hence be explained by dopant absorption to the metal surface. Increasing R_{ct} indicated the build up of a protective surface formed as a result metal oxidation and dopant absorption.

7.3 Characterisation of Local Corrosion Behaviour for ICP Coatings

Local corrosion behaviour of a defect was investigated for ICP coatings on AA2024-T3 and ZA using SVET.

PAn/co-poly coated AA2024-T3 exhibited a strong interaction between PAn/co-poly and AA2024-T3 for both “air” and “heat” dried PAn coatings. This resulted in a strong anodic current within a coating defect while the polymer coating displayed cathodic current. This current distribution pattern continued throughout exposure and visual detection of corrosion product suggested that no protective oxide was formed under the set conditions.

In situ Raman spectroscopy mapping with and without the presence of O_2 in the electrolyte suggest that the polymer undergoes reduction to LB by galvanic coupling with the metal surface and that LB can be reoxidised by the presence of O_2 in the electrolyte. The reoxidation step occurred more readily at greater distance from the artificial defect. Under the conditions investigated, reoxidation of reduced polymer by O_2 form the partially oxidised non- conductive form of EB.

Low activity was observed for AA2024-T3 coated with electrochemically synthesised P3OP-*p*TS (10^{-8} S/cm). No oxidation current was observed within the defect site. No corrosion product was detected, even after prolonged exposure, suggesting that electrochemically synthesised P3OP-*p*TS provided corrosion inhibition to AA2024-T3 and did not just perform as a simple physical barrier coating.

A coating defect area introduced onto AA2024-T3 coated with chemically synthesised P3OP-ClO_4 show anodic behaviour, with cathodic reaction occurring on the coated area. The oxidation current within the defect decreased over time. Prolonged immersion was accompanied by colour changes within the polymer coating near the defect area. This suggests that the polymer induced oxidation of the metal within the defect area as the polymer itself undergoes reduction. The presence of the decreasing anodic current and the absence of any visible corrosion product could indicate that a protective oxide is formed within the defect.

Defect area of AA2024-T3 coated with chemically synthesised P3OP-*p*TS displayed a low anodic current, with cathodic current observable over the coated area. The anodic current within the defect decreased over time. A colour change in the polymer coating near the defect towards a lighter green colour was indicative of polymer reduction. The presence of a decreasing anodic current and the absence of any visible corrosion product even after 68 hours immersion suggest that the coating affords AA2024-T3 significant corrosion protection within a coating defect.

Observations of conductive P3OP on AA2024-T3 suggested corrosion inhibition within the defect involving the formation of a protective surface induced by the polymer coating as a result of the polymer undergoing reduction. Material possessing higher conductivity displayed better corrosion inhibition that could arise from a greater redox charge, hence induce the formation of a thicker more protective oxide.

Bare ZA corrodes rapidly under the test conditions with temporary anodic and cathodic sites resulting in metal dissolution. Unchanged corrosion current and rapid formation of corrosion product suggested that oxidation product formed doesn't limit metal dissolution.

When a defect was introduced into the substrate, exposing the underlying steel, the Zn/Al layer cathodically protects the steel via sacrificial oxidation of the Zn/Al while the reduction reaction occurs within the defect.

Electrochemically synthesised P3OP-*p*TS on ZA effectively limited the current flow within a coating defect exposing the Zn/Al surface. The defect area presented reduction with oxidation dispersed over the coating. The reduction current within the defect and the absence of any visible corrosion product suggested that electrochemically synthesised P3OP-*p*TS provided effective protection against corrosion of ZA within a coating defect. When the underlying steel was exposed, electrochemically synthesised P3OP- *p*TS alters the corrosion process otherwise observed, with oxidation observed within the defect only after prolonged exposure.

Results presented have demonstrated the concept of corrosion inhibition of AA2024-T3 and for ZA using ICP, with the mechanism of protection through anodic inhibition suggested. Results have also demonstrated the concept of protection afforded defect areas not covered by the coating.

Future work should aim to improve mechanical and film forming properties of the polymer and include long term corrosion studies using insulating top coats in order to evaluate these materials for commercial use.

Chapter 8- References

1. D. A. Jones, *Principles of Prevention of Corrosion, Second Edition*. 1995.
2. Y. P. Virmani, *Corrosion Cost and Preventive Strategies in the United States, Report by CC Technologies Laboratories, Inc. to Federal Highway Administration (FHWA), Office of Infrastructure Research and Development, Report FHWA-RD-01-156*. 2001.
3. D. W. Hoeppner, Chandrasekaran, V., Taylor, A., Proceedings of the 20th Symposium of the International Committee on Aeronautical Fatigue, ICAF, 1999: p. 253.
4. R. L. Twite and G. P. Bierwagen, Progress in Organic Coatings, 1998. **33**(2): p. 91.
5. D. W. DeBerry, Journal of the Electrochemical Society, 1985. **132**(5): p. 1022.
6. J. R. Davis, *Corrosion: Understanding the Basics*. 2000.
7. J. E. Hatch, *Aluminum: properties and physical metallurgy*. 1984, Metals Park, Ohio: American Society for Metals.
8. M. W. Kendig, A. J. Davenport and H. S. Isaacs, Corrosion Science, 1993. **34**(1): p. 41.

9. L. Xia and R. L. McCreery, Journal of the Electrochemical Society, 1998. **145**(9): p. 3083.

10. M. W. Kendig and R. G. Buchheit, Corrosion, 2003. **59**(5): p. 379.

11. P. A. Schweitzer, *Encyclopedia of Corrosion Technology; Second Edition, Revised and Expanded*. 2004.

12. P. Chandrasekhar, *Conducting Polymers, Fundamentals and Applications: A practical Approach*. 1999: Kluwer Academic Publishers, Hingham, MA.

13. H. Shirakawa, E. J. Louis, A. G. MacDiarmid, C. K. Chiang and A. J. Heeger, Journal of the Chemical Society, Chemical Communications, 1977(16): p. 578.

14. G. G. Wallace, G. M. Spinks and L. A. P. Kane-Maguire, *Conductive Electroactive Polymers: Intelligent Materials Systems, Second Edition*. 2002.

15. S. K. Dhawan and D. C. Trivedi, Journal of Applied Polymer Science, 1995. **58**(4): p. 815.

16. M.-C. Bernard, V. T. Bich, S. Cordoba de Torresi and A. Hugot-Le Goff, Synthetic Metals, 1997. **84**(1-3): p. 785.

17. M.-A. De Paoli, A. Zanelli, M. Mastragostino and A. M. Rocco, Journal of Electroanalytical Chemistry, 1997. **435**(1-2): p. 217.

18. B. Sankaran and J. R. Reynolds, Macromolecules, 1997. **30**(9): p. 2582.

19. R. Kingston, Chemistry in Britain, 1999. **35**(10): p. 24.

20. M. C. Bernard and A. Hugot-Le Goff, Synthetic Metals, 1999. **102**(1-3): p. 1342.

21. G. Sonmez, C. K. F. Shen, H. Meng and F. Wudl, Polymer Preprints (American Chemical Society, Division of Polymer Chemistry), 2003. **44**(2): p. 352.

22. M. Huang, W. Feng and X. Li, Shihua Jishu Yu Yingyong, 2003. **21**(5): p. 311.

23. H. H. Rmaile, D. S. Salloum and J. B. Schlenoff, Abstracts of Papers, 227th ACS National Meeting, Anaheim, CA, United States, March 28-April 1, 2004, 2004: p. POLY.

24. H.-L. Wang, M. J. Marsella, D.-K. Fu, T. M. Swager, A. G. MacDiarmid and A. J. Epstein, Book of Abstracts, 210th ACS National Meeting, Chicago, IL, August 20-24, 1995(Pt. 2): p. PMSE.

25. A. G. MacDiarmid, H.-L. Wang, J.-W. Park, D.-K. Fu, M. J. Marsella, T. M. Swager, Y. Wang, D. D. Gebler and A. J. Epstein, Proceedings of SPIE-The International Society for Optical Engineering, 1995. **2528**(Optical and Photonic Applications of Electroactive and Conducting Polymers): p. 2.

26. S.-J. Park, W.-S. Chae and K.-J. Kim, Analytical Science & Technology, 1995. **8**(4): p. 637.

27. K. Uehara, T. Ichikawa, T. Serikawa, S. Yoshikawa, S. Ehara and M. Tsunooka, Thin Solid Films, 1998. **322**(1-2): p. 198.

28. R. Pokrop, M. Zagorska, M. Kulik, I. Kulszewicz-Bajer, B. Dufour, P. Rannou, A. Pron, E. Gondek and J. Sanetra, Molecular Crystals and Liquid Crystals, 2004. **415**: p. 93.

29. T. Umeda, Y. Hashimoto, H. Mizukami, A. Fujii and K. Yoshino, Japanese Journal of Applied Physics, Part 1: Regular Papers, Brief Communications & Review Papers, 2005. **44**(6A): p. 4155.

30. V. Seshadri and G. A. Sotzing, Optical Science and Engineering, 2005. **99**(Organic Photovoltaics): p. 495.

31. A. A. Apostoluk, L. Rocha, C. Fiorini-Debuisschert, C. Sentein, P. Raimond, L. Setti, A. Fraleoni-Morgera and J.-M. Nunzi, Materials Science, 2005. **22**(4): p. 397.

32. K. C. Persaud, Materials Today (Oxford, United Kingdom), 2005. **8**(4): p. 38.

33. L. Jiang, H.-K. Jun, Y.-S. Hoh, J.-O. Lim, D.-D. Lee and J.-S. Huh, Sensors and Actuators B: Chemical, 2005. **105**(2): p. 132.

34. P. Anzenbacher, K. Jursikova, D. Aldakov, M. Marquez and R. Pohl, Tetrahedron, 2004. **60**(49): p. 11163.

35. M. Ferreira, C. J. L. Constantino, J. Riul, A., K. Wohnrath, R. F. Aroca, J. A. Giacometti, J. Oliveira, O. N. and L. H. C. Mattoso, Polymer, 2003. **44**(15): p. 4205.

36. E. Sezer, O. Yavuz and A. S. Sarac, Journal of the Electrochemical Society, 2000. **147**(10): p. 3771.

37. H. B. Mark, Jr. and J. F. Rubinson, Proceedings - Electrochemical Society, 1999. **99-23**(Chemical Sensors IV): p. 104.

38. J. N. Barisci, T. W. Lewis, G. M. Spinks, C. O. Too and G. G. Wallace, Journal of Intelligent Material Systems & Structures, 1998. **9**(9): p. 723.

39. A. Montanari, A. Pezzani, A. Cassara, A. Quaranta and R. Lupi, Progress in Organic Coatings, 1996. **29**(1-4): p. 159.

40. P. J. Kinlen, J. E. Heider and D. E. Hubbard, Sensors and Actuators, B: Chemical, 1994. **B22**(1): p. 13.

41. M. Zhu, Z. Jiang and W. Jing, Sensors and Actuators B: Chemical. **In Press, Corrected Proof**.

42. A. A. Syed, E. Genies and C. Santier, Mater. Solid State Batteries, Proc. Reg. Workshop, 1986: p. 435.

43. K. West, B. Zachau-Christiansen, T. Jacobsen, E. Hiort-Lorenzen and S. Skaarup, British Polymer Journal, 1988. **20**(3): p. 243.

44. P. Huelser and F. Beck, Journal of the Electrochemical Society, 1990. **137**(7): p. 2067.

45. R. S. Fishman, D. A. Kurtze and G. P. Bierwagen, Progress in Organic Coatings, 1993. **21**(4): p. 387.

46. M. R. Tarasevich, G. V. Zhutaeva and K. A. Radyushkina, Russian Journal of Electrochemistry (Translation of Elektrokhimiya), 1995. **31**(10): p. 1064.

47. X. L. Wei, Y. Z. Wang, S. M. Long, C. Bobeczko and A. J. Epstein, Journal of the American Chemical Society, 1996. **118**(11): p. 2545.

48. A. Zalewska, W. Wieczorek and J. Przyluski, New Materials for Fuel Cell and Modern Battery Systems II, Proceedings of the International Symposium on New Materials for Fuel Cell and Modern Battery Systems, 2nd, Montreal, July 6-10, 1997, 1997: p. 850.

49. J. Kan, H. Xue and S. Mu, Journal of Power Sources, 1998. **74**(1): p. 113.

50. J. K. S. Mu, Journal of the Electrochemical Society of India, 2000. **49**(2): p. 103.

51. K. Chang, T. Viswanathan and L. Qiu, Abstracts of Papers, 222nd ACS National Meeting, Chicago, IL, United States, August 26-30, 2001, 2001: p. PMSE.

52. J. Kan, L. Xiang and L. Yongfang, Bulletin of Electrochemistry, 2002. **18**(10): p. 477.

53. A. Lisowska-Oleksiak, Zeszyty Naukowe Politechniki Gdanskiej, Chemia, 2002. **50**: p. 3.

54. M. Despotopoulou and M. T. Burchill, Progress in Organic Coatings, 2002. **45**(2-3): p. 119.

55. Z.-Y. Yang, L. Wang, N. E. Drysdale and M. Doyle, Macromolecules, 2003. **36**(22): p. 8205.

56. W. A. Ferrando, Journal of Power Sources, 2004. **130**(1-2): p. 309.

57. T. W. Lewis, G. G. Wallace, C. Y. Kim and D. Y. Kim, Synthetic Metals, 1997. **84**(1-3): p. 403.

58. Terje A. Skotheim, Ronald L. Elsenbaumer, John R. Reynolds, *Handbook of conducting polymers, 2nd ed.* 1998, New York: M. Dekker.

59. A. G. MacDiarmid, J. C. Chiang, M. Halpern, W. S. Huang, S. L. Mu, N. L. D. Somasiri, W. Wu and S. I. Yaniger, Molecular Crystals and Liquid Crystals, 1985. **121**(1-4): p. 173.

60. M. Galkowski, M. A. Malik, P. J. Kulesza, H. Bala, K. Miecznikowski, R. Wlodarczyk, L. Adamczyk and M. Chojak, Journal of the Electrochemical Society, 2003. **150**(6): p. B249.

61. M. Tiitu, A. Talo, O. Forsen and O. Ikkala, Polymer. **In Press, Corrected Proof**.

62. A. Mirmohseni, K. Valiegbal, G. G. Wallace, Journal of Applied Polymer Science, 2003. **90**(9): p. 2525.

63. J. O. Stoffer, O. C. Sitton, N. I. D. Somasiri and L. C. Hung, Polymeric Materials Science and Engineering, 1991. **65**: p. 230.

64. F. D. R. Amado, E. Gondran, J. Z. Ferreira, M. A. S. Rodrigues and C. A. Ferreira, Journal of Membrane Science, 2004. **234**(1-2): p. 139.

65. W. Pan, S. L. Yang, G. Li and J. M. Jiang, European Polymer Journal, 2005. **41**(9): p. 2127.

66. E. Ruckenstein and S. Yang, Polymer, 1993. **34**(22): p. 4655.

67. S. P. Armes, M. Aldissi and S. F. Agnew, Synthetic Metals, 1989. **28**(1-2): p. C837.

68. R. Racicot, R. L. Clark, H. B. Liu, S. C. Yang, M. N. Alias and R. Brown, *Thin film conductive polymers on aluminum surfaces: interfacial charge-transfer and anticorrosion aspects*, in *Proceedings of SPIE-The International Society for Optical Engineering*. 1995. p. 251.

69. R. J. Racicot, R. L. Clark, H. B. Liu, S. C. Yang, M. N. Alias and R. Brown, Materials Research Society Symposium Proceedings, 1996. **413**(Electrical, Optical, and Magnetic Properties of Organic Solid State Materials III): p. 529.

70. R. J. Racicot, S. C. Yang and R. Brown, Materials Research Society Symposium Proceedings, 1997. **458**(Interfacial Engineering for Optimized Properties): p. 415.

71. R. Racicot, R. Brown and S. C. Yang, Synthetic Metals, 1997. **85**(1-3): p. 1263.

72. S. C. Yang, R. J. Racicot, R. L. Clark, H. Liu, R. Brown and M. N. Alias, *Electroactive polymer coatings for corrosion control on metal*. 1997, (The Board of Governors for Higher Education, State of Rhode Island and Providence Plantations, USA). Application: WO

WO. p. 41 pp.

73. S. C. Yang, R. Brown, R. Racicot, Y. Lin and F. McClarnon, ACS Symposium Series, 2003. **843**(Electroactive Polymers for Corrosion Control): p. 196.

74. D. E. Tallman, Y. Pae and G. P. Bierwagen, Corrosion (Houston), 2000. **56**(4): p. 401.

75. S. F. Cogan, M. D. Gilbert, G. L. Holleck, J. Ehrlich and M. H. Jillson, Journal of the Electrochemical Society, 2000. **147**(6): p. 2143.

76. A. J. Epstein, J. A. O. Smallfield, H. Guan and M. Fahlman, Synthetic Metals, 1999. **102**(1-3): p. 1374.

77. J. He, V. J. Gelling, D. E. Tallman and G. P. Bierwagen, Polymer Preprints (American Chemical Society, Division of Polymer Chemistry), 2000. **41**(2): p. 1774.

78. N. G. Thompson and J. H. Payer, *Corrosion Testing Made Easy: DC Electrochemical Test Methods*. 1998, Houston, TX: National Association of Corrosion Engineers.

79. W. S. Tait, *An Introduction to Electrochemical Corrosion Testing for Practicing Engineers & Scientists*. 1994, St. Clair, Racine, WI, USA: Pair O Docs Pubns.

80. R. B. Sheldon, W. Dean, J. Hack, H. P. Haynes, G. S. Scully, J. R. Sprowls, *Corrosion Tests and Standards: Application and Interpretation*. 1995: ASTM Philadelphia, PA 19103.

81. U. Rammelt and G. Reinhard, Progress in Organic Coatings, 1992. **21**(2-3): p. 205.

82. A. Amirudin, Progress in Organic Coatings, 1995. **26**(4): p. 1.

83. W. Furbeth, Corrosion, 2000. **56**(7): p. 768.

84. R. Cottis, S. Turgoose, Electrochemical Impedance and Noise, NACE International, Houston, TX

85. F. Mansfeld, C. H. Tsai and H. Shih, ASTM Special Technical Publication, 1992. **STP 1154**(Comput. Model. Corros.): p. 186.

86. E. P. M. van Westing, G. M. Ferrari and J. H. W. De Wit, Corrosion Science, 1993. **34**(9): p. 1511.

87. B. Boukamp, Equivalent Circuit (EQUIVCRT.PAS) Users Manual 2nd, revised edition, CT88/265/128, CT89/214/128, University of Twente, Enschede, the Netherlands 1989.

88. S. A. Ashraf, F. Chen, C. O. Too and G. G. Wallace, Polymer, 1996. **37**(13): p. 2811.

89. J. A. Walker, L. F. Warren, E. F. Witucki, Journal of Polymer Science Part A: Polymer Chemistry, 1988. **26**(5): p. 1285.

90. Y. Xia, J. M. Wiesinger, A. G. MacDiarmid and A. J. Epstein, Chemistry of Materials, 1995. **7**(3): p. 443.

91. J. K. Avlyanov, Y. Min, A. G. MacDiarmid and A. J. Epstein, Synthetic Metals, 1995. **72**(1): p. 65.

92. K. Kaeriyama and H. Masuda, Synthetic Metals, 1991. **41**(1-2): p. 389.

93. H. Masuda and K. Kaeriyama, Journal of Materials Science, 1991. **26**(20): p. 5637.

94. K. Kaeriyama and H. Masuda, British Polymer Journal, 1990. **23**(1-2): p. 141.

95. T. Schauer, A. Joos, L. Dulog and C. D. Eisenbach, Progress in Organic Coatings, 1998. **33**(1): p. 20.

96. P. Li, T. C. Tan and J. Y. Lee, Synthetic Metals, 1997. **88**(3): p. 237.

97. J. He, V. J. Gelling, D. E. Tallman and G. P. Bierwagen, Journal of the Electrochemical Society, 2000. **147**(10): p. 3661.

98. D. E. Tallman, Y. Pae and G. P. Bierwagen, Corrosion, 2000. **56**(4): p. 401.

99. B. del Amo, L. Veleva, A. R. Di Sarli and C. I. Elsner, Progress in Organic Coatings, 2004. **50**(3): p. 179.

100. W. J. Lorenz and F. Mansfeld, Corrosion Science, 1981. **21**(9-10): p. 647.

101. B. Wessling, Advanced Materials, 1994. **6**(3): p. 226.

102. D. A. Wrobleski, B. C. Benicewicz, K. G. Thompson and C. J. Bryan, Polymer Preprints (American Chemical Society, Division of Polymer Chemistry), 1994. **35**(1): p. 265.

103. W.-K. Lu, *Corrosion protection of steels by coatings containing electrically conductive polymers*. 1996. p. 139 pp.

104. P. J. Kinlen, V. Menon and Y. W. Ding, Journal of the Electrochemical Society, 1999. **146**(10): p. 3690.

105. J. He, V. J. Gelling, D. E. Tallman, G. P. Bierwagen and G. G. Wallace, Journal of the Electrochemical Society, 2000. **147**(10): p. 3667.

106. C. Vargel, *Corrosion of aluminium*. 2004: Elsevier Science.

107. Personal Communication, D. E. Tallman

108. V. J. Gelling, *The study of polypyrrole as a corrosion inhibitor of aluminum alloy 2024-T3*. 2002. p. 220 pp.

109. P. J. Kinlen, V. Menon and Y. Ding, Journal of the Electrochemical Society, 1999. **146**(10): p. 3690.

110. T. P. McAndrew, Trends in Polymer Science (Cambridge, United Kingdom), 1997. **5**(1): p. 7.

111. B. C. Beard and P. Spellane, Chemistry of Materials, 1997. **9**(9): p. 1949.

112. M. C. Bernard, A. Hugot-LeGoff, S. Joiret, N. N. Dinh and N. N. Toan, Synthetic Metals, 1999. **102**(1-3): p. 1383.

113. R. M. Torresi, S. de Souza, J. E. Pereira da Silva and S. I. Cordoba de Torresi, Electrochimica Acta, 2005. **50**(11): p. 2213.

114. J. C. Seegmiller, J. E. Pereira da Silva, D. A. Buttry, S. I. Cordoba de Torresi and R. M. Torresi, Journal of the Electrochemical Society, 2005. **152**(2): p. B45.

115. T. D. Nguyen, T. A. Nguyen, M. C. Pham, B. Piro, B. Normand and H. Takenouti, Journal of Electroanalytical Chemistry, 2004. **572**(2): p. 225.

116. A. Hugot-Le Goff and M. C. Bernard, Synthetic Metals, 1993. **60**(2): p. 115.

117. J. E. P. da Silva, S. I. C. de Torresi, D. L. A. de Faria and M. L. A. Temperini, Synthetic Metals, 1999. **101**(1-3): p. 834.

118. A. G. MacDiarmid and A. J. Epstein, Synthetic Metals, 1994. **65**(2-3): p. 103.

119. J. E. Pereira da Silva, D. L. A. de Faria, S. I. Cordoba de Torresi and M. L. A. Temperini, Macromolecules, 2000. **33**(8): p. 3077.

120. J. Tanaka, N. Mashita, K. Mizoguchi and K. Kume, Synthetic Metals, 1989. **29**(1): p. 175.

121. T. Hagiwara, T. Demura and K. Iwata, Synthetic Metals, 1987. **18**(1-3): p. 317.

Appendix A.1

Fitting parameters of EIS data for bare AA2024-T3 in DHS

Exposure time (h)	Y_{dl}	n_{dl}	R_{ct} (Ω)	χ^2
1	1.7E-05	0.91	5.7E+04	7.3E-03
24	1.7E-05	0.89	3.5E+04	3.2E-03
48	2.0E-05	0.87	2.4E+04	6.6E-03
216	3.7E-05	0.84	2.5E+03	4.1E-03

Appendix A.2

Fitting parameters of EIS data for "air dried" Pan/co-poly coated AA2024-T3 in DHS

Exposure time (h)	Y_c	n_c	R_c	χ^2
48	5.4E-07	0.68	2.6E+03	6.2E-03
120	5.6E-07	0.67	1.7E+03	5.7E-03
216	8.2E-07	0.63	1.9E+03	8.9E-04
432	1.3E-06	0.60	8.8E+02	9.7E-04

	Y_{dl}	n_{dl}	R_{ct}	
1	2.1E-05	0.85	9.9E+03	9.5E-03
48	3.5E-05	0.61	5.8E+04	
120	4.1E-05	0.59	6.3E+04	
216	5.6E-05	0.54	5.0E+04	
432	4.6E-05	0.65	3.4E+04	

Appendix A.3

Fitting parameters of EIS data for "heat treated" Pan/co-poly coated AA2024-T3 in DHS

Exposure time (h)	Y_c	n_c	R_c	χ^2
3	4.5E-07	0.72	1.9E+02	2.2E-03
48	3.4E-07	0.71	3.3E+02	9.7E-04
168	4.0E-07	0.70	3.7E+02	7.9E-04
312	4.0E-07	0.71	2.9E+02	5.8E-04
504	3.6E-07	0.71	3.7E+02	6.1E-04

	Y_2	n_2	R_2
3			
48	3.1E-06	0.76	8.0E+02
168	3.2E-06	0.81	4.6E+02
312	8.1E-06	0.71	4.2E+02
504	9.1E-06	0.64	5.8E+02

	Y_{dl}	n_{dl}	R_{ct}
3	1.4E-05	0.90	3.6E+04
48	1.3E-05	0.91	2.8E+05
168	1.4E-05	0.88	3.7E+05
312	9.1E-06	0.93	4.0E+05
504	1.1E-05	0.93	1.9E+05

Appendix A.4

Fitting parameters of EIS data for P3OP-pTS synthesised using method by Ashraf coated AA2024-T3 in DHS

Exposure time (h)	Y_c	n_c	R_c	W_R	W_T	W_P	χ^2
1	4.8E-06	0.60	3.5E+03	3.8E+04	4.2E-01	4.7E-01	3.2E-03
24	3.3E-08	0.84	5.4E+02	7.0E+04	1.6E-00	4.9E-01	1.7E-03
216				3.9E+04	7.2E-01	4.5E-01	4.7E-03

Appendix A.5

Fitting parameters of EIS data for electrochemically synthesised P3OP-ClO_4 deposit fraction coated AA2024-T3 in DHS

Exposure time (h)	Y_c	n_c	R_c	χ^2
1	1.1E-07	0.84	1.2E+04	3.3E-03
48	3.3E-07	0.79	7.8E+03	5.4E-03
216	2.8E-07	0.82	5.3E+03	6.9E-03

	Y_{dl}	n_{dl}	R_{ct}
1	1.1E-05	0.84	1.25E+05
48	8.5E-06	0.82	2.08E+06
216	8.3E-06	0.79	3.53E+06

Appendix A.6

Fitting parameters of EIS data for electrochemically synthesised P3OP-ClO_4 solution fraction coated AA2024-T3 in DHS

Exposure time (h)	Y_c	n_c	R_c	χ^2
1	6.7E-06	7.4E-01	1.5E+02	2.8E-02

	Y_{dl}	n_{dl}	R_{ct}	χ^2
1	1.7E-05	8.7E-01	3.3E+02	
120	1.5E-05	8.7E-01	1.9E+03	2.5E-02
216	1.2E-05	7.1E-01	3.1E+03	6.2E-03

Appendix A.7

Fitting parameters of EIS data for electrochemically synthesised P3OP-pTS solution fraction coated AA2024-T3 in DHS

Exposure time (h)	Y_{dl}	n_{dl}	R_{ct}	χ^2
1	2.11E-06	6.76E-01	2.62E03	1.09E-02
24	2.40E-06	6.88E-01	3.70E+03	4.39E-03
216	1.17E-05	4.63E-01	1.65E+04	4.26E-03

Appendix A.8

Fitting parameters of EIS data for chemically synthesised P3OP-ClO_4 coated AA2024-T3 in DHS

Exposure time (h)	Y_{dl}	n_{dl}	R_{ct}	χ^2
2	1.35E-05	0.59	3.40E+05	5.00E-02
48	2.14E-05	0.89	3.44E+05	1.47E-03
144	1.91E-05	0.88	4.46E+05	5.03E-04
384	1.77E-05	0.89	5.54E+05	3.07E-3
672	1.99E-05	0.86	1.22E+05	9.32E-04

Appendix A.9

Fitting parameters of EIS data for chemically synthesised P3OP-pTS coated AA2024-T3 in DHS

Exposure time (h)	Y_c	n_c	R_c	χ^2
2	3.51E-06	0.92	3.54E+03	1.45E-02
48	2.09E-06	0.92	2.41E+04	5.97E-04
144	1.78E-06	0.92	4.75E+04	1.52E-03
312	1.69E-06	0.91	3.40E+04	1.9E-03

	Y_{dl}	n_{dl}	R_{ct}
2	4.35E-06	0.82	3.31E+04
48	3.82E-06	0.82	1.66E+05
144	9.66E-06	0.84	1.54E+05
312	1.98E-05	0.72	1.17E+05